Quantitative coherent anti-Stokes Raman scattering micro-spectroscopy:

Theory and applications

Von der Fakultät Mathematik und Physik der Universität Stuttgart
zur Erlangung der Würde eines Doktors der Naturwissenschaften
(Dr. rer. nat.) genehmigte Abhandlung

Vorgelegt von

Dipl. phys. Dipl. Ing. (BA) Gregor F. M. Hehl

aus Stuttgart

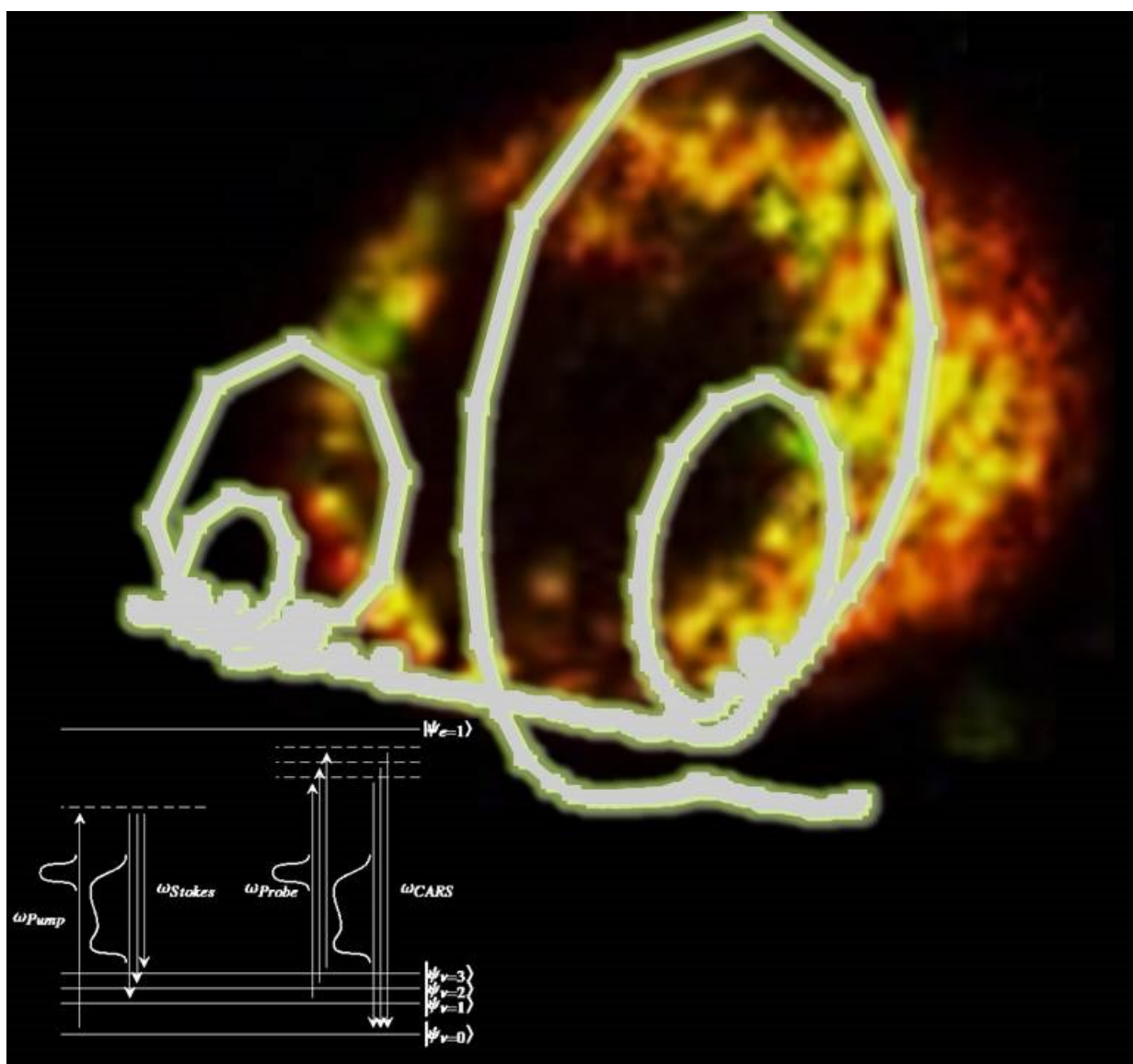Hauptberichter: Prof. Dr. Jörg Wrachtrup
Mitberichter: Prof. Dr. Martin Dressel

Tag der mündlichen Prüfung: 16.04.2015

Durchgeführt am 3. Physikalischen Institut der Universität Stuttgart
in der Arbeitsgruppe von Dr. Andreas Volkmer

2015

Meiner Mutter Ingeborg Anna Hehl gewidmet

Contents

1 Einleitung

Eine Vielzahl wissenschaftlicher Erkenntisse sind durch die optische Spektroskopie, der Untersuchung der Wechselwirkung von Licht mit Materie, erzielt worden. Allen Techniken gemeinsam ist, daß aufgrund der Untersuchung der gestreuten Strahlung Information über die untersuchte Probe gewonnen wird. Unter denjenigen Spektroskopiemethoden, die sichtbares oder infrarotes Licht verwenden, bieten die Vibrationsspektroskopien wie die spontane Raman Spektroskopie den großen Vorteil, dass sie keine Marker benötigen und es somit gestatten, die Physik oder Chemie einer Probe betreffende Informationen ohne jegliche Probenpräparation zu ermitteln. Die Kombination von spontaner Raman-Spektroskopie mit optischer Mikroskopie ergibt ein Werkzeug, das in der Lage ist Strukturen auf der sub-μm Skala zu untersuchen. Der Nachteil der spontanen Raman-Spektroskopie ist allerdings der geringe Streuquerschnitt, der sich in lange Aufzeichnungsdauern für Spektren übersetzt, die es oft verhindern bspw. niedrig konzentrierte Proben zu untersuchen. Andere Techniken, wie die oberflächenverstärkte Raman Spektroskopie (engl. Surface-enhanced Raman spectroscopy (SERS)) oder die spitzenverstärkte Raman Spektroskopie (engl. Tip-enhanced Raman spectroscopy (TERS)), überkommen diese Begrenzung, indem das gemessene Signal um mehrere Größenordnungen angehoben wird. Sie beruhen allerdings auf einem direkten Kontakt der Probe mit einem Substrat oder einer Spitze und gehören deshalb zu den invasiven Methoden. Mit dem Aufkommen der Kohärenten Anti-Stokes-Raman-Streuung (engl. Coherent anti-Stokes Raman Scattering (CARS)) Mikrospektroskopie war es erstmals möglich, diesen Nachteil zu beseitigen: Nun konnte die Aufzeichnungsdauer von Spektren um bis zu drei Größenordnungen reduziert werden. Die Herausforderung bei der Verwendung der CARS-Mikrospektroskopie besteht nunmehr in der Aufbereitung der Spektren.

Die Theorie besagt, dass CARS- und spontane Raman-Spektroskopie denselben Informationsgehalt aufweisen. Dies konnte unter Verwendung von Phasenrückgewinnung der komplexen Suszeptibilität und anschließender Rekonstruktion der spontanen Ramanantwort bereits für Proben mit stark überlappenden Banden gezeigt werden (siehe Rinia et. al. [1]). Eine überzeugende Rekonstruktion der spontanen Ramanantwort in Fällen bei welchen vibronische und elektronische Antwort der Probe spektral überlappen stand jedoch bis heute aus. Sobald diese Bedingung erfüllt ist, ist das Ergebnis einer allein auf Phasenrückgewinnung basierenden Rekonstruktion

falsch. Dieses Unvermögen der anerkannten Rekonstruktionsmethoden, die korrekte vibronische Antwort $\chi_{Res}^{(3)}(\nu)$ bei gegebener spektraler Überlappung mit der elektronischen Antwort $\chi_E^{(3)}$ zu rekonstruieren, stellte selbstverständlich ein schwerwiegendes Problem dar. Dies manifestiert sich besonders bei der Rekonstruktion spektral hochaufgelöster Spektren, die stark überlappende Banden aufweisen und somit besonders empfindlich auf Phasenfehler sind (siehe Camp et. al. [2]). Diese Situation verschärfte sich sogar noch für Mischungen unterschiedlicher chemischer Komponenten. Auf der Basis derartig rekonstruierter Spektren konnten somit keinerlei quantitative Aussagen getroffen werden. Die Entwicklung und Anwendung einer Methode, die die quantitative Interpretation der erhaltenen Spektren erlaubt, ist zentraler Aspekt dieser Arbeit. Es wird dargelegt, dass selbst bei signifikanter spektraler Überlappung zwischen vibronischer Suszeptibilität $\chi_{Res}^{(3)}(\nu)$ und elektronischer Suszeptibilität $\chi_E^{(3)}$ bei Anwendung dieser neuen Technik CARS- und spontane Raman-Mikrospektroskopie denselben Informationsgehalt aufweisen. Zur Phasenrückgewinnung wird die Maximum-Entropie-Methode (MEM) verwendet. Bei Beginn dieser Arbeit veranschlagte die MEM basierte Berechnung der Phasenspektren deutlich mehr Zeit als die Aufzeichnungsdauern der Spektren betrug. Eine Reduktion des Rechenaufwands um drei Größenordnungen war wünschenswert. In dieser Arbeit wird ein solcher Algorithmus entwickelt und präsentiert. Ein anderer Mangel der MEM-basierten Phasenrückgewinnung betraf die Endbereiche der Phasenspektren, wo deutliche Abweichungen von den tatsächlichen Phasenspektren auffielen. Dieses Problem wird in dieser Arbeit durchgehend als Fensterung bezeichnet werden und es werden Methoden zur Vermeidung dieser Fensterung entwickelt und präsentiert. Die Rauschunterdrückung von Sätzen von Spektren unter Verwendung der Singulärwertzerlegungsmethode (engl. singular value decomposition (SVD) method), die vor sechs Jahren Standard war, stellt ein anderes Thema dar. Unter gewissen Bedingungen resultierte SVD in verfälschten Spektren, was eine robustere Methode zur Rauschunterdrückung notwendig machte. Eine neuartige und auf alle Arten von hyperspektralen Daten anwendbare Rauschunterdrückungsmethode wird vorgeschlagen. Sie bewies sich auch noch in Fällen, in denen SVD nicht mehr verwendet werden kann (siehe Abschnitt A.4.2). Letztendlich wurde der Einfluss des effektiven nichtresonanten Untergrundes auf rekonstruierte $Im[\chi_{Res}^{(3)}(\nu)]$ Amplituden bislang nicht ausreichend erörtert und wird deshalb in Appendix A.6.1 diskutiert. Ausgestattet mit dieser neuen und leistungsstarken Technik werden einige aktuelle Fragestellungen der Material- und Biowissenschaften in einer Art und Weise beleuchtet, wie es keine andere Spektroskopietechnik momentan vermag.

Die erste Anwendung stellt die Gewinnung von hoch aufgelöster 3D Strukturinformation von Polymeren dar. Da solche Messungen hunderttausende von Spektren beinhalten können und somit bei Verwendung von spontaner Ramanspektroskopie viele Stunden Zeit in Anspruch nehmen würden, waren derartige Messungen bisher nicht praktikabel. CARS-Mikrospektroskopie hingegen erlaubt die Gewinnung hoch aufgelöster 3D Strukturinformation binnen Minuten. Die

zweite Anwendung verwendet CARS-Mikrospektroskopie zur quantitativen und nichtinvasiven Analyse der chemischen Struktur biologisch relevanter Lipide. In den Biowissenschaften stellt die Aufnahme und der intrazelluläre Transport von Lipoproteinen niedriger Dichte (engl. low density Lipoprotein (LDL)) in menschlichen Makrophagen ein hochaktuelles Thema dar. Die Verwendung invasiver Methoden erlaubt die Untersuchung einiger Aspekte der LDL Aufnahme und des intrazellulären LDL Transportes wie etwa die Bestimmung der Größen von Lipid speichernden Organellen unter Verwendung von Fluoreszenzspektroskopie oder die detaillierte Bestimmung der Lipidzusammensetzung unter Verwendung von Massenspektroskopie. Die nichtinvasive und schnelle Bestimmung der chemischen Struktur biologisch relevanter Lipide in lebenden Zellen war jedoch bisher nicht möglich. Eine derartige Bestimmung von örtlicher Verteilung solcher Lipide, ihrer Kettenlängen n_{C-C}, sowie ihres Sättigungsgrades $n_{C=C}$ in lebenden menschlichen Makrophagenzellen wird sowohl auf Einzelzellen-Niveau als auch auf Einzelorganellen-Niveau demonstriert.

Die Arbeit ist wie folgt gegliedert: Im Grundlagenkapitel Kap. 3 werden die zur Beschreibung von Vibrationsspektren benötigten physikalischen Prinzipien dargelegt. Beginnend mit der spontanen Raman Streuung in Abschnitt 3.1 werden wir in Abschnitt 3.2 fortfahren mit der Beschreibung von Pico Sekunden CARS, wo die Suszeptibilität $\chi^{(3)}_{Res}$ kohärent in einem schmalen Frequenzintervall abgetastet wird. Das ps-CARS Schema wird dann in Abschnitt 3.2.1 generalisiert um ein Kontinuum vieler gleichzeitig abgetasteter Frequenzen, oder in anderen Worten, multiplex-CARS Spektroskopie, zu beschreiben. Die verschiedenen Aspekte, inwiefern die Probe oder die messtechnischen Umstände das Linienprofil von CARS Spektren beeinflussen, werden ausführlich in Abschnitt 3.2.2 behandelt. Die Rekonstruktion des spontanen Ramanspektrums beinhaltet die Phasenrückgewinnung der komplexen Suszeptibilität $\chi^{(3)}_{Res}(\nu)$. Ihre Notwendigkeit wird zusammen mit gängigen Vorgehensweisen im Abschnitt 3.3 besprochen. Die notwendigen Transformationen sind im Appendix A.1 zusammengefasst. Nach einem kurzen Vergleich der existierenden Phasenrückgewinnungsmethoden wird die Maximum Entropy Methode (MEM) erläutert. Material und Methoden, die allen Ergebniskapiteln gemein sind, sind in Kapitel 4 aufgeführt. Hier sind die zur Bestimmung von quantitativer Information aus rekonstruierten Ramanspektren verwendeten univariaten und multivariate Methoden zu finden. Probenspezifische Messbedingungen, die Probenvorbereitung betreffende Prozeduren und Ähnliches ist stets zu Beginn der Ergebniskapitel beschrieben. Im Kapitel 5 werden drei unbefriedigende Aspekte gängiger Realisierungen MEM-basierter Phasenrückgewinnung behandelt. Die in Kapitel 5 entwickelten und getesteten Werkzeuge werden zur Beantwortung aktueller Fragen der Materialwissenschaft in Kapitel 6 sowie der Biowissenschaft in Kapitel 7 und 8 verwendet, wo CARS-Mikrospektroskopie zur nichtinvasiven, quantitativen Untersuchung von biologisch relevanten Lipiden dient. Das Ergebnis des Kapitels 7 ist die Vorraussetzung zur chemischen Identifikation von Lipiden in komplexen heterogenen Systemen wie lebenden Zellen, was das

Thema des folgenden Kapitels 8 darstellt. Unabhängig der gewählten Rekonstruktionsmethode weist die CARS-Mikrospektroskopie einige Eigenarten auf, die so bei der spontanen Raman-streuung nicht gegeben sind. Diese sind der Einfluss des nichtresonanten Beitrages $\chi_{NR}^{(3)}$, des Referenzspektrums welches zur Normierung aller Spektren verwendet wird, und letztlich unterscheidet sich das Rauschen in rekonstruierten Raman Spektren von dem Rauschen in spontanen Raman Spektren. Diese Aspekte stellen die Motivation für Appendix A.6 dar. Hier werden alle denkbaren Fälle, wie ein nichtresonanter Beitrag $\chi_{NR}^{(3)}$ zu einem CARS Spektrum beitragen kann, simuliert, verglichen und detailliert diskutiert.

2 Introduction

Many insights in various scientific disciplines are owed to optical spectroscopy, the study of the interaction of light and matter. All techniques have in common that the analysis of the spectrum of the scattered light yields information regarding the matter or sample of interest. Among the spectroscopy techniques that use visible light or infrared light, vibrational spectroscopies like spontaneous Raman scattering spectroscopy offer the great advantage of being label-free and thus allow to obtain information regarding the physics or chemistry of a sample of interest without any sample preparation being necessary. The combination of spontaneous Raman scattering spectroscopy with optical microscopy results in a tool capable of analyzing structures on the sub-μm length scale. However, the disadvantage of spontaneous Raman scattering spectroscopy is the small scattering cross-section that translates into long spectrum acquisition times that often prevent the analysis of e.g. low concentrated samples. Other techniques like Surface-enhanced Raman spectroscopy (SERS) or Tip-enhanced Raman spectroscopy (TERS) overcome this limitation by increasing the measured signal by orders of magnitude, but rely on a direct contact of the sample with a substrate or a tip and thus are invasive. With the advent of Coherent anti-Stokes Raman Scattering (CARS) micro-spectroscopy it was possible to overcome this disadvantage: Now the spectrum acquisition times could be reduced by up to three orders of magnitude. The challenge when using coherent Raman scattering spectroscopy is the analysis of the spectra.

In theory, coherent Raman scattering spectroscopy yields the same information as spontaneous Raman scattering spectroscopy. This has been demonstrated by retrieving the phase of the complex susceptibility and subsequent reconstruction of the spontaneous Raman response for samples exhibiting highly overlapping bands (see Rinia et. al. [1]). However, no convincing reconstruction has been shown yet for cases when the vibrational and the electronic response of the sample spectrally overlap. Whenever this condition was fulfilled, the reconstruction result based solely on a phase retrieval was wrong. The inability of the state of the art reconstruction schemes to reconstruct the correct vibrational susceptibility $\chi_{Res}^{(3)}(\nu)$ as soon as it exhibits significant spectral overlap with the electronic susceptibility $\chi_E^{(3)}$ of course posed a serious problem. This became particularly apparent when reconstructing spectrally high resolved spectra exhibiting overlapping bands that are highly sensitive to phase errors (see Camp et. al. [2]).

The situation became even worse for mixtures of distinct chemical components. As a result, no quantitative statements could be made based on such reconstructed spectra. The development and application of such an analysis technique allowing a quantitative interpretation of the obtained spectra is the central topic of this thesis. It will be demonstrated that when using this new technique the same information is obtained by means of fast CARS micro-spectroscopy, as when spontaneous Raman scattering spectroscopy is used even in cases where the vibrational and the electronic susceptibilities $\chi_{Res}^{(3)}(v)$ and $\chi_E^{(3)}$, respectively, exhibit significant spectral overlap. The phase retrieval will be performed using the maximum entropy method (MEM). When starting this thesis, the MEM based calculation of the phase spectra required significantly more time than the acquisition of the spectra. A reduction of the computational time for the MEM based phase retrieval by three orders of magnitude was desirable. In this thesis such an algorithm will be developed and presented. Another shortcoming of the MEM based phase retrieval concerned the spectral ends of the phase spectra, where strong deviations from the true phase spectra could be observed. This problem will be referred to as windowing throughout this thesis and methods to prevent this windowing are developed and presented. Another topic concerns the denoising of sets of spectra using the singular value decomposition (SVD) method that was state of the art six years ago. On certain conditions SVD turned out to result in falsified spectra and a more robust method for the denoising was needed. Such a new denoising scheme, applicable for all kinds of hyperspectral data will be proposed, that showed to be still applicable, where SVD cannot be used (see section A.4.2). Finally, the impact of the effective nonresonant background on the reconstructed $Im[\chi_{Res}^{(3)}(v)]$ amplitudes was found to be not considered enough so far and will be discussed in appendix A.6.1. With these new and powerful techniques light will be shed on topics of current research in the material and life sciences in a way, no other spectroscopy technique is capable of.

The first application is the extraction of highly resolved 3D physical structure information of polymers. Because such a measurement involves hundreds of thousands of spectra and would take many hours this is not feasable using spontaneous Raman spectroscopy, whereas multiplex CARS microscopy allows highly resolved 3D physical structure information extraction within minutes. The second application uses multiplex CARS microscopy for the quantitative and noninvasive analysis of the chemical structures of biologically relevant lipids. In life science, the uptake and intracellular transport of low density lipoproteins (LDL) in human macrophages is of high interest. The use of invasive methods allowed to analyze certain aspects of the LDL uptake and intracellular transport such as the determination of the size of lipid organelles using fluorescence spectroscopy or of the detailed lipid composition using mass spectroscopy. It was however not possible to determine the chemical structures of biologically relevant lipids in a non-invasive and fast manner inside the living cell. This will be directly demonstrated in living human macrophages by characterizing the spatial distribution of lipids, of their chain length

n_{C-C}, and of their degrees of acyl chain unsaturation $n_{C=C}$ on the single-cell and single-organelle levels.

   This thesis is organized as follows: In the fundamentals ch. 3 the physical principles needed in order to describe vibrational spectra are given. Starting with spontaneous Raman scattering spectroscopy, we will proceed describing picosecond CARS, where the susceptibility $\chi_{Res}^{(3)}$ of interest is probed in a coherent way in one narrow frequency interval. This scheme will be generalized in order to describe a continuum of many simultaneously probed frequencies, or in other words, multiplex-CARS spectroscopy. Emphasis is put on the various aspects, how the lineshape of the CARS spectra is influenced by the sample and/or the measurement conditions. The reconstruction of the spontaneous Raman spectrum involves the retrieval of the phase of the complex susceptibility $\chi_{Res}^{(3)}(\nu)$. Its necessity along with the state of the art approaches is discussed in section 3.3. The transforms involved are discussed in the appendix A.1. After a short comparison of existing phase retrieval methods, the maximum entropy method (MEM) will be discussed. The materials and methods shared by the results chapters are given in ch. 4. The methods used to extract quantitative information out of reconstructed Raman data, involving univariate and multivariate analysis methodology, are given here. Sample specific measurement conditions, sample preparation procedures etc. can be found in the materials section at the beginning of each result chapter. Three unsatisfactory aspects in the current realisations of MEM-based spectral phase retrieval will be addressed in ch. 5. The tools that have been developed and tested in chapter 5 are applied two answer open questions in material science in chapter 6 and in lipidomics in chapter 7 and 8, where CARS micro-spectroscopy is used for the quantitative and noninvasive analysis of the chemical structures of biologically relevant lipids. The results of chapter 7 serve as a prerequisite for the chemical identification of lipids in complex and heterogeneous systems, such as living cells, which will be the subject of ch. 8. Independent of the reconstruction scheme used, hyperspectral CARS imaging has some peculiarities that do not exist in spontaneous Raman scattering. These are the influence of the nonresonant part of $\chi_{NR}^{(3)}$, the influence of the reference spectrum used to normalize all spectra with, and finally the noise in reconstructed CARS spectra differs from the noise in spontaneous Raman spectra. These aspects are the motivation for the appendix A.6, where first all possible cases, how the nonresonant part of $\chi_{NR}^{(3)}$ can contribute to the CARS spectrum are simulated, compared and discussed in detail.

3 Fundamentals

In this chapter first the classical description of Raman scattering is presented, starting with the Maxwell equations that describe the interaction of light with matter. Spontaneous Raman scattering (SR) can then be seen as the incoherent special case of the third-order scattering process discussed here, coherent anti-Stokes Raman-scattering (CARS). After a brief historical overview for each scattering process, each process will first be described semi-classically, and then the connection to the quantum mechanical description will be drawn.

The representations used to discuss the analogies and differences among the scattering processes will be the susceptibility in the complex plane and the quantum mechanical picture. The descriptions of the spontaneous and coherent Raman effects are based on refs. [3], [4], [5], and [6]. In a nonmagnetic medium with relative permeability $\mu_r = 1$, a magnetic field $\mathbf{B} = \mu_0 \mathbf{H}$, the vacuum permeability μ_0, and the magnetic field strength $\mathbf{H}$, the Maxwell equations read:

$$\nabla \mathbf{B} = 0 \tag{3.1}$$

$$\nabla(\epsilon_0 \mathbf{E} + \mathbf{P}) = \rho_{free} \tag{3.2}$$

$$\nabla \times \mathbf{H} = \frac{\partial}{\partial t}(\epsilon_0 \mathbf{E} + \mathbf{P}) + \mathbf{j} \tag{3.3}$$

$$\nabla \times \mathbf{E} = -\frac{\partial}{\partial t}\mathbf{B}. \tag{3.4}$$

Here, ϵ_0 denotes the vacuum permittivity, $\mathbf{E}$ the electric field, and $\mathbf{P}$ the polarization. We assume that the medium has neither free currents $\mathbf{j}$ nor free charges ρ_{free}. So we set $\mathbf{j} = 0$ and $\rho_{free} = 0$. The vacuum permittivity ϵ_0 and permeability μ_0 are linked with the vacuum speed of light $c_0 = \sqrt{\frac{1}{\epsilon_0 \mu_0}}$. The material dependent relative permittivity ϵ_r and permeability μ_r are linked with the index of refraction $n = \sqrt{\epsilon_r \mu_r}$. The electric susceptibility χ_{el} and magnetic susceptibility χ_{mag} are then given by $\epsilon_r = 1 + \chi_{el}$ and $\mu_r = 1 + \chi_{mag}$, respectively. As we defined $\chi_{mag} = 0$, for the remainder of this thesis any susceptibilities are of electric nature. By taking the curl of eq. 3.4 and some rearrangements, we find the wave equation

$$\nabla \times \nabla \times \mathbf{E}(\mathbf{r}, t) + \frac{\partial^2 \mathbf{E}(\mathbf{r}, t)}{c_0^2 \partial t^2} = -\frac{\partial^2 \mathbf{P}(\mathbf{r}, t)}{\epsilon_0 c_0^2 \partial t^2}. \tag{3.5}$$

The induced polarization $\mathbf{P}$ is in general a nonlinear function of the electric field. When we introduce the wave vector $\mathbf{k}$ and the frequency ω of the electric field $\mathbf{E}(\omega, \mathbf{k})$ and expand this

induced polarization $\mathbf{P}$, we obtain:

$$\mathbf{P}(\omega, \mathbf{k}) = \epsilon_0 \chi^{(1)}(\omega_1, k_1) \mathbf{E}(\omega_1, k_1) + \epsilon_0 \chi^{(2)}(\pm\omega_1 \pm \omega_2, \pm k_1 \pm k_2) \mathbf{E}(\omega_1, k_1) \mathbf{E}(\omega_2, k_2)$$

$$+ \epsilon_0 \chi^{(3)}(\pm\omega_1 \pm \omega_2 \pm \omega_3, \pm k_1 \pm k_2 \pm k_3) \mathbf{E}(\omega_1, k_1) \mathbf{E}(\omega_2, k_2) \mathbf{E}(\omega_3, k_3) + \dots \qquad (3.6)$$

$$= \mathbf{P}^{(1)} + \mathbf{P}^{(2)} + \mathbf{P}^{(3)} + \dots \quad .$$

In eq. 3.6, we have introduced the linear polarization $\mathbf{P}^{(1)}$, the second-order nonlinear polarization $\mathbf{P}^{(2)}$, and the third-order nonlinear polarization $\mathbf{P}^{(3)}$. $\chi^{(1)}$ is the linear susceptibility, and $\chi^{(n)}$ ($n = 2, 3, \dots$) are the nonlinear susceptibility tensors of rank (n+1).

3.1 Spontaneous Raman scattering

The Raman effect describes the appearance of sidebands in the spectrum of narrowband light scattered by a Raman active sample. The frequency difference between the sidebands and the incoming light is independent of its frequency and characteristic for the sample molecule. The effect was predicted by Mandelstam in 1918 and by Smekal in 1923 [7]. The effect is either interpreted as a fine structure splitting of the Rayleigh scattering by Mandelstam or as the optical analogue of the Compton effect by Raman [8]. All interpretations led to its successful experimental observation first reported 1928 by C.V. Raman and K.S. Krishnan [8] in India, and independently by G. Landsberg and L. Mandelstam [9] in 1928 in Russia. The experimental observation was termed second light in Raman's nomenclature and combinatorial scattering of light in the nomenclature used in Russia. Depending which literature is consulted, Landsberg and Mandelstam or Raman and Krishnan are credited for first observing the effect. Raman's discovery was made on February 16th and Landsberg and Mandelstam's on February 21st 1928. Letters by Raman and Krishnan to Nature [8] were published on March 31st 1928, whereas Landsberg and Mandelstam's published in Naturwissenschaften on July 13th [9]. However, India celebrates National Science Day on February 28th to honor the memory of Raman's discovery in 1928. In Raman's and Krishnan's publications a very clear explanation of the nature of the phenomenon is given, and both are cited by Mandelstam and Landsberg. In the end it was the half page article by Raman [10] published on April 21st, which in 1930 gained him a full Nobel Prize in Physics only two years after his publication.

Let us first derive the classical description of the spontaneous Raman scattering on the microscopic level, and how it allows studying vibrations of nuclei. We consider a molecule whose nuclei have a single vibrational mode of frequency ω_0, and an incident light field $\mathbf{E} = \mathbf{E}_0 cos(\omega_L t)$ with the peak field amplitude $\mathbf{E}_0$. Because of its high frequency ($\omega_L >> \omega_0$), the incident light field with frequency ω_L interacts with the electrons within the sample, not with the nuclei of the sample directly. The incident light field is displacing the electron density against the nuclei, and in this manner is inducing the microscopic dipole moment $\mathbf{p} = \alpha \mathbf{E}(\mathbf{r}, t)$. Here,

α is the polarizability tensor, which depends on the vibrational nuclear coordinate $Q(t)$ of the nuclei, oscillating with the resonance frequency ω_0. If we consider only the linear term of the vibrational amplitude $Q(t)$, we obtain a time depending polarizability α:

$$\alpha(t) = \alpha_0 + \frac{d}{dQ}Q(t), \tag{3.7}$$

where α_0 denotes the time independent electrical polarizability. Assuming harmonic motion, the vibrational amplitude $Q(t)$ is given by $Q(t) = Q_0 cos(\omega_0 t + \phi)$. If we insert this expression into eq. 3.7, we obtain:

$$\alpha(t) = \alpha_0 + \alpha' cos(\omega_0 t + \phi), \tag{3.8}$$

where $\alpha' = (\frac{d\alpha}{dQ})_0 Q_0$. If we insert eq. 3.8 into $\mathbf{p}(t) = \alpha(t)\mathbf{E}_0 cos(\omega_L t)$, we obtain the following series for the dipole moment:

$$\mathbf{p}(t) = \underbrace{\alpha_0\mathbf{E}_0 cos(\omega_L t)}_{Rayleigh} + \underbrace{\frac{1}{2}\alpha'\mathbf{E}_0 cos((\omega_L + \omega_0)t + \phi)}_{anti-Stokes\ Raman} + \underbrace{\frac{1}{2}\alpha'\mathbf{E}_0 cos((\omega_L - \omega_0)t + \phi)}_{Stokes\ Raman}. \tag{3.9}$$

In eq. 3.9 we see three dipole terms, the Rayleigh component at the same frequency as that of the incident light field, the Stokes component appearing with respect to ω_0 at a smaller frequency $\omega_{Stokes} = \omega_L - \omega_0$, and the anti-Stokes component appearing at a higher frequency $\omega_{anti-Stokes} = \omega_L + \omega_0$. Because in spontaneous Raman scattering the molecular vibrations are considered to be stochastic and independent of each other, the phase ϕ of the vibrational nuclear coordinates oscillations can take any value and is fully stochastic. This represents the incoherent nature of spontaneous Raman scattering. For N_{Scat} scattering molecules per unit volume, the macroscopic polarization $\mathbf{P}$ is related to the microscopic dipole moment by $\mathbf{P} = N_{Scat}\mathbf{p}$. The spontaneous Raman Stokes scattering intensity, which is typically measured in a spontaneous Raman scattering experiment, is then expressed by

$$I(\omega_L - \omega_0) \propto N_{Scat}z\sigma_{Raman}(\omega_L - \omega_0)|E_0|^2, \tag{3.10}$$

where z is the interaction path length in the Raman active medium. In this classical description, the spontaneous Raman scattering cross-section σ_{Raman} for the Stokes scattering process can then be expressed in the following form [11]:

$$\sigma_{Raman,Q(\omega_L-\omega_S)} \propto \left|\frac{d\alpha}{dQ_0}\right|^2. \tag{3.11}$$

Next, we will discuss the polarization dependence of the spontaneous Raman scattering. The geometry for detection of scattered Raman light under $90°$ is given in fig. 3.1. If linear z-polarized light enters along the y-axis and the Raman scattered light is observed under $90°$ along the x-axis, the degree of Raman depolarization ρ_{depol} is defined as the ratio of the Raman intensities $I_\parallel$ and $I_\perp$ detected perpendicular and parallel to the xz-plane, respectively:

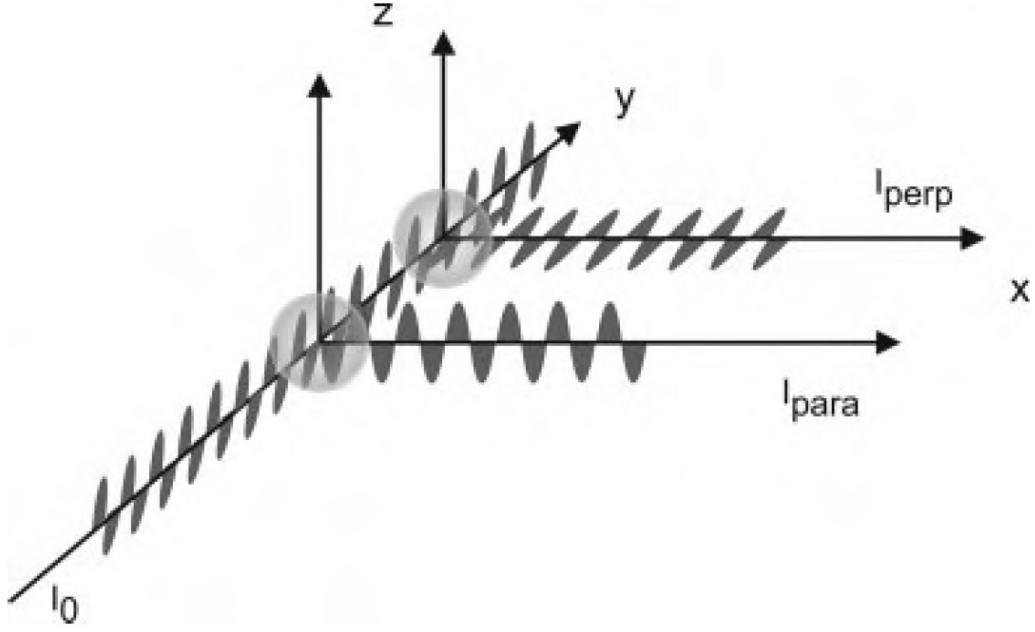$$\rho_{depol} \equiv \frac{I_\perp}{I_\parallel}. \tag{3.12}$$

Figure 3.1: Geometry for the polarization-dependent Raman detection, taken from ref. [5].

The degree of depolarization of a Raman band is theoretically described by ref. [5]:

$$\rho_{depol} = \frac{3\gamma_s^2 + 5\gamma_{as}^2}{45\overline{\alpha}^2 + 4\gamma_s^2} \tag{3.13}$$

with the mean polarizability $\overline{\alpha}$, the symmetric anisotropy γ_s, and the antisymmetric anisotropy γ_{as}. The degree of depolarization can range from $\rho_{depol} = 0$ for a fully polarized Raman band to $\rho_{depol} = \frac{3}{4}$ for a fully un-polarized Raman band.

The above classical derivation of Raman scattering intensities (eqs. 3.10 and 3.11) provide only a qualitative description of the spontaneous Raman scattering. It fails in quantitatively describing scattering intensities, because it does not take the population densities of the ground and vibrational states into account [4]. This is why we need a quantum mechanical description in order to fully describe the Raman scattering. Generally, the absorption of a photon, where its energy matches the energy difference $\hbar\omega_L = \hbar(\omega_{v=1} - \omega_{v=0})$ between an initial state $|\psi_{v=0}\rangle$ and a final state $|\psi_{v=1}\rangle$, is a first-order transition that depends on the transition dipole moment $\langle\psi_{v=0} | \mathbf{p} | \psi_{v=1}\rangle$. Here, the macroscopic polarization is given by $\mathbf{P} = N_{Scat}\langle\psi_{v=0} | \mathbf{p} | \psi_{v=1}\rangle$. As depicted in fig. 3.2, a Raman like transition is a second-order process. Therefore, the two-photon Raman transition dipole moment is given by $\langle\psi_{v=0} | \mathbf{p} | \psi_{virt}\rangle\langle\psi_{virt} | \mathbf{p} | \psi_{v=1}\rangle$. The virtual state $|\psi_{virt}\rangle$ is not a stationary state representing a solution of the time-independent Schrödinger equation. Thus, it does not correspond to a sharp defined energy level. Furthermore, we have to take all quantum states as possible intermediate states into account. In order to simplify the photon picture, only one virtual state $|\psi_{virt}\rangle$ is plotted in fig. 3.2. After introducing the electric dipole moment operators $\hat{p}_\rho$ and $\hat{p}_\sigma$ for the Cartesian coordinates ρ and σ, respectively,

11

an expression for the Raman polarizability tensor component $(\alpha_{\rho\sigma})_{10}$ is given in ref. [4]:

$$(\alpha_{\rho\sigma})_{10} = \frac{1}{\hbar} \sum_{virt,virt\neq 0,1} \left[\frac{\langle \psi_{v=1} \mid \hat{p}_\rho \mid \psi_{virt}\rangle\langle\psi_{virt} \mid \hat{p}_\sigma \mid \psi_{v=0}\rangle}{\omega_{virt} - \omega_{v=0} - \omega_L - i\Gamma_{virt}} + \frac{\langle \psi_{v=1} \mid \hat{p}_\sigma \mid \psi_{virt}\rangle\langle\psi_{virt} \mid \hat{p}_\rho \mid \psi_{v=0}\rangle}{\omega_{virt} - \omega_{v=1} + \omega_L + i\Gamma_{virt}} \right],$$

(3.14)

where Γ_{virt} is the half width of the virtual state related to its lifetime. Calculating the spontaneous Raman scattering cross-section σ_{Raman} using Raman polarizability tensor components expressed in eq. 3.14 is not trivial and lenghty, even when several simplifying approximations are taken into account (see Placzek et. al. [12]). The interested reader is referred to ch. 9 in Mukamel [6], where the quantum mechanically derived Raman cross-section $\sigma_{Raman,\ 10}(\omega_L - \omega_0)$ is given as:

$$\sigma_{Raman,\ 10}(\omega_L - \omega_0) \propto \frac{4\omega_L(\omega_L - \omega_0)^3}{9\hbar^2 c^4} \sum |(\alpha_{\rho\sigma})_{10}|^2.$$

(3.15)

Based on earlier work of Hellwarth [13], Mukamel proposes that the sum over all Raman transition amplitudes $\sum |(\alpha_{\rho\sigma})_{10}|^2$ is directly proportional to the imaginary part of the third order susceptibility $\chi^{(3)}(\omega)$, so that we can rewrite the spontaneous Raman cross-section as:

$$\sigma_{Raman,\chi^{(3)}} \propto Im[\chi^{(3)}_{Res}(\omega)].$$

(3.16)

Eq. 3.16 thus directly represents the relation between the spontaneous Raman and coherent Raman scattering experiments. We will provide an experimental verification of the validity of eq. 3.16 in this thesis.
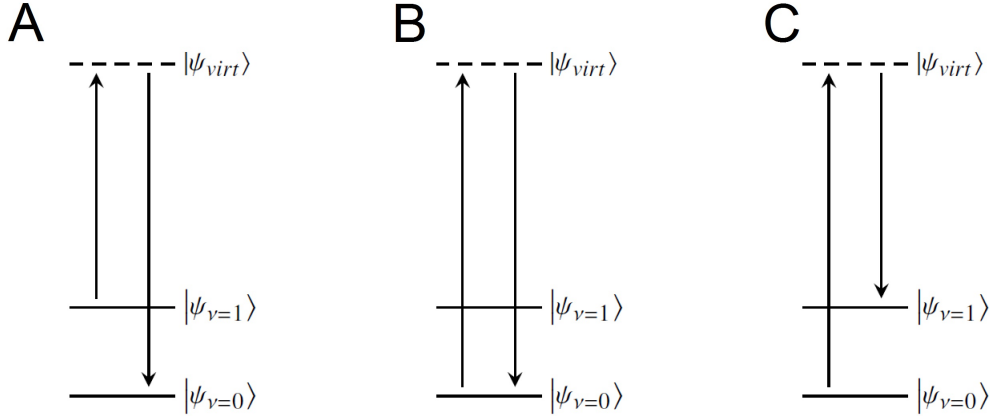

Figure 3.2: Energy level diagrams for (B) the Rayleigh, (C) the Stokes Raman, and (A) the anti-Stokes Raman scattering processes.

3.2 Coherent anti-Stokes Raman scattering

Coherent anti-Stokes Raman scattering (CARS) was first experimentally reported by Maker and Terhune [14] in 1965, both at this time being employed in the Ford motors cars company. Unlike in spontaneous Raman scattering, where a single laser excitation field is used, in CARS three incident laser fields $\mathbf{E}_{Pump}$, $\mathbf{E}_{Probe}$ and $\mathbf{E}_{Stokes}$ at frequencies ω_{Pump}, ω_{Probe} and ω_{Stokes}, respectively, interact with the nonlinear sample making CARS a four-wave mixing process. The energy level diagram for the CARS process using narrow-band picosecond (ps)-pulses is shown in fig. 3.3. When the frequency difference $\omega_{Pump} - \omega_{Stokes}$ is matching a vibrational resonance
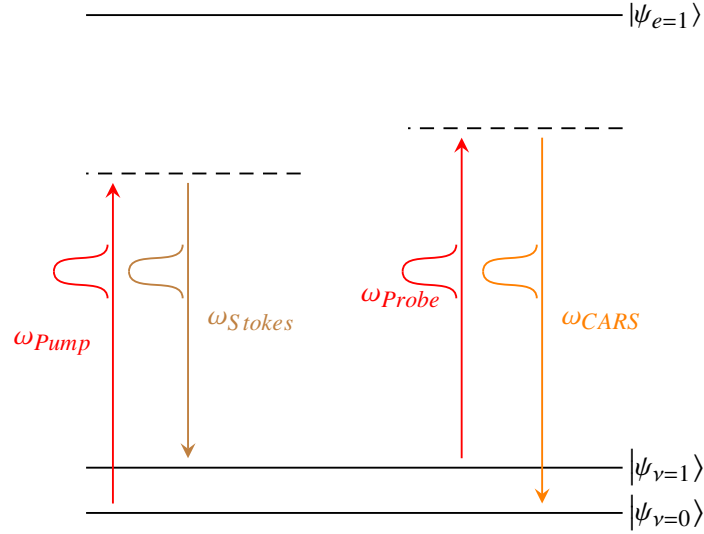
Figure 3.3: Energy level diagram for the CARS process using narrow band ps-pulses. $|\psi_{v=0,1}\rangle$ and $|\psi_{e=1}\rangle$ denote the vibrational and electronic resonant states, respectively.

frequency, the CARS signal is resonantly enhanced. Depending on whether three distinct fields, or only two fields, $\mathbf{E}_{Pump}$ and $\mathbf{E}_{Stokes}$ are incident, the terms non-degenerate and degenerate CARS are used, respectively. To interact with a nonlinear $\chi^{(3)}$-active medium, the incident fields have to be spatially and temporally overlapped. When the phase-matching condition $\Delta\mathbf{k} = \mathbf{k}_{CARS} - (\mathbf{k}_{Pump} + \mathbf{k}_{Probe} - \mathbf{k}_{Stokes}) \approx 0$ is fulfilled, the third-order nonlinear polarization $\mathbf{P}^{(3)}_{CARS} \propto \chi^{(3)}\mathbf{E}_{Pump}\mathbf{E}_{Probe}\mathbf{E}^*_{Stokes}$ is induced and a new coherent field is emitted at the new CARS frequency $\omega_{CARS} = \omega_{Pump} + \omega_{Probe} - \omega_{Stokes}$. The nonlinear susceptibility $\chi^{(3)}$ is a tensor of rank 4 with 81 entries. By convention, the tensor elements of $\chi^{(3)}$ are distinguished by the Cartesian polarization components of the CARS, pump, probe, and Stokes fields. When these fields are monochromatic, linearly polarized, and copropagate collinearly, the ith component of the induced polarization reads [15]:

$$P_i^{(3)}(\omega_{CARS}) =$$

$$\frac{6}{m_{deg}!} \sum_{jkl} \chi^{(3)}_{ijkl}(-\omega_{CARS}; \omega_{Pump}, \omega_{Probe}, -\omega_{Stokes}) \times E_j(\omega_{Pump})E_k(\omega_{Probe})E_l(\omega_{Stokes})^* \quad (3.17)$$

with m_{deg} being the number of equal input frequencies. The CARS intensity I_{CARS}, which is experimentally detected, is then:

$$I_{CARS} = \left| P^{(3)}_{CARS} \right|^2 \propto \left| \chi^{(3)} \right|^2. \tag{3.18}$$

In the most general case, all 81 tensor elements of $\chi^{(3)}_{ijkl}$ are different [16]. In degenerate CARS, which is the case dealt with throughout this thesis, in a transparent, optically inactive and isotropic medium, only two independent tensor elements $\chi^{(3)}_{1111}$ and $\chi^{(3)}_{1221}$ remain. The quantity $\chi^{(3)}_{ijkl}$ can be split into a nonresonant part $\chi^{(3)}_{ijkl\ NR}$, which arises from electronic contributions, and a vibrationally resonant part $\chi^{(3)}_{ijkl\ Res}$. Being far off an electronic resonance $|\psi_{e=1}\rangle$, as illustrated in fig. 3.3, $\chi^{(3)}_{ijkl\ NR}$ is assumed to be frequency-independent and a purely real quantity. If we consider an isolated Raman resonance, we obtain for the resonant tensor elements [17]:

$$\chi^{(3)}_{1111\ Res} = \frac{A_{1111}}{\omega_0 - (\omega_{Pump} - \omega_{Stokes}) - i\Gamma} = CN_{Scat}\Gamma\frac{\overline{\alpha}^2 + (\frac{4}{45})\gamma_s^2}{\omega_0 - (\omega_{Pump} - \omega_{Stokes}) - i\Gamma} \tag{3.19}$$

$$\chi^{(3)}_{1221\ Res} = \frac{A_{1221}}{\omega_0 - (\omega_{Pump} - \omega_{Stokes}) - i\Gamma} = CN_{Scat}\Gamma\frac{(\frac{1}{15})\gamma_s^2}{\omega_0 - (\omega_{Pump} - \omega_{Stokes}) - i\Gamma}. \tag{3.20}$$

Both eq. 3.19 and eq. 3.20 describe a complex Lorentzian profile of a damped harmonic oscillator with resonance frequency ω_0, a damping constant 2Γ, and amplitude A_{ijkl}. The amplitudes are directly proportional to the number density of scatterers N_{Scat}. C is a proportionality constant. In combination with eq. 3.18, we find the quadratic dependence of the measured CARS signal on N_{Scat}. The parameters $\overline{\alpha}$ and γ_s have already been introduced in eq. 3.13 for the spontaneous Raman scattering case. With $\gamma_{as} = 0$ in the transparent medium, we can define the following depolarization ratios for the resonant and the nonresonant coherent Raman scattering in eq. 3.21 and eq. 3.22, respectively:

$$\rho_{depol\ Res} = \frac{\chi^{(3)}_{1221\ Res}}{\chi^{(3)}_{1111\ Res}} = \frac{3\gamma_s^2}{45\overline{\alpha}^2 + 4\gamma_s^2} \tag{3.21}$$

$$\rho_{depol\ NR} = \frac{\chi^{(3)}_{1221\ NR}}{\chi^{(3)}_{1111\ NR}} = \frac{1}{3}. \tag{3.22}$$

While eq. 3.21 is equivalent to eq. 3.13 describing the degree of depolarization for the spontaneous Raman case, eq. 3.22 has no spontaneous Raman scattering counterpart. The value of $\frac{1}{3}$ is a result of Kleinmann's symmetry [18], where $\chi^{(3)}_{1122\ NR} = \chi^{(3)}_{1212\ NR} = \chi^{(3)}_{1221\ NR} = \frac{\chi^{(3)}_{1111\ NR}}{3}$. When the pump/probe, the Stokes, and the CARS fields are parallel polarized, $\chi^{(3)}_{1111}$ is probed. With this polarization geometry being fulfilled throughout this thesis, the subscripts representing the Cartesian coordinates will be skipped in the subsequent discussions. For example, $\chi^{(3)}$ will be used instead of $\chi^{(3)}_{1111}$.

The quantum mechanical description of the CARS process makes use of the density matrix $\rho_{\mathbf{D}} = |\psi\rangle\langle\psi|$, where the time-averaged macroscopic polarization is described as $\langle\mathbf{P}\rangle =$

$N_{Scat}tr(\rho_{\mathbf{D}}\mathbf{P})$. Perturbation theory allows then to calculate the third-order terms of the nonlinear polarization $\mathbf{P}^{(3)}$ and the components of the third-order susceptibility $\chi^{(3)}$. The detailed quantum mechanical description of the CARS process is beyond the scope of this thesis. The interested reader is referred to visit the comprehensive treatments given by Boyd [16] or Mukamel [6].

3.2.1 Multiplex CARS

When narrow-band ps-pulses are used in CARS, only a narrow frequency range of the Raman spectrum is probed. In order to cover a broader range, either the frequency difference between the two spectrally narrow fields, $\omega_{Pump} - \omega_{Stokes}$, needs to be consecutively swept through, or a broadband Stokes field exciting a manifold of Raman modes simultaneously is required. In the latter approach of multiplex CARS detection, either a broadband fs-laser Stokes pulse or a supercontinuum (SC) Stokes pulse is used. As is illustrated in fig. 3.4, within the spectral bandwidth of the broadband Stokes field, the nonlinear third-order polarization for all vibrational resonances is induced, which is expressed in the frequency domain as follows [19]:
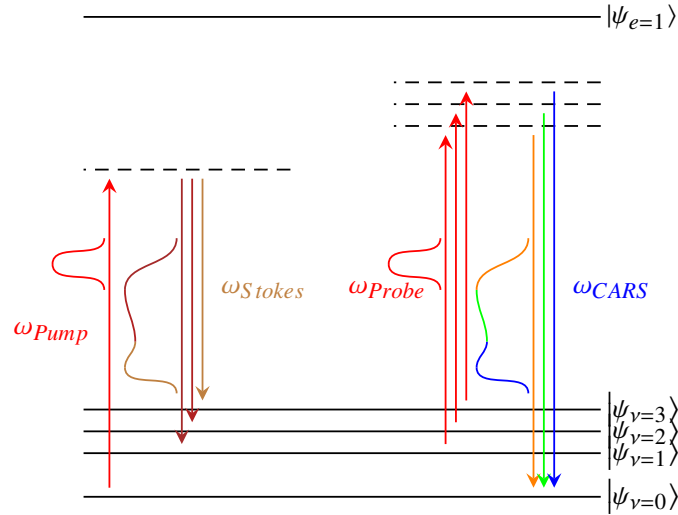
Figure 3.4: Energy level diagram for the multiplex CARS process using a narrowband pump/probe pulse and a broadband Stokes pulse. $|\psi_{v=i}\rangle$ $(i = 0, \ldots, 3)$ and $|\psi_{e=1}\rangle$ denote the vibrational and electronic states, respectively.

$$\mathbf{P}^{(3)}(\omega_{CARS}) = \iiint_{-\infty}^{\infty} \chi^{(3)}(-\omega_{CARS} : \omega_{Pump}, \omega_{Probe}, -\omega_{Stokes})$$
$$\mathbf{E}_{Pump}(\omega_{Pump})\mathbf{E}^{*}_{Stokes}(\omega_{Stokes})\mathbf{E}_{Probe}(\omega_{Probe}) \tag{3.23}$$
$$\delta(\omega_{Pump} - \omega_{Stokes} + \omega_{Probe} - \omega_{CARS})d\omega_{Stokes}d\omega_{Pump}d\omega_{Probe}.$$

Because in a typical experiment the Stokes field is spectrally much broader than the pump field, eq. 3.23 can be approximated by:

$$\mathbf{P}^{(3)}(\omega_{CARS}) =$$

$$\chi^{(3)}(-\omega_{CARS} : \omega_{Pump}, \omega_{Probe}, -\omega_{Stokes})\mathbf{E}_{Pump}(\omega_{Pump})\mathbf{E}^*_{Stokes}(\omega_{Stokes})\mathbf{E}_{Probe}(\omega_{Probe}).$$

$$(3.24)$$

For degenerate CARS, with eq. 3.18 the measured power spectrum then corresponds to

$$I_{CARS}(\omega_{CARS}) \propto |\chi^{(3)}(-\omega_{CARS} : \omega_{Pump}, \omega_{Pump}, -\omega_{Stokes})|^2|\mathbf{E}_{Pump}(\omega_{Pump})|^4|\mathbf{E}_{Stokes}(\omega_{Stokes})|^2.$$

$$(3.25)$$

In order to become independent of the Stokes intensity spectral profile $|\mathbf{E}_{Stokes}(\omega_{Stokes})|^2$, as well as of the spectral sensitivity curves of the detection system components, in practice, the measured CARS spectrum of the sample is normalized with a reference spectrum

$$S(\omega_{CARS}) = \frac{I_{CARS\ sample}(\omega_{CARS})}{I_{CARS\ ref}(\omega_{CARS})}.$$

$$(3.26)$$

The reference spectrum $I_{CARS\ ref}(\omega_{CARS})$ must be purely nonresonant and measured under the exact same conditions as the measured sample spectrum $I_{CARS\ sample}(\omega_{CARS})$ of interest.

3.2.2 The CARS line shape

In this section, the CARS spectral line shape $I_{CARS}(\nu)$ as a function of wavenumbers $\nu = \frac{10^{-2}\omega}{2\pi c}$ in cm^{-1} will be discussed in more detail. As Druet et. al. [20] and Voroshilov et. al. [21] pointed out, the assumption of a purely real nonresonant background $\chi^{(3)}_{NR}$ and a vibrational resonant susceptibility $\chi^{(3)}_{Res}(\nu) = |\chi^{(3)}_{Res}(\nu)|e^{i\phi_{Res}(\nu)}$ with the purely vibrational resonance phase spectrum $\phi_{Res}(\nu)$ as defined in eq. 3.19, is no more valid when either the frequency of the pump field ν_{Pump} or that of the CARS field $\nu_{CARS} = 2\nu_{Pump} - \nu_{Stokes}$ approaches an electronic resonance. To account for the latter, they have introduced an additional phase angle ϕ_R that represents a constant phase shift between $\chi^{(3)}_{Res}(\nu)$ and $\chi^{(3)}_{NR}$. Furthermore, the presence of a nearby purely electronic susceptibility is assumed, which is described by an additional complex background term $\chi^{(3)}_E e^{i\phi_E}$, where ϕ_E and $\chi^{(3)}_E$ are frequency independent constants. The full model for the third-order complex susceptibility $\chi^{(3)}_{tot}(\nu)$ used in all subsequent simulations is then given by

$$\chi^{(3)}_{tot}(\delta) = \chi^{(3)}_{NR} + \chi^{(3)}_E e^{i\phi_E} + \chi^{(3)}_{Res}(\delta)e^{i\phi_R} = \left|\chi^{(3)}_{tot}(\delta)\right| e^{i\phi_{tot}(\delta)}, \tag{3.27}$$

where $\delta = \nu_0 - (\nu_{Pump} - \nu_{Stokes})$ is the detuning from the Raman resonance frequency ν_0 or relative Raman shift. Substitution into eq. 3.18 and eq. 3.19 yields an expression for the CARS line shape

$$I_{CARS}(\delta) = \left|\chi^{(3)}_{tot}(\delta)\right|^2 = \left|\chi^{(3)}_{NR} + \chi^{(3)}_E e^{i\phi_E} + \frac{A}{\delta - i\Gamma}e^{i\phi_R}\right|^2. \tag{3.28}$$

In the following simulations, we emphasize on the relationship between $I_{CARS}(\delta)$ and the total phase $\phi_{tot}(\delta) = tan^{-1} \frac{Im[\chi_{tot}^{(3)}(\delta)]}{Re[\chi_{tot}^{(3)}(\delta)]}$ of the total third order susceptibility $\chi_{tot}^{(3)}(\delta)$. First, we discuss the simple case where the frequencies of all fields are assumed to be far off any electronic resonance, so that $\phi_R = 0$ and $\chi_E^{(3)} = 0$. In this case, eq. 3.28 reduces to:

$$I_{CARS}(\delta) = \left|\chi_{tot}^{(3)}(\delta)\right|^2 = \left|\chi_{Res}^{(3)}(\delta) + \chi_{NR}^{(3)}\right|^2 = \left|\chi_{Res}^{(3)}(\delta)\right|^2 + 2Re[\chi_{Res}^{(3)}(\delta)]\chi_{NR}^{(3)} + \chi_{NR}^{(3)}{}^2 \,, \qquad (3.29)$$

and the total phase spectrum is then given by:

$$\phi_{tot}(\delta) = tan^{-1}\left[\frac{|\chi_{Res}^{(3)}(\delta)|sin(\phi_{Res}(\delta))}{\chi_{NR}^{(3)} + |\chi_{Res}^{(3)}(\delta)|cos(\phi_{Res}(\delta))}\right]. \qquad (3.30)$$

The total CARS intensity consists then of three terms, which add up to the dispersive, Fano-type CARS line shape, as shown for a single Lorentzian Raman resonance in fig. 3.5.
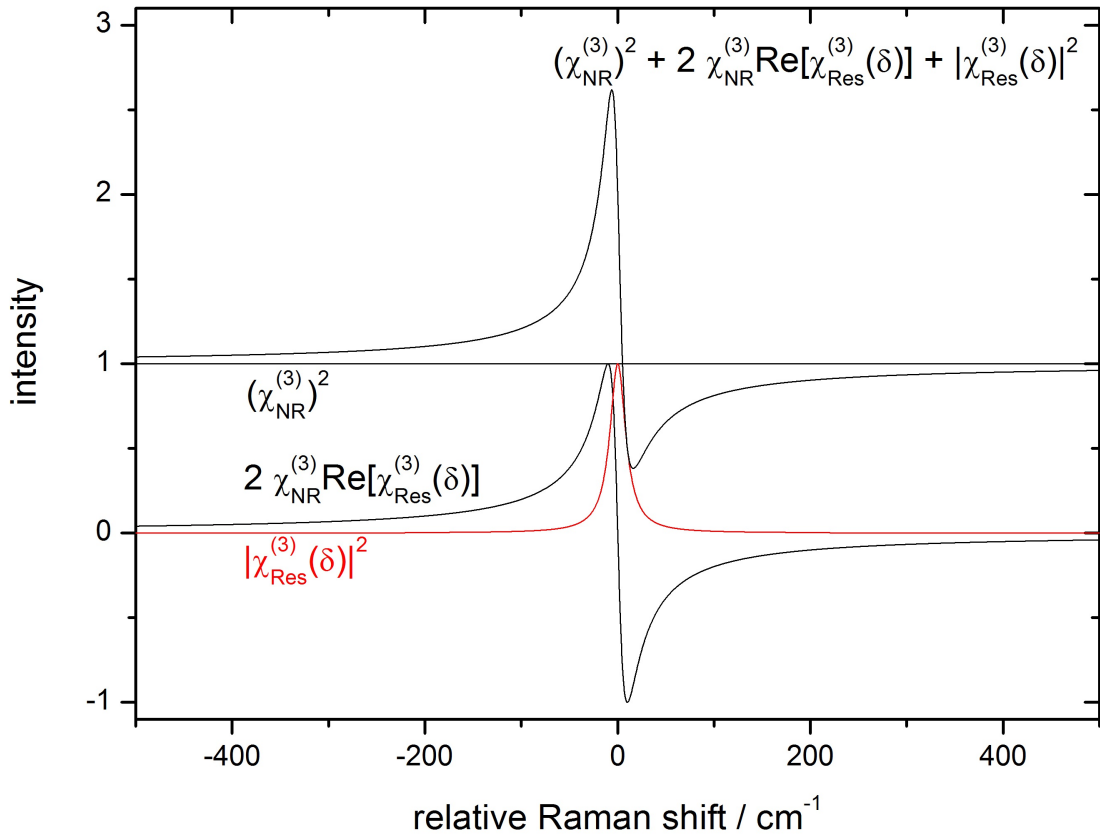
Figure 3.5: Simulation of a CARS spectral profile of an isolated vibrational resonance in the presence of a real and constant susceptibility contribution, using eq. 3.28 with $\phi_R = 0$ and $\chi_E^{(3)} = 0$. The simulation parameters are $\Gamma = 20\ cm^{-1}$, $A = 1\ cm^{-1}$, and $\chi_{NR}^{(3)} = 1$.

In fig. 3.6 A, $\chi_{tot}^{(3)}(\delta)$ used for the simulation of the intensities in fig. 3.5 is shown in the complex plane. The resonance follows a circle with a diameter of $\frac{A}{\Gamma}$, and is peaking at zero detuning ($\delta = 0$). In fig. 3.6 B, the same $\chi_{tot}^{(3)}(\delta)$ is shown in a frequency-resolved manner together with the projections on the real and imaginary planes. In fig. 3.6 C, the corresponding CARS spectrum $I_{CARS}(\delta)$ and the total phase spectrum $\phi_{tot}(\delta)$ are shown.
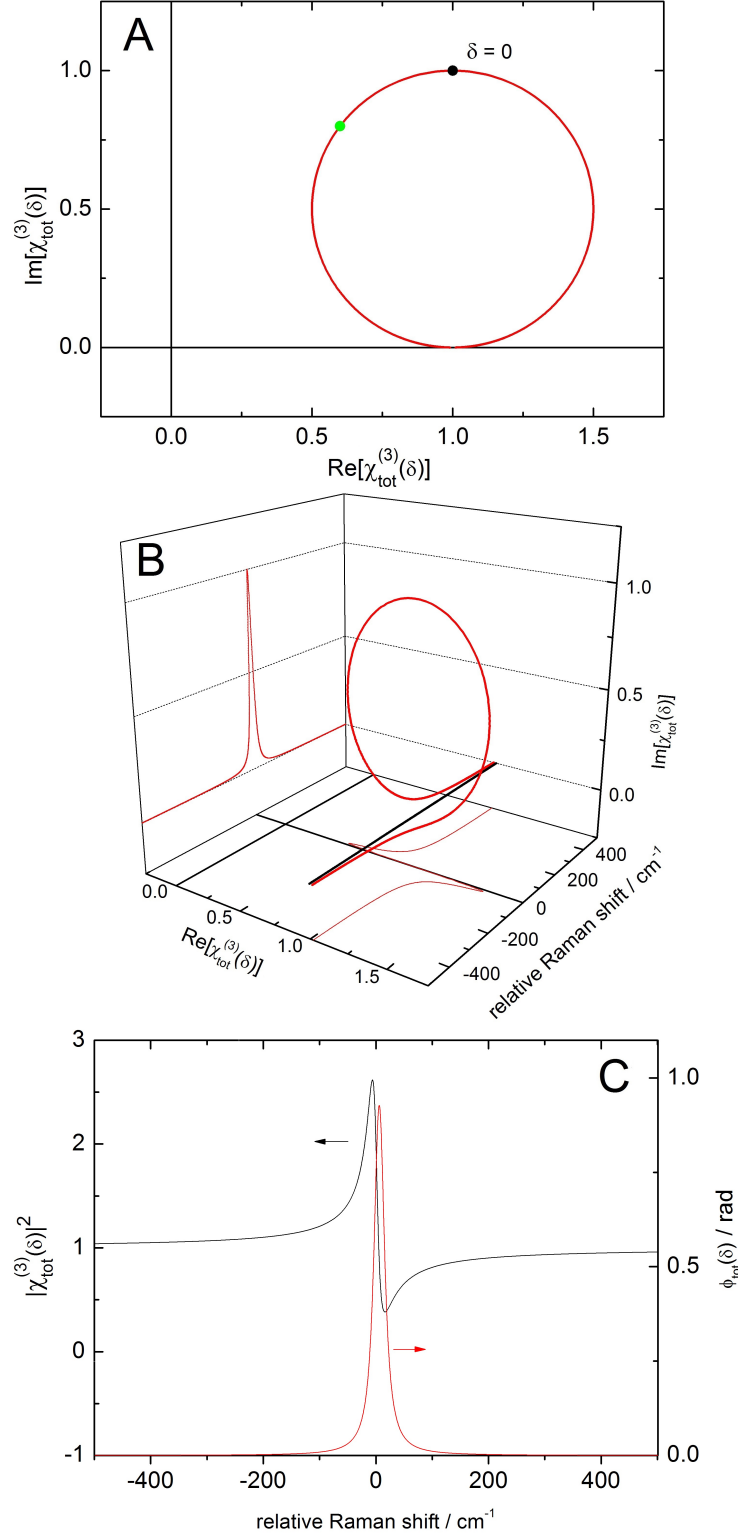
Figure 3.6: Simulation of a complex $\chi_{tot}^{(3)}(\delta)$ for an isolated vibrational resonance $\chi_{Res}^{(3)}(\delta)$ in the presence of a real and constant susceptibility $\chi_{NR}^{(3)}$ (A) in the complex plane and (B) in a frequency-resolved manner together with the projections on the real and imaginary planes. (C) The corresponding CARS spectrum $I_{CARS}(\delta) = \left|\chi_{tot}^{(3)}(\delta)\right|^2$ and the total phase spectrum $\phi_{tot}(\delta)$, calculated using eq. 3.29 and eq. 3.30, respectively. The simulation parameters were the same as used in fig. 3.5.

The total phase spectrum $\phi_{tot}(\delta)$ in fig. 3.6 C is symmetric around its maximum value, which corresponds to a detuning $\delta > 0$, as indicated by the green point in fig. 3.6 A. In the limiting cases being far off the vibrational resonance, $|\delta| \gg \Gamma$, the CARS spectrum takes the constant value of $lim_{|\delta|\gg\Gamma} \; |\chi_{tot}^{(3)}(\delta)|^2 = (\chi_{NR}^{(3)})^2$, and the total phase is zero, $lim_{|\delta|\gg\Gamma} \; \phi_{tot}(\delta) = 0$.

1. **Concentration dependence of $\chi_{tot}^{(3)}(\delta)$ at fixed $\chi_{NR}^{(3)}$**

As can be seen from eq. 3.19, the concentration of molecular scatterers is proportional to the amplitude A of the Lorentzian line that describes the vibrational resonance. Next, we elucidate this concentration dependence of the complex $\chi_{tot}^{(3)}(\delta)$, the CARS line shape $I_{CARS}(\delta)$, and the phase spectrum $\phi_{tot}(\delta)$ for the simple case described by eq. 3.29 and eq. 3.30. Fig. 3.7 shows the corresponding simulations for increasing vibrational amplitudes A at a fixed value of $\chi_{NR}^{(3)}$. With increasing amplitude A, the maximum intensity of the CARS spectrum increases quadratically, and the spectral position of the maximum approaches the resonance frequency from $\delta < 0$. The spectral position of the corresponding minimum on the other hand diverges to $+\infty$. The total phase spectrum $\phi_{tot}(\delta)$ does not show any dispersive character, and its spectral width and center frequency increase with increasing amplitude A, approaching $\phi_{tot}(\delta) = \phi_{Res}(\delta)$ for the limiting case where $\left|\chi_{Res}^{(3)}(\delta)\right| \gg \left|\chi_{NR}^{(3)}\right|$. With $|\delta| \gg \Gamma$ being far off the vibrational resonance, all CARS spectra take the value of $\left|\chi_{NR}^{(3)}\right|^2$, while the total phase spectrum $\phi_{tot}(\delta)$ becomes zero.

2. **The influence of $\chi_{NR}^{(3)}$ on $\chi_{tot}^{(3)}(\delta)$ at a fixed $\chi_{Res}^{(3)}(\delta)$**

For the simple case described by eq. 3.29 and eq. 3.30, we next study the influence of $\chi_{NR}^{(3)}$ on $\chi_{tot}^{(3)}(\delta)$ at a fixed $\chi_{Res}^{(3)}(\delta)$. Fig. 3.8 shows the corresponding simulations of $\chi_{tot}^{(3)}(\delta)$, the CARS spectrum $\left|\chi_{tot}^{(3)}(\delta)\right|^2$, and the total phase $\phi_{tot}(\delta)$ for increasing values of $\chi_{NR}^{(3)}$. Only for $\chi_{NR}^{(3)} = 0$, the spectral position of the maximum of the CARS line matches the resonance center frequency, and the total phase $\phi_{tot}(\delta)$ changes from 0 for $\delta \ll 0$ to π for $\delta \gg 0$. Hence, in the limiting case where $\chi_{NR}^{(3)} \ll \left|\chi_{Res}^{(3)}\right|$, the total phase represents the vibrational phase, i.e. $\phi_{tot}(\delta) = \phi_{Res}(\delta)$. With increasing $\chi_{NR}^{(3)}$, the spectral position of the maximum of the CARS line shifts to more negative detuning values, and a minimum in the CARS spectrum becomes more pronounced. Again, the spectral width and center frequency of the total phase spectrum $\phi_{tot}(\delta)$ decrease with increasing $\chi_{NR}^{(3)}$, and the phase does not show any dispersive character. With $|\delta| \gg \Gamma$ being far off the vibrational resonance, all CARS intensities take the value of $\left|\chi_{NR}^{(3)}\right|^2$, and the total phase spectrum $\phi_{tot}(\delta)$ is zero.
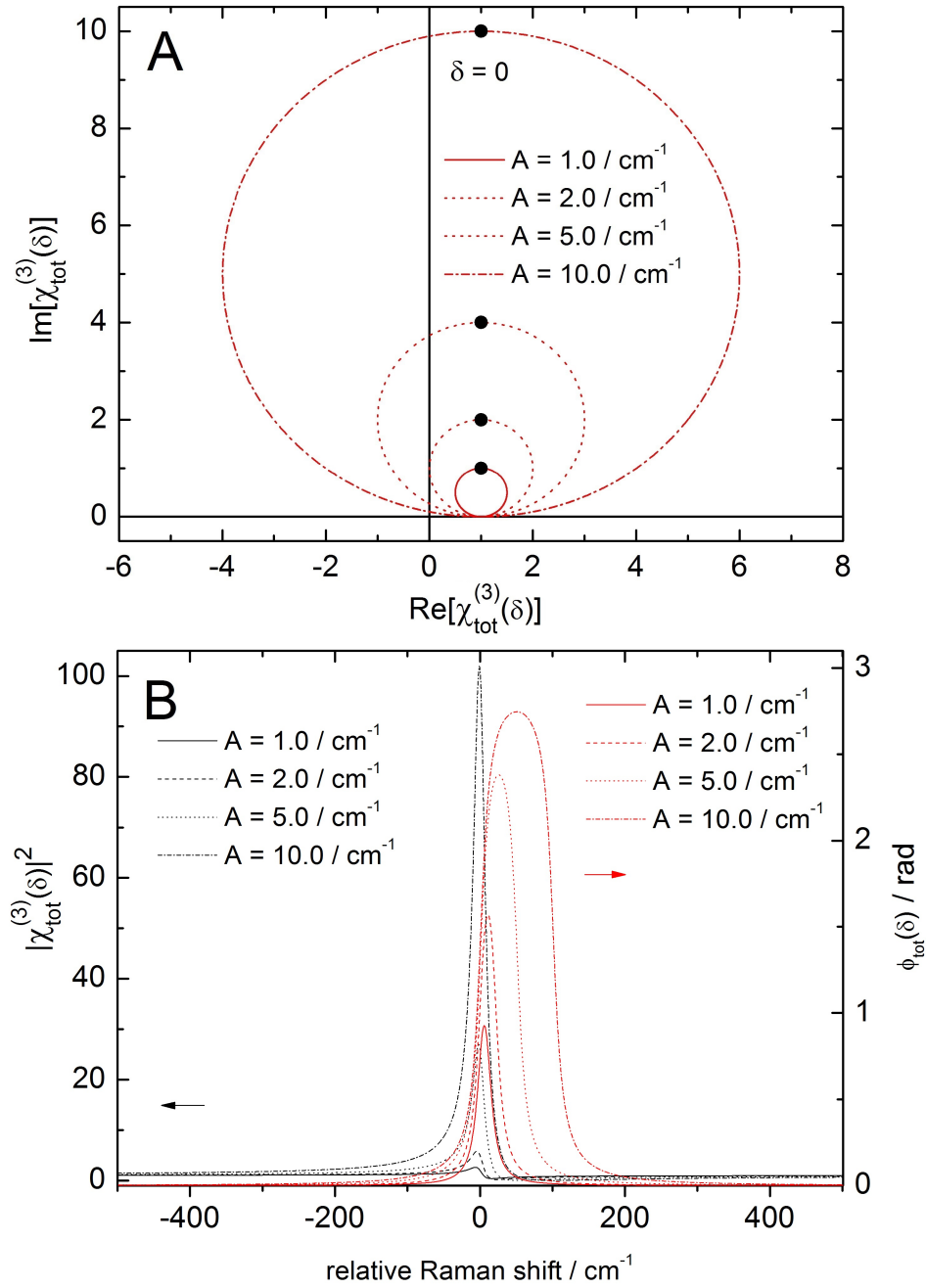
19

Figure 3.7: Simulation of the concentration dependence of the complex $\chi_{tot}^{(3)}(\delta)$ for an isolated vibrational resonance $\chi_{Res}^{(3)}(\delta)$ of increasing vibrational amplitude A in the presence of a fixed $\chi_{NR}^{(3)}$. (A) Plots of $\chi_{tot}^{(3)}(\delta)$ in the complex plane. All resonances follow circles and peak for zero detuning. (B) CARS spectra $\left|\chi_{tot}^{(3)}(\delta)\right|^2$ are shown together with the total phase spectra $\phi_{tot}(\delta)$, calculated using eq. 3.29 and eq. 3.30, respectively. The simulation parameters are $\Gamma = 20\ cm^{-1}$, $\chi_{NR}^{(3)} = 1$, and the amplitude values are $A = 1.0\ cm^{-1}$, $2.0\ cm^{-1}$, $5.0\ cm^{-1}$, and $10.0\ cm^{-1}$.

Looking at the frequency dependence of $\chi_{tot}^{(3)}(\delta)$, e.g. in fig. 3.6 A, it becomes clear that for a given amplitude A and value of $\chi_{NR}^{(3)}$, the spectral points of maximum and minimum

CARS intensity, $\delta_{I_{CARS}(\delta)=max}$ and $\delta_{I_{CARS}(\delta)=min}$, respectively, lie on a line going through the origin of the complex plane.
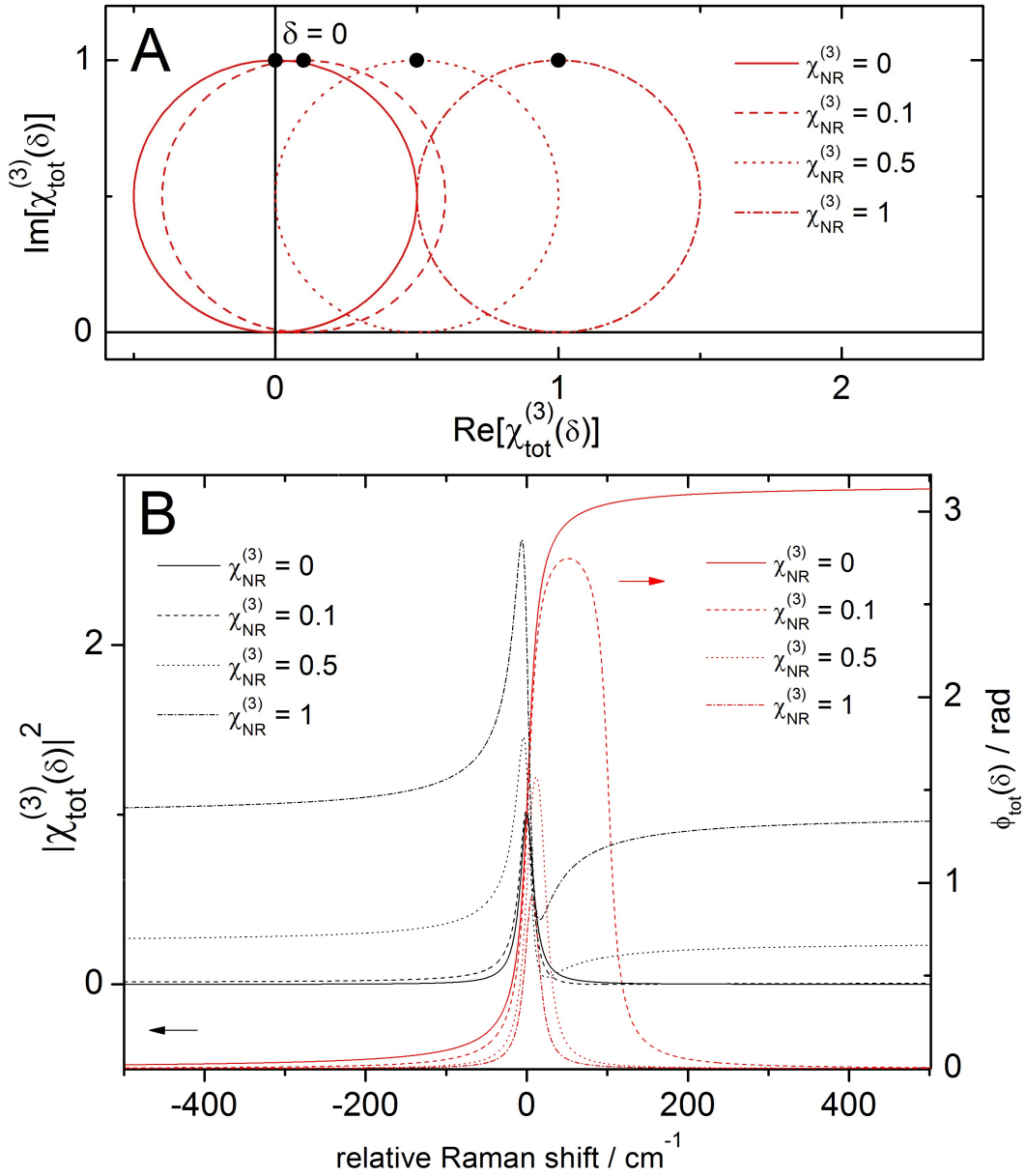

Figure 3.8: Simulation of the complex $\chi_{tot}^{(3)}(\delta)$ for an isolated complex vibrational resonance $\chi_{Res}^{(3)}(\delta)$ in the presence of an increasing nonresonant background contribution $\chi_{NR}^{(3)}$. (A) Plot of $\chi_{tot}^{(3)}(\delta)$ in the complex plane. The resonances follow circles that peak at zero detuning ($\delta = 0$), and are shifted along the real axis by the amount of the simulated $\chi_{NR}^{(3)}$. (B) CARS lines shapes $\left|\chi_{tot}^{(3)}(\delta)\right|^2$ and total phase spectra $\phi_{tot}(\delta)$, calculated using eq. 3.29 and eq. 3.30, respectively. The simulation parameters are $\Gamma = 20\ cm^{-1}$, $A = 1.0\ cm^{-1}$, and the values for $\chi_{NR}^{(3)}$ are 0, 0.1, 0.5, and 1.0.

The spectral positions of the maximum of the total phase $\phi_{tot}(\delta)$ spectrum, its first and its second inflexion point $\delta_{\frac{\partial^2 \phi_{tot}(\delta)}{\partial \delta^2}=max}$ and $\delta_{\frac{\partial^2 \phi_{tot}(\delta)}{\partial \delta^2}=min}$, respectively, lie within the spectral window spanned by $\delta_{I_{CARS}(\delta)=max}$ and $\delta_{I_{CARS}(\delta)=min}$. The following conditions are fulfilled:

$$\delta_{I_{CARS}(\delta)=max} < \delta_{\frac{\partial^2 \phi_{tot}(\delta)}{\partial \delta^2}=max} < \delta_{\phi_{tot}(\delta)=max} < \delta_{\frac{\partial^2 \phi_{tot}(\delta)}{\partial \delta^2}=min} < \delta_{I_{CARS}(\delta)=min}. \tag{3.31}$$

In general, whenever the circle described by $\chi_{Res}^{(3)}(\delta)$ extends into the second quadrant of the complex plane, both the spectral position of the CARS minimum $\delta_{I_{CARS}(\delta)=min}$ and the second inflexion point of the total phase $\delta_{\frac{\partial^2 \phi_{tot}(\delta)}{\partial \delta^2}=min}$ diverge to $+\infty$. This is an important aspect in the phase retrieval of an unknown CARS spectrum where $\chi_{Res}^{(3)}(\delta) \gg \chi_{NR}^{(3)}$.

3. **The influence of a phase factor $e^{i\phi_R}$ on $\chi_{tot}^{(3)}(\delta)$**

Next, the influence of an additional phase shift ϕ_R between $\chi_{Res}^{(3)}(\delta)$ and $\chi_{NR}^{(3)}$, as expressed by the phase factor $e^{i\phi_R}$ in eq. 3.27, will be discussed. This will be the case when any frequency of the pump/probe, Stokes, and CARS fields is close to an electronic resonance. For the sake of simplicity the electronic susceptibility term is still assumed to be negligible, i.e. $\chi_E^{(3)} = 0$, and eq. 3.27 reduces to

$$\chi_{tot}^{(3)}(\delta) = \chi_{NR}^{(3)} + \chi_{Res}^{(3)}(\delta)e^{i\phi_R} = \chi_{NR}^{(3)} + |\chi_{Res}^{(3)}(\delta)|e^{i(\phi_{Res}(\delta)+\phi_R)} = |\chi_{tot}^{(3)}(\delta)|e^{i\phi_{tot}(\delta)}. \tag{3.32}$$

The total phase spectrum $\phi_{tot}(\delta)$ is then obtained from eq. 3.32 as

$$\phi_{tot}(\delta) = tan^{-1}\left[\frac{|\chi_{Res}^{(3)}(\delta)|sin(\phi_{Res}(\delta) + \phi_R)}{\chi_{NR}^{(3)} + |\chi_{Res}^{(3)}(\delta)|cos(\phi_{Res}(\delta) + \phi_R)}\right]. \tag{3.33}$$

Using eq. 3.32, we find the CARS spectrum $I_{CARS}(\delta)$ to be

$$I_{CARS}(\delta) = \left|\chi_{tot}^{(3)}(\delta)\right|^2 = (\chi_{NR}^{(3)})^2 + |\chi_{Res}^{(3)}(\delta)|^2 + 2\chi_{NR}^{(3)}|\chi_{Res}^{(3)}(\delta)|cos(\phi_{Res}(\delta) + \phi_R). \tag{3.34}$$

Fig. 3.9 shows the simulations of the complex $\chi_{tot}^{(3)}(\delta)$, the CARS line shape $\left|\chi_{tot}^{(3)}(\delta)\right|^2$, and the total phase spectrum $\phi_{tot}(\delta)$ for different values of ϕ_R. As can be seen in fig. 3.9 A, the effect of the additional phase factor $e^{i\phi_R}$ is a rotation of $\chi_{Res}^{(3)}(\delta)$ in the complex plane around the point $[\chi_{NR}^{(3)}, 0]$. As shown in fig. 3.9 B, the CARS and phase spectra for $\phi_R = 0$ and $\phi_R = \pi$ are point reflections of each other. Here, the order of constructive and destructive interference in the CARS spectrum is swapped. With the course of $\chi_{Res}^{(3)}(\delta)$ no longer being restricted to the first and second quadrant of the complex plane (see fig. 3.9 A), the total phase spectrum $\phi_{tot}(\delta)$ itself becomes dispersive for values $\phi_R \neq 0, \pi$. Note that the point of zero detuning ($\delta = 0$) is rotating with increasing ϕ_R until for $\phi_R = \pi$ the phase is the vertical reflection of the phase for $\phi_R = 0$. With $|\delta| \gg \Gamma$ being far off the vibrational resonance, the CARS spectrum still takes the value $\left|\chi_{NR}^{(3)}\right|^2$ independent of ϕ_R, and the total phase still becomes zero.
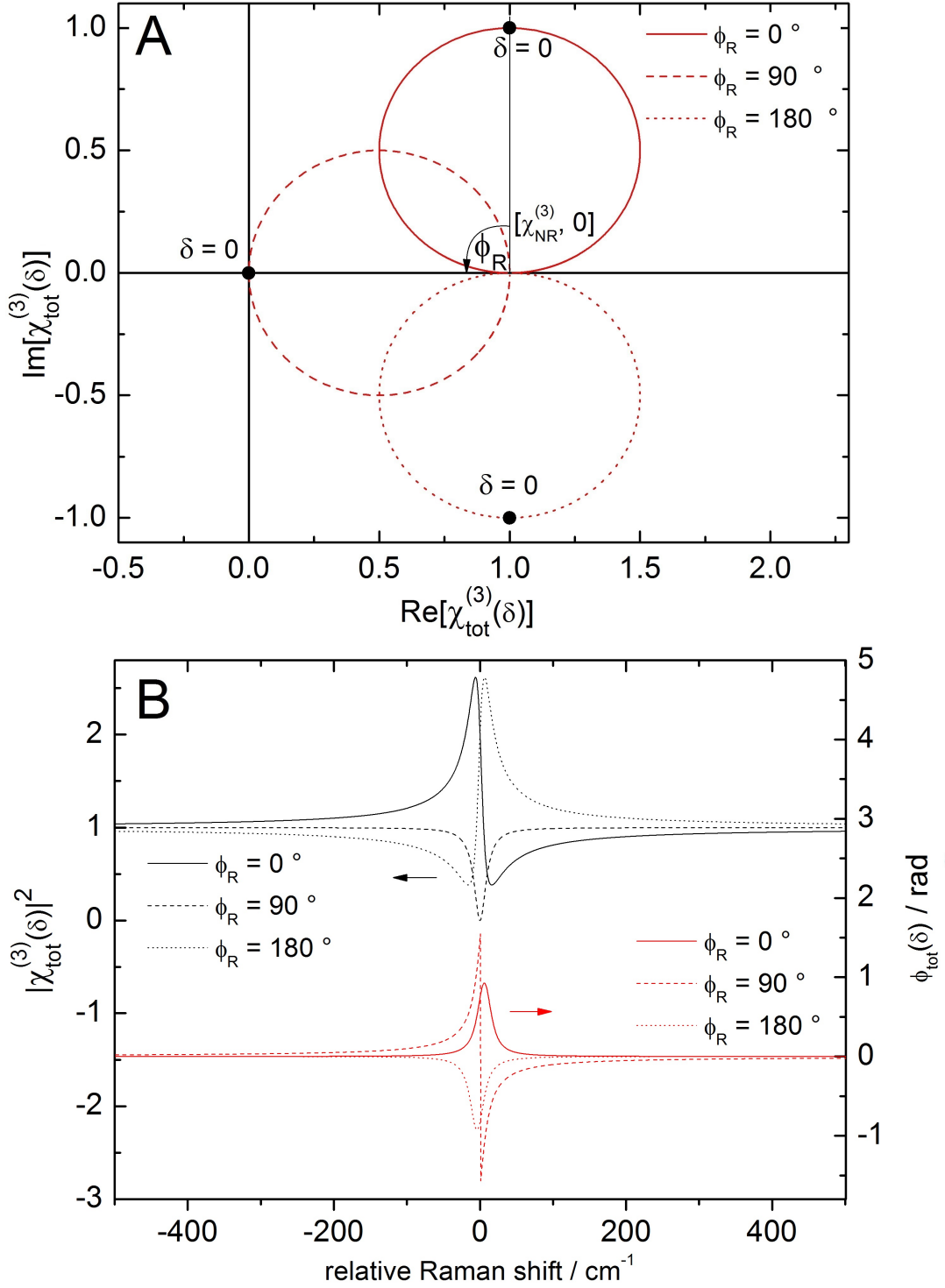
Figure 3.9: Simulation of a complex $\chi_{tot}^{(3)}(\delta)$ for an isolated complex vibrational resonance $\chi_{Res}^{(3)}(\delta)$ in the presence of a real nonresonant background $\chi_{NR}^{(3)}$ and an increasing phase shift ϕ_R between a fixed $\chi_{NR}^{(3)}$ and $\chi_{Res}^{(3)}(\delta)$. (A) Plot of $\chi_{tot}^{(3)}(\delta)$ in the complex plane calculated using eq. 3.32. The resonance follows a circle that is rotated by the phase angle ϕ_R around the point $[\chi_{NR}^{(3)}, 0]$. (B) CARS line shapes $|\chi_{tot}^{(3)}(\delta)|^2$ and total phase spectra $\phi_{tot}(\delta)$, calculated using eq. 3.34 and eq. 3.33, respectively. The simulation parameters are $A = 1$, $\Gamma = 20\ cm^{-1}$, $\chi_{NR}^{(3)} = 1$, and $\phi_R = 0, \frac{\pi}{2}, \pi$.

Simulation of the full model of $\chi_{tot}^{(3)}(\delta)$ according to eq. 3.27

Finally, the full model of $\chi_{tot}^{(3)}(\delta)$ given by eq. 3.27, which consists of a rotation of the vibrational resonance $\chi_{Res}^{(3)}(\delta)$ by the phase angle ϕ_R [20],[21], an additional electronic susceptibility contribution $\chi_E^{(3)}e^{i\phi_E}$, and a constant nonresonant background $\chi_{NR}^{(3)}$, will be discussed. For this most general case, the total phase spectrum $\phi_{tot}(\delta)$ is directly derived from eq. 3.28 as

$$\phi_{tot}(\delta) = tan^{-1}\left[\frac{\chi_E^{(3)}sin(\phi_E) + |\chi_{Res}^{(3)}(\delta)|sin(\phi_{Res}(\delta) + \phi_R)}{\chi_{NR}^{(3)} + \chi_E^{(3)}cos(\phi_E) + |\chi_{Res}^{(3)}(\delta)|cos(\phi_{Res}(\delta) + \phi_R)}\right], \tag{3.35}$$

and the CARS line shape is found as

$$I_{CARS}(\delta) = \left|\chi_{tot}^{(3)}(\delta)\right|^2 = (\chi_{NR}^{(3)})^2 + (\chi_E^{(3)})^2 + |\chi_{Res}^{(3)}(\delta)|^2 + 2\chi_{NR}^{(3)}\chi_E^{(3)}cos(\phi_E)$$

$$+2\chi_{NR}^{(3)}|\chi_{Res}^{(3)}(\delta)|cos(\phi_{Res}(\delta) + \phi_R) + 2\chi_E^{(3)}|\chi_{Res}^{(3)}(\delta)|cos(\phi_E - \phi_{Res}(\delta) - \phi_R). \tag{3.36}$$

Fig. 3.10 shows the corresponding simulation of the complex $\chi_{tot}^{(3)}(\delta)$, the CARS line shape $|\chi_{tot}^{(3)}(\delta)|^2$, and the total phase spectrum $\phi_{tot}(\delta)$ for the parameters $\chi_E = 1.5$, $\phi_E = \frac{\pi}{3}$ and $\phi_R = -\frac{\pi}{8}$. As can be seen in fig. 3.10 A, the effect of the additional electronic susceptibility term $\chi_E^{(3)}e^{i\phi_E}$ is a translation of $\chi_{Res}^{(3)}(\delta)$ in the complex plane from the point $[\chi_{NR}^{(3)}, 0]$ to $[\chi_{NR}^{(3)} + \chi_E^{(3)}cos(\phi_E), \chi_E^{(3)}sin(\phi_E)]$. The phase factor $e^{i\phi_R}$ then rotates the vibrational resonance $\chi_{Res}^{(3)}(\delta)$ around the point $[\chi_{NR}^{(3)} + \chi_E^{(3)}cos(\phi_E), \chi_E^{(3)}sin(\phi_E)]$. As shown in fig. 3.10 B, both the CARS and total phase spectra show a varying degree of constructive and destructive interference, which depends on the amplitudes and signs of $\chi_E^{(3)}$, ϕ_E and ϕ_R. Compared to the simple case where $\chi_E^{(3)} = 0$ and $\phi_R = 0$ (see eq. 3.29 and eq. 3.30), both the CARS and the total phase spectra exhibit dispersive character and have constant offset values. With $|\delta| \gg \Gamma$ being far off the vibrational resonance, we can define an effective complex susceptibility $\chi_{E\,eff}^{(3)}$ that combines all frequency independent contributions to the total susceptibility $\chi_{tot}^{(3)}(\delta)$ given by eq. 3.28, and that describes the new origin of the purely vibrational resonance in the complex plane:

$$lim_{|\delta|\gg\Gamma}\ \chi_{tot}^{(3)}(\delta) = \chi_{E\,eff}^{(3)} = |\chi_{E\,eff}^{(3)}|e^{i\phi_{E\,eff}} = \chi_{NR}^{(3)} + \chi_E^{(3)}e^{i\phi_E}, \tag{3.37}$$

where

$$\phi_{E\,eff} = tan^{-1}\left[\frac{sin(\phi_E)\chi_E^{(3)}}{\chi_{NR}^{(3)} + cos(\phi_E)\chi_E^{(3)}}\right]. \tag{3.38}$$

In this limiting case, the CARS intensity is then given by $|\chi_{E\,eff}^{(3)}|^2$:

$$lim_{\delta\gg\Gamma}|\chi_{tot}^{(3)}(\delta)|^2 = |\chi_{E\,eff}^{(3)}|^2 = \chi_{NR}^{(3)\,2} + 2\chi_{NR}^{(3)}\chi_E^{(3)}cos(\phi_E) + \chi_E^{(3)\,2}. \tag{3.39}$$

Consequently, eq. 3.38 and eq. 3.39 yield the offset values of the simulated CARS and total phase spectra shown in fig. 3.10 B to be $\phi_{E\ eff}$ and $|\chi^{(3)}_{E\ eff}|^2$, respectively.
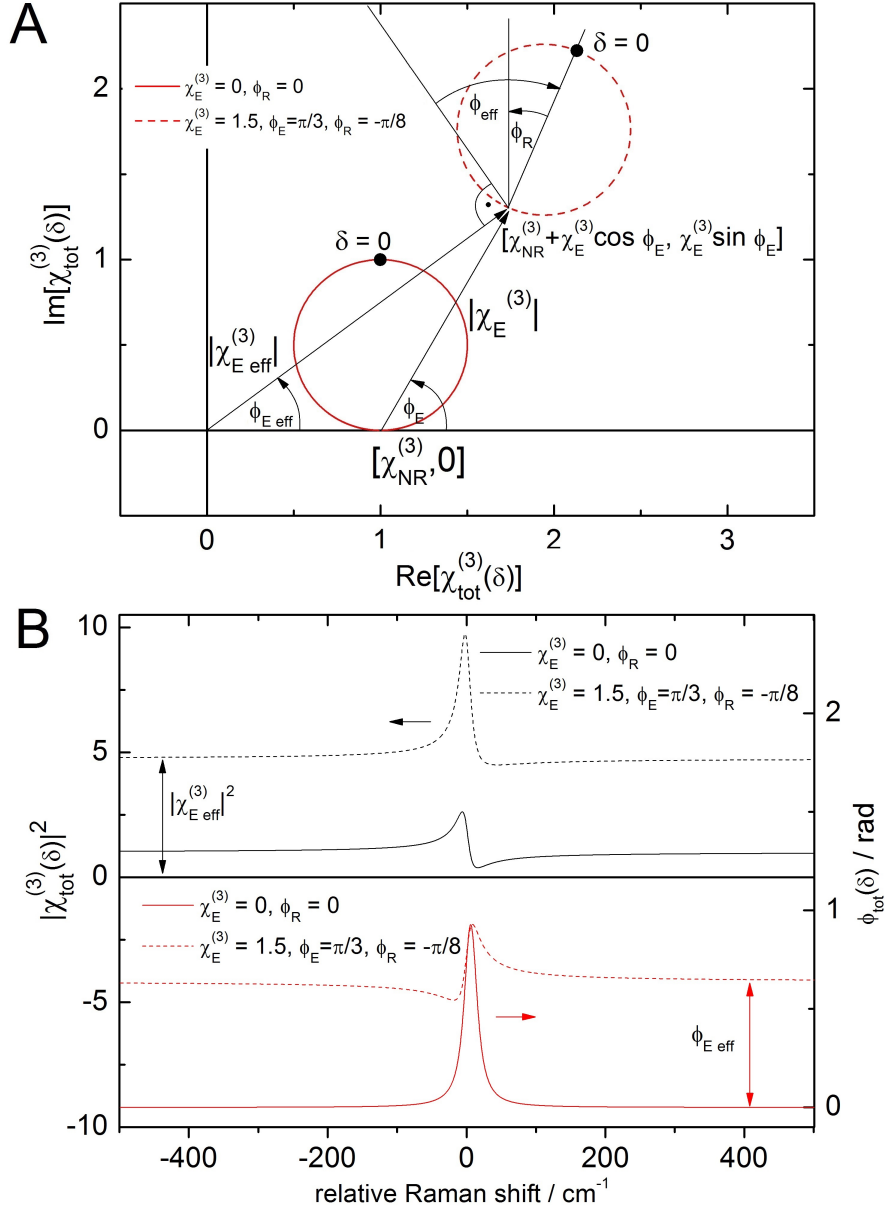

Figure 3.10: Simulation of a complex $\chi^{(3)}_{tot}(\delta)$ for an isolated single vibrational resonance $\chi^{(3)}_{Res}(\delta)$ in the presence of a real nonresonant background $\chi^{(3)}_{NR}$, an additional electronic susceptibility term $\chi^{(3)}_E e^{i\phi_E}$, and a phase shift ϕ_R between a fixed $\chi^{(3)}_{NR}$ and a fixed $\chi^{(3)}_{Res}(\delta)$. (A) The resonance calculated using eq. 3.27 follows a circle in the complex plane that is rotated by the phase angle ϕ_R, and whose origin is translated by $\chi^{(3)}_E e^{i\phi_E}$. (B) CARS spectrum $I_{CARS}(\delta)$ and total phase spectrum $\phi(\delta)$ calculated using eq. 3.36 and 3.35, respectively. The simulation parameters are $A = 1$, $\Gamma = 20\ cm^{-1}$, $\chi^{(3)}_{NR} = 1$, and $\chi^{(3)}_E = 0$, $\phi_R = 0$ (solid line) or $\chi^{(3)}_E = 1.5$, $\phi_E = \frac{\pi}{3}$ and $\phi_R = -\frac{\pi}{8}$ (dotted line).

Note that both offset values are independent of the parameter ϕ_R. Using eq. 3.37 and eq. 3.38, we can rewrite the general expression for the total susceptibility as follows:

$$\chi_{tot}^{(3)}(\delta) = \chi_{E\ eff}^{(3)} + \chi_{Res}^{(3)}(\delta)e^{i\phi_R} = \left[|\chi_{E\ eff}^{(3)}| + \chi_{Res}^{(3)}(\delta)e^{i(\phi_R - \phi_{E\ eff})}\right]e^{i\phi_{E\ eff}}, \qquad (3.40)$$

which results in an expression for the CARS spectra given by:

$$I_{CARS}(\delta) = \left|\chi_{tot}^{(3)}(\delta)\right|^2 = \left||\chi_{E\ eff}^{(3)}| + \chi_{Res}^{(3)}(\delta)e^{i(\phi_R - \phi_{E\ eff})}\right|^2. \qquad (3.41)$$

As can be seen, the complex pure vibrational resonance $\chi_{Res}^{(3)}(\delta)$ then appears rotated by an effective phase shift:

$$\phi_{eff} = \phi_R - \phi_{E\ eff}, \qquad (3.42)$$

which together with the effective nonresonant constant $\left|\chi_{E\ eff}^{(3)}\right|$ describes any deviation of the CARS line shape from the pure Lorentzian resonance line $\left|\chi_{Res}^{(3)}(\delta)\right|$. From eq. 3.42 follows that for the special case of $\phi_R = \phi_{E\ eff} \neq 0$, the effective phase shift ϕ_{eff} is zero, and the corresponding total phase spectrum $\phi_{tot}(\delta)$ would not appear dispersive. Only the phase offset $\phi_{E\ eff}$ would still be present. In other words, the pure vibrational resonance $\chi_{Res}^{(3)}(\delta)$ would be in phase with the effective non-resonant susceptibility $\chi_{E\ eff}^{(3)}$.

We have to keep in mind that in the actual experiment only the CARS spectrum is accessible. In the most general case, all discussed parameters will change the shape and amplitudes of the measured CARS spectrum. Without the knowledge of ϕ_{eff} and of $\left|\chi_{E\ eff}^{(3)}\right|$, the desired Raman response spectrum $Im[\chi_{Res}^{(3)}(\delta)]$ cannot be reconstructed correctly. Therefore, knowledge of the whole spectrum is indispensable in order to extract these parameters from a measured CARS spectrum and to draw quantitative conclusions, e.g. regarding concentrations of molecular scatterers!

3.3 Phase retrieval and reconstruction of complex $\chi^{(3)}(\nu)$ in multiplex CARS

3.3.1 Phase retrieval

"The life as we know it, would be very different without the FFT."

Charles Van Loan

In order to draw quantitative conclusions from the measured CARS power spectrum $S(\nu)$, the complex function $\chi_{Res}^{(3)}(\nu)$ containing the full vibrational information has to be retrieved. This can be done by fitting the CARS spectrum with a model of complex Lorentzian bands using eq. 3.29 [22]. However, this approach is not suitable for unknown and/or inhomogeneous line

shapes. In order to obtain $\chi_{Res}^{(3)}(\nu)$ in a model-independent way, the vibrational phase $\phi_{Res}(\nu)$ has to be retrieved. Among other methods valid only for single isolated resonances (e.g. [23], [24]), two established methods for the phase retrieval will be presented and compared in this section. The first approach is based on integral transforms, such as the Kramers-Kronig relations [25], [26] and the Hilbert/Bose transform. The second approach is the maximum entropy method (MEM), first applied to CARS spectra by Vartiainen [27].

3.3.1.1 The Kramers-Kronig (KK) method

When the KK method is used for retrieving the spectral phase $\phi(\nu)$ of an unknown complex susceptibility $\chi^{(3)}(\nu) = |\chi^{(3)}(\nu)|e^{i\phi(\nu)}$ from a CARS power spectrum $S(\nu) = |\chi^{(3)}(\nu)|^2$, one proceeds by taking the logarithm of $\chi^{(3)}(\nu)$ [28], [29], [30]

$$ln\left[\chi^{(3)}(\nu)\right] = ln\left[\sqrt{S(\nu)}\right] + i\phi(\nu)\,. \tag{3.43}$$

The real part of $ln\left[\chi^{(3)}(\nu)\right]$ is a function of the measured power spectrum $S(\nu)$, while the imaginary part directly represents the desired phase spectrum $\phi(\nu)$. Both the real and imaginary parts are coupled by the KK relations as follows:

$$\phi(\nu) = -\frac{\mathscr{P}}{\pi}\int_{-\infty}^{+\infty}\frac{ln\left[\sqrt{S(\nu')}\right]}{\nu - \nu'}d\nu' \tag{3.44}$$

$$ln\left[\sqrt{S(\nu)}\right] = \frac{\mathscr{P}}{\pi}\int_{-\infty}^{+\infty}\frac{\phi(\nu')}{\nu - \nu'}d\nu'. \tag{3.45}$$

Here, $\mathscr{P}$ denotes the Cauchy principal value, so that $lim_{\nu\to\infty}\phi(\nu) = 0$ and $lim_{\nu\to\infty}ln\left[\sqrt{S(\nu)}\right] = 0$. We identify the right hand sides as the Hilbert transforms $\mathscr{H}$ of $ln\sqrt{S(\nu)}$ and $\phi(\nu)$, which form a Hilbert pair. In practice, the calculation of $\phi(\nu) = \mathscr{H}(ln\sqrt{S(\nu)})$ is performed using the discrete Hilbert transform (DHT) (see appendix A.1.2). In Cicerone and Vartiainen [31], phase retrieval by time domain KK (TDKK), a KK variant where causality is ensured by usage of the Heavyside function, and by the maximum entropy method (MEM) are stated to be functionally equivalent for a large range of CARS cases. However, the KK method has various disadvantages: As first shown by Kircheva et. al. [29] and Vartiainen et. al. [32], for the case of a meromorphic response function that is described by a degenerate third-order nonlinear susceptibility, the KK method fails. Because of the shortcomings of the FFT as a spectral predictor (see the discussion in section 3.3.1.2), problems with the KK method can also be expected, if the spectral window consists of sparse data samples, e.g. less than hundred values.

3.3.1.2 The maximum entropy method (MEM)

The maximum entropy method is a variational principle to estimate a power spectrum by a certain measure of entropy. MEM became very popular in time series analysis for geophysical,

speech, sonar, radar data processing [33], only to count a few, in obtaining the power spectral density (PSD) [34], [35], [36], [37], and especially for the phase retrieval in spectroscopy [38]. There are many different approaches that predict the power spectrum $S(v)$ of a time series, ranging from simply applying the FFT via moving average models (or all-zero models) to autoregressive (AR, or all-pole) models. The MEM method is equivalent to an AR spectral estimator for the one-dimensional case [33]. It is important to mention that the simple approach of calculating the autocorrelation function (ACF) using the FFT of a time series $g_m(t) = g(t_m)$ as PSD is limited. Problems arise in distinguishing between the spectral response of two signals (frequency resolution [33], [37]), and also in windowing, which is the leakage of energy from the main lobe into side lobes. The spectral predictors can be classified into non-parametric approaches, for which no a priori information is needed (for example periodograms and the Welch' method), and in parametric approaches. The latter assume an underlying autoregressive (AR) process, such as MEM as introduced by Burg [39]. Burg was interested in a power spectrum $S(v)$, for which the measured data are given in terms of a time series $g_m(t)$. The corresponding ACF values $C(m)$ can then be calculated from $g_m(t)$.

Here, on the other hand, we want to use MEM for retrieving the phase from a measured power spectrum $S(v)$. The conventional way to calculate $S(v)$ out of the first M ACF values via $C(m) = \mathscr{F}S(v)$ is to assume $C(m) = 0$ for $|m| > M$ [40]. The number m is the order or the mth lag. Burg assumes (and earlier Shannon [41]) that these ACF values $C(m)$ are non-zero, but are such that they add no information to the process. The entropy of a stationary time series $g_m(t)$, where its statistical properties remain unchanged with time, is related to $S(v)$ as [37]:

$$h \propto \int_{v_0}^{v_1} \log S(v) dv. \tag{3.46}$$

Adding no information corresponds to maximizing the entropy h, which is given by

$$\frac{\partial}{\partial C(m)} \propto \int_{v_0}^{v_1} \log S(v) dv = 0, |m| > M. \tag{3.47}$$

The measured power spectrum can be fitted using the MEM model [37]:

$$S(v) = |f(v)|^2 = \frac{|\beta|^2}{\left|1 + \sum_{k=1}^{M} a_k e^{(-2\pi i k v)}\right|^2} , \tag{3.48}$$

with a_k and $\beta = |b_0|^2$ being the MEM coefficients, and $f(v)$ is a complex model function. In order to obtain the a_k and β coefficients, we will not use the Burg technique [39], but use systems theory. The MEM is equivalent to least-squares fitting an all-pole model to the data [42]. As mentioned, we assume that the sequence $g_m(t)$ belongs to an autoregressive (AR) and stationary process. That means, the sequence $g_m(t)$ is predictable from linear combinations (LC's) of past output values g_{m-k} ($k = 1, \ldots, M$), and of an error sequence $e_m(t)$ due to white noise as only input [43]:

$$g_m(t) = -\sum_{k=1}^{M} a_k g_{m-k}(t) + e_m(t). \tag{3.49}$$

The relationship between the AR-parameters a_k and the ACF $C(m)$ is given by the Yule-Walker equation [33]:

$$
\begin{bmatrix}
C(0) & C^*(1) & \ldots & C^*(M) \\
C(1) & C(0) & \ldots & C^*(M-1) \\
\vdots & \vdots & \ddots & \vdots \\
C(M) & C(M-1) & \ldots & C(0)
\end{bmatrix}
\begin{bmatrix}
1 \\
a_1 \\
\vdots \\
a_M
\end{bmatrix}
=
\begin{bmatrix}
b_0 \\
0 \\
\vdots \\
0
\end{bmatrix},
\tag{3.50}
$$

where the first matrix $\mathbf{C}(m, n)$ is the autocorrelation matrix. Only for a stationary process $g_m(t)$, the matrix $\mathbf{C}(m, n) = \langle g_m, g_n \rangle$ $(m, n \in \mathbb{Z})$ satisfies $\mathbf{C}(m, n) = \mathbf{C}(m + k, n + k)$ $(m, n, k \in \mathbb{Z})$. That means that the autocorrelation matrix does not depend on two independent variables, but only on their difference. In this case, the system given in eq. 3.50 will be a Toeplitz system. Otherwise, it would be a more complex Gram system [44]. Furthermore the matrix $\mathbf{C}(m, n)$ is symmetric. If an inverse matrix exists, $\mathbf{C}(m, n)$ is symmetric positive definite (SPD) [45]. In the frequency domain, input and output are connected via their z-transforms. For a finite record of $g_m(t)$, the ACF can only be approximated [42], which is done using the all-pole model derived by taking the z-transform of eq. 3.49 and $z = e^{i2\pi\nu}$ [38]. We obtain

$$
f(\nu) = \frac{E(\nu)}{1 + \sum_{k=1}^{M} a_k e^{-i2\pi k\nu}} \quad ,
\tag{3.51}
$$

with the prediction coefficients a_k and $E(\nu)$ being the Fourier transform of the error sequence $e_m(t)$, i.e.: $E(\nu) = \mathscr{F}(e_m(t))$, where the gain factor is 1. By solving eq. 3.50, we obtain the coefficients a_k and β. Using eq. 3.49, the time response of the system $g_m(t)$ is obtained as a byproduct [46]. When we compare eq. 3.48 with eq. 3.51, and define the phase for the complex denominator in eq. 3.51 as $\phi_{MEM}(\nu) = arg\left\{1 + \sum_{k=1}^{M} a_k e^{-i2\pi k\nu}\right\}$ [47], we have found the complex function $f(\nu)$ as

$$
f(\nu) = \frac{|\beta| e^{-i\phi_{MEM}(\nu)}}{|1 + \sum_{k=1}^{M} a_k e^{(-i2\pi k\nu)}|} = \mathscr{F} g(t).
\tag{3.52}
$$

In summary, with the autocorrelation coefficients $C(m)$ given by $\mathscr{F} S(\nu)$, we can calculate the time response $g(t)$ using the coefficients a_k and β obtained from eq. 3.50, and obtain the MEM phase as

$$
\phi_{MEM}(\nu) = arg\{f(\nu)\} = arg\{\mathscr{F} g(t)\}.
\tag{3.53}
$$

How the autocorrelation coefficients $C(m)$ are efficiently calculated will be discussed in section 5.1. How the system of equations given in eq. 3.50 can be efficiently solved will be the topic of section 5.2.

When compared with the KK method, MEM gives good phase retrieval results, even when only small spectral regions and/or data sampling are available. MEM is more data adaptive than the KK method in the sense that no extrapolations beyond the frequency boundaries of the

measured power spectrum are necessary. MEM offers the possibility of freely choosing up to which order the phase retrieval is performed, a feature that is not available in the KK method. This feature of MEM can be used for the drastic reduction of noise and of the computational cost. MEM is therefore the method of choice for the analysis of CARS spectra throughout this thesis.

3.3.2 Estimation of the error-phase spectrum

As Vartiainen et. al. [48] have pointed out, the MEM based phase retrieval reduces the problem of finding the phase $\phi_{MEM}(v)$ belonging to the measured modulus spectrum $S(v)$ to the problem of finding an error-phase $\phi_{error}(v)$, which is superimposed to the desired pure vibrational phase spectrum $\phi_{Res}(v)$. The same holds for the KK based phase retrieval [31]. Because the phase of the nonresonant contribution $\chi_{NR}^{(3)}$ is the reference, a prerequisite for the correct phase retrieval is the presence of at least one anchor point within the CARS power spectrum, which is not affected by any nearby vibrational resonance. In general, the error-phase $\phi_{error}(v)$ is slowly varying with frequency. Possible origins include: First, the error-phase $\phi_{error}(v)$ is simply a consequence of the discretisation of the measured power spectrum. Secondly, the appearance of the error-phase $\phi_{error}(v)$ is due to an erroneous reference spectrum for eliminating the Stokes profile (see eq. 3.26), as for example due to contributions of two photon fluorescence signals. In summary, the error-phase $\phi_{error}(v)$ represents the accumulated experimental imperfections, and thus needs to be distinguished from the effective phase ϕ_{eff} discussed in section 3.2.2, which is a sample-specific property. No matter if KK or MEM phase retrieval is used, the removal of the error-phase $\phi_{error}(v)$ from the retrieved phase, e.g. $\phi_{retrieved}(v) = \phi_{MEM}(v)$ yields the estimated phase $\phi_{estimated}(v)$ as:

$$\phi_{estimated}(v) = \phi_{retrieved}(v) - \phi_{error}(v) \, . \tag{3.54}$$

The desired reconstruction of the complex $\chi^{(3)}(v)$ is then

$$\chi^{(3)}(v) = \sqrt{S(v)} e^{i\phi_{estimated}(v)} \, . \tag{3.55}$$

3.3.2.1 Polynomial error-phase estimation

In order to approximate an error-phase spectrum $\phi_{error}(v)$, the knowledge and supervized selection of a nonresonant subset of point(s) $S_{NR}(v)$ from within the CARS spectrum $S(v)$, or rather a nonresonant subset of point(s) $\phi_{MEM\ NR}(v)$ from within the retrieved MEM-phase spectrum $\phi_{MEM}(v)$ is needed. The estimation of $\phi_{error}(v)$ can be carried out using polynomial or spline fitting. An efficient way is to solve the following polynomial interpolation equation as proposed

by Press [49]:

$$\phi_{error}(\nu) = B_0 + B_1\nu^1 + \ldots + B_p\nu^p \; , \tag{3.56}$$

with the coefficients B satisfying the Vandermonde system $\mathbf{V_{Van}}B = \phi_{error}(\nu)$ (see appendix A.2). The polynomial approximation can iteratively be improved as suggested by Beier [50]. The disadvantage of the described polynomial method is that for a broad spectrum $\phi_{MEM}(\nu)$ and a large set of nonresonant points $\phi_{MEM\;NR}(\nu)$, a high order p is needed for a good approximation of $\phi_{error}(\nu)$. This easily gives rise to fit instabilities. Spline's on the other hand are piecewise defined polynomial functions between several points of $\phi_{MEM\;NR}(\nu)$. From the numerous Spline functions available [51], the Akima type composed of a set of polynomials of order $p \leq 3$ was chosen because it allows to calculate the slope of the error-phase spectrum at a given point $\phi_{MEM\;NR}(\nu)$ using only ±2 neighboring points. This Akima polynomial has to fulfill the following conditions at both values: The function value $\phi_{error}(\nu)$ and its slope must be equal to the corresponding values of the MEM-phase $\phi_{MEM\;NR}(\nu)$. This gives four conditions for two evaluated points, and in this way the polynomial is fully determined [52]. In contrast to the polynomial interpolation equation (eq. 3.56), by using the Akima spline values separated by more than two values have no influence on $\phi_{error}(\nu)$ at all! This results in a good robustness against outliers when compared with other interpolation methods [52], [53]. In practice, when dealing with noisy $\phi_{MEM}(\nu)$ spectra, it is helpful to calculate the mean of the nonresonant regions $\phi_{MEM\;NR}(\nu)$ prior evaluating the Akima Spline.

An alternative method for approximating the error-phase spectrum $\phi_{error}(\nu)$ is based on the wavelet transform (see appendix A.3). This unsupervized error-phase estimation method is highly desirable in cases of an unknown and heterogeneous spectra.

4 Methods

This chapter summarizes all used methods, that are common to all the experimental results shown. Here, the general specifications of the hardware and the data analysis strategy will be described. The reader finds the sample-specific measurement conditions and sample preparation procedures details in the materials section at the beginning of each result chapter.

4.1 The spontaneous Raman microscope

Spontaneous Raman (SR) spectra were recorded using a commercial system (WITec GmbH, Germany: WITec alpha 300 RA). This confocal Raman microscope is equipped with a cw laser source, delivering 37 *mW* at λ_{Ex} = 532 *nm* measured before the objective (Nikon: 100x/0.95 N.A.) focussing the excitation beam into the sample. The backscattered Raman signal is collected using the same objective and separated from the excitation wavelength using a dichroic beamsplitter. The Raman scattered light is then coupled into a multi-mode fibre (fibres with 25 *μm* and 50 *μm* have been used, as will be indicated in section 5.4.1, 6.2.2 and 7.2.3) and passed to a lens based spectrometer with > 60 % throughput (WITec GmbH, Germany: UHTS300, focal length 300 *mm*, aperture ratio f/4, microscope optimized gratings with 1800 *lines/mm* or 600 *lines/mm* blazed for 532 *nm* excitation). The spectrometer is equipped with a peltier-cooled CCD camera (Andor: Newton DU 970N-UVB-353 EMCCD, 200 x 1600 pixels, 606 spectra / second in full vertical binning, 1515 spectra / second in crop mode, 16 bit digitization, max. read out rate 2.5 *MHz*). The sample was scanned using a three-axis piezo-scan table (Physik Instrumente: P-527K 056), which has an operating displacement of 200 *μm* in x and y direction, and 20 *μm* in z direction. Some spectra (see section 7.2.3) have been recorded with a precursor of the WITec 300 system, the WITec CRM-200 system (WITec GmbH, Germany), which however has the same key specifications apart from the objective (Nikon ELWD, 40x/ 0.6 N.A.).

4.2 The multiplex CARS microscope

The homebuildt CARS setup has been developed over the past years in the lab and consists over several options for laser excitation and imaging systems. The CARS setup used is given in fig. 4.1. The setup uses two laser pulse trains with a repetition rate of 76 *MHz* delivered
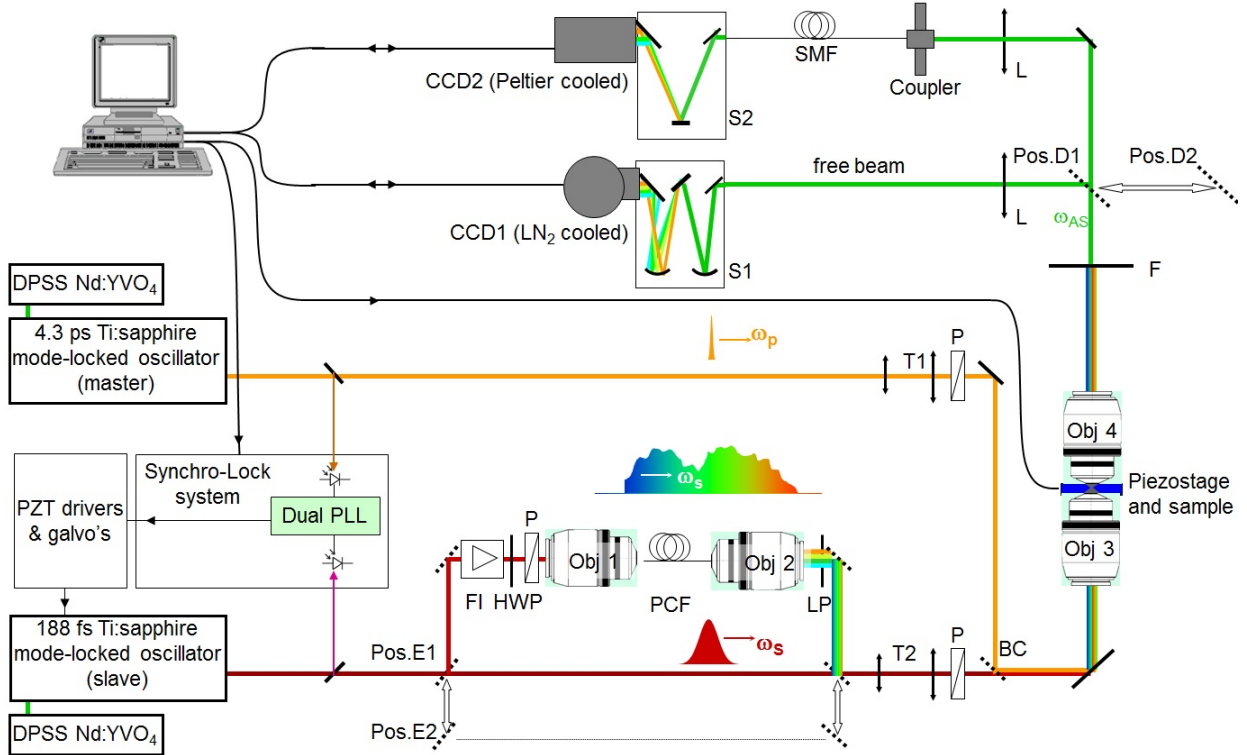
Figure 4.1: The multiplex CARS microscope. For the resulting specifications in dependence of the movable mirrors **E** and **D** see tab. 4.1. See text for details.

by two mode-locked Ti:sapphire (Coherent: MIRA 900-D and MIRA 900-P) laser oscillators, that are pumped by two Nd:YVO$_4$ lasers (Coherent: Verdi V6 and V10, respectively). With one Ti:sapphire laser oscillator running in the ps mode (pulse duration 4.3 *ps*) serving as the narrow band pump source, and the other Ti:sapphire laser oscillator running in the fs mode (pulse duration 188 *fs*) and serving as the broad pulse source, a multiplex CARS spectral range of $\approx 400~cm^{-1}$ can be covered. When the fs pulses are fed into a photonic crystal fibre (**PCF**, NKT: NL-PM 750, Femtowhite) using the mirror (**E**), a supercontinuum (SC) is generated and the frequency range of the multiplex CARS spectrum can be extended to $\approx 4000~cm^{-1}$. To avoid backreflections from the fiber into the oscillator, a Faraday isolator (**FI**) is used. The combination of a half-wave plate and a Polarizer (**HWP + P**) serves for controlling the power. Only the wavelength components > 800 *nm* of the generated SC are used for Stokes pulse excitation by applying a longpass (**LP**) filter. Using telescopes (**T1** and **T2**), the pump and Stokes beams are collimated and their diameters are set to match the diameter of the back aperture of the focussing objective (**Obj 3**). Polarizers (**P**) assure that both beams are linear

polarized and parallel oriented. After combining both collimated beams using a dichroic beam combiner (**BC**), the copropagating pulse trains are fed into an inverted microscope (Olympus: IX 71) and focussed into a sample using an 60x/1.2 N.A. w. (Olympus UPlanSApo) objective (**Obj 3**). The temporal overlap between the pump and the Stokes pulses is achieved by an active electronic synchronisation unit (Coherent: **Synchrolock**-AP), which consists of monitoring a part of the Ti:sapphire outputs with photodiodes, and feeding these photodiode signals into a dual-phase locked loop (PLL), with one loop operating at the fundamental pulse repetition rate, and the second loop on the 175th harmonic at 14 GHz. It is this second loop, that enables a stable synchronisation with 55 fs timing jitter. The pulse repetition rate of one oscillator (slave) is controlled via the adjustment of the cavity length in a three-stage process (using a DC motor as first stage, a LF galvanometer driven delay line as second stage, and a HF-piezo actuator as the third stage), while the second oscillator (master) is running free [54]. A control knob allows to adjust for temporal overlap of the pump and Stokes pulses. Having achieved spatial and temporal overlap of pump and Stokes pulse trains in the sample, a CARS signal can be generated. The generated CARS light is collected in the forward-direction using an 60x/0.9 N.A. w. (Olympus LUMPlanFI/IR) objective (**Obj 4**), and spectrally separated from the pump and Stokes wavelength using a shortpass filter (**F**). Depending on the position of the detection mirror (**D**), the CARS signal is passed either as a free beam to an astigmatism corrected Czerny-Turner spectrometer (**S1**, Acton Research: SpectraPro-150, focal length 150 mm, aperture ratio f/4, scanning range 0-2800 nm using a 600 $lines/mm$ grating) equipped with a liquid nitrogen (LN_2) cooled CCD camera (**CCD1**, Princeton Instruments: Spec-10:100B, 100 x 1340 pixels, minimum readout 2.58 ms per spectrum, 16 bit digitization, max. read out rate 1 MHz). Alternatively, the collected light was coupled into a custom made single-mode fibre (**SMF**, OZ optics: SMJ-3S5-633-4/125-3-2) and into the spectrometer / CCD-system described in section 4.1. The sample can be scanned using either a three-axis piezo-scan table (Physik Instrumente: PZT P-517.3CL), which has an operating displacement of 100 μm in x and y direction, and 20 μm in z direction, or using the scanning table described in section 4.1. All experiment control and data acquisition software was written in house by Dr. Alexander Kovalev, a former member of the group. The resulting spectral specifications are depending on the excitation source and detection system used and are summarized in tab. 4.1. Note that the lower limit for the spectral resolution is determined by the spectral width of the pump pulses and therefore is in all combinations approximately 4 cm^{-1}. Depending on the spectrometer used, the intrinsic spectral resolution of the spectrometer is 3.7 cm^{-1} or 1.2 cm^{-1}, thus not reducing the actual resolution given by the pump pulse.

Table 4.1: Specifications of the multiplex CARS microscope for the different excitation sources and detection systems used.

Excitation source / detection system used	CARS spectral range covered	maximum spectral resolution	minimum integration time t_{int}	used in section
ps-SC/CCD1	$4000\ cm^{-1}$	$4\ cm^{-1}$	$2.58\ ms$	section 7.2.4 and 8.2.3
ps-fs/CCD1	$400\ cm^{-1}$	$4\ cm^{-1}$	$2.58\ ms$	section 6.2.3
ps-fs/CCD2	$400\ cm^{-1}$	$4\ cm^{-1}$	$670\ \mu s$	section 6.2.3

4.3 Data analysis of spontaneous Raman spectra

This section describes, how to extract molecular information of interest out of the experimental Raman raw data. Unless otherwise indicated, data analysis steps were coded in MATLAB r12 (MathWorks). An overview of the analysis steps 1.-8. for spontaneous Raman spectra is given in the flowchart fig. 4.2.

1. **Dark count correction and frequency calibration**

   The CCD cameras used are cooled in order to reduce the thermal noise that leads to a frequency independent signal even when the CCD array is not illuminated at all. This offset does not contain any information concerning the vibrational contrast and thus has to be subtracted. The wavenumber axis is calibrated using the Rayleigh peak as a reference for zero Raman shift.

2. **Cosmic ray removal**

   High-energy particles, that can be of cosmic origin, give raise for spikes in the recorded spectra at random spectral positions and times. The cosmic ray removal (CRR) is performed using a filter, that exploits the abrupt change in the recorded signal intensity caused by such events. Values detected as cosmic rays are replaced by the median of the neighboring values. The CRR is performed using the WITec software.

3. **Background subtraction**

   If the Raman spectrum of a solvent or a substrate (e.g. a glass coverslip) is superimposed to the sample spectra, then these components represent a background spectrum. A weighted subtraction of this independently measured background components is performed.
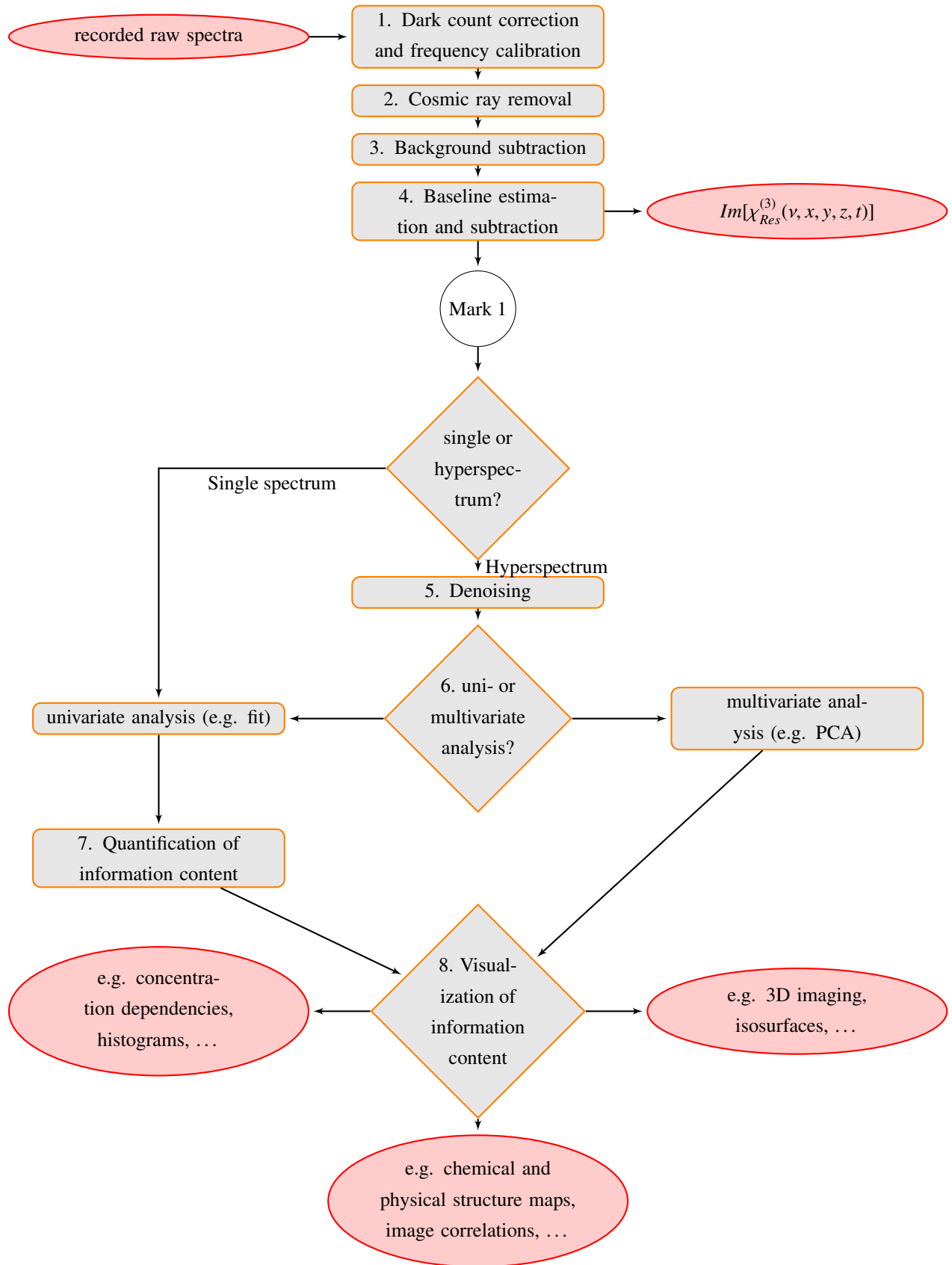
Figure 4.2: Flow chart of the spontaneous Raman data processing pipeline separated into data preconditioning (before mark 1) and data analysis (after mark 1).

<p style="text-align: center;">4. Baseline estimation and subtraction</p>

4. | Baseline estimation and subtraction

If for example additional fluorescence from the sample is superimposed on the Raman spectrum, it can be estimated as a baseline. This can be done with a polynomial approach or a wavelet prism approach [55], see the methods described in appendix A.3. It is however necessary to assure that the data are equidistant, before e.g. a polynomial is fitted to the data. This is achieved using the akima spline interpolation described in section 3.3.2.1.

5. | Denoising

Prior to extracting quantitative information from the background-corrected Raman spectrum, it is appropriate to increase the data's SNR by reducing the noise level without reducing the signal level. In cases, where the signals are above the noise level, the singular value decomposition (SVD) procedure described in appendix A.4.1 can be used. However, if relatively small signal amplitudes within the noise level or even below are present, SVD is inappropriate. Small signal amplitudes present in a certain Raman spectrum of a hyperspectrum can be removed by SVD and/or appear after performing SVD at a wrong spatial position. In these cases an alternative method based on the bilateral filter was developed and applied, see appendix A.4.2. Which denoising scheme is used in the particular applications is mentioned in the detailed method chapters of the particular result chapter.

6. | Univariate or multivariate analysis

Depending whether a single spectrum or a hyperspectral data set is analyzed, the information content is extracted by univariate or multivariate data analysis methods described in section 4.5. Univariate data analysis methods analyze one-dimensional data-sets like single spectra or line-scans, while multivariate data analysis methods like the principal component analysis (PCA) analyze a complete hyperspectrum at once. It is however important to note, that results obtained by multivariate data analysis methods are only valid for the particular data set of interest and they cannot be translated to other data sets by implication.

7. | Quantification of the information content

Prior to visualization, the information content first must be quantified. In the case of a single Raman spectrum, this can be the peak amplitude of a resonance representing the concentration of a substance, or the ratio of peak amplitudes representing e.g. the volume fraction of a substance in the crystalline state. In the case of a hyperspectrum, the information content can be the volume of e.g. lipid droplets or the size distribution of certain domains.

<p style="text-align: center;">37</p>

8. Visualization of information content

Depending on the dimensionality of the information content, the results are plotted as a line-scan, histogram, image, or three dimensional distribution.

4.4 Data analysis of CARS spectra

Unless otherwise indicated, data analysis steps concerning the recorded CARS spectra were coded in MATLAB r12 (MathWorks). An overview of the analysis steps 1.-11. for CARS spectra is given in the flowchart in fig. 4.3. The subsequent steps can involve a denoising of $\chi^{(3)}_{Res}(\nu, x, y, z, t)$ (as described in section 4.3), and again univariate or multivariate analysis, quantification of the information content and visualisation, depending on the dimensionality of the data. These analysis steps are equivalent to the ones in the spontaneous Raman case and are shown in the flowchart fig. 4.2 after Mark 1.

1. Dark count correction

Like in the SR case, the dark counts due to thermal noise do not contain any information and must be removed in order to not falsify the subsequent analysis of the CARS spectra. The sensitivity of the latter on the offset level is discussed in appendix A.5. The average dark count value can be obtained from the recorded raw spectra in spectral regions, where either

a. the shortpass filter has blocked any CARS signal,

b. or outside the CARS spectral bandwidth.

Then this value can be subtracted from every raw spectrum. Within one spectrum, the dark count value derived by a. and b. can be different. It turned out, that subtracting the smaller of these two values leads to the better result.

2. Cosmic ray removal

Cosmic ray removal (CRR) is performed using the WITec software as in the SR case.

3. Frequency calibration

Due to refractive index inhomogeneity in the sample in combination with the $\approx 1.2\ m$ long free beam-path between the sample and the spectrometer, the center position, where the CCD array is hit, can change. In this way the deflection of the beam translates into a shift of the whole spectrum along the wavelength scale. If not corrected, this frequency shift could later be interpreted by mistake as frequency shifts of the reconstructed Raman bands. Furthermore, the elimination of the Stokes pulse profile according to eq. 3.26 is only possible, when the sample and reference spectra are identically frequency calibrated.

If not, eq. 3.26 is introducing parasite oscillations that would again be interpreted as vibrational information in the following steps of the analysis and therefore falsify the spectral interpretation. The known wavelength edge of the shortpass filter (**F** in fig. 4.1) is used as a spectral marker. When expressed in units of spectral pixels, the frequency shift typically is in the range of max. ± 2 pixel, corresponding to max. $\pm 7.4 \; cm^{-1}$, when the 600 $lines/mm$ grating is used. In order to detect and correct the shift more exact, first the resolution of the spectra is increased by using the Akima spline interpolation described in section 3.3.2. It was found, that the most robust and reliable way to detect this position is not finding the maximum of the derivative of the spectrum, but to detect the spectral position of the edge, where the spectrum has reached 50 % of the maximum transmission value of the spectrum in the region of the edge. Each raw spectrum is backshifted by the value obtained. In this way an image of the spectral shift correction value $\Delta v(x, y, z, t)$ is generated, that represents a map of the local pixel deflection.

4. Correction for etaloning artefacts of the CCD detector

Etaloning is an issue when back-illuminated CCD arrays are used. The thickness of the back-thinned CCD chip is in the range of the detected CARS signals wavelength. Thus, the chip acts like an etalon. The light is reflected between the front and back-surfaces and interferes with each other, resulting in a spectral modulation of the measured spectrum known as etaloning. The amplitude of this spectral modulation depends on the actual CARS intensity and is therefore changing within a heterogeneous sample. This is why this spectral modulation cannot be eliminated by using eq. 3.26 where a single modulated reference CARS spectrum is used. Any remaining modulation due to etaloning in the CARS spectra would be interpreted as vibrational information in the following steps of the analysis, and therefore falsify the spectral interpretation. In order to obtain an etaloning modulation spectrum under identical experimental conditions used for recording the CARS spectra, a CARS spectrum of a nonresonant sample is measured. This is filtered using a robust Loess filter in order to extract the oscillatory part only, resulting in the etaloning modulation spectrum oscillating around 1. Etaloning is then removed for each raw spectrum by dividing it with the etaloning modulation spectrum.

5. Correction for intra-Stokes background contributions

When using an ultra-broadband Stokes excitation as in the combinations E1/D1 or E1/D2, and when the spectral width of the Stokes pulse spectrum is bigger than the frequency difference $(v_{Pump} - v_{Stokes})$, not only one, but two CARS fields are generated at each sample position, and the coherent sum of these two is recorded. The first CARS field is generated by the interaction of pump and Stokes pulses in the sample according to eq. 3.24. Its intensity spectrum is given by $I_{CARS}(v)$. The second CARS field is generated by

the combination of intra-Stokes components, and thus is independent of the pump pulse. This intra-Stokes CARS field adds up with the CARS field of the sample in a coherent manner on the CCD chip. The intra-Stokes CARS intensity $I_{NTO}(\nu)$ can be independently recorded, when the temporal overlap of the pump pulse is not fulfilled. The homodyne mixing of the two CARS fields yields the following total recorded spectral intensity:

$$I_{total}(\nu) = I_{CARS}(\nu) + I_{NTO}(\nu) + 2\sqrt{I_{CARS}(\nu)I_{NTO}(\nu)}cos(\phi_{CARS} - \phi_{NTO}) \ . \qquad (4.1)$$

Assuming that the relative phase difference between both fields is negligible ($\phi_{CARS} \approx \phi_{NTO}$), the CARS spectrum of the sample that is free of intra-Stokes contributions is:

$$I_{CARS}(\nu) = \left(\sqrt{I_{total}(\nu)} - \sqrt{I_{NTO}(\nu)} \right)^2 \ . \qquad (4.2)$$

This correction has to be carried out for both the sample and reference spectra, $I_{total\ sample}(\nu)$ and $I_{total\ ref}(\nu)$, respectively, with the intra-Stokes background generated under equal conditions. Because both intra-Stokes spectra, $I_{NTO\ sample}(\nu)$ and $I_{NTO\ ref}(\nu)$, depend on the Stokes profile, they have the same spectral shape and only differ by a factor c, when $\chi_{NR\ ref}^{(3)} \neq \chi_{NR\ sample}^{(3)}$: $I_{NTO\ sample}(\nu) = cI_{NTO\ ref}(\nu)$. The factor c can be determined from a nonresonant region of $I_{total\ sample}(\nu)$ of the sample. Having determined the factor c, the correction of the measured total CARS spectrum of the sample then reads:

$$I_{CARS\ sample}(\nu) = \left(\sqrt{I_{total\ sample}(\nu)} - \sqrt{cI_{NTO\ ref}(\nu)} \right)^2 \ . \qquad (4.3)$$

In an analogous manner, $I_{total\ ref}(\nu)$ is corrected and yields $I_{CARS\ ref}(\nu)$.

6. **Calculation of the normalized CARS spectrum** $S(\nu, x, y, z, t)$

Having performed the previous steps for both the sample spectrum $I_{sample}(\nu, x, y, z, t)$ and the reference spectrum $I_{ref}(\nu)$, the normalized CARS spectrum $S(\nu, x, y, z, t)$ is calculated according to eq. 3.26 (see also the discussion in appendix A.6). Prior to the subsequent data analysis steps, each normalized CARS spectrum $S(\nu, x, y, z, t)$ needs to be converted into an equidistant wavenumber axis. A negative and thus physically meaningless CARS spectrum $S(\nu, x, y, z, t)$ can be caused by noise at the destructive side of strong resonances. In these cases, smoothing of the CARS spectrum $S(\nu, x, y, z, t)$ only in this spectral region is performed.
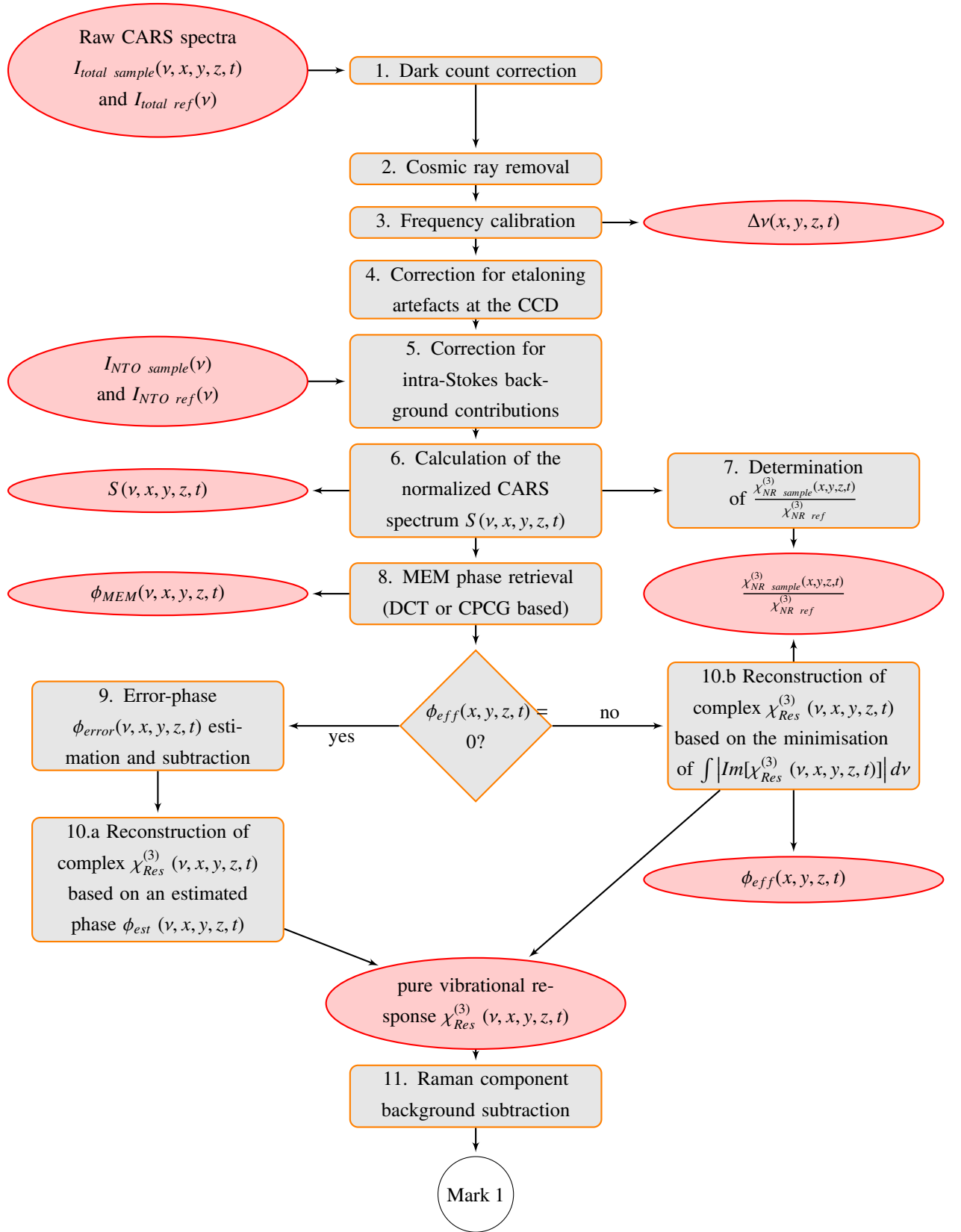
Figure 4.3: Flow chart showing the CARS spectra analysis pipeline, consisting of pre-conditioning, two options for the reconstruction of $\chi_{Res}^{(3)}(\nu, x, y, z, t)$, and a background subtraction. The subsequent analysis steps are the same as in the spontaneous Raman case, see the flow chart in fig. 4.2 after mark 1.

7. **Determination of** $\frac{\chi^{(3)}_{NR\ sample}(x,y,z,t)}{\chi^{(3)}_{NR\ ref}}$

The importance and the influence of the ratio $\frac{\chi^{(3)}_{NR\ sample}(x,y,z,t)}{\chi^{(3)}_{NR\ ref}}$ is discussed in appendix A.6. This ratio can be derived in a supervised way from nonresonant regions of the normalized CARS spectrum as follows:

$$S_{NR}(x,y,z,t) = \left[\frac{\chi^{(3)}_{NR\ sample}(x,y,z,t)}{\chi^{(3)}_{NR\ ref}}\right]^2 \forall \nu,\ where:\ \chi^{(3)}(\nu,x,y,z,t) = \chi^{(3)}_{NR}(x,y,z,t)\ .$$

(4.4)

In section 5.3.3, an alternative and unsupervized method is described. Performed for each sample spectrum in a hyperspectral data set, a map of $\frac{\chi^{(3)}_{NR}(x,y,z,t)sample}{\chi^{(3)}_{NR\ ref}}$ is obtained. Note, when CARS spectra reconstructed with different reference spectra are compared, the factor $\frac{\chi^{(3)}_{NR}(x,y,z,t)sample}{\chi^{(3)}_{NR\ ref}}$ must be scaled according to the ratio of the different $\chi^{(3)}_{NR}$ of the different references used, see appendix A.6 for a detailed discussion.

8. **MEM phase retrieval (DCT or CPCG based)**

Subsequent phase retrieval of all normalized CARS spectra $S(\nu,x,y,z,t)$ is performed using the DCT or CPCG MEM algorithms, as newly developed in this thesis and discussed in detail in chapter 5. As a result, we obtain the phase spectra $\phi_{MEM}(\nu,x,y,z,t)$ as given in eq. 3.53.

9. **Error-phase** $\phi_{error}(\nu,x,y,z,t)$ **estimation and subtraction**

Either a polynomial (see section 3.3.2.1) or a wavelet prism based (see appendix A.3) error-phase estimation is performed, and the obtained error-phase $\phi_{error}(\nu,x,y,z,t)$ is subtracted from the MEM phase $\phi_{MEM}(\nu,x,y,z,t)$, resulting in an estimation of the vibrational phase according to eq. 3.54.

10. **Reconstruction of complex** $\chi^{(3)}_{Res}(\nu,x,y,z,t)$

    a. **Reconstruction of complex** $\chi^{(3)}_{Res}(\nu,x,y,z,t)$ **based on an estimated phase**
    $\phi_{est}(\nu,x,y,z,t)$

    The reconstruction of the complex $\chi^{(3)}_{Res}(\nu,x,y,z,t)$ is performed according to eq. 3.55, resulting in the full characterization of the real and imaginary part of the vibrational Raman response. However, only in cases where $\phi_{eff}(x,y,z,t) = 0$ is fulfilled, this step will result in reconstructed Raman spectra $Im[\chi^{(3)}_{Res}(\nu,x,y,z,t)]$ that match spectra obtained by spontaneous Raman spectroscopy.

b. **Reconstruction of complex** $\chi_{Res}^{(3)}(\nu, x, y, z, t)$ **based on the minimisation of** $\int \left| Im[\chi_{Res}^{(3)}(\nu, x, y, z, t)] \right| d\nu$

The reconstruction of the complex $\chi_{Res}^{(3)}(\nu, x, y, z, t)$ is based on the minimisation of $\int \left| Im[\chi_{Res}^{(3)}(\nu, x, y, z, t)] \right| d\nu$ using a frequency independent phase shift $\phi_{eff}(x, y, z, t)$ and the ratio $\frac{\chi_{NR\ sample}^{(3)}(x,y,z,t)}{\chi_{NR\ ref}^{(3)}}$ as optimisation parameters. These two parameters are obtained in an unsupervised manner. This new procedure has been developed in this thesis, and will be discussed in section 5.3.3. In this way, the reconstruction is performed without any a priori assumptions. If the SNR however is poor, a supervised determination of the ratio $\frac{\chi_{NR\ sample}^{(3)}(x,y,z,t)}{\chi_{NR\ ref}^{(3)}}$ is more accurate. In the case of $\phi_{eff}(x, y, z, t) = 0$, both schemes 10.a and 10.b result in the same reconstructed complex $\chi_{Res}^{(3)}(\nu, x, y, z, t)$.

11. **Raman component background subtraction**

In the case of a known solvent Raman spectrum $Im[\chi_{Res\ solvent}^{(3)}(\nu)]$ (e.g. water), we can subtract its weighted component from the reconstructed $Im[\chi_{Res}^{(3)}(\nu, x, y, z, t)]$ spectrum.

4.5 Quantification of the information content

This section lays out the analysis methods used in order to quantify the information content of a vibrational spectrum. Before going into details, first the term hyperspectrum $\chi^{(3)}(\nu, x, y, z, t)$ is defined as a multidimensional array, or tensor of rank two or higher. Concerning both, the spontaneous Raman and CARS data sets, the analysis of the spectrally and spatially resolved data can be divided into multivariate and univariate methods. In terms of analyzing hyperspectra, univariate methods only analyze one-dimensional subsets of the hyperspectrum at a time. Multivariate methods, on the other hand, use a certain model to the whole tensor. Here, only univariate methods will be treated and in particular curve fitting.

4.5.1 Used fit model

What method is used in particular depends on the application. When spectral details like amplitude ratios or band positions need to be analyzed, decomposition of the spectrum using a certain fit model is the method of choice.

4.5.1.1 Curve fitting

The Raman line profile is typically described by a Lorentzian:

$$Im[\chi_{Res}^{(3)}] = L(\nu) = \frac{A\Gamma_L}{(\nu_0 - \delta)^2 + \Gamma_L^2} \ , \tag{4.5}$$

where the subscript L refers to the Lorentzian. In the real world, the presence of Gaussian broadening implies that eq. 4.5 is convoluted with a Gaussian lineshape [56]:

$$G(\nu) = e^{-\left[\frac{(\nu_0 - \delta)}{\Gamma_G}\right]^2} , \tag{4.6}$$

where Γ_G is the FWHM of the Gaussian line shape. The convolution results in the Voigt profile $V(\nu)$:

$$V(\nu) = (G * L)(\delta) = A \int_{-\infty}^{+\infty} G(\delta')L(\delta - \delta')d\delta' = A \int_{-\infty}^{+\infty} e^{-\left[\frac{(\nu_0 - \delta')}{\Gamma_G}\right]^2} \frac{\Gamma_L}{(\nu_0 - (\delta - \delta'))^2 + \Gamma_L^2}d\delta' . \tag{4.7}$$

Unfortunately, eq. 4.7 cannot be deposited in a closed analytical way to be evaluated by a certain fitting routine. Note, that in eq. 4.7 there are two different line width's, Γ_L and Γ_G. However, only one representative linewidth per resonance is assumed in the analysis performed throughout this thesis that is $\Gamma_L = \Gamma_G = \Gamma$. Then eq. 4.7 becomes a pseudo Voigt (PSV) profile, defined as a weighted sum of eq. 4.5 and eq. 4.6:

$$V(\nu)_{Pseudo} = (1 - \mu)G(\nu) + \mu L(\nu) , \tag{4.8}$$

with μ being the relative weight of the Lorentzian contributions. As Meier [56] is pointing out, the model eq. 4.8 allows to obtain good results when fitting a single band in a spectrum $Im[\chi_{Res}^{(3)}(\nu, x, y, z, t)]$ with four parameters. Therefore, the decomposition model used to fit n profiles reads:

$$Im[\chi_{Res}^{(3)}(\nu, x, y, z, t)] = \sum_{i=1}^{n} V(\nu)_{Pseudo\ i}$$

$$= \sum_{i=1}^{n} A_i \left[\mu_i \frac{\Gamma_i}{(\nu_{0\ i} - \delta)^2 + \Gamma_i^2} + (1 - \mu_i)e^{-\left[\frac{(\nu_{0\ i} - \delta)}{\Gamma_i}\right]^2} \right] . \tag{4.9}$$

The actual fit algorithm used was a trusted-region reflective method provided by the MATLAB function *lsqcurvefit*. The accuracy of the fit depends on the SNR of the input data, which represents the general disadvantage of using univariate fitting routines. The computational cost is high and a linearisation of eq. 4.9 in order to use fast linear algebra methods is not straight forward. However, curve fitting is performed in order to analyze each spectrum individually, yielding for every spectrum and for every ith resonance the peak amplitude A_i, the area $\int_{\nu_2}^{\nu_2} V(\nu)_{Pseudo\ i}d\nu$, the width Γ_i, the weight μ_i, and the center frequency $\nu_{0\ i}$. The obtained fit parameters allow the generation of peak amplitude and ratio maps, and can be analyzed further using statistical methods, as will be discussed next.

4.5.2 Statistical methods

In practice, the hyperspectral data sets $\chi^{(3)}(\nu, x, y, z, t)$ can contain thousands of Raman spectra accompanied with a high dimensionality of the data. In this section, the statistical tools used in

order to obtain degrees of correlation, histogram distributions, and 2D image autocorrelations based on the extracted fit parameters will be outlined.

4.5.2.1 Determination of the degree of correlation

In some cases, one is interested in the determination of correlations between different fit parameters or quantities extracted from the hyperspectral data set. Here, the covariance matrix **Cov** containing information regarding the variances and correlations between the components of the hyperspectral parameter data set is calculated. The covariance matrix contains the variances $V_{j,j}$ on the main diagonal. The measure for determining the degree of correlation $C_{i,j}$ is the *zero*th lag of the normalized covariance function and is related to the covariance matrix **Cov** as follows:

$$C_{i,j} = \frac{Cov_{i,j}}{\sqrt{Cov_{i,i}V_{j,j}}} \quad . \tag{4.10}$$

4.5.2.2 Parameter distribution histogram analysis

For hyperspectra, often a global analysis concerning the distribution of a certain spectroscopic parameter or of a derived quantity is needed. MATLAB routines were written that in an automated way generate histograms of the quantities of interest, determine the statistical parameters of the distributions by fitting the latter to a linear combinations of Gaussian distributions, and determine the degrees of correlation. If the distributions modality is two or higher, it makes sense to select one species in the correlation plot and map the spatial distribution of this subset of the data only.

4.5.2.3 Image autocorrelation analysis

In order to determine the size and number statistics of a quantity of interest (for example, the image contrast within a 2D image) in an automated way, image correlation analysis (ICA) was performed. For an image quantity $i(x, y)$ in the spatial domain, the normalized 2D autocorrelation function (ACF) can be defined as follows [57]:

$$g(\eta, \xi) = \frac{\langle i(x,y)i(x+\eta, y+\xi) - i(x,y)\rangle}{\langle i(x,y)\rangle^2} - 1 = \frac{G(\eta, \xi)}{\langle i(x,y)\rangle^2} - 1 \quad . \tag{4.11}$$

Here the brackets $\langle\rangle$ denote spatial averaging, η and ξ are the spatial lag coordinates in x and y, respectively, and $G(\eta, \xi)$ is the autocorrelation function $G(\eta, \xi) = \langle i(x,y)i(x+\eta, y+\xi)\rangle$. The actual calculation of $G(\eta, \xi)$ is performed using the FFT [58]:

$$G(\eta, \xi) = \mathscr{F}^{-1}\left[(\mathscr{F}i(x,y))(\mathscr{F}^*i(x,y))\right] \quad . \tag{4.12}$$

Every object in $i(x, y)$ having a size exceeding one pixel will lead to $g(\eta, \xi) > 0$ at the corresponding spatial frequency lag. Uncorrelated noise in $i(x, y)$ will accumulate to a spike at zero

lag $(\eta, \xi) = (0, 0)$ with magnitude $g_{Noise}(0, 0)$. The ACF is fitted with a linear combination of 2D-Gaussians and one offset:

$$g(\eta, \xi) = g(0, 0)e^{-\left[\left(\frac{\eta}{w_\eta'}\right)^2 + \left(\frac{\xi}{w_\xi'}\right)^2\right]} + g_{Noise}(0, 0)e^{-\left[\frac{\eta^2 + \xi^2}{w_{Noise'}^2}\right]} + g_0 \ . \qquad (4.13)$$

The first 2D Gaussian term contains the desired size and number statistics of the correlated objects. The number density of those objects N_{Obj} in units of $\frac{objects}{\mu m^2}$ is related to the magnitude of $g(0, 0)$ by $N_{Obj} = \frac{1}{g(0,0)A}$, where A is the total image area of the input image. The e^{-2} radii of the object size along the η and ξ dimensions are given by w_η' and w_ξ', respectively. We define the 2D-size of an object as the full width half maxima by $w_\eta = w_\eta' \sqrt{2ln(4)}$ and $w_\xi = w_\xi' \sqrt{2ln(4)}$. The second Gaussian term represents the noise peak at zero lag $(\eta, \xi) = (0, 0)$. The last term g_0 is an offset and is needed because of the apodisation problem arising when the Fourier transform is applied to a data set $i(x, y)$ with restricted size. This results in an ACF that has not completely vanished, even at the maximum lags. ICA will be applied to obtain the distribution of domain sizes derived from $i(x, y)$-maps of the degree of crystallinity in polymers (see ch. 6).

5 Novel concepts in MEM-based phase retrieval

"If I had 60 minutes to cut down a tree, I would spend 40 minutes sharpening the ax and 20 minutes cutting it down."

Abraham Lincoln

In this chapter, three unsatisfactory aspects in the current realisations of MEM based spectral phase retrieval will be addressed. First, a new way of calculating the autocorrelation coefficients $C(m)$ in MEM is presented. The second aspect concerns the optimization of the algorithm used for solving the eigenvalue problem (EP) in MEM by implementing a new Toeplitz solver. The third aspect addresses new general concepts of reconstructing the desired complex purely vibrational susceptibility $\chi_{Res}^{(3)}(\nu)$. These three theoretical innovations and novel concepts will then be evaluated using experimental CARS data of toluene.

5.1   New approaches of calculating the autocorrelation coefficients in MEM

Coventionally, the reconstruction of $Im[\chi_{Res}^{(3)}(\nu)]$ using MEM as described in section 3.3 calculates the autocorrelation coefficients $C(m)$ using the FFT. The complex-valued FFT-MEM, as originally developed for phase retrieval by Vartiainen [27], possesses the windowing problem at the spectral ends, which is caused by the finite frequency window covered by the measurement, and arises when a spectrum has not equal values at its end-points. As a consequence, large deviations are observed at the spectral end-points, when the reconstructed $Im[\chi_{Res}^{(3)}(\nu)]$ spectrum is compared with its spontaneous Raman spectrum. To circumvent this problem, the squeezing procedure in MEM phase retrieval was previously introduced by Vartiainen et. al. [48]. A squeezing parameter K is introduced and the maximum entropy model given in eq. 3.51 for the CARS spectrum $S(\nu, x, y, z, t, K)$ is then modified as follows:

$$S(\nu, x, y, z, t, K) = \left| \frac{\beta(x, y, z, t, K)}{1 + \sum_{k=1}^{M} a_k(x, y, z, t, K)e^{-2\pi i k \nu}} \right| = \left| \frac{\beta(x, y, z, t, K)}{A_M(\nu, x, y, z, t, K)} \right| \quad . \qquad (5.1)$$

Here, the normalized frequency ν defined by the lower and upper limit of the CARS spectrum, ν_{min} and ν_{max}, respectively, is introduced:

$$\nu = \frac{1}{(2K+1)}\left(\frac{\nu_{CARS} - \nu_{min}}{\nu_{max} - \nu_{min}} + K\right); \quad \nu_{min} \leq \nu_{CARS} \leq \nu_{max}; \quad K = 0, 1, \ldots \quad . \tag{5.2}$$

Now $S(\nu, x, y, z, t, K)$ is defined via the squeezing parameter as

$$S(\nu, x, y, z, t, K) = \begin{cases} S(\nu_{min}, x, y, z, t); 0 \leq \nu < \frac{K}{2K+1} & ; \nu_{CARS} < \nu_{min} \\ S(\nu, x, y, z, t) \quad ; \frac{K}{2K+1} \leq \nu \leq \frac{K+1}{2K+1} ; \nu_{min} \leq \nu_{CARS} \leq \nu_{max} \\ S(\nu_{max}, x, y, z, t); \frac{K+1}{2K+1} < \nu \leq 1 \quad ; \nu_{CARS} > \nu_{max} \end{cases} \tag{5.3}$$

The CARS spectrum in eq. 5.1 is now decomposed into M Fourier components A_M:

$$A_M(\nu, x, y, z, t; K) = 1 + \sum_{k=1}^{M} a_k(x, y, z, t, K)e^{-2\pi i k\nu} \quad . \tag{5.4}$$

The ME coefficients a_k and β are then determined by solving eq. 3.50, where the autocorrelation coefficients $C(m)$ are calculated at a discrete set of normalized frequencies $\nu_n = n/N$ ($n = 0, 1, \ldots, N$) with $N = (2K+1)(N_0 - 1) + 1$, where N_0 denotes the number of data samples in $S(\nu, x, y, z, t, K)$, via the discrete Fourier transform (DFT):

$$C(m, K) = N^{-1} \sum_{n=0}^{N-1} S(\nu_n, x, y, z, t, K)e^{2\pi i m \nu_n}; \quad K = 0, 1, \ldots \quad . \tag{5.5}$$

In order to separate into the real and the imaginary parts, eq. 5.5 can be rewritten as:

$$C(m; K) = N^{-1}\left[\sum_{n=0}^{N-1} S(\nu_n, x, y, z, t, K)\cos(\frac{2\pi m n}{N}) \pm i \sum_{n=0}^{N-1} S(\nu_n, x, y, z, t, K)\sin(\frac{2\pi m n}{N})\right] \quad . \tag{5.6}$$

This result of the DFT represents the magnitudes and phase angles belonging to the normalized frequency ν_n. The DFT transform kernel is linear, separable, and symmetric. It has fixed basis functions, and fast implementations are available. However, being a complex transformation, the DFT assumes that both amplitude and phase are encoded in the spectrum $S(\nu_n, x, y, z, t, K)$. Moreover, the implicit periodicity of the DFT gives rise to boundary discontinuities at the spectrum end-points, which leads to a significant high-frequency content. In addition to the fact that many DFT coefficients are needed in order to not loose information encoded in the CARS spectrum, the artefact caused by the boundary discontinuities will remain, even if all DFT coefficients are calculated up to the Nyquist frequency of $\nu_{Nyq} = N/2$. The drawback of this squeezing procedure is the increased number of sample points and number M of unknown parameters.

To overcome these problems, I have introduced the discrete cosine transform (DCT, $\mathscr{D}$) for phase retrieval. Eq. 5.7 gives the definition of the DCT as given in [59]:

$$\begin{aligned} C(m) &= \mathscr{D}(S(\nu_n, x, y, z, t)) \\ &= w \sum_{n=1}^{N} S(\nu_n, x, y, z, t)\cos\left(\frac{\pi(2n-1)(k-1)}{2N}\right); k = 1, 2, \ldots, N; \end{aligned} \tag{5.7}$$

$$\text{where} \quad w = \begin{cases} \sqrt{\frac{1}{N}} & k = 1 \\ \sqrt{\frac{2}{N}} & 2 \leq k \leq N \end{cases}.$$

Though using real cosine basis functions only, eq. 5.7 is not the real part of the DFT described in eq. 5.6. What makes the DCT superior to the DFT? The DCT transform of a CARS spectrum $S(\nu_n, x, y, z, t)$ consisting of N_0 samples is generating a symmetric spectrum $S(\nu_n, x, y, z, t)'$ of $2N_0$ samples by appending a reversed copy to itself (see fig. 5.11 in section 5.4.2). Subsequently a $2N_0$ DFT is performed on $S(\nu_n, x, y, z, t)'$.

The main properties of the DCT are: The DCT results in N_0 nonzero cosine terms and N_0 zero sine terms. The DCT is making the transform of $S(\nu_n, x, y, z, t)$ periodic, and thus is removing the windowing phenomenon. Another useful property of the DCT is that any correlation in the spectrum $S(\nu_n, x, y, z, t)$ will lead to energy compaction superior to that of the DFT, a useful feature in data and high-frequency content reduction, (see the semi-logarithmic plot of the $|C(m, K)|$ coefficients spectrum, calculated using the DFT and the DCT transform in fig. 5.12 in section 5.4.2). Eqs. 5.6 and 5.7 look very much alike. However, because the squeezing procedure is no longer needed, using eq. 5.7 results in a reduction of the computation time.

For N_0 samples in a CARS spectrum and calculating the maximum number $M = N_0$ autocorrelation coefficients, the phase retrieval applying the conventional DFT based approach needs two DFT calculations to calculate the vectors $A_M(\nu, K = 0)$ (eq. 5.4) and $C_M(m, K = 0)$ (eq. 5.6). Then, the Toeplitz-matrix of size N_0^2 (eq. 3.50) must be solved. Using the MATLAB Cooley-Tukey based FFT function [60], the computational cost for each DFT step is of the order $O(N_0 log N_0)$, and for solving the Toeplitz-matrix using the MATLAB Levinson command is of $O(N_0^2)$. The overall computational cost is therefore of order $O(N_0^2 + 2N_0 log N_0)$, where solving the Toeplitz-matrix accounts for approximately 80%. Using the same DFT MEM-approach with the additional squeezing procedure with $K = 1$, the length of the vectors $A_M(\nu, K = 1)$ (eq. 5.4) and $C_M(m, K = 1)$ (eq. 5.6) are $3N_0$, and the Toeplitz-matrix is now of size $9N_0^2$ and real. The corresponding computational cost is therefore of the order $O(9N_0^2 + 6N_0 log 3N_0)$, which is roughly one order of magnitude higher than without squeezing ($K = 0$). In contrast, the DCT MEM approach requires only one DFT calculation for the vector $A_M(\nu)$, one DFT-based DCT calculation for the vector $C_M(m)$ of $O(N_0 log N_0)$ [61], and solving the Toeplitz-matrix. The corresponding computational cost is therefore the same as for the DFT based approach without squeezing ($K = 0$), and is of the order $O(N_0^2 + 2N_0 log N_0)$.

5.2 Implementation of a new Toeplitz solver

In order to drastically reduce the computational cost of solving the eigenvalue problem (EP) containing a Toeplitz matrix (see eq. 3.50), it is worth to take care of how the Toeplitz matrix is actually inverted. This sub-chapter discusses four different generations of Toeplitz solvers, listed in tab. 5.1.

Table 5.1: Comparion of computational costs of four generations of Toeplitz solvers.

Gen.	Name	computational cost	reference
1	Cholesky-algorithm	$O\ N_0^3$	[62]
2	Levinson Durbin recursion algorithm	$O\ N_0^2$	[63]
3	Various so called fast direct solvers	$O\ N_0(logN_0)^2$ $\ldots O\ N_0(logN_0)^3$	[64], [65]
4	Super-fast conjugated gradient based solver	$O\ N_0log(N_0)$	[66]

Gauß-elimination and Cholesky-algorithm

The Gauß-elimination and the Cholesky-decomposition belong to the class of direct solvers, which give the exact solution of the EP in a finite number of steps. The basic idea of the Gauß-elimination is to transform the EP **Ca=b** into **LUa=b** with a lower left triangular matrix **L** and an upper right triangular matrix **U**. We are interested in the computational cost for solving this EP involving a matrix **C** of size N_0^2 and a vector of size N_0. The costs for performing the multiplications $\mathbf{a} = \mathbf{U}^{-1}\mathbf{b}$ and $\mathbf{b} = \mathbf{L}^{-1}\mathbf{b}$ sum up to the total cost of $O\ (\frac{N_0^3}{3} + N_0^2 - \frac{N_0}{3})$ [67]. For a large, symmetric, positive definite (SPD) matrix, the Cholesky-decomposition $\mathbf{C} = \mathbf{LL}^T$ [62] is reducing the cost of the LU-decomposition to $O\ (\frac{N_0^3}{6} + \frac{N_0^2}{2} + \frac{N_0}{3})$. However, the cost is still of order $O\ N_0^3$. CCD cameras easily have 1000 spectral pixels, which translates to $N_0 = 1000$ for the length of the input vector. A large hyperspectrum can then contain 10^6 or more spectra, so that we have to invert 10^6 matrices of size N_0^2. Therefore, the Cholesky-decomposition with a cost of order $O\ N_0^3$ is not suitable: If one multiplication is performed in 10^{-9} *sec*, the matrix inversions for such a hyperspectrum would take $10^6 N_0^3 10^{-9}$ *sec* ≈ 11.4 *days*!

Levinson Durbin recursion algorithm

Solving eq. 3.50 with a computational cost of $O\ N_0^2$ is possible, when the Levinson Durbin recursion algorithm is used [63], [68]. The basic idea is to start solving the simple $N_0 \times N_0$ problem with $N_0 = 1$. Subsequently, the corresponding problem for $N_0 + 1$ is solved. Thus, using lower order solutions, the next order solution is obtained inductively. A rather compact

description of the algorithm can be found in ref. [69], which will briefly be given in the appendix A.7. The algorithm needs $O\,M$ multiplications and additions to go from step M to $M + 1$. M is the maximum lag number as introduced in section 3.3.1.2. This results in a computational cost of $O\,N_0^2$ calculations. When the algorithm by Trench [70] is used, the exact cost is $O\,4N_0^2$. Further improvements by Zohar [71] reduced the cost to $O\,3N_0^2$. When compared with the Cholesky-decomposition, this already is a drastic reduction of the computational cost. Using the example given above, this gives $10^6 N_0^2 10^{-9}\ sec \approx 16.7\ minutes$, which is still not really satisfactory.

5.2.1 Fast and superfast solvers

Fast direct solvers

In the 1980s various so called fast direct solvers have been developed [64], [65]. To directly cite Strang [72]: *"The mathematics is beautiful. It (the methods) uses subtle algebraic properties of transforms to produce an exact solution. The algorithms are somewhat outside the usual range of numerical linear algebra ..."*. Some of these algorithms can be applied for our case of symmetric, positive definite Toeplitz matrices [73]. With a computational cost ranging from $O\,N_0(logN_0)^2$ to $O\,N_0(logN_0)^3$, using the example given above, we obtain between $10^6 10^3 (log(10^3))^2 10^{-9}\ sec = 48\ sec$ and $10^6 10^3 (log(10^3))^2 10^{-9}\ sec = 329\ sec$, which only represents a marginal reduction in computation time. Therefore, these solvers will not be discussed in detail here. The interested reader is referred to ref. [74]. Fortunately, there exists a more stable and even faster way of inverting a Toeplitz matrix, which will be discussed next.

Circulant preconditioned conjugated gradient method

> *"What is eternal is circular and what is circular is eternal."*
>
> Aristotle [384 - 322 BC]

Before introducing this *4*th generation Toeplitz solver, let us have a closer look at the Toeplitz matrix **C**. It has constant diagonal elements, and every entry C_{i-j} only depends on the difference $i - j$. With this invariance, the matrix **C** is a convolution matrix. The continuous counterpart of eq. 3.50 is then a convolution:

$$\int_0^1 c(t - s)a(s)ds = b(t), \tag{5.8}$$

where the integration is performed within the finite, normalized interval [0 1]. Exactly these integration boundaries give rise to the windowing at the spectral ends. After performing the Fourier transform, eq. 5.8 becomes **Ca** = **b**. However, because **C** is finite, the Fourier transform cannot give an explicit solution. As Strang [72] pointed out: The transform method is still the

51

key, but only in the periodic case it will work without difficulty. The periodic case for a discrete problem corresponds to a special case of Toeplitz matrices, i.e. the circulant matrix. In contrast to the general properties of symmetric, positive definite (SPD) Toeplitz matrices, in a circulant matrix $\mathbf{C}_{Circulant}$ each entry only depends on the difference between its row and column index modulo N_0: $C_{Circulant\ ij} = C_{Circulant\ kl}$, where $j - i \equiv l - k\ (mod\ N_0)$, and $N_0 \times N_0$ is the size of the matrix. The direct comparison of a symmetric and real Toeplitz matrix with a real circulant matrix makes this point more clear:

$$\mathbf{C}_{Toeplitz} = \begin{bmatrix} C(0) & C(1) & \dots & \dots & C(M) \\ C(1) & C(0) & C(1) & \dots & C(M-1) \\ \vdots & \vdots & \vdots & \ddots & \vdots \\ \vdots & \vdots & \vdots & \ddots & C(1) \\ C(M) & C(M-1) & \dots & C(1) & C(0) \end{bmatrix} \quad (5.9)$$

$$\mathbf{C}_{Circulant} = \begin{bmatrix} C(0) & C(M) & \dots & \dots & C(1) \\ C(1) & C(0) & C(M) & \dots & C(2) \\ \vdots & \vdots & \vdots & \ddots & \vdots \\ \vdots & \vdots & \vdots & \ddots & C(M) \\ C(M) & C(M-1) & \dots & C(1) & C(0) \end{bmatrix}. \quad (5.10)$$

We see that $\mathbf{C}_{Circulant}$ is not symmetric, but the value $C(1)$ appears again in the upper right corner. In general, a symmetric Toeplitz matrix is fully determined by the first column, which makes N_0 entries (with N_0 being equal M), while a symmetric circulant matrix has only $\frac{N_0}{2} + 1$ degrees of freedom. As described above, the usual way to solve eq. 3.50 containing a Toeplitz matrix 5.9 is a direct method, such as using the Levinson Durbin recursion with computational cost of $O\ N_0^2$. For circulants, on the other hand, the discrete FFT of $\mathbf{a}$ and $\mathbf{b}$ is used. For every circulant, the matrix-vector division and multiplication is performed in only $N_0 log(N_0)$ operations by diagonalizing the circulant matrix $\mathbf{C}_{Circulant}$ using the Fourier matrix $\mathbf{F}$ [75]:

$$\mathbf{C}_{Circulant} = \mathbf{F}_{N_0} \mathbf{\Lambda} \mathbf{F}_{N_0}^{-1}, [\mathbf{F}_{N_0}]_{j,k} = \frac{1}{\sqrt{N_0}} e^{-\frac{2\pi i(j-1)(k-1)}{N_0}}; 1 \le j, k \le N_0\ , \quad (5.11)$$

where $\mathbf{\Lambda}$ is a diagonal matrix holding the eigenvalues λ_k

$$\lambda_k = \sum_{j=0}^{N_0-1} C_{Circulant\ j}\ e^{\frac{2\pi ijk}{N_0}}; k = 0, \dots, (N_0 - 1) \quad (5.12)$$

of $\mathbf{C}_{Circulant}$ [76]. Now, the matrix-vector products $\mathbf{C}_{Circulant}\mathbf{a}$ and $\mathbf{C}_{Circulant}^{-1}\mathbf{a}$ are computed via FFT as

$$\mathbf{C}_{Circulant}\mathbf{a} = \mathscr{F}^{-1}(\mathscr{F}(\mathbf{a}) * \mathscr{F}(\mathbf{c})) \quad (5.13)$$

$$\mathbf{C}_{Circulant}^{-1}\mathbf{a} = \mathscr{F}^{-1}\frac{\mathscr{F}(\mathbf{a})}{\mathscr{F}(\mathbf{c})} \quad (5.14)$$

in $N_0 log(N_0)$ operations for every vector $\mathbf{a}$. Here, the vector $\mathbf{c}$ is the first column of $\mathbf{C}_{Circulant}$. The eigenvalues of $\mathbf{C}_{Circulant}$ are given by

$$\lambda_k = \mathscr{F}(\mathbf{c}) \; . \tag{5.15}$$

However, we still have to solve the Toeplitz system. How do the nice properties of the circulant $\mathbf{C}_{Circulant}$ help to solve eq. 3.50? At this point, the technique of preconditioning comes into play. The idea behind preconditioning is that instead of solving eq. 3.50, we solve

$$\mathbf{M}^{-1}\mathbf{C}_{Toeplitz}\mathbf{a} = \mathbf{M}^{-1}\mathbf{b} \; , \tag{5.16}$$

where $\mathbf{M}$ is a preconditioner matrix. Solving eq. 5.16 requires less calculation steps than solving eq. 3.50, provided that the eigenvalues of $\mathbf{M}^{-1}\mathbf{C}_{Toeplitz}$ are more clustered around unity than those of $\mathbf{C}_{Toeplitz}$. Normally, the eigenvalues of Toeplitz matrices are not clustered [77]! Likewise, the product $\mathbf{C}_{Toeplitz}\mathbf{a}$ is calculated as follows: Any Toeplitz Matrix of the form given by eq. 5.9 can be embedded into a circulant matrix $\tilde{\mathbf{C}}_{Circulant}$ of size $2N_0$ x $2N_0$ using the matrix $\mathbf{W}$, where $\mathbf{W}_{ij} = w_{i-j}, w_i = C_{Toeplitz \; i-N_0}$ for $i > 0$, $w_i = C_{Toeplitz \; i+N_0}$ for $i < 0$, and an arbitrary element w_0 [78]:

$$\mathbf{W} = \begin{bmatrix} 0 & C(M) & \ldots & C(2) & C(1) \\ C(M) & 0 & C(M) & \ldots & C(2) \\ \vdots & \vdots & \vdots & \ddots & C(M) \\ C(1) & C(2) & \ldots & C(M) & 0 \end{bmatrix} \; . \tag{5.17}$$

This increase of the size of the embedded matrix $\mathbf{C}_{Toeplitz}$ is compensated by the fact that the product $\tilde{\mathbf{C}}_{Circulant} \; \tilde{\mathbf{a}}$ can efficiently be computed as

$$\begin{bmatrix} \mathbf{C}_{Toeplitz} & \mathbf{W} \\ \mathbf{W} & \mathbf{C}_{Toeplitz} \end{bmatrix} \begin{bmatrix} \mathbf{a} \\ 0 \end{bmatrix} = \begin{bmatrix} \mathbf{C}_{Toeplitz}\mathbf{a} \\ \mathbf{W}\mathbf{a} \end{bmatrix} \; . \tag{5.18}$$

Only $2N_0 \; log(2N_0) = 2N_0 \; logN_0 + 2N_0 \; log2$ operations are required, while a general matrix-vector multiplication takes $(2N_0)^2$ operations [79]. Instead of using the preconditioner matrix $\mathbf{M}^{-1}$ in eq. 5.16, we solve the preconditioned system

$$\tilde{\mathbf{C}}_{Circulant} \; \tilde{\mathbf{a}} = \begin{bmatrix} \mathbf{C}_{Toeplitz}\mathbf{a} \\ \mathbf{W}\mathbf{a} \end{bmatrix} = \tilde{\mathbf{b}} \; . \tag{5.19}$$

The first row of $\tilde{\mathbf{C}}_{Circulant}$ reads

$$\tilde{\mathbf{c}} = [C(0), C(1), \ldots, C(M), 0, C(M), \ldots, C(1)] \; , \tag{5.20}$$

which is the first row of $\mathbf{C}_{Toeplitz}$ followed by its reversed copy without its first value $C(0)$. With $\tilde{\mathbf{c}}$ defining the circulant $\tilde{\mathbf{C}}_{Circulant} = circ(\tilde{\mathbf{c}})$ periodic boundary conditions are ensured. The circulant matrix $\tilde{\mathbf{C}}_{Circulant}$ is now a symmetric matrix, and a Toeplitz matrix buildt using the

vector $\tilde{\mathbf{c}}$ equals the circulant matrix $\tilde{\mathbf{C}}_{Circulant}$. Note that this is exactly what is done in the DCT prior performing a DFT.

Next, the idea behind the iterative conjugate gradient (CG) method [80] will be briefly discussed. The CG method was first described by Hestenes et. al. [66]. If the matrix $\tilde{\mathbf{C}}_{Circulant}$ is SPD, eq. 5.19 is solved by minimizing the quadratic form $\mathbf{f}(\tilde{\mathbf{a}})$ with a minimum of iteration steps [81]. The quadratic form $\mathbf{f}(\tilde{\mathbf{a}})$ is a scalar function of a vector and reads:

$$\mathbf{f}(\tilde{\mathbf{a}}) = \frac{1}{2}\tilde{\mathbf{a}}^T\tilde{\mathbf{C}}_{Circulant}\tilde{\mathbf{a}} - \mathbf{b}^T\tilde{\mathbf{a}} + const. \tag{5.21}$$

Let us first consider the simple method of steepest descent, where for each iteration step i the negative gradient $-\nabla\mathbf{f}(\tilde{\mathbf{a}}_i) = \tilde{\mathbf{b}} - \tilde{\mathbf{C}}_{Circulant}\tilde{\mathbf{a}}_i$ and the point $\alpha_{min\ i}$ along the direction $\mathbf{d}_i$ that minimises $\mathbf{f}(\tilde{\mathbf{a}}_i)$ are calculated. With the residual $\mathbf{r}_i = -\nabla\mathbf{f}(\tilde{\mathbf{a}}_i)$ being a measure of how far off we are from the minimum, we can express $\alpha_{min\ i} = \frac{\mathbf{r}_{i-1}^T\mathbf{r}_{i-1}}{\mathbf{r}_{i-1}^T\tilde{\mathbf{C}}_{Circulant}\mathbf{r}_{i-1}}$ [81]. The steepest descent method can then be written as:

$$
\begin{aligned}
&\tilde{\mathbf{a}}_0, \mathbf{r}_0 = \mathbf{b} = 0 && \text{Initial guess}\\
&\quad\textbf{for i=1:k} && \text{Loop body, do until some stop condition is fulfilled}\\
&\alpha_{min\ i} = \frac{\mathbf{r}_{i-1}^T\mathbf{r}_{i-1}}{\mathbf{r}_{i-1}^T\tilde{\mathbf{C}}_{Circulant}\mathbf{r}_{i-1}} && \text{minimize } \mathbf{f}(\tilde{\mathbf{a}})\\
&\mathbf{r}_i = \tilde{\mathbf{b}} - \tilde{\mathbf{C}}_{Circulant}\tilde{\mathbf{a}}_i && \text{calculate } i\text{th residual}\\
&\tilde{\mathbf{a}}_i = \tilde{\mathbf{a}}_{i-1} + \alpha_{min\ i}\mathbf{r}_{i-1} && \text{refine solution vector } \tilde{\mathbf{a}}
\end{aligned}
\tag{5.22}
$$

The quadratic form $\mathbf{f}(\tilde{\mathbf{a}})$ is only symmetric, when all the eigenvalues of $\tilde{\mathbf{C}}_{Circulant}$ are the same. Only in this case, the gradient will directly point towards the minimum. In the general case, $\mathbf{f}(\tilde{\mathbf{a}})$ will be elliptic. Because the two search directions of subsequent iterations $\mathbf{d}_i$ and $\mathbf{d}_{i-1}$ are orthogonal to each other, the algorithm will result in a zigzag path to the minimum and often the same directions will be followed. Therefore, the convergence will be rather poor. Unlike in the steepest descent method, in the circulant preconditioned conjugate gradient (CPCG) method, the two search vectors $\mathbf{d}_i$ and $\mathbf{d}_{i-1}$ are defined to be A-orthogonal, i.e. they have conjugate directions, and fulfill:

$$\mathbf{d}_i^T\tilde{\mathbf{C}}_{Circulant}\mathbf{d}_{i-1} = 0 \ . \tag{5.23}$$

The combination of a conjugate gradient (CG) and circulant preconditioning (CP) was first proposed by Reid [82]. As a result, the initial residual error can be expressed as a sum of A-orthogonal components, with the conjugate directions method eliminating one of these components with every iteration step. It can be proven that this procedure will converge for a matrix of size $N_0 \times N_0$ after N_0 steps. A simple way to compute this set of A-orthogonal search vectors $\mathbf{d}_i$ is to calculate the Gram-Schmidt coefficients ζ_i using the Gram-Schmidt orthogonalisation

(Gram [83] and Schmidt [84]). However, this approach has the disadvantages of high computational cost of $O(N_0^3)$ and needs to keep all previous search vectors $\mathbf{d}_i$ in the memory. CPCG is avoiding these disadvantages by making not only the new search directions $\mathbf{d}_i$, but also the residuals A-orthogonal. By repeatedly applying a matrix to a vector a Krylov subspace is created, which reduces the complexity per iteration from ON_0^2 to OM (with M being the number of nonzero entries of $\tilde{\mathbf{C}}_{Circulant}$), and most of the Gram-Schmidt coefficients ζ_i disappear. The CGCP algorithm can be written as [80]:

$$
\begin{aligned}
&\tilde{\mathbf{c}}' = \mathscr{F}(\tilde{\mathbf{c}}) && \text{precompute the Fourier transform of } \tilde{\mathbf{c}} \\
&\tilde{\mathbf{a}}_0 = 0 && \text{Initial guess} \\
&\zeta_0 = \mathbf{r}_0 = \mathbf{d}_0 = \mathbf{b} && \text{Initialisation} \\
&\textbf{for i=1:k} && \text{Loop body, do until some stop condition is fulfilled} \\
&\mathbf{z}_i = \mathscr{F}^{-1}(\mathscr{F}(\mathbf{r}_i)/\tilde{\mathbf{c}}'); && \text{calculate matrix-vector product } \tilde{\mathbf{C}}_{Circulant}^{-1}\mathbf{r}_i \\
&\zeta_i = \frac{\mathbf{z}_i^T\mathbf{r}_i}{\mathbf{z}_{i-1}^T\mathbf{r}_{i-1}} && \text{calculate Gram-Schmidt coefficients (Fletcher-Reeves formula)} \\
&\mathbf{d}_i = \mathbf{z}_i + \zeta_i\mathbf{d}_{i-1} && \text{update the direction-vector} \\
&\mathbf{A}_i = \mathscr{F}^{-1}(\tilde{\mathbf{c}}'\mathscr{F}(\mathbf{d}_i)) && \text{calculate matrix-vector product } \tilde{\mathbf{C}}_{Circulant}\mathbf{d}_i \\
&\alpha_{min\ i} = \frac{\mathbf{r}_i^T\mathbf{r}_i}{\mathbf{d}_i^T\mathbf{A}_i} && \text{minimize } \mathbf{f}(\tilde{\mathbf{a}}) \\
&\tilde{\mathbf{a}}_i = \tilde{\mathbf{a}}_{i-1} + \alpha_{min\ i}\mathbf{d}_i && \text{refine solution vector } \tilde{\mathbf{a}} \\
&\mathbf{r}_i = \mathbf{r}_{i-1} - \alpha_{min\ i}\mathbf{A}_i && \text{refine residuals}
\end{aligned}
\tag{5.24}
$$

The vectors $\mathbf{z}_i$ and $\mathbf{A}_i$ hold the temporary matrix-vector products, and $\mathbf{b} = |\beta|^2$ denotes a vector of form $\mathbf{b} = [1\ 0\ldots0]$. As a result four FFT's are necessary for each iteration step.

In the CPCG algorithm given in eq. 5.24, the Fourier-transform of the circulant vector $\tilde{\mathbf{c}}$, (see eq. 5.13 and 5.14) is performed as $\tilde{\mathbf{c}}' = \mathscr{F}(\tilde{\mathbf{c}})$ before the loop with $\tilde{\mathbf{c}}$ being the result of embedding $\mathscr{D}(S(v))$. It is not necessary to make the vector periodic twice. One can start directly with embedding the CARS spectrum $S(v)$ into the circulant vector $\tilde{\mathbf{c}}'$. In this way, the number of transforms needed for the phase retrieval is reduced. When we introduce an operator $\aleph_{CPCG}$ that accepts a CARS spectrum $S(v)$ and solves the EP given in eq. 5.19 using the algorithm given in eq. 5.24, the expression of the MEM phase retrieval (eq. 3.53) can be written directly as

$$
\phi_{MEM}(v) = arg\left[\mathscr{F}(\aleph_{CPCG}(S(v)))\right].
\tag{5.25}
$$

The convergence speed of this iterative method to solve eq. 3.50 is mainly given by the computational cost necessary to calculate the matrix-vector products. Consulting again our example given above, four DFT calculations of length $2N_0$ are needed per iteration step. The correspond-

ing computing time per step is therefore $8N_0 log2N_0 \, 10^{-9} \, sec = (8N_0 logN_0 + 8N_0 log2) \, 10^{-9} \, sec \approx 60 \, sec$. Typically, less then 5 iteration steps suffice.

The main properties of the CPCG method are summarized as follows:

1. Computational cost per iteration step is only $O \, (2N_0 log(2N_0))$.

2. Fast convergence, each iteration step gives a better approximation as the previous step. Typically less then 5 iterations are necessary.

3. CPCG is very storage efficient: Each step requires the calculation of two inner products of vectors of length $2N_0$, and one multiplication of the coefficient matrix with a vector of length $2N_0$. Thus, the CPCG method is a matrix-free method.

4. The original matrix is unaltered during the iteration.

In summary, the simulated number of computing operations as a function of the number of the spectral data points N_0 is compared for the different MEM phase retrieval approaches in fig. 5.1. As can be seen, the number of operations for the CPCG method with five iteration steps
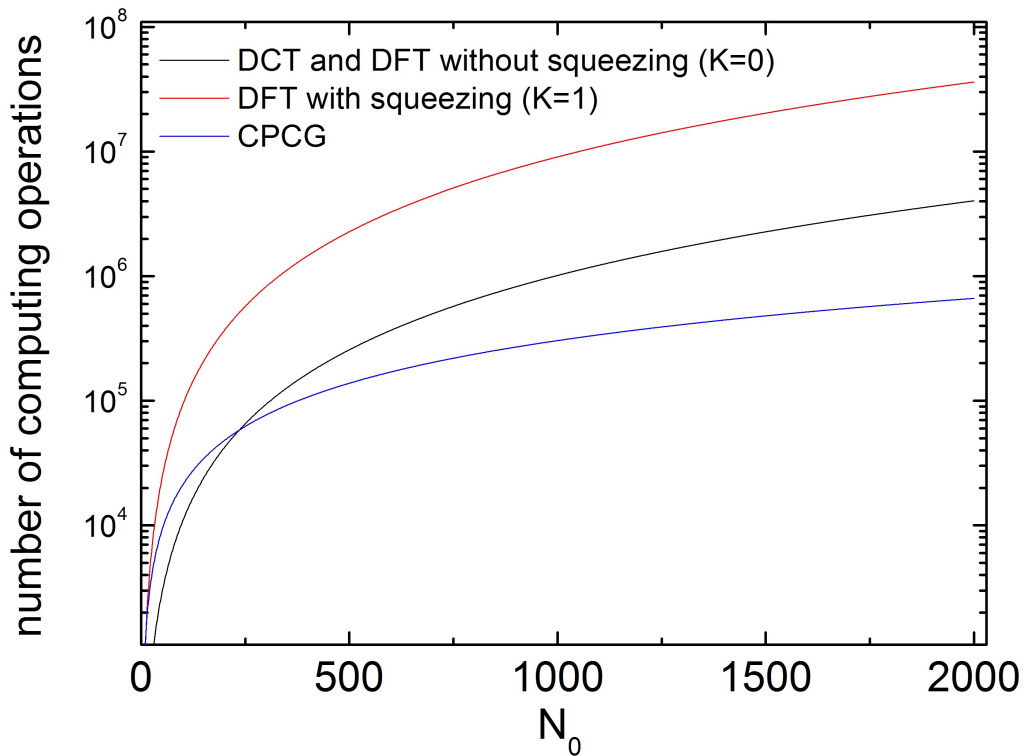
Figure 5.1: Semilogarithmic plot of the simulated number of computing operations as a function of the number of the spectral data points N_0 for the four MEM phase retrieval approaches DFT with ($K = 0$) and ($K = 1$), DCT, and CPCG. Using five iteration steps, the crossover of the DCT MEM curve with the CPCG MEM curve was found to be at $N_0 \approx 235$.

is much less than either the DFT based approach without squeezing ($K = 0$) or the DCT based approach, especially, when N_0 becomes large. A crossover is achieved for $N_0 \approx 235$ where $5(8N_0 log N_0 + 8N_0 log 2) = N_0^2 + 2N_0 log N_0$.

Finally, we will address three points concerning the further speed up of the CPCG algorithm given in eq. 5.24. First, it is useful to insert the element w_0 in the embedding matrix $\mathbf{W}$ (see eq. 5.17) as often as necessary in order to obtain a matrix $\tilde{\mathbf{C}}_{Circulant}$ of size $2^k \times 2^k$, ($k \in \mathbb{N}$). Secondly, the Fletcher-Reeves formula $\zeta_i = \frac{\mathbf{z}_i^T \mathbf{r}_i}{\mathbf{z}_{i-1}^T \mathbf{r}_{i-1}}$ for the calculation of the Gram-Schmidt coefficients is only one of many formulas known in literature [85]. I have tested as well the Polak-Ribiere formula $\zeta_i = \frac{\mathbf{z}_i^T (\mathbf{r}_i - \mathbf{r}_{i-1})}{\mathbf{z}_{i-1}^T \mathbf{r}_{i-1}}$ [86] and the original Hestenes-Stiefel formula $\zeta_i = \frac{\mathbf{z}_i^T (\mathbf{r}_i - \mathbf{r}_{i-1})}{\mathbf{d}_{i-1}^T (\mathbf{r}_i - \mathbf{r}_{i-1})}$ [66]. The rate of convergence was found to be the highest, when the Fletcher-Reeves formula was used. However, a good result for a smaller number of iterations (four) is obtained, when the Polak-Ribiere formula is modified to $\zeta_i = \frac{\mathbf{z}_i^T (\mathbf{r}_i - 0.15 \mathbf{r}_{i-1})}{\mathbf{z}_{i-1}^T \mathbf{r}_{i-1}}$. Thirdly, introducing a damping factor in the update of the direction-vector $\mathbf{d}_i = \mathbf{z}_i + 0.52 \zeta_i \mathbf{d}_{i-1}$ was found to result in a further reduction of the number of iterations needed to three. This represents the limits of the CPCG solver approach regarding the computational speed. In order to even further reduce the computational cost from $O\, N_0 log N_0$ to $O\, N_0$, the hierarchical $\mathfrak{H}$-Matrices introduced by Hackbusch in 1999 [87] may offer a powerful alternative.

5.3 New concepts of reconstructing $\chi_{\mathbf{Res}}^{(3)}(\nu)$

A nearby electronic resonance affects the CARS spectrum $S(\nu)$ and thus influences the retrieved phase spectrum. As was discussed in section 3.2.2, the complex vibrational susceptibility $\chi_{Res}^{(3)}(\nu)$ is then rotated by an additional phase angle ϕ_R and translated by an additional complex and frequency-independent electronic susceptibility $\chi_E^{(3)} e^{i\phi_E}$ in the complex plane. A total $\chi_{tot}^{(3)}(\nu)$ (eq. 3.39) is obtained, whose real and imaginary parts still form a Hilbert pair. In order to disentangle the electronic and vibrational contributions to the total susceptibility, and thus to obtain the pure vibrational phase needed to reconstruct the spontaneous Raman response of the sample, knowledge of the effective phase angle ϕ_{eff} (eqs. 3.42 and 3.38) and of the effective nonresonant electronic susceptibility $\chi_{E\,eff}^{(3)}$ (eq. 3.39) are required. Since $|\chi_{E\,eff}^{(3)}|^2$ is defined as the CARS intensity far off any vibrational resonance (see eq. 3.37), S_{NR}, we can determine its value from the actual measurement by $|\chi_{E\,eff}^{(3)}| = \sqrt{S_{NR}}$. No matter if the MEM or the KK based phase retrieval is used, the effective phase ϕ_{eff} needs to be determined by using an additional concept.

5.3.1 Determination of the effective phase ϕ_{eff} of $\chi_{tot}^{(3)}(\nu)$ using Hilbert pairs

A similar problem of how to determine an effective phase factor ϕ_{eff} has commonly been encountered in nuclear magnetic resonance (NMR) spectroscopy, where in 1969 Ernst [88] proposed the use of the functional

$$\phi_{eff} = tan^{-1} \frac{\int_{\nu_{min}}^{\nu_{max}} q_1(\nu) d\nu}{\int_{\nu_{min}}^{\nu_{max}} q_2(\nu) d\nu} \ . \tag{5.26}$$

Here, the idea is to integrate over two functions $q_1(\nu)$ and $q_2(\nu)$ that form a Hilbert pair, or are quadrature components of each other. This idea was later applied by Bostick [28] to CARS spectroscopy. In order to act only on the pure complex vibrational susceptibility of interest $\chi_{Res}^{(3)}(\nu)$, we first have to subtract the effective nonresonant contribution $|\chi_{E\ eff}^{(3)}|^2$ to the measured CARS spectrum $S(\nu)$, extracted from its nonresonant region of $S_{NR}(\nu)$. To obtain a suitable Hilbert pair, we then define [30]

$$q_1(\nu) = S(\nu) - |\chi_{E\ eff}^{(3)}|^2 \tag{5.27}$$

and

$$q_2(\nu) = \mathscr{H} S(\nu) \ , \tag{5.28}$$

Here $\mathscr{H} S(\nu)$ represents the Hilbert transform of $S(\nu)$ (see appendix A.1.2).

Alternatively, the real and imaginary parts of the reconstructed susceptibility $\chi_{tot}^{(3)}(\nu) = \sqrt{S(\nu)} e^{i\phi_{estimated}(\nu)}$, as obtained by using the conventional reconstruction procedure (see section 3.3.2) with $|\chi_{E\ eff}^{(3)}| = \sqrt{S_{NR}(\nu)}$ subtracted also form a suitable Hilbert pair:

$$q_1(\nu) = Re[\chi_{tot}^{(3)}(\nu) - \chi_{E\ eff}^{(3)}] \tag{5.29}$$

and

$$q_1(\nu) = Im[\chi_{tot}^{(3)}(\nu)] \ . \tag{5.30}$$

With $\chi_{E\ eff}^{(3)}$ and ϕ_{eff} being known, the wanted vibrational resonant susceptibility $\chi_{Res}^{(3)}(\nu)$ is then obtained by back rotation in the complex plane via:

$$\chi_{Res}^{(3)}(\nu) = [\chi_{tot}^{(3)}(\nu) - \chi_{E\ eff}^{(3)}] e^{-i\phi_{eff}} \ . \tag{5.31}$$

The determination of ϕ_{eff} using the functional eq. 5.26 is not satisfactory for real data involving noise and background. For example, even for the simulated case of $\phi_{eff} = \frac{\pi}{6}$, $\chi_{E\ eff}^{(3)} = 1$ and $A = 1\ cm^{-1}$ using eq. 5.26 and the Hilbert pair defined in eqs. 5.27 and 5.28, ϕ_{eff} can only be extracted with a relative error of 20 percent. This translates into a relative amplitude error of the reconstructed Raman response of approximately one percent. The relative error for

the extracted phase factor ϕ_{eff} slightly reduces to 17 percent, when the Hilbert pair defined by eqs. 5.29 and 5.30 is used. Furthermore, the estimation of ϕ_{eff} using eq. 5.26 is very sensitive to errors in the baseline of the measured CARS spectrum $S(v)$, due to the integration over a wide spectral region, as was already pointed out by Ernst [88]. Because of these deficiencies, more robust ways for the determination of ϕ_{eff} are required.

5.3.2 Determination of the effective phase ϕ_{eff} of $\chi_{tot}^{(3)}(v)$ using the ratio of maximum to minimum excursions in the retrieved estimated phase or the reconstructed $Im[\chi_{tot}^{(3)}(v)]$ spectrum

Ernst [88] also suggested the determination of the effective phase ϕ_{eff} by using the ratio of maximum to minimum excursion, thus avoiding the use of Hilbert transforms. Here, we have further developed this concept for CARS. As derived in appendix A.8 (see eq. A.50), a simple expression approximates the dependence of ϕ_{eff} on the normalized ratio r_{phase} of maximum to minimum phase excursions of the retrieved estimated phase spectrum $\phi_{estimated}(v)$:

$$\phi_{eff}(r_{phase}) = \delta_R cos^{-1}\left(\frac{2}{r_{phase}} - 1\right) \ , \tag{5.32}$$

with

$$r_{phase} = \frac{max(\phi_{estimated}(v)) - min(\phi_{estimated}(v))}{max(\phi_{estimated}(v))} \ . \tag{5.33}$$

Here, $\phi_{estimated}(v)$ is defined according to eq. 3.54, and δ_R is a sign correction parameter defined in eq. A.49 in appendix A.8. The accuracy of the extraction of ϕ_{eff} using eq. 5.32 and eq. 5.33 is illustrated in fig. 5.2, where the extracted ϕ_{eff} values are plotted as a function of the introduced simulated ϕ_{eff} vales for various ratios of $\frac{|\chi_{Res}^{(3)}(v)|}{\chi_{E\ eff}^{(3)}}$ ranging from 0.1 to 1. The biggest relative errors for the extracted ϕ_{eff} values occur, when $\chi_{E\ eff}^{(3)} \geq sin(\phi_{eff})Im[\chi_{Res}^{(3)}(v)]$ is no more fulfilled (eq. A.46). However, error propagation through the reconstruction of the complex susceptibility (eq. 3.55) and its backrotation by ϕ_{eff} (eq. 5.31) results in relative errors of the $Im[\chi_{Res}^{(3)}(v)]$ amplitudes not exceeding one percent for $\frac{\chi_{Res}^{(3)}(v)}{\chi_{NR}^{(3)}} > 1.5$. For the above example given in section 5.3.1, the relative error of ϕ_{eff} is only 7 percent, which propagates into a relative error of $Im[\chi_{Res}^{(3)}(v)]$ amplitudes of approximately 0.7 percent.

Does this approach work for all phase angles ϕ_{eff} and ratios $\frac{\chi_{E\ eff}^{(3)}}{|\chi_{Res}^{(3)}(v)|}$? What is the minimum signal-to-noise (SNR) of a measured CARS spectrum needed for a reliable extraction of the ϕ_{eff} values? To answer these questions, we next determine the relative errors made in the reconstruction of $Im[\chi_{Res}^{(3)}(v)]$ amplitudes based on the extracted ϕ_{eff} values of simulated CARS spectra with known $\phi_{eff}, \chi_{E\ eff}^{(3)}$, and $\chi_{Res}^{(3)}(v)$ parameters. In the 2D plots in fig. 5.3 A and B, the relative errors of $Im[\chi_{Res}^{(3)}(v)]$ amplitudes are shown as a function of ϕ_{eff} and $\chi_{E\ eff}^{(3)}/|\chi_{Res}^{(3)}|$ without and with the correction of ϕ_{eff}, respectively. In fig. 5.3 A, the relative error in $Im[\chi_{Res}^{(3)}(v)]$
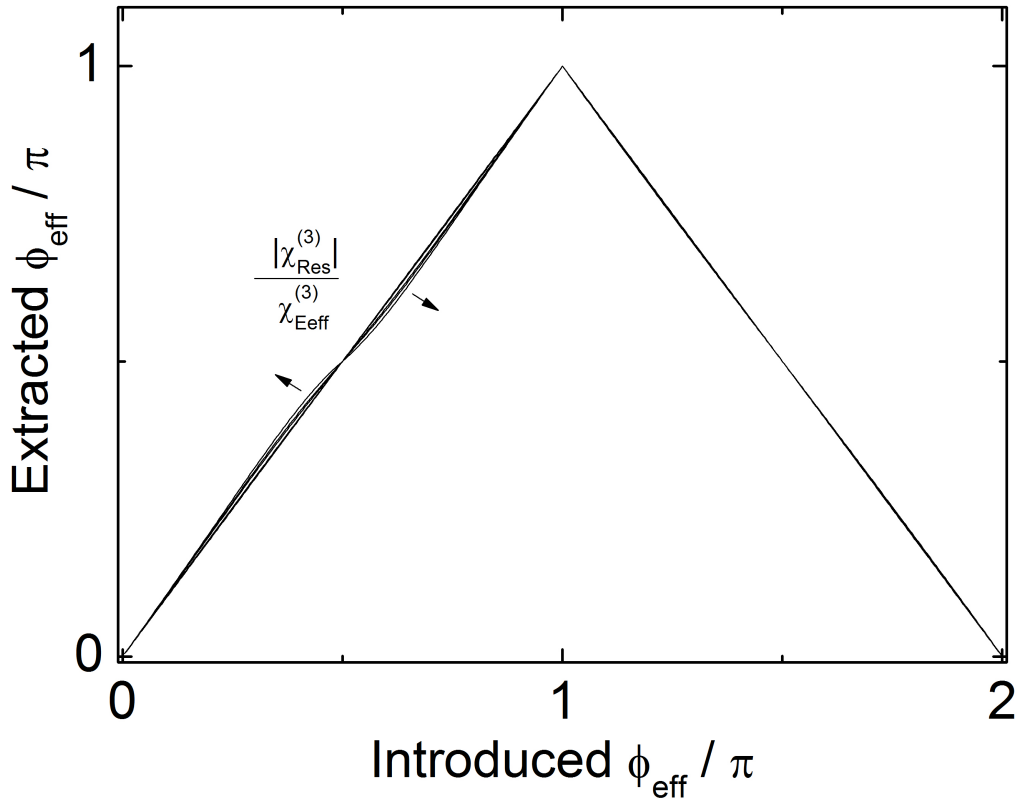
Figure 5.2: Dependence of the analytically determined ϕ_{eff} values using eqs. 5.32 and 5.33 extracted from simulated CARS spectra as a function of the simulated input ϕ_{eff} values and given $\frac{|\chi_{Res}^{(3)}(\nu)|}{\chi_{E\ eff}^{(3)}}$ values amounting to 0.1, 0.2, 0.5, 0.83, 0.91 and 1. Simulations were performed for a single resonance of amplitude $A = 1 cm^{-1}$ and $\chi_{E\ eff}^{(3)} = 1$.
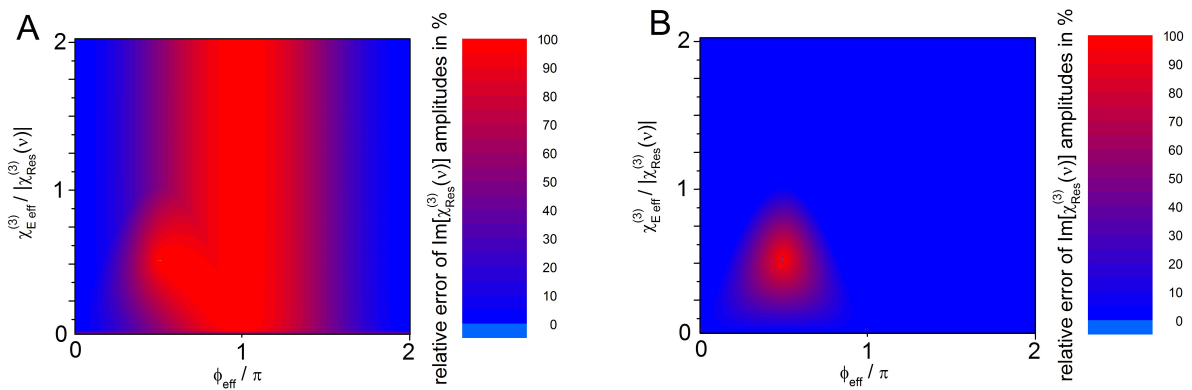
Figure 5.3: 2D plots of the relative error in the reconstructed $Im[\chi_{Res}^{(3)}(\nu)]$ amplitudes as a function of ϕ_{eff} and $\frac{\chi_{E\ eff}^{(3)}}{|\chi_{Res}^{(3)}(\nu)|}$ (A) without and (B) with correction of ϕ_{eff} according to eq. 5.31. Extraction of ϕ_{eff} was done by using eq. 5.32 and eq. 5.33. Simulations were performed for a single resonance of amplitude $A = 1\ cm^{-1}$.

monotonically increases from zero for $\phi_{eff} = 0$ to 100 % for $\phi_{eff} = \pi$. The latter corresponds to an $Im[\chi^{(3)}_{Res}(\nu)]$ amplitude pointing downwards in the complex plane. A further increase of ϕ_{eff} results in a decrease of the error to zero at $\phi_{eff} = 2\pi$. In the region $0 \leq \frac{\chi^{(3)}_{E\ eff}}{|\chi^{(3)}_{Res}(\nu)|} \leq 1$, the error builds a local maximum at $\phi_{eff} = \pi/2$ and $\frac{\chi^{(3)}_{E\ eff}}{|\chi^{(3)}_{Res}(\nu)|} = 0.5$. This is the limiting case excluded by eq. A.46 (see appendix A.8), where the CARS spectrum $S(\nu)$ is simply a frequency-independent constant, and therefore the estimated phase will be zero. When correcting for ϕ_{eff} using eq. 5.31, this maximum in the $Im[\chi^{(3)}_{Res}(\nu)]$ error persists, as can be seen in fig. 5.3 B, while for all remaining ratios of $\frac{\chi^{(3)}_{E\ eff}}{|\chi^{(3)}_{Res}(\nu)|}$, that are not excluded by eq. A.46, the correction of the $Im[\chi^{(3)}_{Res}(\nu)]$ amplitude errors induced by ϕ_{eff} works satisfactory.

Using the same approach described above for the estimated phase spectrum, we next determine ϕ_{eff} using the ratio of maximum to minimum excursions of the uncorrected $Im[\chi^{(3)}_{tot}(\nu)]$ spectrum. For that, we define the ratio

$$r_{Im[\chi^{(3)}_{tot}(\nu)]} = \frac{max(Im[\chi^{(3)}_{tot}(\nu)]) - min(Im[\chi^{(3)}_{tot}(\nu)])}{max(Im[\chi^{(3)}_{tot}(\nu)])} \quad . \tag{5.34}$$

Substituting $r_{Im[\chi^{(3)}_{tot}(\nu)]}$ instead of r_{phase} into eq. 5.32 allows us to extract ϕ_{eff}, and via eq. 5.31 the determination of $Im[\chi^{(3)}_{Res}(\nu)]$. The 2D plots in fig. 5.4 A and B show the relative errors of reconstructed $Im[\chi^{(3)}_{Res}(\nu)]$ amplitudes as a function of ϕ_{eff} and $\frac{\chi^{(3)}_{E\ eff}}{|\chi^{(3)}_{Res}(\nu)|}$ without and with correction for ϕ_{eff}, respectively. The results shown in fig. 5.4 are very much alike to those shown in
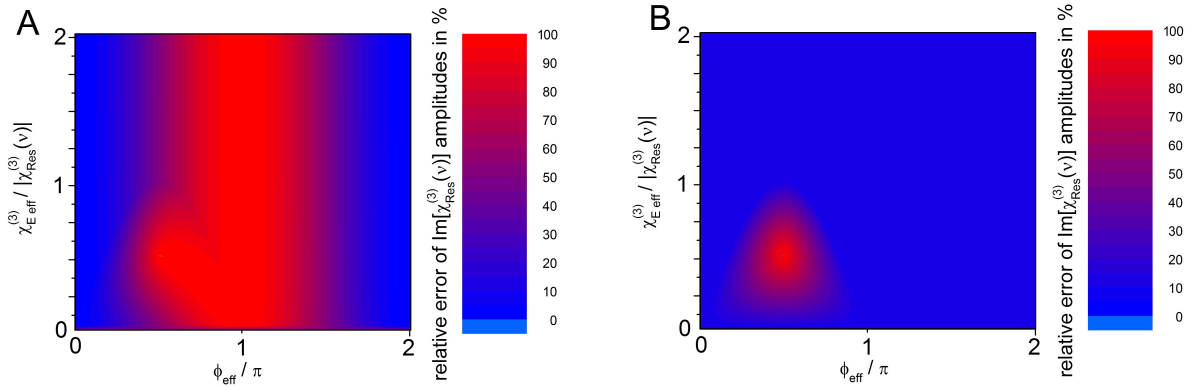
Figure 5.4: 2D plots of the relative error in the reconstructed $Im[\chi^{(3)}_{Res}(\nu)]$ amplitudes as a function of ϕ_{eff} and $\frac{\chi^{(3)}_{E\ eff}}{|\chi^{(3)}_{Res}(\nu)|}$ (A) without and (B) with corrections according to eq. 5.31. ϕ_{eff} was extracted using eq. 5.33 and eq. 5.35. Simulation were performed for a single resonance of amplitude $A = 1\ cm^{-1}$.

fig. 5.3, indicating that the determination and correction of ϕ_{eff} using the ratio of maximum to minimum excursions in the retrieved estimated phase $\phi_{estimated}$ and the reconstructed $Im[\chi^{(3)}_{Res}(\nu)]$ are equivalent. For the example used in section 5.3.1, we obtain an error of 0.7 % for the reconstructed $Im[\chi^{(3)}_{Res}(\nu)]$ amplitude. But using the approach based on the reconstructed $Im[\chi^{(3)}_{Res}(\nu)]$, no error-phase estimation is necessary.

Next, we added noise to the simulated CARS spectra $S(\nu)$. The minimum SNR needed in order to not exceed a relative error of 10 % in the reconstructed $Im[\chi_{Res}^{(3)}(\nu)]$ amplitudes was found to be approximately 10.

In conclusion, we have introduced a method for the removal of the dispersive character in the $Im[\chi_{tot}^{(3)}(\nu)]$ spectrum using the ratio of maximum to minimum excursions of the retrieved phase spectrum $\phi_{estimated}(\nu)$ or the reconstructed $Im[\chi_{tot}^{(3)}(\nu)]$ spectrum itself. It was demonstrated by simulations that the method works for all effective phase factors ϕ_{eff} and ratios $\frac{\chi_{E\,eff}^{(3)}}{|\chi_{Res}^{(3)}(\nu)|}$, provided that the criterion given in eq. A.46 and a SNR $\geq$ 10 of the CARS spectrum are fulfilled. However, because for the extraction of ϕ_{eff} a resonant region of $S(\nu)$ needs to be chosen manually, this method is not unsupervised! The determination and correction of ϕ_{eff} is working reliably, provided the maximum and minimum excursions of the estimated phase or of the $Im[\chi_{tot}^{(3)}(\nu)]$ spectrum are obtained for an isolated Raman resonance, such as a strong and narrow Raman line. However, this approach must fail when vibrational bands overlap, such that the maximum of one band resides at the minimum of the neighboring band. Because of these limitations, an unsupervised method to determine both ϕ_{eff} and $\chi_{E\,eff}^{(3)}$ simultaneously is desirable, which is applicable to any complex CARS spectrum with overlapping bands.

5.3.3 Unsupervised determination of both the effective phase ϕ_{eff} and the effective nonresonant contribution $\chi_{E\,eff}^{(3)}$ of $\chi_{tot}^{(3)}(\nu)$

"... überlegte ich oft, ob nicht etwa eine vernünftigere Anordnung von Kreisen zu finden sei, von welchen alle erscheinende Ungleichmässigkeit abhinge..."

Copernicus (Commentariolus, 1509)

In this section, an unsupervised method for the reconstruction of the pure vibrational susceptibility $\chi_{Res}^{(3)}(\nu)$ from a measured CARS spectrum in the presence of a nearby electronic resonance is developed that is generally applicable for a CARS spectrum consisting of overlapping bands. Before going into the math of this new approach, it is useful to recapitulate from ch. 3 what we know about the consequences of ϕ_{eff}, $\phi_{E\,eff}$, and $\chi_{E\,eff}^{(3)}$ on the measured CARS power spectrum $S(\nu)$:

1. As shown in section 3.2.2, a rotation of a vibrational resonance around $[\chi_{NR}^{(3)}, 0]$ by the angle $\phi_R \neq \phi_{eff}$ in the complex plane (see fig. 3.9) does not lead to an offset phase, but rather to a dispersive shape of the total phase spectrum $\phi_{tot}(\nu)$.

2. A translation of the vibrational resonance by $\chi_E^{(3)}e^{i\phi_E}$ in the complex plane (see fig. 3.10) leads also to a dispersive shape of the total phase spectrum for $\phi_{eff} \neq 0$ and to an offset phase $\phi_{E\,eff}$ (see eq. 3.27). Because $\phi_{E\,eff}$ is factoring out in the description of the

measured CARS spectrum (eq. 3.40 and eq. 3.41), neither the MEM nor the KK methods are able to retrieve this offset phase directly.

5.3.4 The case of a single chemical component

As discussed in ch. 3, both the full model for the total susceptibility $\chi_{tot}^{(3)}(\nu)$ and the model used in MEM phase retrieval (see eqs. 3.27 and 3.48) provide analytical expressions describing one and the same measured CARS intensity spectrum. Hence, we can write for the CARS spectrum

$$S(\nu) = \left| \sqrt{S(\nu)} e^{i\phi_{MEM}(\nu)} \right|^2 = \left| \chi_{E\ eff}^{(3)} | + \chi_{Res}^{(3)}(\nu) e^{i\phi_{eff}} \right|^2 \quad , \tag{5.35}$$

where $\phi_{MEM}(\nu)$ is the retrieved phase spectrum. $\chi_{E\ eff}^{(3)}$ and ϕ_{eff} are specific for the single chemical component under investigation, and are defined by eq. 3.39 and eq. 3.42, respectively. Assuming the identity of both models for the complex susceptibility, we obtain an expression for the desired pure vibrational complex susceptibility spectrum of that single chemical component

$$\chi_{Res}^{(3)}(\nu) = \sqrt{S(\nu)} e^{i(\phi_{MEM}(\nu) - \phi_{eff})} - |\chi_{E\ eff}^{(3)}| e^{-i\phi_{eff}} \quad . \tag{5.36}$$

Written in matrix form, the real and imaginary parts of $\chi_{Res}^{(3)}(\nu)$ are then given by:

$$\begin{bmatrix} Re[\chi_{Res}^{(3)}(\nu)] \\ Im[\chi_{Res}^{(3)}(\nu)] \end{bmatrix} = \begin{bmatrix} cos(\phi_{eff}) & -sin(\phi_{eff}) \\ -sin(\phi_{eff}) & cos(\phi_{eff}) \end{bmatrix} \times \sqrt{S(\nu)} \begin{bmatrix} cos(\phi_{MEM}(\nu)) \\ sin(\phi_{MEM}(\nu)) \end{bmatrix} - |\chi_{E\ eff}^{(3)}| \begin{bmatrix} cos(\phi_{eff}) \\ -sin(\phi_{eff}) \end{bmatrix} . \tag{5.37}$$

From eq. 5.37 follows that the correct Raman response $Im[\chi_{Res}^{(3)}(\nu)]$ is directly reconstructed from a measured CARS spectrum $S(\nu)$ and its retrieved phase spectrum, $\phi_{MEM}(\nu)$, provided that both ϕ_{eff} and $|\chi_{E\ eff}^{(3)}|$ have been correctly determined. Note, that the determination and the correction of an phenomenological error-phase $\phi_{error}(\nu)$, as described in section 3.3.2, now is redundant.

In order to determine both parameters in an unsupervised manner, we here exploit the properties of a pure Raman response spectrum. If reconstructed correctly, all vibrational resonances contributing to the measured CARS spectrum exhibit non-negative $Im[\chi_{Res}^{(3)}(\nu)]$ amplitudes ($Im[\chi_{Res}^{(3)}(\nu)] > 0$), and the area below the reconstructed $Im[\chi_{Res}^{(3)}(\nu)]$ spectrum is maximized, i.e. $\int_{\nu_1}^{\nu_2} Im[\chi_{Res}^{(3)}(\nu)] d\nu = MAX$. In order to demonstrate the sensitivity of this integral to deviations of the purely vibrational resonance response, CARS spectra of a single Lorentzian resonance were simulated for $0 \leq \phi_{eff} \leq 2\pi$ and $0.1 \leq \chi_{E\ eff}^{(3)} \leq 1$, and the MEM-phase was retrieved using the DCT-MEM (eq. 3.55). Then, the reconstructed $Im[\chi_{tot}^{(3)}(\nu)]$ spectra were numerically integrated and plotted as a function of ϕ_{eff} in fig. 5.5. The $\int Im[\chi_{tot}^{(3)}(\nu)] d\nu$ curve is a cosine-like function, and around its desired maximum, a change of ϕ_{eff} will only result in a small change of $\int Im[\chi_{tot}^{(3)}(\nu)] d\nu$. However, the $\int |Im[\chi_{tot}^{(3)}(\nu)]| d\nu$ curve is much steeper for ϕ_{eff} near zero, and thus its minimization offers a higher sensitivity in the determination of ϕ_{eff}.
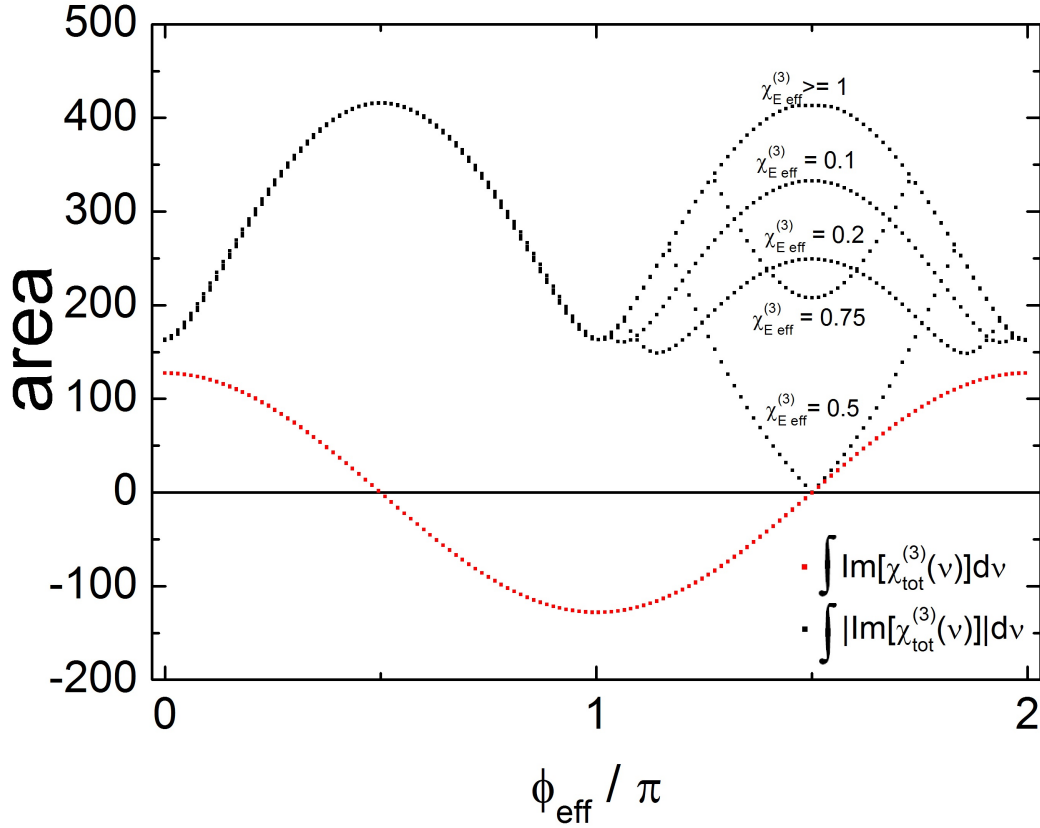
Figure 5.5: $\int |Im[\chi_{tot}^{(3)}(\nu)]| d\nu$ (black curve) and $\int Im[\chi_{tot}^{(3)}(\nu)] d\nu$ (red curve) as a function of ϕ_{eff} as obtained from the reconstructed $Im[\chi_{tot}^{(3)}(\nu)]$ using the DCT-MEM phase and eq. 3.55. A single Lorentzian resonance (see eq. 3.27) and $\chi_{E\ eff}^{(3)}$ values of 0.1, 0.2, 0.5, 0.75 and 1 were simulated.

When $\frac{|\chi_{E\ eff}^{(3)}|}{|\chi_{Res}^{(3)}(\nu)|} \leq 1$, $\int |Im[\chi_{tot}^{(3)}(\nu)]| d\nu$ shows also a dependence on the ratio $\frac{|\chi_{E\ eff}^{(3)}|}{|\chi_{Res}^{(3)}(\nu)|}$. We see from eqs. 5.36 and 5.37, that for a measured CARS spectrum $S(\nu)$ and its retrieved phase spectrum $\phi_{MEM}(\nu)$ one can obtain the unknown parameters ϕ_{eff} and $\chi_{E\ eff}^{(3)}$ of the single chemical component by solving the following minimisation problem:

$$F_1(\phi_{eff}, |\chi_{E\ eff}^{(3)}|) = \int_{\nu_1}^{\nu_2} \left| Im[\chi_{Res}^{(3)}(\nu)] \right| d\nu =$$

$$\int_{\nu_1}^{\nu_2} \left| \sqrt{S(\nu)} \left(sin(\phi_{MEM}(\nu) - \phi_{eff}) \right) - |\chi_{E\ eff}^{(3)}| sin(-\phi_{eff}(\nu)) \right| d\nu = MIN \ .$$

(5.38)

This functional is efficiently solved using an Ansatz of a constant effective phase, where ϕ_{eff} is assumed to be frequency independent in the spectral range of interest. The second parameter $\chi_{E\ eff}^{(3)}$ can also be obtained simultaneously solving the functional eq. 5.38 because it is functionally independent from ϕ_{eff}. In this way, the approach given by eq. 5.38 is fully unsupervized! Note, that a criterion similar to eq. 5.38 can of course also be derived for the real part of the $\chi_{Res}^{(3)}(\nu)$ spectrum. As can be seen in fig. 5.5, $\int |Im[\chi_{Res}^{(3)}(\nu)]| d\nu$ is a π-periodic function of ϕ_{eff}. Similar to the phase extrema used in eq. 5.32, a case analysis is needed to determine if

64

$\phi_{eff} \in [-\frac{\pi}{2}, \frac{\pi}{2})$ or $\phi_{eff} \in (\frac{\pi}{2}, \frac{3\pi}{2}]$. The corresponding sign correction factor δ_R is here determined by the order of the appearance of the relative minimum S_{min} and maximum S_{max} in the CARS spectrum:

$$\delta_R = \begin{cases} 1 & \nu\big|_{S_{max}(\nu)} < \nu\big|_{S_{min}(\nu)} \\ -1 & \nu\big|_{S_{min}(\nu)} < \nu\big|_{S_{max}(\nu)} \end{cases} . \tag{5.39}$$

If we complete eq. 5.36 with eq. 5.39, we obtain:

$$\chi_{Res}^{(3)}(\nu) = \sqrt{S(\nu)}e^{i\delta_R(\phi_{MEM}(\nu)-\phi_{eff})} - |\chi_{E\ eff}^{(3)}|e^{-i\delta_R\phi_{eff}} . \tag{5.40}$$

Next, we will evaluate the relative errors made in the reconstruction of relative $Im[\chi_{Res}^{(3)}(\nu)]$ amplitudes using eq. 5.38 and eq. 5.40 from simulated CARS spectra with known ϕ_{eff}, $\chi_{E\ eff}^{(3)}$, and $\chi_{Res}^{(3)}(\nu)$ spectrum. In the 2D plots in fig. 5.6 A and B, the relative errors of $Im[\chi_{Res}^{(3)}(\nu)]$ amplitudes are shown as a function of ϕ_{eff} and $\frac{\chi_{E\ eff}^{(3)}}{|\chi_{Res}^{(3)}(\nu)|}$ without and with the correction of the extracted ϕ_{eff} and $\chi_{E\ eff}^{(3)}$ values, respectively. The discussion given for figs. 5.3 and 5.4 holds
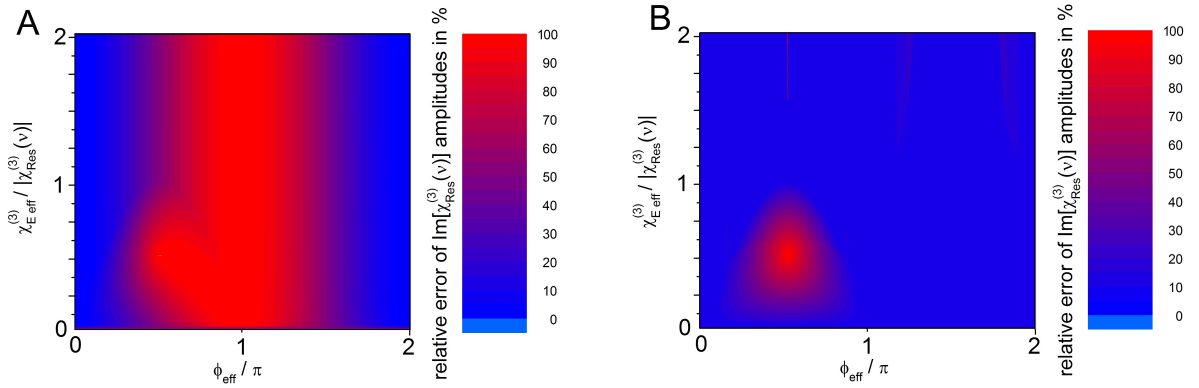
Figure 5.6: 2D plots of the relative error in the reconstructed $Im[\chi_{Res}^{(3)}(\nu)]$ amplitudes as a function of ϕ_{eff} and $\frac{\chi_{E\ eff}^{(3)}}{|\chi_{Res}^{(3)}(\nu)|}$ (A) without and (B) with correction of ϕ_{eff} according to eq. 5.40. ϕ_{eff} was extracted by solving the minimisation problem given eq. 5.38. Simulations were performed for a single resonance of amplitude $A = 1\ cm^{-1}$.

here as well. This simulation for an isolated resonance indicates that the determination and correction of ϕ_{eff} and $\chi_{E\ eff}^{(3)}$ using eq. 5.38 and eq. 5.40 works satisfactorily, similar to the method described in section 5.3.2. For the example used in section 5.3.1, the error for the reconstructed $Im[\chi_{Res}^{(3)}(\nu)]$ amplitudes is negligible.

Once $\chi_{E\ eff}^{(3)} = \chi_{E\ eff}^{(3)}(\chi_{NR}^{(3)}, \chi_E^{(3)}, \phi_E, \phi_R)$ and $\phi_{eff} = \phi_{eff}(\chi_{NR}^{(3)}, \chi_E^{(3)}, \phi_E, \phi_R)$ are determined with negligible errors using eq. 5.38, it is possible to estimate ϕ_E, ϕ_R, $\chi_{NR}^{(3)}$, and $\chi_E^{(3)}$ by fitting the nonresonant part of the measured CARS and the retrieved phase spectra to eq. 3.39 and eq. 3.35, respectively.

This approach is demonstrated for the simulation example shown in fig. 3.10. The obtained parameter values are listed and compared with their respective simulation input values in tab. 5.2. As can be seen from tab. 5.2, the extraction of ϕ_{eff} and $\chi^{(3)}_{E\,eff}$ from a simulated CARS

Table 5.2: Comparison of extracted values of $\chi^{(3)}_{NR}$, $\chi^{(3)}_{E\,eff}$, $\chi^{(3)}_{E}$, ϕ_{eff}, ϕ_R, ϕ_E, and $\phi_{E\,eff}$ using eqs. 5.38, 3.38, 3.39, and 3.42 with those input values used for the simulation of the CARS spectrum (eq. 3.28).

Parameter	simulated value	extracted value	relative error
$\phi_{E\,eff}$	0.639	0.583	8.8 %
$\chi^{(3)}_{E\,eff}$	$\lvert 1.5e^{\phi_E} + \chi^{(3)}_{NR}\rvert = 2.179$	2.180	0.0 %
$\chi^{(3)}_{NR}$	1	1.097	9.7 %
$\chi^{(3)}_{E}$	1.5	1.665	11.0 %
ϕ_{eff}	$\phi_R - \phi_{E\,eff} = -1.031$	-0.986	4.3 %
ϕ_R	$-\frac{\pi}{8} = -0.3927$	-0.403	2.7 %
ϕ_E	$\frac{\pi}{3} = 1.0472$	0.953	9.0 %

spectrum and the corresponding MEM-phase spectrum using eq. 5.38 recovers the respective simulation input parameters satisfactory. The subsequent estimation of ϕ_R, ϕ_E, $\chi^{(3)}_{NR}$, and $\chi^{(3)}_{E}$ also recovers their respective simulation input values satisfactory. While the relative error for ϕ_R is below 3 %, higher relative errors of about 10 % are obtained for ϕ_E, $\chi^{(3)}_{NR}$, and $\chi^{(3)}_{E}$ due to their stronger functional dependence (see eq. 3.27). In conclusion, this simulation example for an isolated Raman resonance demonstrates that it is possible, to extract and fully characterize each electronic and vibrational contribution to the total complex susceptibility according to the model given in eq. 3.27 from the knowledge of a measured CARS spectrum and a retrieved phase spectrum.

Next, we will come back to our initial question whether the method using eqs. 5.38 and 5.40 not only handles a spectrum of an isolated resonance but also a spectrum of overlapping resonances. For this purpose we will demonstrate our approach for a simulated CARS spectrum of a lipid (FAME 18:1, see section 7.3.2) in water, with a highly congested CH-stretching region. Here, we assume that the lipid and water behave as a single chemical component, which is described by a single set of ϕ_{eff} and $\lvert\chi^{(3)}_{E\,eff}\rvert$. The CARS spectrum was simulated using a model for $\chi^{(3)}_{Res}(\nu)$ containing both lipid and water resonances and eq. 5.35. ϕ_{eff} was then determined using eq. 5.38. The pure complex $Im[\chi^{(3)}_{Res}(\nu)]$ of the vibrational response was then reconstructed using the DCT-MEM approach and eq. 5.40. The simulation is performed using $\chi^{(3)}_{E\,eff} = 1$ and for two distinct values of ϕ_{eff}: $\phi_{eff} = 0°$ and $\phi_{eff} = 30°$. The results are presented in fig. 5.7. Without noise, for a simulated $\phi_{eff} = 0°$, values of $\phi_{eff} = 1°$ and $\chi^{(3)}_{E\,eff} = 0.9837$ are determined, and for a simulated $\phi_{eff} = 30°$, $\phi_{eff} = 29°$ and $\chi^{(3)}_{E\,eff} = 1.0003$
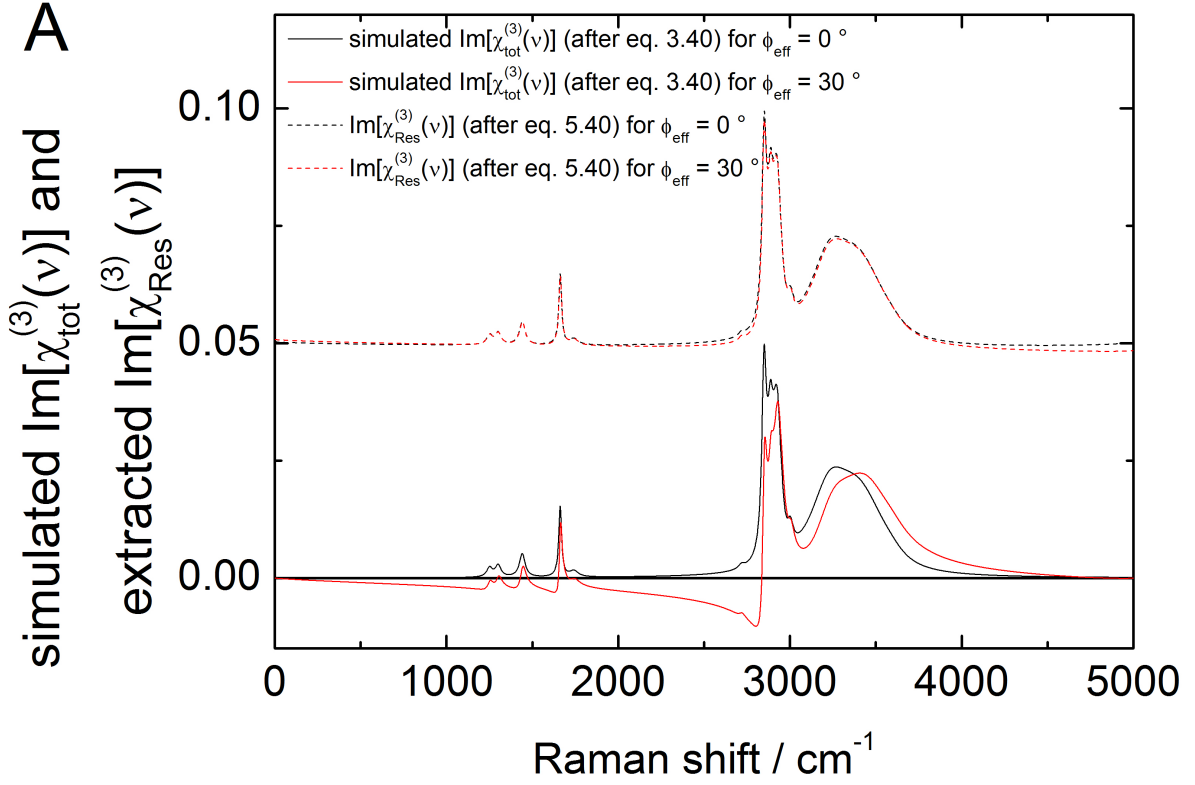
Figure 5.7: Reconstruction of the pure vibrational response of simulated CARS spectra of a FAME-lipid-water sample, exhibiting overlapping bands in the highly congested CH-stretching region. The simulation is performed using $\chi^{(3)}_{E\,eff} = 1$ and for two ϕ_{eff} values: $\phi_{eff} = 0°$ (black curves) and $\phi_{eff} = 30°$ (red curves). Shown are the input $Im[\chi^{(3)}_{tot}(\nu)]$ spectra simulated according to eq. 3.40 together with the respective $Im[\chi^{(3)}_{Res}(\nu)]$ spectra, as extracted using the functional (eqs. 5.38 and 5.40). The latter are offset by 0.05 units.

are determined. With added noise corresponding to a SNR of 25 in the CH-stretching region and a SNR of 7.5 in the fingerprint region of that CARS spectrum for a simulated $\phi_{eff} = 0°$ values of $\phi_{eff} = 4°$ and $\chi^{(3)}_{E\,eff} = 1.0033$ are determined, and for a simulated $\phi_{eff} = 30°$, $\phi_{eff} = 29°$ and $\chi^{(3)}_{E\,eff} = 1.0005$ are determined. The relative errors in ϕ_{eff} and $\chi^{(3)}_{E\,eff}$ do not exceed 4° and 1.6%, respectively. When compared with the isolated single resonance band, the errors have not increased significantly.

In conclusion, the novel method applies well for spectra containing overlapping bands and noise too! The small differences between simulated and extracted ϕ_{eff} and $\chi^{(3)}_{E\,eff}$ are due to the broad water bands, whose $Im[\chi^{(3)}_{Res}(\nu)]$ is even at 5000 cm^{-1} not exactly zero. Additionally, the MEM procedure intrinsically does only give exactly zero in the nonresonant regions at the spectral ends. A subsequent correction of the background will however remove these residual differences concerning the baseline, when simulated and reconstructed $\chi^{(3)}_{Res}(\nu)$ are compared.

5.3.5 The case of a mixture of distinct chemical components

In the previous section, we have treated the case of a single chemical component with its characteristic ϕ_{eff} and $\chi^{(3)}_{E\,eff}$ values. Here, we will extend this approach for a mixture of n chemical components, which do not interact with each other, and each have their distinct $\phi_{eff\,j}$ and $\chi^{(3)}_{E\,eff\,j}$ values ($j = 1 \ldots n$).

In analogy to the expression for the total susceptibility of a single chemical component given in eq. 3.40, the model for the mixture then reads

$$\chi^{(3)\,mix}_{tot}(\nu) = \sum_{j=1}^{n} c_j \left[|\chi^{(3)}_{E\,eff\,j}| e^{i\phi_{E\,eff\,j}} + \chi^{(3)}_{Res\,j}(\nu) e^{i\phi_{R\,j}} \right] \;, \tag{5.41}$$

where c_j are the fractions of the jth component with $\sum_{j=1}^{n} c_j = 1$. With ν being far off the vibrational resonances, we can define an effective complex susceptibility $\chi^{(3)\,mix}_{E\,eff}$ that combines all frequency independent contributions of $\chi^{(3)\,mix}_{tot}(\nu)$:

$$\chi^{(3)\,mix}_{E\,eff} = |\chi^{(3)\,mix}_{E\,eff}| e^{i\phi^{mix}_{E\,eff}} = \sum_{j=1}^{n} c_j |\chi^{(3)}_{E\,eff\,j}| e^{i\phi_{E\,eff\,j}} \;, \tag{5.42}$$

where

$$|\chi^{(3)\,mix}_{E\,eff}|^2 = \sum_{j=1}^{n} c_j^2 |\chi^{(3)}_{E\,eff\,j}|^2 + 2 \sum_{\substack{j,k=1 \\ j\neq k}}^{n} c_j c_k |\chi^{(3)}_{E\,eff\,j}| |\chi^{(3)}_{E\,eff\,k}| \cos(\phi_{E\,eff\,j} - \phi_{E\,eff\,k}) \;, \tag{5.43}$$

and

$$\phi^{mix}_{E\,eff} = \tan^{-1} \left[\frac{\sum_{j=1}^{n} c_j |\chi^{(3)}_{E\,eff\,j}| \sin(\phi_{E\,eff\,j})}{\sum_{j=1}^{n} c_j |\chi^{(3)}_{E\,eff\,j}| \cos(\phi_{E\,eff\,j})} \right] \;. \tag{5.44}$$

Using eqs. 5.42 - 5.44, we can rewrite eq. 5.41 as follows:

$$\chi^{(3)\,mix}_{tot}(\nu) = \left\{ |\chi^{(3)\,mix}_{E\,eff}| + \sum_{j=1}^{n} c_j \chi^{(3)}_{Res\,j}(\nu) e^{i(\phi_{R\,j} - \phi^{mix}_{E\,eff})} \right\} e^{i\phi^{mix}_{E\,eff}} \;. \tag{5.45}$$

As can be seen, each vibrational resonance component, $\chi^{(3)}_{Res\,j}(\nu)$, then appears rotated by an effective phase shift:

$$\phi^{mix}_{eff\,j} = \phi_{R\,j} - \phi^{mix}_{E\,eff} \;. \tag{5.46}$$

Note that for the single component case of $n = 1$, eqs. 5.42, 5.44 , 5.45, and 5.46 reduce to eqs. 3.37, 3.38, 3.40, and 3.42, respectively. However, in the general case of a mixture of n components eqs. 5.43 and 5.44 describe a coupling of all n components. Eq. 5.45 results then in an expression for the CARS spectrum given by

$$S(\nu) = |\sqrt{S^{mix}(\nu)} e^{i\phi^{mix}_{MEM}(\nu)}|^2 = \left| |\chi^{(3)\,mix}_{E\,eff}| + \sum_{j=1}^{n} c_j \chi^{(3)}_{Res\,j}(\nu) e^{i\phi^{mix}_{eff\,j}} \right|^2 \;. \tag{5.47}$$

Assuming the identity of both the model used in MEM phase retrieval (see eq. 3.27 and eq. 3.28) and $\chi_{tot}^{(3)\ mix}(\nu)$ (eq. 5.45) for the complex susceptibility of the mixture, we obtain an expression for the pure vibrational susceptibility spectrum of the nth component $\chi_{Res\ n}^{(3)}(\nu)$:

$$\chi_{Res\ n}^{(3)}(\nu) =$$
$$\frac{1}{(1 - \sum_{j=1}^{n-1} c_j)} \left[\sqrt{S^{mix}(\nu)}e^{i(\phi_{MEM}^{mix}(\nu) - \phi_{eff\ n}^{mix})} - |\chi_{E\ eff}^{(3)\ mix}|e^{-i\phi_{eff\ n}^{mix}} - \sum_{j=1}^{n-1} c_j\chi_{Res\ j}^{(3)}(\nu)e^{i(\phi_{eff\ j}^{mix} - \phi_{eff\ n}^{mix})} \right].$$
$$(5.48)$$

Unlike for the single-component case of $n = 1$, where eq. 5.48 reduces to eq. 5.36, the extraction of the pure vibrational resonance $\chi_{Res\ n}^{(3)}(\nu)$ of an n-component mixture requires pior knowledge of the relative fractions, phase shifts, and susceptibilities of all $(n-1)$ remaining species. Even with $\chi_{Res\ j}^{(3)}(\nu)$ and $\phi_{eff\ j}^{mix}$ ($j = 1 \ldots (n-1)$) known from independent single-component measurements, the fractions c_j of the $(n-1)$ components cannot be correctly determined and directly be subtracted from the mixture spectrum as long as $\chi_{E\ eff}^{(3)\ mix}$ and $\phi_{E\ eff}^{mix}$ are unknown.

By simply applying the single-component functional (eq. 5.38) to an n-component mixture, the curve shown in fig. 5.5 for a single component will not be sinusoidal any more. This is illustrated in fig. 5.8 for a two-component mixture of a lipid and water used for the simulation in fig. 5.7, where $\int |Im[\chi_{tot}^{(3)\ mix}(\nu)]|d\nu$ is simulated as a function of the phase shift value of lipids ($\phi_{eff\ 2}$) and for the cases of $\phi_{eff\ 2} = \phi_{eff\ 1}$ and $\phi_{eff\ 2} = \phi_{eff\ 1} + 30°$. As can be seen, for the simulated case of distinct phase shifts, the curve shows deviations from the symmetric sinusoidal curve obtained for the case of no phase shift. This information could of course be useful, because it allows to tell, whether a single or a mixture of non-interacting species are contributing to a given CARS spectrum. Note that this is a coherent feature not offered by spontaneous Raman spectroscopy!

Because $\chi_{E\ eff}^{(3)\ mix}$ and $\phi_{E\ eff}^{mix}$ couple all n species of the mixture with each other, the fractions c_j and the pure vibrational response $\chi_{Res\ n}^{(3)}(\nu)$ can only be obtained by making simplifying approximations. We first assume that all n components share an identical electronic contribution to their complex susceptibilities, such as $\phi_{E\ eff} = \phi_{E\ eff\ j}$ and $|\chi_{E\ eff}^{(3)}| = |\chi_{E\ eff\ j}^{(3)}|$ for all $j = 1 \cdots n$. In this case, eqs. 5.43, 5.44, and 5.46 simplify to

$$|\chi_{E\ eff}^{(3)\ mix}| = |\chi_{E\ eff}^{(3)}| \ , \tag{5.49}$$

$$\phi_{E\ eff}^{mix} = \phi_{E\ eff} \ , \tag{5.50}$$

and

$$\phi_{eff\ j} = \phi_{R\ j} - \phi_{E\ eff} \ . \tag{5.51}$$
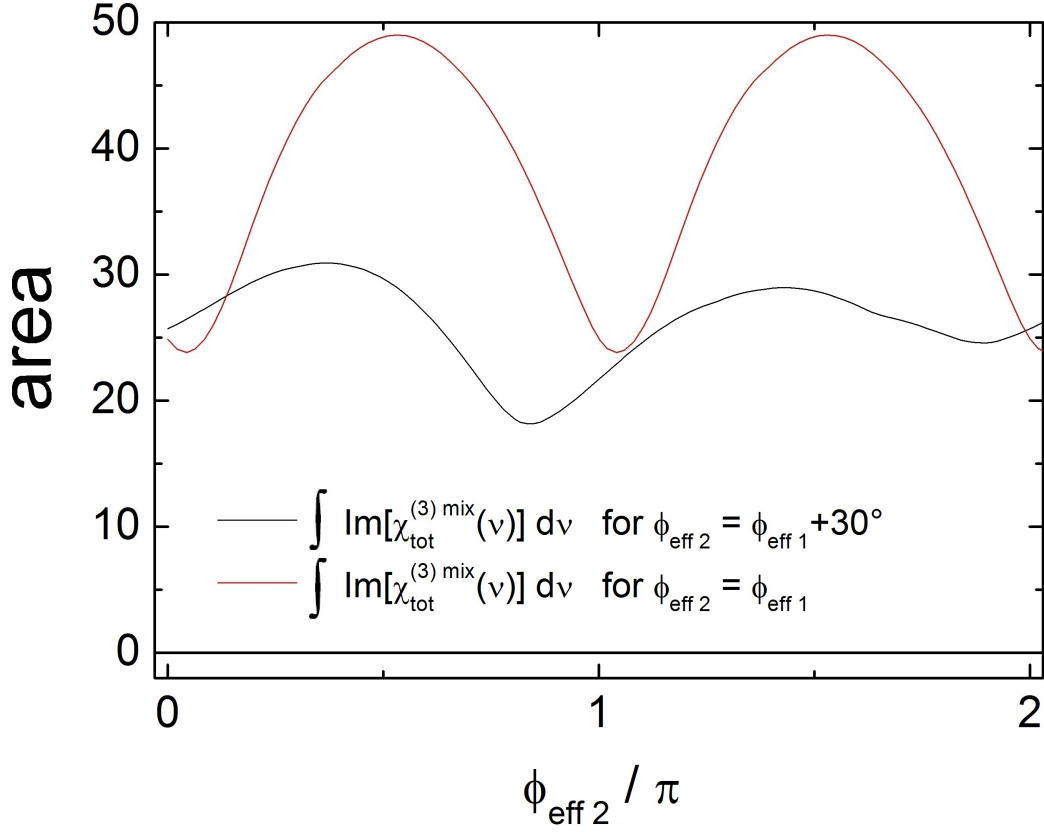
Figure 5.8: $\int |Im[\chi_{tot}^{(3)\ mix}(\nu)]|d\nu$ as a function of $\phi_{eff\ 2}$ for a two-component mixture of a lipid (component 2) and water (component 1, see fig. 5.7) for the cases where $\phi_{eff\ 2} = \phi_{eff\ 1}$ (red curve) and $\phi_{eff\ 2} = \phi_{eff\ 1} + 30°$ (black curve), as obtained from the reconstructed $Im[\chi_{tot}^{(3)\ mix}(\nu)]$ using the DCT-MEM phase and the single-component functional F_1 (eq. 5.38).

Eq. 5.48 then reduces to

$$\chi_{Res\ n}^{(3)}(\nu) = \frac{1}{1 - \sum_{j=1}^{n-1} c_j} \left[\sqrt{S^{mix}(\nu)} e^{i(\phi_{MEM}^{mix}(\nu) - \phi_{eff\ n})} - |\chi_{E\ eff}^{(3)\ mix}| e^{-i\phi_{eff\ n}} - \sum_{j=1}^{n-1} c_j \chi_{Res\ j}^{(3)}(\nu) e^{i(\phi_{eff\ j} - \phi_{eff\ n})} \right]$$

(5.52)

In analogy to the single-component case described in the preceding section, we define a minimization problem in order to obtain the pure vibrational response of $\chi_{Res\ n}^{(3)}(\nu)$, provided all $(n-1)$ components are known from independent experiments:

$$F_n(\phi_{eff\ n}, |\chi_{E\ eff}^{(3)\ mix}|) = \int_{\nu_1}^{\nu_2} d\nu |Im[\chi_{Res\ n}^{(3)}(\nu)]|$$

$$= \int_{\nu_1}^{\nu_2} d\nu \frac{1}{1 - \sum_{j=1}^{n-1} c_j} \left\| \left[\sqrt{S^{mix}(\nu)} sin(\phi_{MEM}^{mix}(\nu) - \phi_{eff\ n}) - |\chi_{E\ eff}^{(3)\ mix}| sin(-\phi_{eff\ n}) \right] \right.$$

$$\left. - \sum_{j=1}^{n-1} c_j Im[\chi_{Res\ j}^{(3)}(\nu) e^{i(\phi_{eff\ j} - \phi_{eff\ n})}] \right\| = MIN \ .$$

(5.53)

Solving eq. 5.53 directly represents a minimization problem with $(n+1)$ free fit parameters. For complex mixtures with large n, this results in large fit errors due to the large free fit parameter space. This drawback can be circumvented, when the relative fractions of all $(n-1)$ components are also known. In this case, the functional eq. 5.53 yields $\phi_{eff\,n}$ and $|\chi_{E\,eff}^{(3)\,mix}|$ directly, and $\chi_{Res\,n}^{(3)}(\nu)$ is obtained according to eq. 5.52.

For the simplest mixture of two non-interacting components, the functional then reads

$$
F_2(\phi_{eff\,2}, |\chi_{E\,eff}^{(3)\,mix}|) = \int_{\nu_1}^{\nu_2} d\nu \frac{1}{1-c_1} \left| \left\{ \sqrt{S^{mix}(\nu)} \sin(\phi_{MEM}^{mix}(\nu) - \phi_{eff\,2}) - |\chi_{E\,eff}^{(3)\,mix}| \sin(-\phi_{eff\,2}) \right. \right.
$$
$$
\left. \left. - c_1 \left(Re[\chi_{Res\,1}^{(3)}(\nu)] \sin(\phi_{eff\,1} - \phi_{eff\,2}) + Im[\chi_{Res\,1}^{(3)}(\nu)] \cos(\phi_{eff\,1} - \phi_{eff\,2}) \right) \right\} \right|
$$
$$
= MIN \ .
$$

(5.54)

With prior knowledge of $\chi_{Res\,1}^{(3)}(\nu)$ and $\phi_{eff\,1}$ from an independent experiment recorded under identical conditions, solving eq. 5.54 provides estimates of $\phi_{eff\,2}$ of the second component, $|\chi_{E\,eff}^{(3)\,mix}|$, and the fraction c_1 of the first component. Substitution into eq. 5.52 finally yields the pure vibrational response of the second component, $\chi_{Res\,2}^{(3)}(\nu)$. As a result, both vibrational responses and their relative fractions making up the mixture are obtained in an unsupervized manner.

The relative fraction c_j $(j = 1 \cdots (n-1))$ can independently be approximated provided that spectral features can be identified, which are only characteristic for the jth species, and do not overlap with a spectral feature of any other species. This will next be demonstrated for the two-component case, where $\chi_{Res\,1}^{(3)}(\nu)$ and $\phi_{eff\,1}$ are known, and its relative fraction c_1 in the mixture with an unknown second species has to be determined. The error made when the first component is rotated by an estimated effective phase shift ϕ_{eff}^{est}, which is obtained when its mixture with the unknown second species is approximated by using the single-component functional (eq. 5.38), i.e. $F_1(\phi_{eff}^{est}, |\chi_{E\,eff}^{(3)\,mix}|)$, is given by:

$$
\Delta\chi_{Res\,1}^{(3)}(\nu) = \chi_{Res\,1}^{(3)\,est}(\nu, \phi_{eff}^{est}) - \chi_{Res\,1}^{(3)}(\nu, \phi_{eff\,1}) = \chi_{Res\,1}^{(3)}(\nu, \phi_{eff\,1})(e^{i(\phi_{eff}^{est} - \phi_{eff\,1})} - 1) \qquad (5.55)
$$

where $\phi_{eff\,1}$ and $\chi_{Res\,1}^{(3)}(\nu)$ have been correctly obtained from the CARS spectrum of the pure first species by solving eq. 5.40 and using $F_1(\phi_{eff\,1}, |\chi_{E\,eff\,1}^{(3)\,mix}|)$ (eq. 5.38), respectively. Here, $\chi_{Res\,1}^{(3)\,est}(\nu, \phi_{eff}^{est}) = \chi_{Res\,1}^{(3)\,est}(\nu, \phi_{eff\,1})e^{i\phi_{eff}^{est}}$ is obtained using eq. 5.40 for the first species and ϕ_{eff}^{est}. In order to obtain an estimate for the fraction c_1, we correct $\chi_{Res\,1}^{(3)\,est}(\nu, \phi_{eff}^{est})$ with the error given by eq. 5.55. Correspondingly, $\chi_{Res}^{(3)\,mix\,est}(\nu, \phi_{eff}^{est})$ is obtained using eq. 5.40 for the mixture and ϕ_{eff}^{est}. By minimizing the difference of the scaled and corrected response of the first species with respect to the estimated response of the mixture, i.e.

$$
\int min \left(0, Im[\chi_{Res}^{(3)\,mix\,est}(\nu, \phi_{eff}^{est})] - c_1 Im[\chi_{Res\,1}^{(3)\,est}(\nu, \phi_{eff}^{est}) - \Delta\chi_{Res\,1}^{(3)}(\nu)] \right) d\nu = 0 \ , \qquad (5.56)
$$

and by calculating eq. 5.56 iteratively, a good estimation of c_1 is obtained.

Using eqs. 5.54 and 5.52, the reconstruction of pure vibrational responses from a mixture of the same two species of FAME 18:1 and water, previously shown in fig. 5.7, will next be demonstrated. Here, distinct phase shift values for the pure lipid and water of $\phi_{eff\ 2} = 30°$ and $\phi_{eff\ 1} = 0°$, respectively, are simulated. The results are presented in fig. 5.9. With an
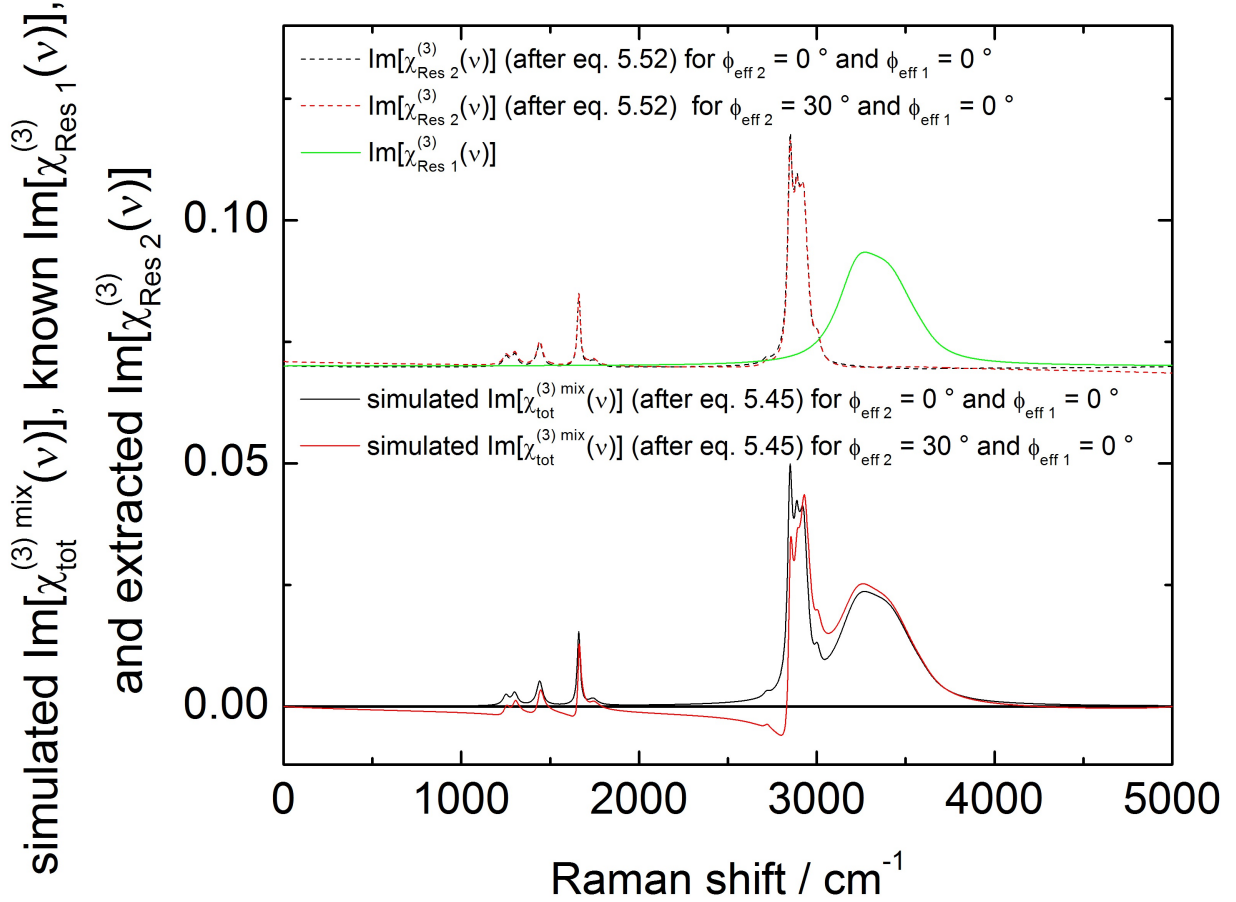
Figure 5.9: Reconstruction of the pure vibrational response of simulated CARS spectra of a mixture of a FAME 18:1 lipid (component 2) and water (component 1). The simulation is performed using $\chi_{E\ eff}^{(3)\ mix} = 1$ and for two $\phi_{eff\ 2}$ values: $\phi_{eff\ 2} = 0°$ (black curves) and $\phi_{eff\ 2} = 30°$ (red curves), while $\phi_{eff\ 1} = 0°$ was fixed. Shown are the input $Im[\chi_{tot}^{(3)\ mix}(\nu)]$ spectra simulated according to eq. 5.45 together with the known $Im[\chi_{Res\ 1}^{(3)}(\nu)]$ spectrum of the pure water component and the $Im[\chi_{Res\ 2}^{(3)}(\nu)]$ spectrum of the lipid component, as extracted using eqs. 5.52, 5.55 and 5.56. The latter are offset by 0.07 units.

extracted angle of 27.5° for the lipid species being very close to the simulated $\phi_{eff\ 2} = 30°$, the reconstruction of the unknown pure vibrational response is satisfactory.

In biological applications of CARS microscopy, image pixel spectra recorded inside a cell typically contain a mixture of cytoplasmic proteins, lipids, and water. To eliminate the influence of water, first pixel spectra with the focus filled with water only (e.g. outside a cell) have to be

identified. Using the functional for a single component (eq. 5.38) will in this case provide the correct $Im[\chi^{(3)}_{Res\ 1}(\nu)]$ and $\phi_{eff\ 1}$ for water. Next, its relative fraction c_1 to each pixel spectrum has to be determined. We eliminate the water contribution in each pixel spectrum by substituting $\chi^{(3)}_{Res\ 1}(\nu)$, $\phi_{eff\ 1}$, and c_1 into the two-component functional given by eq. 5.54. The analysis pipeline for reconstructing a CARS hyperspectrum of a mixture of one known $\chi^{(3)}_{Res\ 1}(\nu)$ and $\phi_{eff\ 1}$ and one unknown species $\chi^{(3)}_{Res\ 2}(\nu)$ and $\phi_{eff\ 2}$ is summarized in fig. 5.10.

5.4 Experimental test of novel concepts in MEM phase retrieval

So far, a new and efficient way of calculating the autocorrelation coefficients in MEM based phase retrieval using the DCT transform has been presented in section 5.1, the implementation of a new Toeplitz solver for eq. 3.50 containing the autocorrelation matrix has been presented and compared in section 5.2, and a theory that allows quantifying an additional phase factor $e^{i\phi_{eff}}$ and removing its influence on the reconstruction of the pure vibrational susceptibility $\chi^{(3)}_{Res}(\nu)$ of the sample of interest has been derived in section 5.3. In this section, these novel concepts will be verified by applying them to experimental data with toluene as sample.

5.4.1 Materials and Methods

Neat toluene (Riedel-de-Haën, SPECTRANAL, 99.9% purity) was used as a strong Raman scattering sample, because it has both sharp narrow bands in the fingerprint region as well as overlapping broad bands in the CH-stretching region. Toluene was transferred into a sample chamber consisting of two microscope cover slips of 150 μm thickness (Roth Chemie, Karlsruhe, Germany, #H877), separated by a spacer with an approximate thickness of 300 μm.

Unpolarized, parallel and perpendicular polarized spontaneous Raman scattering spectra were recorded using 32 mW laser power at an excitation wavelength λ_{Ex} = 532 nm, a 100 x objective, detected using a 50 μm fibre and a 600 g/mm grating with 10 sec integration time.

For the CARS measurements, the setup with Stokes supercontinuum pulse generation and the spectrometer S1 (E in position E1 and mirror D in position D1) was used, as described in section 4.2. The pump wavelength was set to λ_{Pump} = 800.65 nm. The pump and Stokes beam powers were 20 mW and 10 mW, respectively. A time series containing 10 spectra with an integration time of 100 ms per spectrum was recorded, and averaged before further processing. Estimation of ϕ_{eff} and $\chi^{(3)}_{E\ eff}$ was performed using eq. 5.38 within the range from 339 cm^{-1} to 1892 cm^{-1} for the fingerprint region and the range from 2081 cm^{-1} to 3560 cm^{-1} for the CH-stretching region. Additionally, ϕ_{eff} was estimated using eq. 5.32 for the isolated resonance band at 803 cm^{-1}. For the phase retrieval using the CPCG solver, five iterations were used.
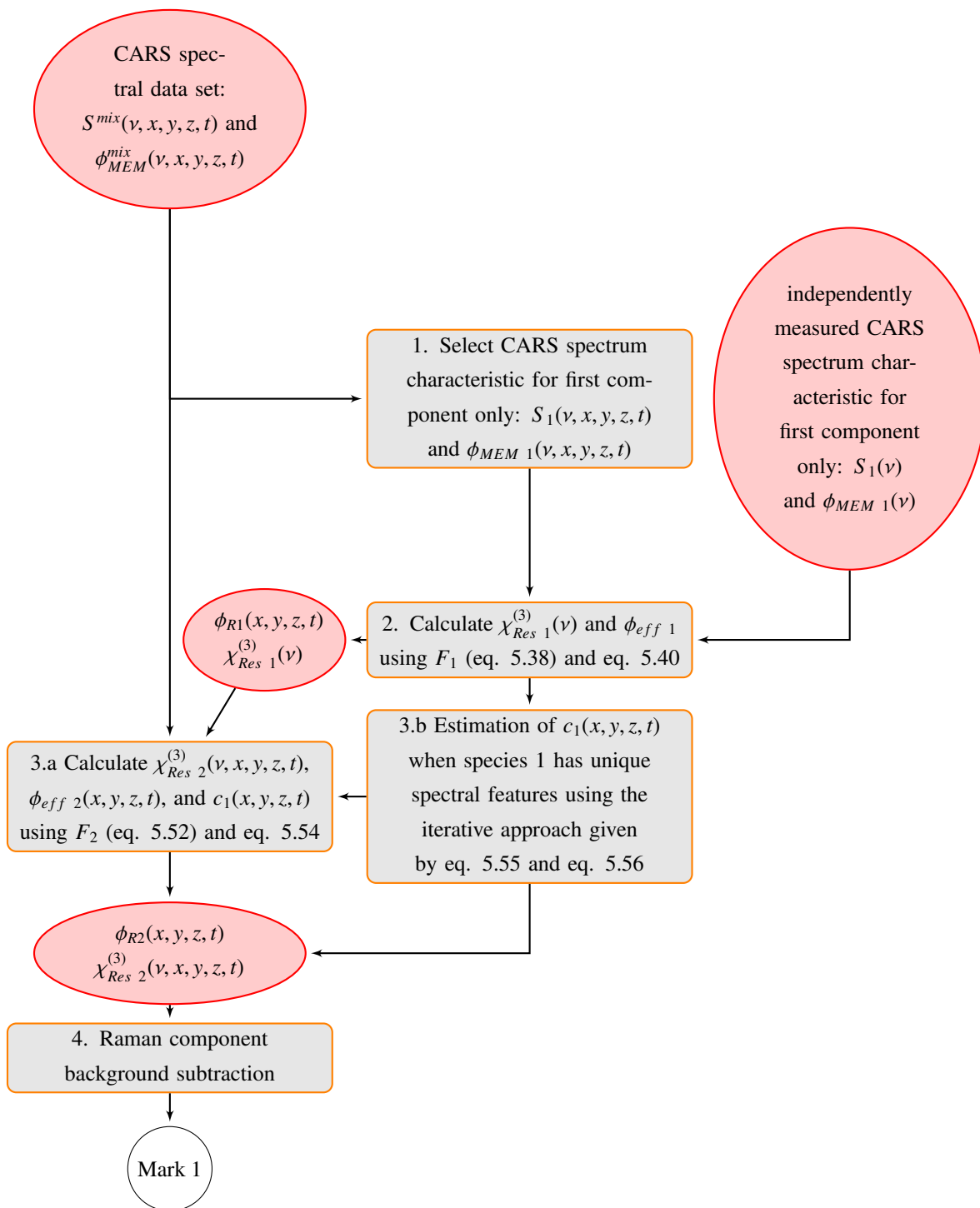
Figure 5.10: Flow chart showing the CARS spectra analysis pipeline for extracting the vibrational responses and relative fractions of the pure components in a two-component mixture. The subsequent analysis steps are the same as in the spontaneous Raman case, see the flow chart in fig. 4.2 after mark 1.

5.4.2 Experimental results

Fig. 5.11 shows the CARS spectra of toluene for the different approaches for calculating the autocorrelation coefficients in MEM based phase retrieval using the DCT (upper spectrum) and DFT ($K = 0$, lower spectrum). The lower spectrum shows the measured CARS spectrum extended with its reversed copy. The dependencies of the autocorrelation factors $|C(m, K)|$ be-
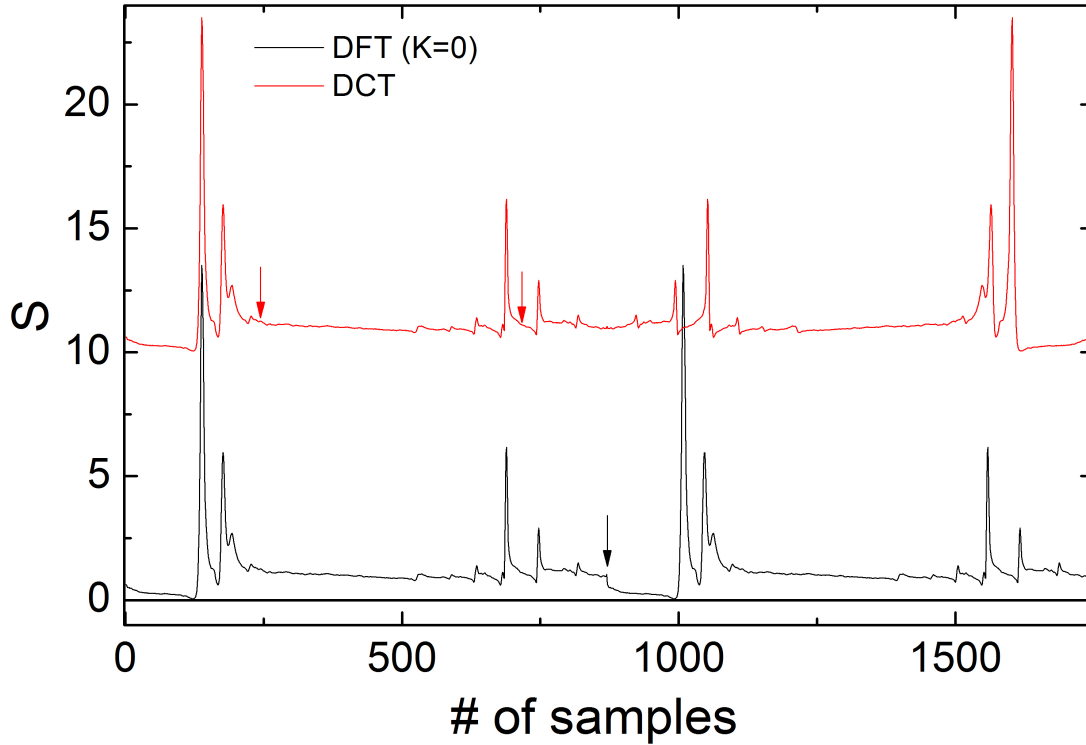
Figure 5.11: Input CARS spectra for the calculation of autocorrelation coefficients in MEM based phase retrieval using the DCT (upper spectrum) and the DFT ($K = 0$, lower spectrum). The discontinuity (black arrow) is avoided in the input spectrum for the DCT transform due to symmetrization. The DCT input spectrum is shifted by 10 units for better visibility. Two values of $S_{NR}(v) = |\chi^{(3)}_{E\,eff}|^2$ are highlighted (red arrows): $|\chi^{(3)}_{E\,eff}|^2 = 1.06$ at 877 cm^{-1} and $|\chi^{(3)}_{E\,eff}|^2 = 1.77$ at 2703 cm^{-1}.

longing to both input CARS spectra are plotted in fig. 5.12. For $m \leq 400$, the values of $|C(m, K)|$ calculated using the DCT exceed those calculated using the DFT, indicating the superior energy compaction of the DCT. This crossover occurs at smaller m for input CARS spectra exhibiting correlations or broader bands, e.g the water band.

The corresponding retrieved MEM-phase spectra $\phi_{MEM}(v, K)$ are shown in fig. 5.13 A together with their estimated error-phase spectra $\phi_{error}(v, K)$ derived using spline fits. Clearly, the DFT based MEM phase without squeezing ($K = 0$) shows the windowing-effect at the spectral
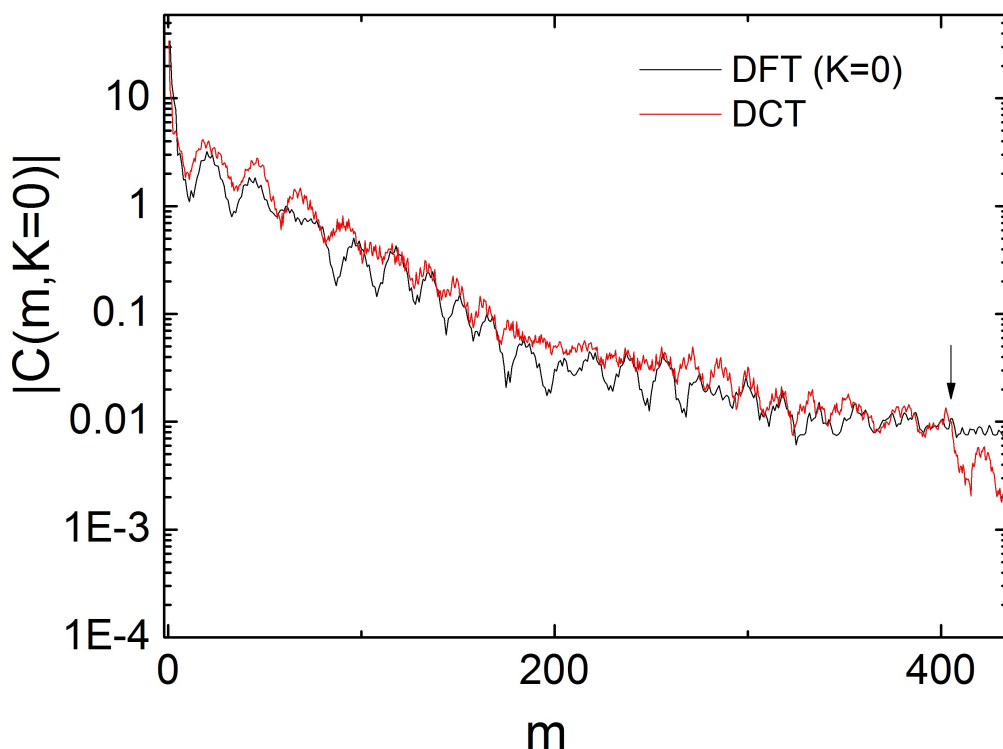
Figure 5.12: The $|C(m, K)|$ spectra corresponding to the DFT and DCT of the CARS input spectra of toluene as shown in fig. 5.11. For $m \leq 400$ (see arrow), more energy is contained in the DCT when compared to that in the DFT ($K = 0$). For the high frequency components ($m > 400$), about a four times higher content is observed in the DFT ($K = 0$). Curves have been smoothed for better visibility.

end-points. This problem is avoided by applying either the DFT MEM-approach with squeezing ($K = 1$), the DCT approach, or the CPCG solver. All three schemes result in the same phase spectrum, revealing sharp narrow bands in the fingerprint region as well as the broad bands in the CH-stretching region on top of a slowly varying error-phase $\phi_{error}(\nu, K)$. In fig. 5.13 B, the corresponding reconstructed $Im[\chi_{tot}^{(3)}(\nu)]$ spectra calculated according to eq. 3.55 are shown. They all look very similar, except for the DFT case with $K = 0$ at the spectral end-points, where the windowing effect results in an unsatisfactory estimation of the error-phase $\phi_{error}(\nu, K = 0)$, and thus erroneous reconstructed amplitudes for the resonances near the spectral end-points. The reconstructed $Im[\chi_{tot}^{(3)}(\nu)]$ spectrum using the DFT based MEM with squeezing $K = 1$ is identical to those using the DCT- or the CPCG-based approaches. All these three approaches are equivalent in terms of reconstruction performance. It is obvious from fig. 5.13 B that the reconstructed $Im[\chi_{tot}^{(3)}(\nu)]$ spectra and its spontaneous Raman counterpart are not matching. Not only are the peak amplitude ratios wrong (see the CH-stretching region), also the narrow bands appear still dispersive, the center frequencies are slightly red shifted, and negative amplitudes at 505 cm^{-1}, 787 cm^{-1}, 1003 cm^{-1} and 2820 cm^{-1} are observed. Moreover, the entire CH-
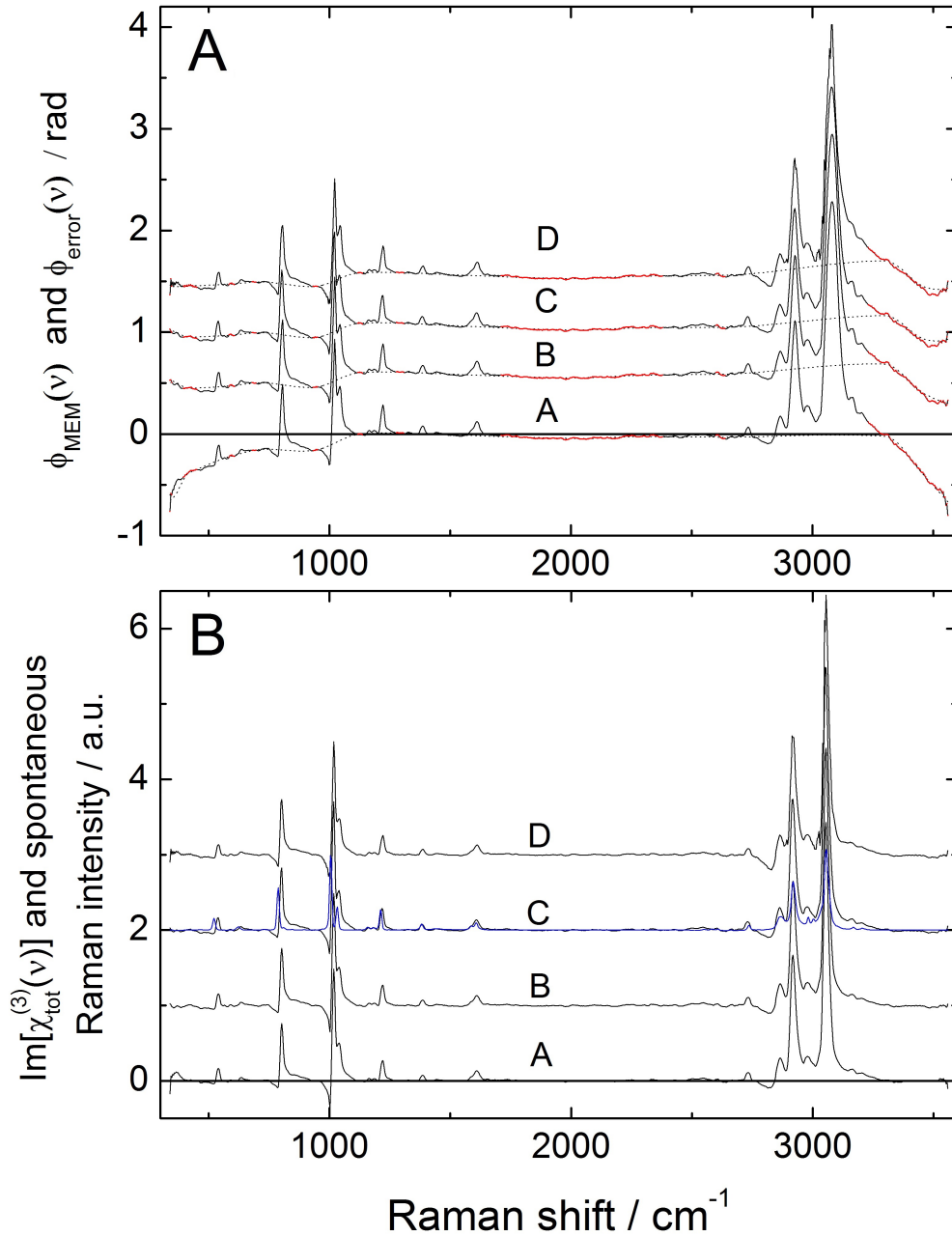
Figure 5.13: (A) Retrieved MEM-phase spectra $\phi_{MEM}(\nu)$ (solid lines) together with the estimated error-phase spectra $\phi_{error}(\nu)$ (dashed lines) and (B) reconstructed $Im[\chi_{tot}^{(3)}(\nu)]$ spectra corresponding to the CARS spectra of toluene as shown in fig. 5.11, using the DFT-based MEM without squeezing ($K = 0$, spectrum A), the DFT-based MEM with squeezing ($K = 1$, spectrum B), the DCT-based MEM (spectrum C), and the CPCG-based MEM (spectrum D). Spectral regions assigned to be off-resonance are highlighted in red. The spectra for the different cases are shifted with respect to each other (A) by 0.5 rad and (B) by 1. Shown in blue is the spontaneous Raman spectrum of toluene for comparison.

stretching region appears distorted, which the error-phase spectra estimations $\phi_{error}(v, K = 0)$ try to compensate by introducing kinks at about 3300 cm^{-1}. In conclusion, this example of toluene illustrates that the removal of the windowing effect in MEM based phase retrieval and the reconstruction with an error-phase estimation according to eq. 3.55 alone do not automatically result in the wanted pure Raman response of the sample. One could easily be mislead of assigning all the spectral components with negative MEM phase values to a non-resonant subset of points $\phi_{NR}(v)$, which are used for the error-phase $\phi_{error}(v, K)$ estimation (see section 3.3.2), resulting in erroneous $Im[\chi_{Res}^{(3)}(v)]$-spectra with underestimated amplitudes and shifted resonance center frequencies!

The solution to this problem is based on the novel concept introduced in section 5.3.3. Briefly, the error-phase $\phi_{error}(v, K)$ is reinterpreted by a physical model for the total nonlinear susceptibility that takes a phase factor $e^{i\phi_{eff}}$ and an effective nonresonant susceptibility $\chi_{E\,eff}^{(3)}$, which are specific properties of the sample, into account! The purely vibrational $Im[\chi_{Res}^{(3)}(v)]$ is then obtained according to eq. 5.36 by using the retrieved MEM-phase spectrum $\phi_{MEM}(v, K)$ instead of the estimated phase spectrum $\phi_{estimated}(v, K)$ directly, and determining ϕ_{eff} and $\chi_{E\,eff}^{(3)}$ via the minimization of the functional given in eq. 5.38. As shown in fig. 5.14 , the reconstructed spectrum of $Im[\chi_{Res}^{(3)}(v)]$ is in good agreement with the corresponding spontaneous Raman scattering spectrum of Toluene. All amplitude ratios almost perfectly match, and the dispersive character and the center frequency shifts of the bands observed in fig. 5.13 B have disappeared. The absolute value of the amplitudes has changed as well. For example, the congested CH-stretching region being resonant from 2820 to 3230 cm^{-1}, unlike as in fig. 5.13, the relative amplitudes now match almost perfectly with those of its spontaneous Raman spectrum. Such good agreement cannot be achieved using the conventional phase retrieval approaches, that use spline or polynomial error-phase estimation schemes.

Fig. 5.15 shows the comparison of the complex $\chi_{Res}^{(3)}(v)$ in a frequency resolved manner using the novel reconstruction concept according to eq. 5.40 (green curve) with the complex $\chi_{tot}^{(3)}(v)$ obtained using the conventional reconstruction approach according to eq. 3.55 (red curve). As can be seen, the conventional reconstruction leads to dispersive line shapes, a real part spectrum not centered around zero, and 'twisted' frequency dependencies where the spectrum leans into the 4th quadrant of the complex plane. Clearly, the new approach is favorable because it directly results in the vibrational response of the sample, $\chi_{Res}^{(3)}(v)$, and in the characterization of the electronic contributions with values of $\chi_{E\,eff}^{(3)} = 1.03$, $\phi_{eff} = 36.1°$ in the fingerprint region and of $\chi_{E\,eff}^{(3)} = 1.33$ and $\phi_{eff} = 4.3°$ in the CH-stretching region. For comparison, using the ratio of maximum to minimum excursions in the retrieved phase spectrum (see section 5.3.2), at 803 cm^{-1}, a value of $\phi_{eff} = 37.8°$ representative for the fingerprint region was determined. When the values for $\chi_{E\,eff}^{(3)}$ are directly extracted from the nonresonant region of the CARS spectrum shown in fig. 5.11, $(\chi_{E\,eff}^{(3)})^2 = 1.06$ is found at 877 cm^{-1}, while $(\chi_{E\,eff}^{(3)})^2 = 1.77$ is found at
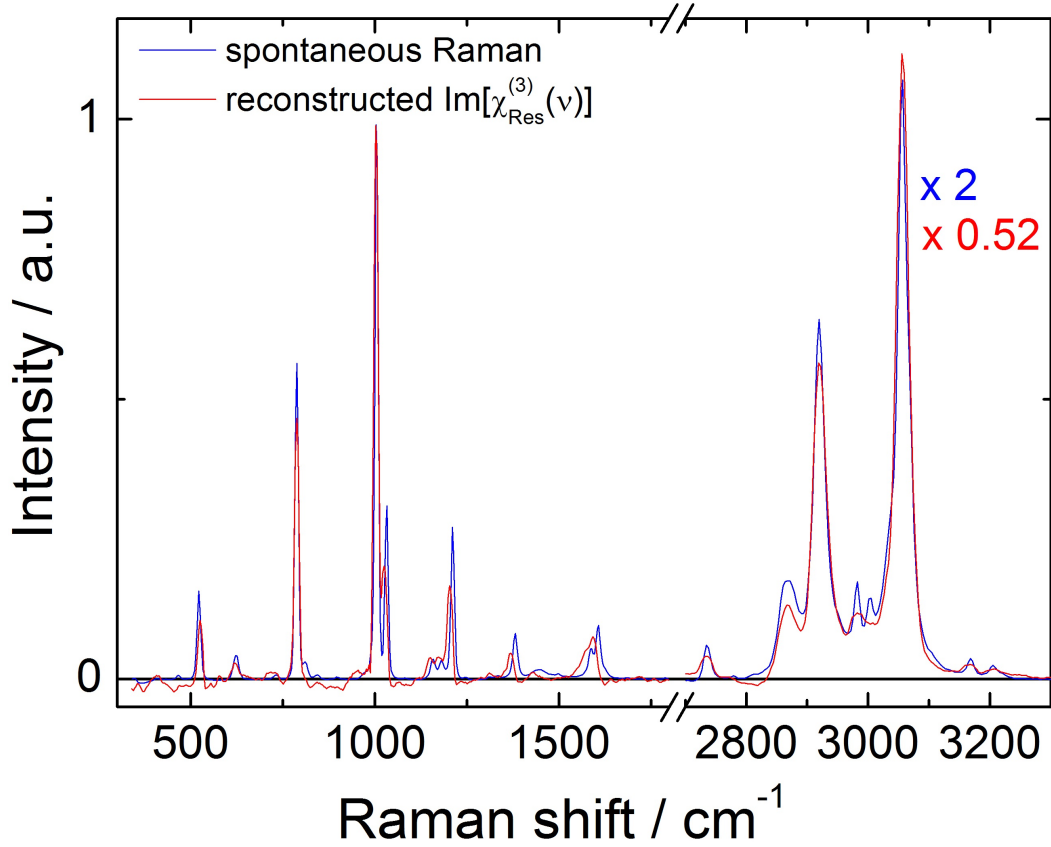
Figure 5.14: Comparison of the reconstructed $Im[\chi_{Res}^{(3)}(\nu)]$ spectrum (red) with the spontaneous Raman scattering spectrum (blue) of toluene. The reconstruction was performed using the DFT based MEM phase with squeezing $\phi_{MEM}(\nu, K = 1)$ (curve B in fig. 5.13 A) and applying eq. 5.40. Subsequent background correction was performed for both spectra using the same set of off-resonant regions. The spectra are normalized to the peak intensities at 1003 cm^{-1} and 3060 cm^{-1} in the fingerprint and CH-stretching regions, respectively.

2703 cm^{-1}. Thus, the $\chi_{E\ eff}^{(3)}$ values directly extracted from the CARS spectra confirm the values extracted from the minimization procedure according to eq. 5.40, and can essentially not be chosen better manually. Being fully unsupervised, the novel concept of reconstructing $\chi_{Res}^{(3)}(\nu)$ using eq. 5.38 and eq. 5.40 is clearly the superior method of choice.

5.5   Summary and Conclusions

In this chapter, three novel strategies for the quantitative analysis of CARS spectra have been introduced.

First, a new approach of calculating the autocorrelation coefficients in the MEM-based retrieval of CARS spectra has been demonstrated. While the reconstruction of an $Im[\chi_{Res}^{(3)}(\nu)]$
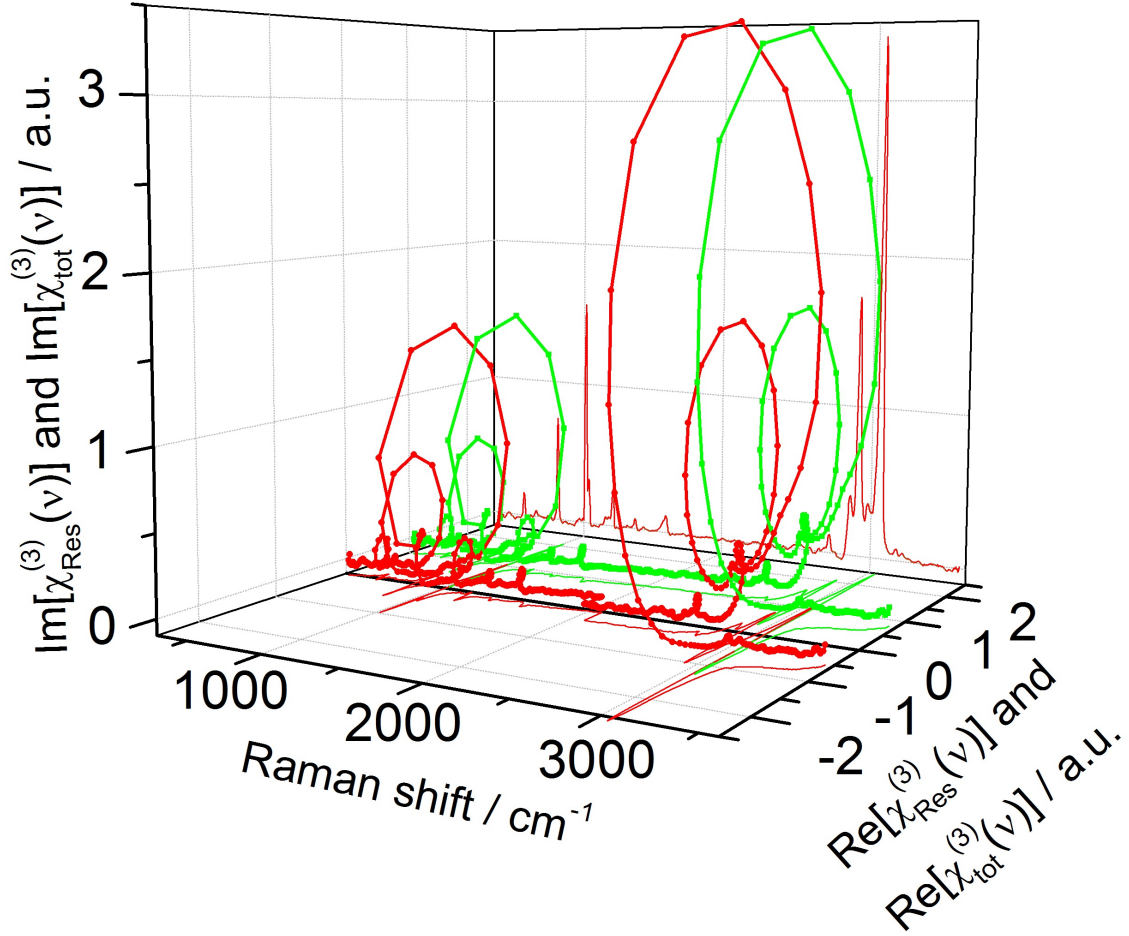
Figure 5.15: The frequency resolved complex $\chi^{(3)}_{Res}(\nu)$ reconstructed from a measured CARS spectrum of neat toluene using the novel reconstruction concept according to eq. 5.40 (green curve) in comparison with the complex $\chi^{(3)}_{tot}(\nu)$ obtained using the conventional reconstruction approach according to eq. 3.55 (red curve).

spectrum based on the novel DCT-based MEM approach has been shown to be identical with that obtained using the conventional DFT-based MEM approach with squeezing, the computation time has been reduced by almost one order of magnitude because only the real parts of the autocorrelation coefficients $C(m)$ are calculated. In conclusion, the proposed DCT-based MEM-phase retrieval combines the speed advantages of the DFT-based MEM-phase retrieval with the advantage of the conventional squeezing of the spectrum, which avoids the windowing problem at the retrieved MEM-phase spectrum end points.

Second, a new Toeplitz solver for the Eigenwert problem in MEM has been successfully implemented. The new circulant preconditioned conjugate gradient (CPCG) based MEM approach has been shown to be faster than the DFT-based MEM with squeezing, and to outperform the DCT-based MEM approach when spectra with more than ≈ 235 samples need to be reconstructed. Its different order of the computational cost makes the CPCG approach better equipped for spectra recorded with higher spectral resolution (more samples), which will be

available in the near future. The CPCG approach then allows performing the MEM-phase retrieval in time spans shorter than the actual acquisition time of a CARS spectrum, thus opening the way towards FPGA-based on-chip CARS spectral analysis!

Third, novel concepts for an unsupervised and quantitative reconstruction of CARS data have been presented, which are summarized by the newly defined functional F_1 (eq. 5.38). As a result, the pure complex vibrational susceptibility $\chi_{Res}^{(3)}(\nu)$ of the sample is obtained via eq. 5.40 together with its third-order electronic susceptibility contributions described by $\chi_E^{(3)}{}_{eff}$ and ϕ_{eff}. Using this novel method, it is not necessary to introduce a frequency-dependent error-phase $\phi_{error}(\nu)$, as is the case in conventional phase retrieval of CARS spectra. In fact, it was shown that the error-phase $\phi_{error}(\nu)$ can be interpreted by the effective phase shift ϕ_{eff} between the pure vibrational response $\chi_{Res}^{(3)}(\nu)$ and the pure electronic response $\chi_E^{(3)}{}_{eff}$ of the sample. When compared with the conventional approach of reconstructing $Im[\chi_{Res}^{(3)}(\nu)]$ from a CARS spectrum (eq. 3.55), the novel concept is superior in cases where the MEM-phase does not return to zero within a given spectral window of the CARS spectrum. The latter can also be caused in a sample with an extreme ratio of $\frac{|\chi_{Res}^{(3)}(\nu)|^2}{|\chi_E^{(3)}{}_{eff}|^2}$. In these cases, the conventional reconstruction approach fails, where the new concept does not. The proposed direct determination of the samples electronic parameters $\chi_E^{(3)}{}_{eff}$ and ϕ_{eff} based on the new concept (eq. 5.38) implies that background contributions to the nonresonant regions within the CARS spectrum are spectrally flat. This means, no fluorescence and more importantly, no windowing at the spectrum end points is allowed. Consequently, only in combination with an approach preventing the windowing problem, such as the newly implementation of the DCT-based MEM approach and the CPCG Toeplitz solver, our novel concept of reconstructing the pure vibrational response of the sample will be feasable in the full spectral range available in the measured CARS spectrum. To my best knowledge, the agreement between our reconstructed Raman response and an independent measured spontaneous Raman scattering spectrum with a level of quality as presented in this chapter is unmatched. Furthermore, we generalized our novel concept of reconstructing the pure vibrational and electronic responses of a molecular sample for mixtures of distinct chemical components that do not interact with each other. By introducing the general form of the functional (eq. 5.53) and the definition eq. 5.52, an unknown species contributing to a mixture can be reconstructed in a quantitative manner, provided prior knowledge about the other mixture components is available. Only in this way, mixtures of several components can be reconstructed in a quantitative manner.

The novel methods developed in this chapter are the prerequisites for the quantitative analysis of CARS spectral experiments presented in chapters 7 and 8.

6 Quantitative mapping of the physical microstructure of thin polymer films

6.1 Motivation

In order to demonstrate the capability of multiplex CARS microscopy to extract the physical structure properties of an unknown molecular sample, we are interested in the physical properties of polymer thin films. The knowledge of their micro-domain structure, its 3D distribution and the size of domains is of high interest for material processing technology. As sketched in fig. 6.1, the polymer chains in a semicrystalline polymer are arranged in ordered phases (crystallites) that are embedded in an amorphous matrix. The chemical structures of the two
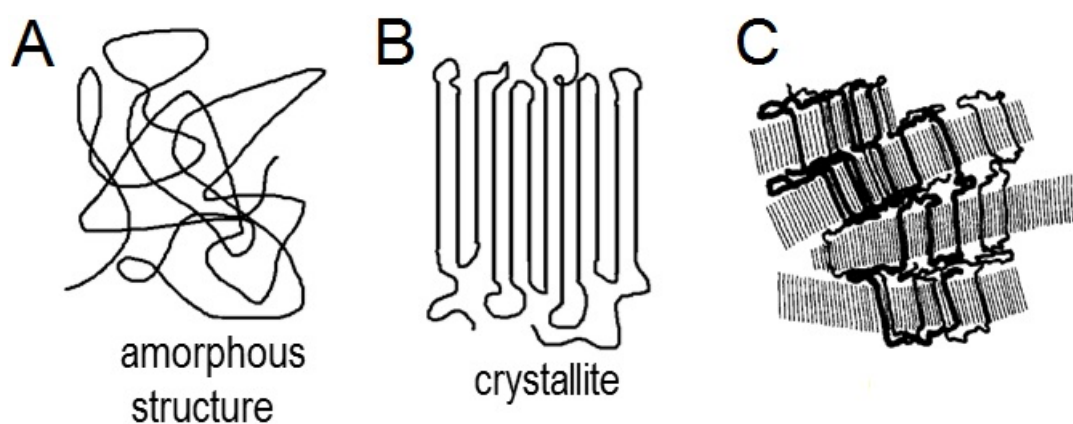
Figure 6.1: Illustration of the arrangement of a polymer macromolecule in amorphous (A) and fully crystalline (B) domains. The combination of both domains results in a heterogeneous micro-domain structure (C). (Taken from [89]).

polymers investigated in this chapter, polypropylene and polyethylene, are given in fig. 6.2. There are several conventional methods to measure crystallinity in polymers. First, there is the differential scanning calorimetry (DSC), where the sample of interest is heated to a certain temperature together with a reference, and the electrical power needed for balancing the temperature of both, sample and reference, is measured. In this way, melting and crystallization of the sample is directly revealed [90]. Consequently, DSC is invasive by nature. It is lacking any
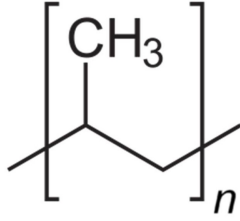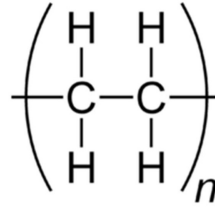
Figure 6.2: Chemical structures of polypropylene and polyethylene.

spatial resolution, and is rather slow with acquisition times in the range of minutes. Then, there is wide-angle X-ray scattering (WAXS) [90], where the crystal structure can be directly determined from the intensity of X-ray bands in a non-invasive manner. However, this technique is again lacking spatial resolution and is rather slow with acquisition times in the range of several minutes [90]. Similar properties hold for conventional NMR spectroscopy, that is noninvasive, but again lacks spatial resolution and is still rather slow with acquisition times in the range of minutes [91]. In contrast, noninvasive Raman scattering microscopy offers sub-micron spatial resolution with acquisition times in the range of 100 ms, when a state of the art confocal Raman microscope is used. Because of the already discussed limitations of spontaneous Raman scattering (see ch. 3), we here exploit the coherent signal enhancement offered by multiplex CARS microscopy in order to demonstrate the high speed 3D mapping of micro-domain structures in thin films of polypropylene (PP) and polyethylene (PE).

In isotropic polymers, characteristic vibrational bands that carry information about the crystallinity, that is a measure for the volume fraction of the polymer macromolecules being in the crystalline phase, needs to be analyzed in order to quantify the 3D micro-domain structure in polymers. Fig. 6.3 shows the reconstructed $Im[\chi_{Res}^{(3)}(\nu)]$ spectra of isotropic polypropylene and polyethylene films in the fingerprint region. In the case of isotactic PP, the two most prominent resonances are at 810 cm^{-1} and 840 cm^{-1}. The resonance at 810 cm^{-1} is assigned to CH_2, C-C and C-CH stretching mode contributions predominantly of the long helical chains present in the crystalline phases, while the resonance at 840 cm^{-1} is assigned to CH_2 rocking and $C - CH_3$ stretching mode contributions predominantly present in the amorphous phase. For polypropylene, we define the normalized amplitude of the 810 cm^{-1} band as follows:

$$c_{PP} = \frac{A(810 cm^{-1})}{\sum_i^n A_i} \; with \; n = 2, 3 \; or \; 4 \, , \tag{6.1}$$

where A_i stands for the peak amplitude of the ith pseudo Voigt (PSV) profile $V_{Pseudo \, i}$ as extracted from the spontaneous or reconstructed Raman spectrum within the Raman shift interval [780 cm^{-1}, 870 cm^{-1}]. In the case of high density PE, the two most prominent resonances are at 1300 cm^{-1} and 1420 cm^{-1} are of interest, which are assigned to the CH_2 twisting mode and to a CH_2

83
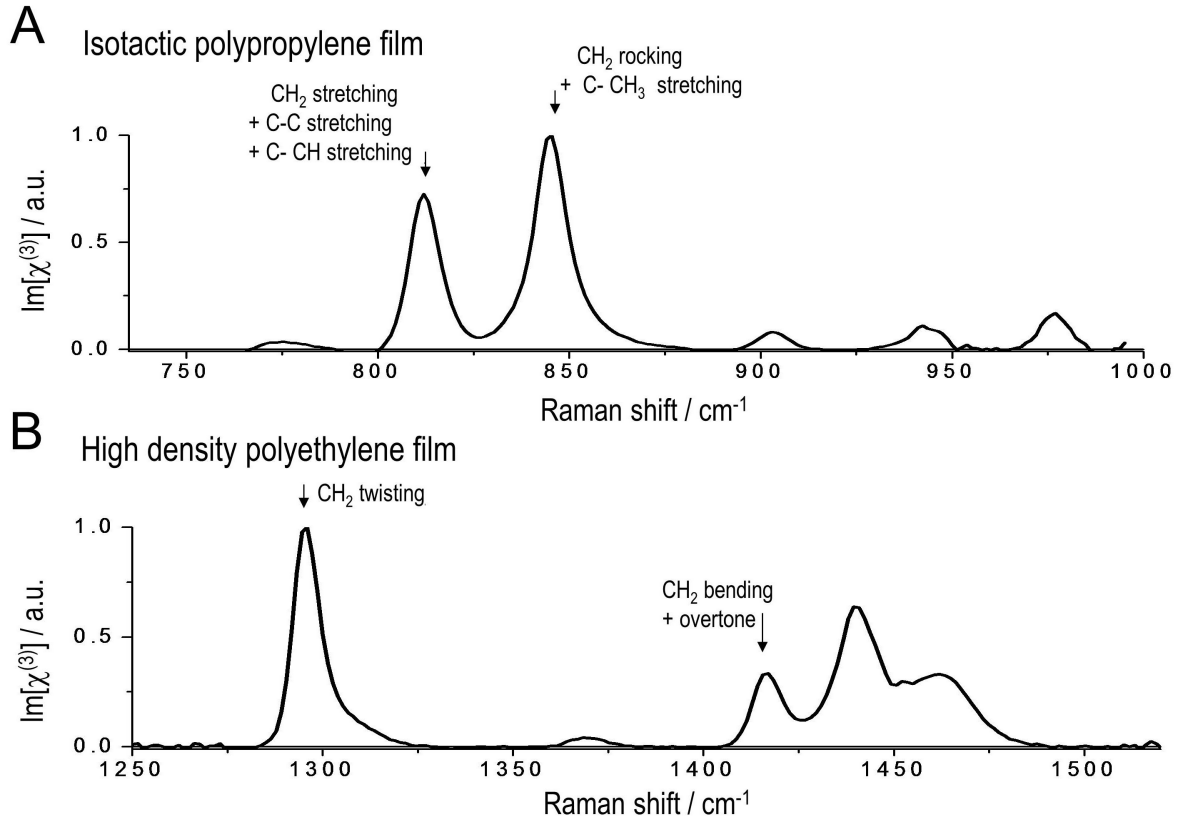
Figure 6.3: Reconstructed $Im[\chi_{Res}^{(3)}(\nu)]$ spectra in the fingerprint region of (A) an isotropic polypropylene film and (B) a high density polyethylene film, as obtained from multiplex CARS measurements.

bending mode with an overtone contribution, respectively. The intensity of the latter arises from the crystalline phases, which leads to the following definition of the normalized amplitude of PE:

$$c_{PE} = \frac{A(1420cm^{-1})}{A(1300cm^{-1})} \,. \tag{6.2}$$

In this chapter, we first evaluate the Raman model for the definition of the normalized amplitude in PP (eq. 6.1). Next, using fast multiplex CARS microscopy, we will demonstrate the 2D mapping of c_{PP} in the isotropic, oriented and necking regions in a drawn PP film, and study the 3D microdomain structures of high crystallinity in isotropic PP and PE. Also, we will evaluate the signal enhancement in CARS by comparing the acquisition times with respect to spontaneous Raman experiments. Finally, we will compare our c_{PP} with crystallinity values obtained using conventional DSC and X-ray techniques for the isotropic PP.

6.2 Materials and methods

6.2.1 Preparation and prior characterization of thin PE and PP films

The preparation and prior characterization of thin PE and PP films were conducted by our collaboration partners, Dr. Goulnara Nikolaeva and Dr. Kirill Prokhorov, at the Prokhorov General Physics Institute, Russian Academy of Sciences, Moscow in Russia. The molecular weights of PE and PP was about 10^5 *Daltons*. Films were fabricated with a force of 50 *kN* at 190 °*C* during 5 *min* and then cooled within 6-7 *min*. Molding conditions were chosen to produce optically transparent films with minimal thickness, which allowed both recording transmission CARS spectra and uniaxial drawing of the films without rupture up to the formation of a necking region. Thicknesses of the non-deformed PP and PE films were about 90 *μm* and 60 *μm*, respectively. The films were drawn on an Instron testing machine at room temperature with the rate of 20 *mm*/*minute*. Non-deformed films were studied by DSC and X-ray analysis. X-ray studies were performed in transmission mode on a DRON-3M diffractometer equipped with an asymmetric quartz monochromator, which focused a primary CuK_α-radiation beam on the detector. X-ray diffraction spectra were recorded in the region of diffraction angles 2Θ ranging from 6 ° to 36 ° in steps of 0.04 °, and an accumulation time of 10 *sec*. Standard procedures where used for the calculation of the degree of crystallinity of PE and PP based on the X-ray spectra, as described in ref. [92] and in ref. [90], respectively. In both cases absolute errors are less than 5 %. Thermal characteristics of the samples were recorded on a DSC 30 calorimeter with TC-15 processor and STAR SW 8.00 Mettler software. Experiments were carried out in nitrogen atmosphere in heating – cooling – heating mode with rates of 10 *K*/*min*. Enthalpy of melting of PP with the degree of crystallinity, equal to 100 %, was found to be $\Delta H_m^0 = 165$ *J*/*g*. Enthalpy of melting of PE with the degree of crystallinity, equal to 100 %, was found to be $\Delta H_m^0 = 290$ *J*/*g*.

6.2.2 Spontaneous Raman scattering spectroscopy

Spontaneous Raman scattering data of polypropylene were recorded using the setup described in section 4.1. The full laser power of 37 *mW* was focussed using the 100x objective in combination with the 25 *μm* fibre and the 1800 *lines*/*mm* grating. The spatial scanning step size was set to 400 *nm*. The integration time was 2 *s* per spectrum. The spectra were background corrected in the region 775.5 cm^{-1} - 885.1 cm^{-1} using a second order polynomial function as described in section 3.3.2.1. In order to increase the SNR for establishing the best fit model, the averages of 1600 spectra recorded in both the oriented and isotropic regions of PP were analyzed. Both mean spectra then were globally fit. The fit model used is described by a linear combination of up to four Lorentzian bands (eq. 4.9) with $\mu_i = 1$ ($i = 1 \ldots 4$). Concerning the

weak bands centered at 825 cm^{-1} and 838 cm^{-1}, all line shape parameters were shared except the amplitudes. For the resonances centered at 810 cm^{-1} and 840 cm^{-1}, all line shape parameters were allowed to vary freely.

6.2.3 Multiplex CARS microscopy

For the fast mapping of c_{PP} and c_{PE} in PP and PE films, respectively, the multiplex CARS setup with the configuration E2-D1 (see fig. 4.1) was used. To probe the vibrational range of interest for PP, the broadband Stokes pulse was centered at λ_{Stokes} = 828.3 nm and the narrowband pump pulse was centered at λ_{Pump} = 775.1 nm. Different regions of interest within the isotropic, the oriented and the necking regions of one and the same drawn PP film were imaged. In the oriented and isotropic regions in PP, the dimensions of the scan areas were 50 $\mu m \times$ 33 μm (100 pixel $\times$ 66 pixel) with a scan step size of 500 nm, the laser powers were 20 mW and 10 mW for the pump and Stokes beam, respectively, and the pixel integration time was 20 ms. In the necking region of PP, the dimension of the scanned area was 100 $\mu m \times$ 10 μm (250 pixel $\times$ 25 pixel) with a scan step size of 400 nm, the laser powers were 40 mW and 20 mW for the pump and Stokes beam, respectively, and the pixel integration time was 50 ms. For performing CARS in the vibrational range of interest for PE, the Stokes pulse was centered at λ_{Stokes} = 868.3 nm and the pump wavelength was centered at λ_{Pump} = 775.1 nm. For the isotropic region in PE, the dimension of the scanned area was 20 $\mu m \times$ 20 μm (50 pixel $\times$ 50 pixel) with a scan step size of 400 nm, the laser powers were 40 mW and 20 mW for the pump and Stokes beam, respectively, and the pixel integration time was 50 ms. For the 3D mapping of c_{PE} in PE, the dimensions of the scanned volume were 50.4 $\mu m \times$ 1.5 $\mu m \times$ 12.1 μm (100 pixel $\times$ 4 pixel $\times$ 31 pixel) with a scan step size of 504 nm, the laser powers were 40 mW and 20 mW for the pump and Stokes beam, respectively, and the voxel integration time was 50 ms. For the 3D mapping of c_{PP} in PP, the multiplex CARS setup with the configuration E2-D2 (see fig. 4.1) was used. Here, the dimensions of the scanned volume were 33.3 $\mu m \times$ 33.3 $\mu m \times$ 10 μm (100 pixel $\times$ 100 pixel $\times$ 30 pixel) with a scan step size of 333 nm, the laser powers were 33 mW and 12 mW for the pump and Stokes beam, respectively, and the voxel integration time was 670 μs.

With all vibrational bands of interest having a SNR much higher than one, the reconstructed $Im[\chi^{(3)}]$ data were denoised using SVD with six singular values σ = 6 (see appendix A.4.1). A two band pseudo Voigt fit model (see eq. 4.9 in section 4.5.1) was used to extract the peak amplitudes for each spectrum. The c_{PP} and c_{PE} values are then calculated as peak ratios according to eq. 6.1 and eq. 6.2, respectively.

6.3 Evaluating the Raman model for the definition of c_{PP} in polypropylene

As shown by Nielsen et. al. [93], the two main resonances at $\approx 810\ cm^{-1}$ and $\approx 840\ cm^{-1}$ (see fig. 6.3 A) appear during solidification of a polypropylene melt as a result of a splitting of a broad resonance centered at $\approx 830\ cm^{-1}$ that is assigned to a melt-like amorphous phase. Consequently, three phases are distinguished: a crystalline phase (helical chains within crystals, represented by the resonance at $\approx 810\ cm^{-1}$), an atactic melt-like phase (represented by the resonance at $\approx 830\ cm^{-1}$), and an isomeric defect phase (short chains in helical conformation, represented by the resonance at $\approx 840\ cm^{-1}$). Fig. 6.4 shows the spontaneous Raman spectra of isotropic and oriented PP together with the global fit result based on three Lorentzian bands. The extracted fit parameters are summarized in tab. 6.1. The three resonances centered at 809.1 cm^{-1}, 833.5 cm^{-1} and 842.1 cm^{-1} have been clearly resolved. Using eq. 6.1 and these three resonances, we obtain:

$$c_{PP}^{3\ bands} = \frac{A(809.1cm^{-1})}{A(809.1cm^{-1}) + A(833.5cm^{-1}) + A(842.1cm^{-1})} \tag{6.3}$$

A close inspection of the residuals in the 830 cm^{-1} region reveals deviations between the fit curve and the experimental data. This observation suggests that the shoulder at $\approx 830\ cm^{-1}$ is composed of at least two bands, and a fourth resonance has to be taken into account when modeling the Raman spectra of PP.

Using a four-band global fit model, a better match with both the isotropic and the oriented PP is achieved, as can be seen in fig. 6.5. As a result, we observe a splitting of the previously identified resonance at $\approx 833.5\ cm^{-1}$ into two resonances centered at 831.4 cm^{-1} and 835.7 cm^{-1}. The corresponding fit results are also summarized in tab. 6.1. A possible assignment for these two weak resonances is based on the resonances observed in syndiotactic polypropylene, where the resonances at 831.4 cm^{-1} and 835.7 cm^{-1} are interpreted as short polymer chains with iterated *gauche-gauche-trans-trans* $(ggtt)_n$ structures for n = 4 and n = 3, respectively [94]. Consequently, the four bands would then be assigned to a crystalline phase (helical chains within crystals, represented by the resonance at 809.1 cm^{-1}), a phase containing $(ggtt)_4$ (represented by the resonance at 831.4 cm^{-1}), a phase containing $(ggtt)_3$ (represented by the resonance at 835.7 cm^{-1}), and an isomeric defect phase (short chains in helical conformation, represented by the resonance at 842.1 cm^{-1}). Using four resonances, eq. 6.1 is recast as:

$$c_{PP}^{4\ bands} = \frac{A(809.1cm^{-1})}{A(809.1cm^{-1}) + A(831.4cm^{-1}) + A(835.7cm^{-1}) + A(842.1cm^{-1})}\ . \tag{6.4}$$

Note, that the resonances at 831.4 cm^{-1} and 835.7 cm^{-1} are very weak, and are only clearly visible in the shown mean spectra obtained with an overall integration time of almost one hour. We can therefore not expect to resolve these weak bands when we use much shorter spectrum
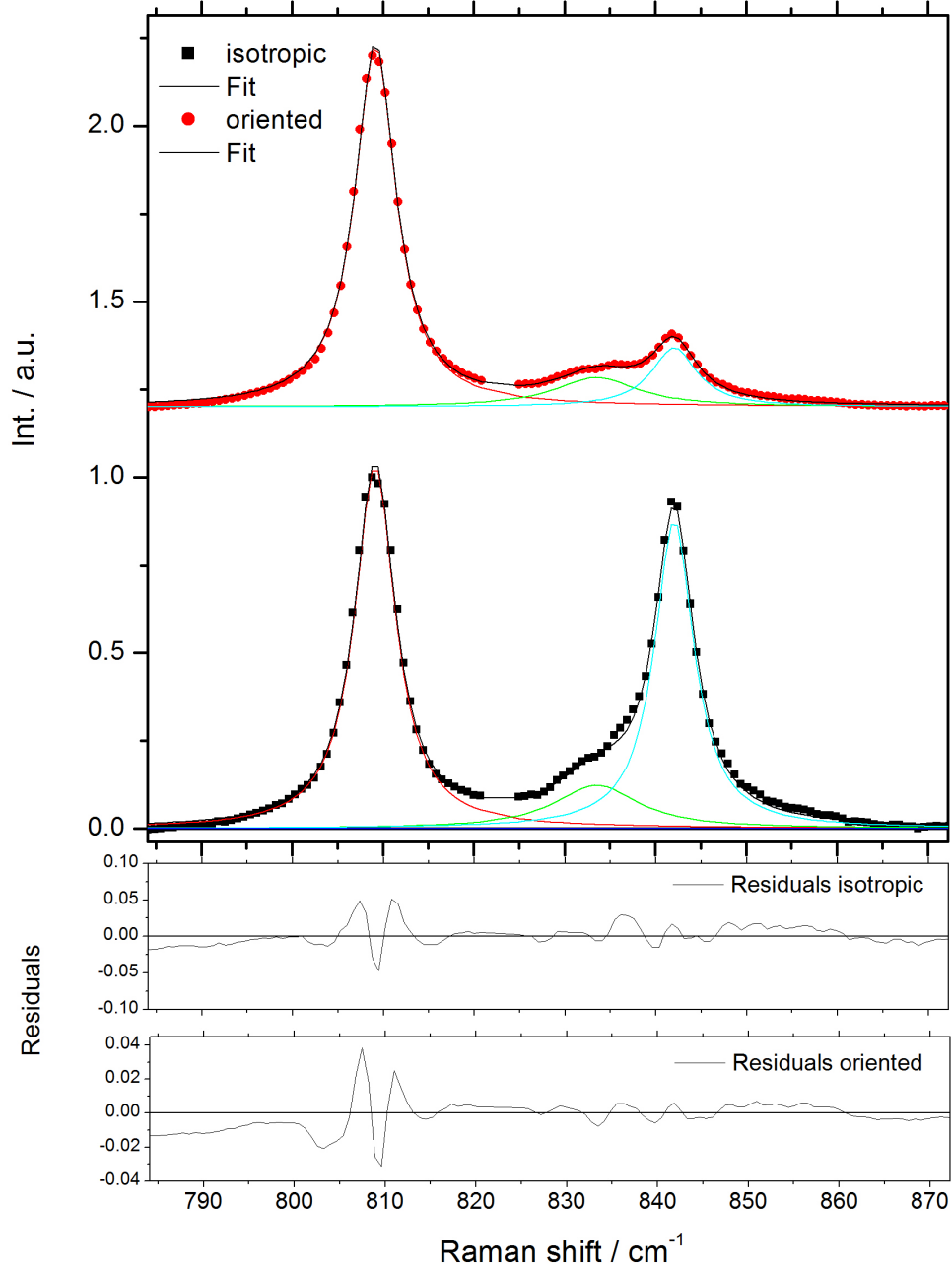
Figure 6.4: Global fit of the spontaneous Raman spectra of isotropic and oriented PP using a three-band fit model (see eq. 4.9 with $\mu_i = 1, i = 1 \ldots 3$).

acquisition times, which results in significantly lower signal to noise ratios with the capability of only resolving the two most intense resonances centered at 809.1 cm^{-1} and 842.1 cm^{-1}. The corresponding fit results are also summarized in tab. 6.1. Using these two resonances only, the c_{PP} defined as:

$$c_{PP}^{2\ bands} = \frac{A(809.1 cm^{-1})}{A(809.1 cm^{-1}) + A(842.1 cm^{-1})} \quad .$$

(6.5)

The calculated normalized amplitudes extracted using the two-, three- and four-band fit models
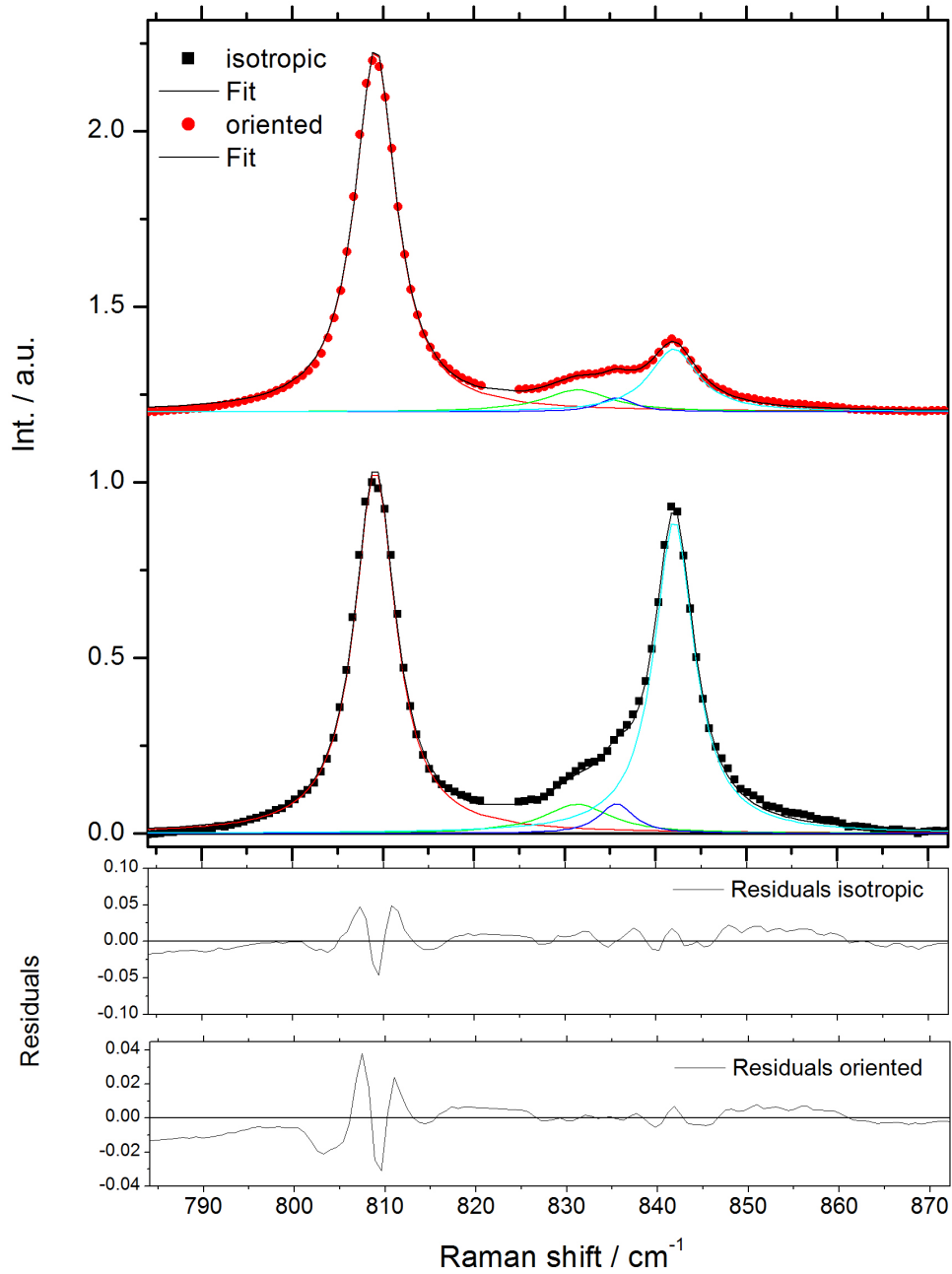
Figure 6.5: Global fit of the same spontaneous Raman spectra of isotropic and oriented PP as shown in fig. 6.4 using a four-band fit model (see eq. 4.9 with $\mu_i = 1, i = 1 \ldots 4$).

according to eq. 6.5, eq. 6.3 and eq. 6.4, respectively, are compared in tab. 6.2. We conclude that the c_{PP} values obtained with the three-band and the more accurate four-band models are identical within the fitting errors. However, the use of the simplified two-band model will yield up to 10 % and 8 % higher c_{PP} values in the cases of isotropic and oriented PP, respectively, thus representing an upper bound for c_{PP}.

Table 6.1: Line shape parameters extracted from global three-band and four-band fit models (see eq. 4.9 with $\mu_i = 1, i = 1 \ldots 4$) of spontaneous Raman scattering spectra of isotropic and oriented PP. (Fit parameters in bold letters are shared).

	Three-band fit model		Four-band fit model		Two-band fit model	
	isotropic PP	oriented PP	isotropic PP	oriented PP	isotropic PP	oriented PP
A_1/cm^{-1}	225.8±0.1	1896.4	227.9	1903.6	228.6	1895.4
$\nu_{0\,1}/cm^{-1}$	809.1±0.1	809.2±0.1	809.1±0.1	809.2±0.1	809.1±0.1	809.2±0.1
Γ_1/cm^{-1}	5.4±0.5	5.5±0.5	5.5±0.5	5.5±0.5	5.5±0.5	5.5±0.5
A_2/cm^{-1}	56.3	316.9	30.2	190.5	225.5	703.9
$\nu_{0\,2}/cm^{-1}$	**833.5±1.0**		**831.4±1.0**		841.9±0.1	840.2±0.1
Γ_2/cm^{-1}	**11.3±2.0**		**9.0±2.0**		6.5±0.5	12.7±0.5
A_3/cm^{-1}	186.0	344.8	15.6	61.7	-	-
$\nu_{0\,3}/cm^{-1}$	842.1±0.1	842.1±0.1	**835.7±1.0**		-	-
Γ_3/cm^{-1}	5.3 ±0.5	6.1±0.5	**4.5±2.0**		-	-
A_4/cm^{-1}	-	-	191.0	388.4	-	-
$\nu_{0\,4}/cm^{-1}$	-	-	842.1±0.1	842.0±0.1	-	-
Γ_4/cm^{-1}	-	-	5.3±0.5	6.5±0.5	-	-
goodness of fit (χ^2)	**0.99784**		**0.99792**		0.99444	

Table 6.2: Comparison of c_{PP} values extracted from spontaneous Raman spectra of isotropic and oriented PP obtained using a two-, a three- and a four-band Lorentzian fit model.

	isotropic polypropylene	oriented polypropylene
$c_{PP}^{2\ bands}$	0.54 ± 0.02	0.86 ± 0.02
$c_{PP}^{3\ bands}$	0.51 ± 0.02	0.80 ± 0.02
$c_{PP}^{4\ bands}$	0.49 ± 0.02	0.79 ± 0.02

6.4 Mapping c_{PP} and c_{PE} by multiplex CARS microscopy

By application of an uniaxial force, the drawn polymer film undergoes a transition from the isotropic state to an oriented state within the so-called necking region that separates the two states from each other, which is illustrated in fig. 6.6. Depending on the actual draw ratio, the transition can occur on a length scale smaller than 50 μm. Thus, high spatial resolution is needed to spatially resolve the changes of the c_{PP} and c_{PE} values across this necking region.

Fig. 6.7 A and B show the 2D maps of c_{PP} in isotropic and oriented regions of one and the same PP film. Here, and for the remainder of the chapter, the two-band model is used for the calculation of c_{PP} values, i.e. $c_{PP} \equiv c_{PP}^{2\ bands}$ for each image pixel according to the definition given in eq. 6.5. For the isotropic region of the polypropylene film shown in fig. 6.7 A,
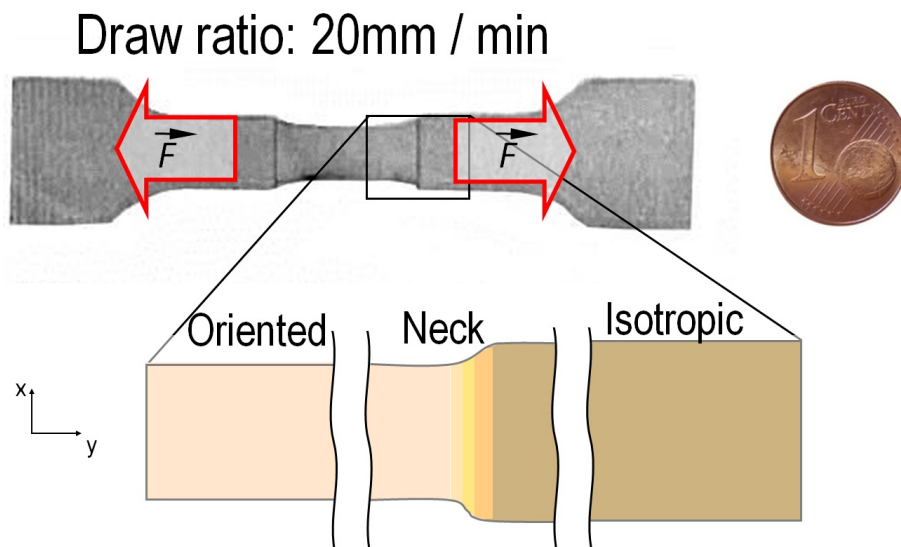
Figure 6.6: Illustration of oriented, necking and isotropic regions in a drawed polypropylene film prepared with a draw ratio of 20 mm/min.
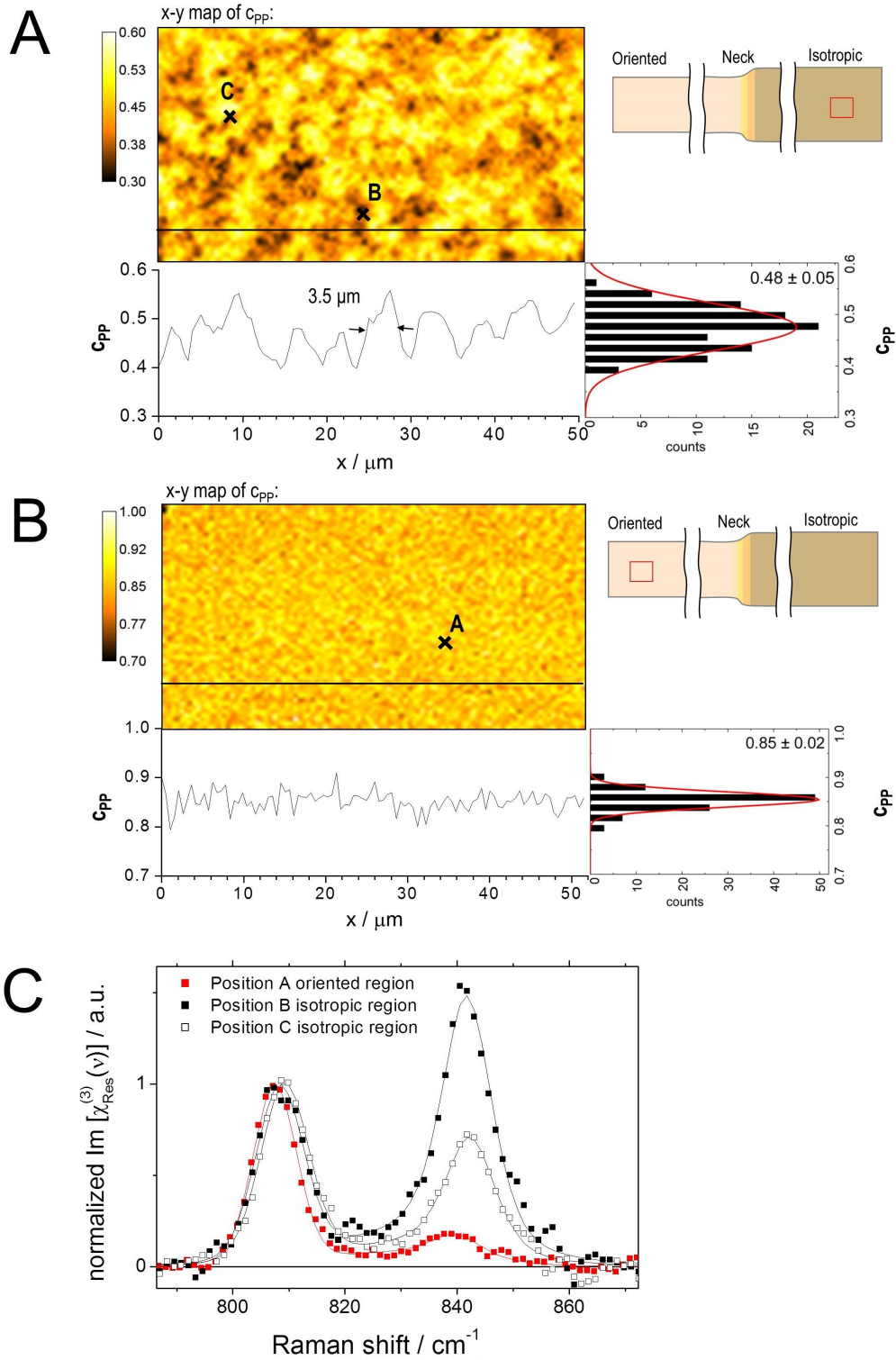
Figure 6.7: c_{PP} maps obtained by multiplex CARS microscopy inside (A) isotropic and (B) oriented regions of a thin PP film as indicated by the inserts. Histograms show the distribution of the c_{PP} values across the indicated line profiles. (C) Comparison of typical reconstructed $Im[\chi_{Res}^{(3)}(\nu)]$ spectra, taken at selected pixels inside the oriented (A) and the isotropic regions (B and C) of PP.

domains with high (position C in the map) and low (position B) c_{PP} values are observed. A lateral profile across the c_{PP} map reveals the average size of these domains to be in the range of 3-4 μm. The distribution of the c_{PP} values along this line profile is centered at $c_{PP} = 0.48$ with a FWHM of 0.1. In the oriented region of the same film of polypropylene, the x-y-map of the c_{PP} appears homogeneous, as is shown in fig. 6.7 B. Its values along the line profile are centered around a mean of $c_{PP} = 0.85$ and distributed within a FWHM of 0.03. Within the diffraction-limited resolution of the setup, no distinct domains are observed. In fig. 6.7 C, the reconstructed $Im[\chi^{(3)}(\nu)]$ spectra taken at positions with low (position B in fig. 6.7 A) and high (position C in fig. 6.7 A) c_{PP} values are shown together with the spectrum from the oriented region (position A in fig. 6.7 B). In fig. 6.8, we are mapping the c_{PP} values in the necking region. When a line profile is plotted across this necking region, we obtain a bimodal distribution, directly revealing the transition from the isotropic to the oriented PP regions. The high c_{PP} distribution inside the
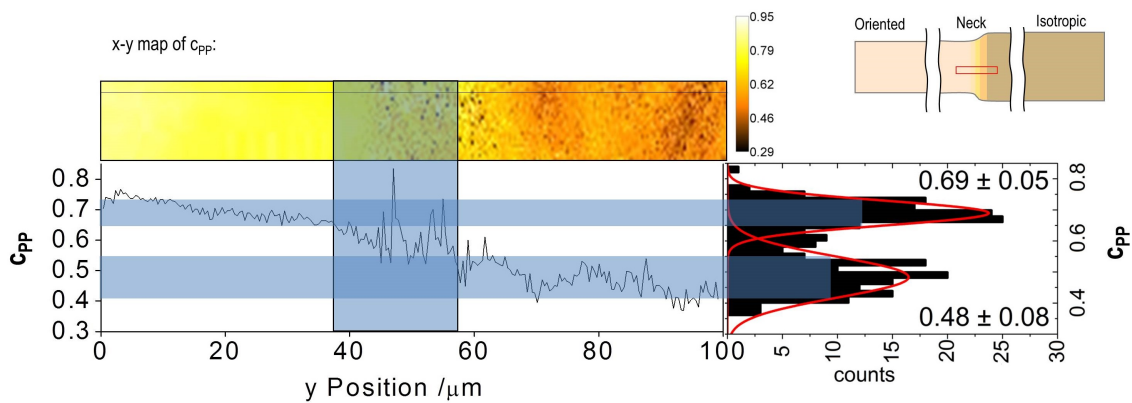
Figure 6.8: c_{PP} map obtained by multiplex CARS microscopy across the necking region of thin PP film prepared with a drawing ratio of 20 mm/min, as indicated by the inset. The histogram shows the bimodal distribution of the c_{PP} values across the indicated line profile.

oriented region is centered at around 0.69 with a FWHM of 0.1, while the low c_{PP} distribution inside the isotropic region is centered at around 0.48 with a FWHM of 0.16. In the isotropic region adjacent to the necking region, the similar c_{PP} values are obtained to those deep inside the isotropic region far away of the necking region. The c_{PP} values obtained in the oriented region adjacent to the necking region however do not match those values obtained deep inside the oriented region far away of the necking region. We observe an asymmetry in terms of how far away from the necking region the c_{PP} values match the values belonging to the limiting cases. By defining the c_{PP} interval between the FWHM values of both sub-distributions as boundaries, the size of the necking region in PP can be determined to be (20 ± 5) μm for this particular draw ratio of 20 $mm/minute$.

So far, all c_{PP} maps shown have been recorded in two spatial dimensions. In order to fully characterize the micro-domain distribution and size, we need to perform multiplex CARS

imaging in all three spatial dimensions. For example, do the microdomains observed inside isotropic polypropylene (fig. 6.7 A) span the whole depth of the PP film? In fig. 6.9 A, the $Im[\chi^{(3)}_{Res}(809.1\ cm^{-1})]$ amplitude reconstructed from a 3D CARS experiment scanning a volume of 33 μm × 33 μm × 10 μm inside isotropic polypropylene film is shown. When passing from
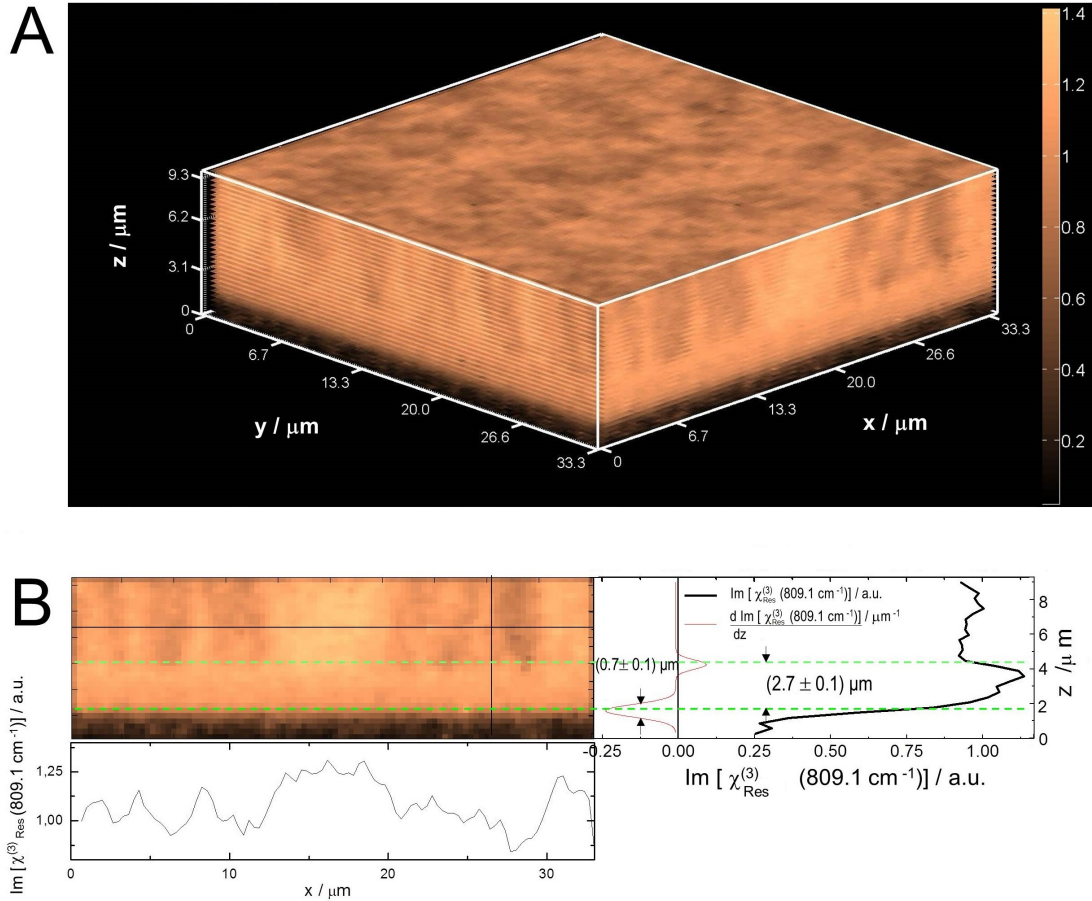
Figure 6.9: (A) 3D-mapping of the $Im[\chi^{(3)}_{Res}(809.1\ cm^{-1})]$, as extracted from fast multiplex CARS microscopy of an isotropic PP film embedded in water. (B) Corresponding x-z-cross-section of the $Im[\chi^{(3)}_{Res}(809.1\ cm^{-1})]$ amplitudes shown together with line profiles along the x- and z-axis, revealing column like structures of increased amplitudes perpendicular to an interfacial layer with homogeneous high amplitudes of thickness (2.7 ± 0.1) μm. This PP-water interface is used to determine the spatial resolution of our multiplex CARS experiment along the z-dimension, which was extracted to be (0.7 ± 0.1) μm from the derivative curve $\frac{d(Im[\chi^{(3)}_{Res}(809.1\ cm^{-1})])}{dz}$.

the inside of the PP film at the top to the PP-water interface at the bottom, vertical domains with high or low $Im[\chi^{(3)}_{Res}(809.1\ cm^{-1})]$ amplitudes are observed. However, close to the interface, a horizontal layer of an increased and constant $Im[\chi^{(3)}_{Res}(809.1\ cm^{-1})]$ amplitude is observed. Passing through the polypropylene interface into bulk water, the amplitude diminishes to zero. In fig. 6.9 B, an amplitude map is shown for a x-z-cross-section plane of the data shown in

fig. 6.9 A together with the line profiles along the x- and z-dimensions. We can use the plotted amplitude profiles along the z-dimension to measure the thickness of the observed interfacial layer as well as the longitudinal spatial resolution of our experiment. The fit of the derivative of the amplitude profile along the z-axis provides the longitudinal resolution, which amounts to $(0.7 \pm 0.1)\,\mu m$, and the thickness of the interfacial layer of $(2.7 \pm 0.1)\,\mu m$. The high longitudinal resolution is a result of the confocal CARS detection scheme using a single-mode fibre with 4 μm core diameter (see section 4.2).

In the next step, the c_{PP} values are calculated for each voxel using eq. 6.5. In order to visualise the 3D microstructure of high- and low-c_{PP} domains, fig. 6.10 A shows the iso-surface at $c_{PP} = 0.57$, which is separating the high-c_{PP} domain enclosured from the low-c_{PP} domain. Here, we can clearly observe the vertical structures inside the isotropic polypropylene that seem
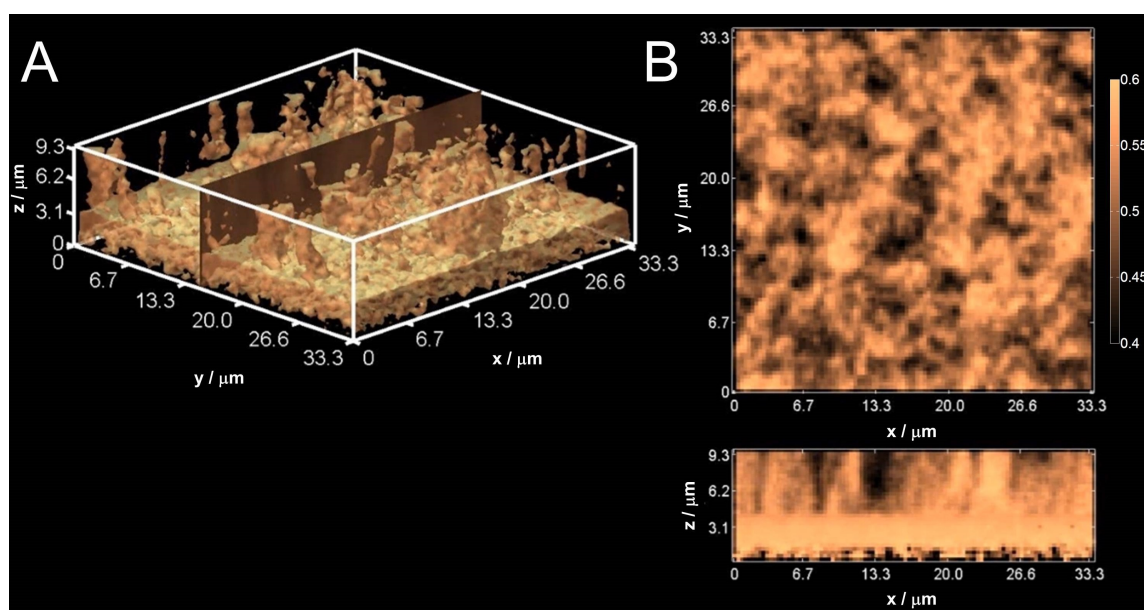
Figure 6.10: Calculated 3D-structure of c_{PP} for the same data set of isotropic polypropylene film shown in fig. 6.9. (A) The iso-surface contouring $c_{PP} = 0.57$ is shown. (B) 2D c_{PP}-maps are shown for representative x-y- and x-z-cross-section-planes.

to sit on top of the horizontal layer of constant and high c_{PP} values at the interface to water. When the 3D-microstructure of c_{PP} is analyzed layer by layer, starting in the x-y-plane inside the isotropic part at the top, the high-c_{PP} domains are directly visualized, as can be seen by fig. 6.10 B. These structures disappear until approximately 500 nm above the interfacial layer of high-c_{PP} values. The mean has values around $c_{PP} = 0.59$ inside the interfacial layer, and decreases with entering deeper into the film. Approximately 3 μm above the interfacial layer, the mean c_{PP} value stabilizes at $c_{PP} = 0.51$. When the x-z-cross-section layers are analyzed, the vertical structures and the interfacial layer with constant and high-c_{PP} values can be observed directly (fig. 6.10 B). Thus, the interfacial layer identified in the amplitude map in fig. 6.9 B can now directly be assigned to the homogeneous interfacial layer in the c_{PP} map!
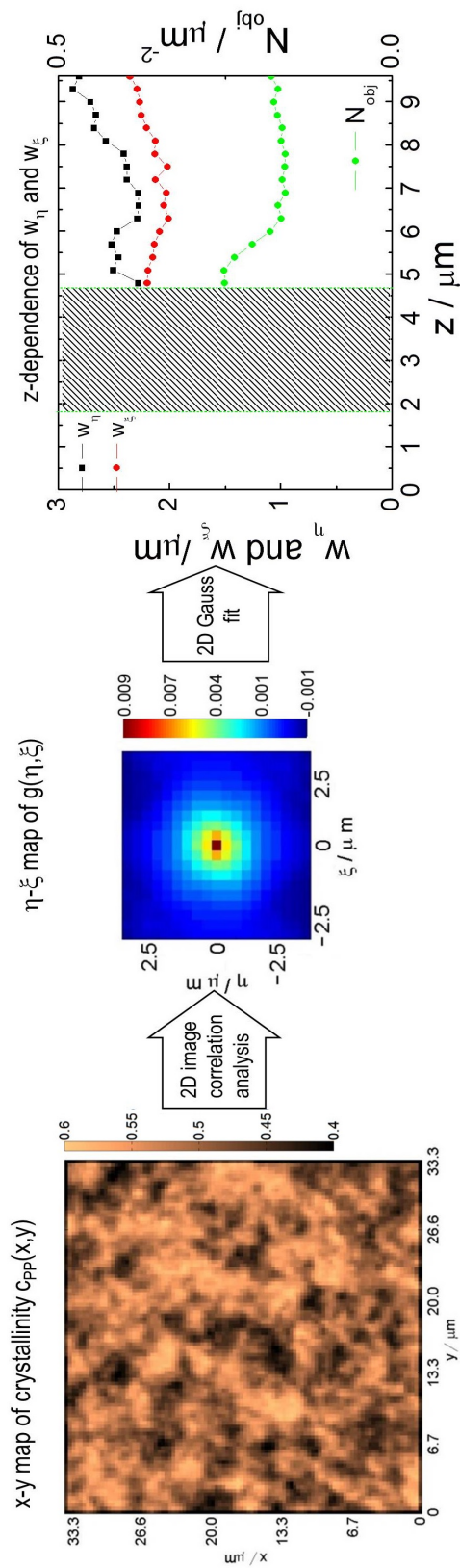
Figure 6.11: 2D image correlation analysis in the x-y-plane of the 3D c_{PP} data of isotropic PP above the interfacial layer (shaded region) shown in fig. 6.10 B. The 2D Gaussian fit (eq. 4.13) to the 2D autocorrelation function $g(\eta, \xi)$ calculated using eq. 4.11 results in the average domain sizes and number densities of the identified high-c_{PP} domains as a function of the z-dimension (see text for details).

In order to adress the question, whether birefringence effects in the polypropylene film influences the calculated c_{PP} maps, the corresponding map of the $\chi^{(3)}_{NR}(x, y, z)$ values, which were extracted from the same $\chi^{(3)}(x, y, z)$ data set, were generated (data not shown). Since no microstructure in the $\chi^{(3)}_{NR}(x, y, z)$ map has been observed, we can conclude that only vibrational resonant features cause the observed microdomain structure of c_{PP}, and birefringence artifacts can be excluded. A possible explanation for the existence of the horizontal interface layer of high c_{PP} values could be the high density of crystallization germs at the beginning of the cooling of the PP film (personal communication by Prof. Eduard Oleinik, Semenov Institute of Chemical Physics, and Dr. Goulnara Nikolaeva, Prokhorov General Physics Institute, Russian Academy of Sciences, Moscow in Russia.).

In order to quantify the 3D distribution of the domain sizes, image correlation analysis of the 2D c_{PP}-maps has been performed for the stack x-y-image sections above the homogeneous interfacial layer. As shown for the x-y-maps in fig. 6.11, the autocorrelation amplitude of the c_{PP}-map is calculated and then fitted with a 2D Gaussian model (eq. 4.13). In this way, the average domain size $w_\eta(z)$ and $w_\xi(z)$ and number density $N_{obj}(z)$ of domains are obtained as a function of z for all $z > 4.5\ \mu m$. No trends along the z-direction are observed for the extracted average domains with the mean value of $\langle w_\eta(z) \rangle = (2.5 \pm 0.2)\ \mu m$ and $\langle w_\xi(z) \rangle = (2.2 \pm 0.1)\ \mu m$, which suggests slightly elliptical domains in the x-y cross-section. The average number density $N_{obj}(z)$ of micro-domains is decreasing with increasing z and stabilises around $z = 6\ \mu m$. The mean value of the density $\langle N_{obj}(z) \rangle$ is $(0.19 \pm 0.03)\ \mu m^{-2}$.

It is interesting that the observed column micro-structures in PP also have been observed in thin PE film. Here, $Im[\chi^{(3)}_{Res}(\nu)]$ spectra reconstructed from multiplex CARS microscopy data using the definition of c_{PE} of PE (eq. 6.2) have been used. In the 2D c_{PE}-map of PE shown in fig. 6.12 A, micro-domains can be observed that are very similar to the ones observed for isotropic polypropylene. The lateral line profile reveals again domains with a mean size of $\approx 2\ \mu m$. The vertical structures that can be observed in the 3D c_{PE}-map of the same sample (fig. 6.12 B) are very similar to the ones observed for polypropylene. The column micro-structures span the measured scan depth of the PE film, which extends over more than $12\ \mu m$.

For the specific cases of isotropic PP and PE, we can directly equate the normalized amplitudes c_{PP} and c_{PE} as defined by eq. 6.1 and eq. 6.2, respectively, to the degree of crystallinity [95],[96], and can compare the crystallinity values obtained by CARS with the reference measurements using the DSC technique, the X-ray technique, and spontaneous Raman scattering. For isotropic PP, very good agreement between the crystallinity values obtained by CARS (c_{PP} = 0.48 ±0.02) with those obtained by spontaneous Raman scattering (c_{PP} = 0.54 ±0.02), is obtained. This result is expected since the spontaneous Raman spectrum and the $Im[\chi^{(3)}_{Res}(\nu)]$ spectrum reconstructed from multiplex CARS yield one and the same Raman response of the sample. The degree of crystallinity of an isotropic PP film of identical preparation history, as

x-y map of c_{PE}:
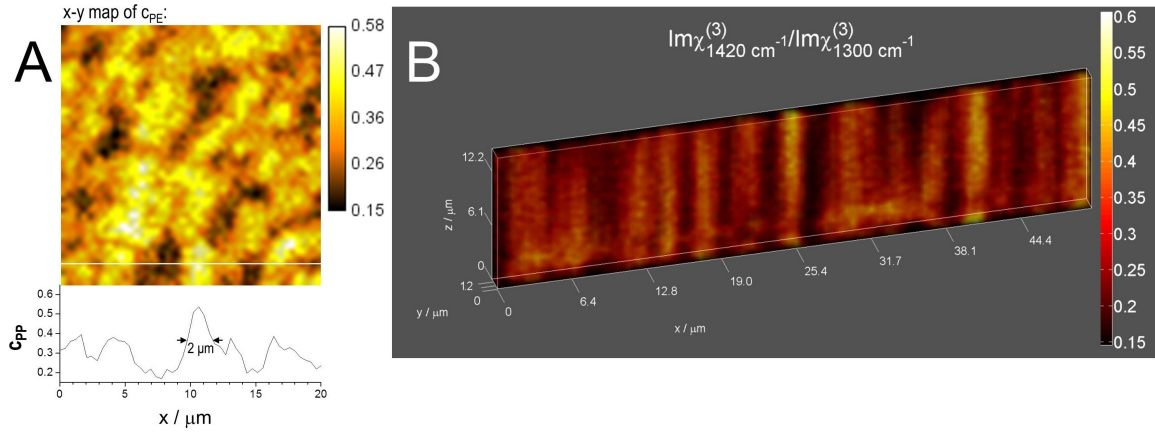
Figure 6.12: (A) 2D c_{PE}-map in the x-y plane and the lateral crystallinity profile along the indicated line of a thin isotropic polyethylene film, as obtained from $Im[\chi^{(3)}_{Res}(\nu)]$ spectra reconstructed from multiplex CARS spectroscopy and the definition of c_{PE} (eq. 6.2). (B) 3D imaging of c_{PE} of the same sample, also revealing column like structures of high c_{PE} perpendicular to the plane of the film.

measured by the DSC technique, amounts to $c_{PP} = 0.69 \pm 0.03$, whereas the degree of crystallinity measured by an X-ray experiment amounts to $c_{PP} = 0.65 \pm 0.03$. Both values coincide within their error bars. However, when compared with Raman-based techniques, DSC and X-ray yield systematically higher values. This has been previously observed by Nielsen et. al. [93], who introduced a scaling factor of 0.93, relating the crystallinity obtained by spontaneous Raman scattering using eq. 6.3 with the crystallinity obtained by DSC. Based on our experimental values, we obtain a corresponding scaling factor of 0.78. Taking into account that the crystallinity values obtained by a two-band Raman model represent an upper bound (see the discussion in section 6.3), we obtain a scaling factor of 0.71.

6.5 Summary and Conclusions

Multiplex CARS microspectroscopy in combination with the reconstruction of the $Im[\chi^{(3)}_{Res}(\nu)]$ Raman response has been demonstrated to be capable of extracting physical structure information in polymers in a label-free and quantitative manner.

In the case of PP, a careful re-examination of the signature Raman bands with high signal to noise ratios in the [780 cm^{-1}, 870 cm^{-1}] range using spontaneous Raman data resulted in both a refined four-band Raman model and a revised definition of the crystallinity in isotropic PP. This careful evaluation revealed a fourth resonance in the spectral range of interest for crystallinity determination of polypropylene that is poorly discussed in literature. As a consequence, the conventional use of a simplified two-band Raman model yields 10 % higher crystallinity values representing an upper bound for Raman-derived crystallinity values in isotropic PP. The crys-

tallinity values obtained using CARS agreed very well with those obtained using spontaneous Raman scattering.

In this application of quantitative multiplex CARS microscopy, we have demonstrated the noninvasive 2D and 3D visualization of the physical micro-structure in polymers with sub-μm spatial resolution in all three spatial dimensions. High and low crystalline micro-domains have been resolved with 330 nm lateral and 700 nm longitudinal spatial resolution in isotropic PP films. This example also demonstrates the enhancement of the SNR, when CARS and SR are compared. Using CARS and the smallest possible readout times of our CCD camera of 670 μs, we still obtain a signal to noise of SNR = 20. Using confocal spontaneous Raman scattering, the same SNR is obtained for pixel dwell times of 800 ms. The enhancement factor turns out to exceed 1000! The stack shown in fig 6.9 consists of image slices, each with 100 pixel $\times$ 100 pixel. Using multiplex CARS imaging, the acquisition per slice takes only 7 seconds. In a spontaneous Raman experiment, this would take almost 2 h! The stack shown consists of 31 slices! Thus, multiplex CARS microscopy offers fast mapping due to short pixel spectrum acquisition times in the sub-ms range.

The new CARS method was applied to spatially resolve the polyolefin deformation in a thin PP film prepared with a drawing ratio of 20 mm/min. As such, 2D maps of the normalized 810 cm^{-1} resonance amplitude revealed μm-sized domains of increased crystallinity in isotropic PP, a homogeneous and high amplitude in oriented PP, and the size of the necking region with a continous transition between the values obtained in isotropic and oriented PP to be $(20 \pm 5)\,\mu m$.

Fast 3D crystallinity imaging has been demonstrated in isotropic PP and PE, revealing both an horizontal interfacial layer of high molecular order at the boundary of the isotropic PP film and extended vertical domains of high crystallinity being orthogonal to it. 2D image correlation analysis of the latter revealed almost equal average domain sizes in the horizontal x and y dimensions, and extended structures along the vertical z-dimension, suggesting the existence of near-cylindrical domains of high crystallinity spanning the whole depth of the polymer film. This observation is an unexpected result, which asks for further investigations into the polymer growth dynamics.

Finally, the crystallinity values obtained for isotropic PP have been compared with DSC and X-ray measurements performed by our collaboration partners. Using a literature value provided by Nielsen et. al. [93] for rescaling the crystallinity values obtained using DSC and X-ray measurements, in the case of polypropylene qualitative agreement with the crystallinity values obtained by CARS was achieved.

The results presented in this chapter demonstrate that multiplex CARS imaging is highly sensitive to the physical structure of polymers, and allows studying their 3D micro-domain structure in a fast and noninvasive way on the sub-μm length scale. To the best of our knowledge, besides multiplex CARS spectroscopy, no other method is capable of mapping physical

structure parameters of macromolecular samples, such as the crystallinity of polymers with such high acquisition speeds and 3D spatial resolution, as demonstrated in this chapter.

7 Quantitative chemical structure analysis of lipids

This chapter demonstrates the capability of CARS microspectroscopy of quantitative and non-invasive analysis of the chemical structures of biologically relevant lipids. The results of this chapter serve as a prerequisite for the chemical identification of lipids in complex and heterogeneous systems, such as living cells, which will be the subject of ch. 8. In this chapter, first the investigated biological lipids will be introduced. Particular emphasis is put on the specific Raman spectral signatures that represent the chemical structures of the lipid molecules. It will then be shown that structural properties can be distinguished based on the spontaneous Raman spectra, and that the same discriminations and conclusions based on these can be drawn from reconstructed $Im[\chi_{Res}^{(3)}(\nu)]$ spectra, obtained from CARS spectroscopy. Finally we will then demonstrate that the results obtained by spontaneous Raman and reconstructed $Im[\chi_{Res}^{(3)}(\nu)]$ in a non-invasive manner agree well with the corresponding chemical analysis results obtained by the gold standard in lipidomics that is mass spectroscopy.

7.1   The lipids of low density lipoproteins

The regulation of lipids and cholesterol in the human body is of great interest in various fields of medicine, such as atherosclerosis, thrombosis, vascular biomedicine and lipidomics. The lipid biochemistry of the living cell involves the uptake of fatty acids (FAs), triglycerides (TAGs), phospholipids (PLs), cholesterol (Chol) and esterified cholesterol (cholesterylesters, CEs). The lipid biochemistry involves the lipid transportation from one compartment within the cell to another and the biochemical reactions that modify their molecular structures. Typical reactions of those lipids are enzyme driven elongation or shortening of their acyl chains, by using for example elongase, and changes in their degree of acyl chain unsaturation by using reductase and desaturase, or by non-enzymatic oxidisation [97]. Concerning Chol and CEs, the typical reaction is their oxidisation resulting in a whole set of oxysterols. Being insoluble in water these lipids are stored and transported as lipoprotein particles. Lipoprotein particles are distinguished by their density and their diameters ranging from 10 to 1000 *nm*. The density ranges

from 0.95 to 1.006 g/ml for very low density lipoprotein (VLDL, diameter of $\approx$ 30-70 nm), from 1.006 to 1.063 g/ml for low density lipoprotein (LDL, "bad" cholesterol, diameter of $\approx$ 20-25 nm) and from 1.063 to 1.21 g/ml for high density lipoprotein ("good" cholesterol, HDL, diameters of $\approx$ 8-11 nm) [98]. In the human body, LDL particles are essential in the transport of Chol, for example from the liver to the body tissue. An LDL particle consists of a water insoluble core (containing approximately 3000 lipid molecules, [97]), which is surrounded by a water soluble monolayer of phospholipids. The detailed composition of a LDL shell is as follows: Approximately 700 phospholipid molecules [99] that encompass phosphatidylcholine (PC, about 450 molecules/LDL particle), sphingomyelin (SM, about 185 molecules/LDL particle), and 80 molecules of lysophosphatidylcholine (lyso-PC) [99]. Embedded is an APOB-100 apoprotein that has 4536 amino acid residues [97]. Additionally, the shell contains unesterified Chol (UC). Literature values for the number of UC molecules in the shell differ: While in ref. [99] 600 UC molecules are assigned to the shell, ref. [100] assignes 400 UC molecules to the shell and 200 to the core. The detailed composition of a LDL core is as follows: 170 TAG and 1600 CE molecules [99] with some of these molecules penetrating into the monolayer shell [97], 200 molecules of UC [100], 10 molecules of phosphatidylethanolamine (PE) [101], 7 molecules of diacylglycerol (DAG) [102], 2 molecules of ceramide (CER) [103] and some phosphatidylinositol [104]. Besides lipids, LDL particles also carry lipophilic antioxidants: 6 molecules of K-tocopherol and traces of Q-tocopherol, carotenoids, oxycarotenoids and ubiquinol-10 [99]. The schematic arrangement of the main constituents of an LDL particle of 20 nm diameter at a temperature above the phase transition of the core CEs at 20 $°C$ is shown in fig. 7.1 A [97]. The water insoluble Chol, CE, and TAG molecules are encapsulated by the water soluble monolayer of phospholipids. The monolayer of 2 nm thickness is the yellowish background. The average composition of the molecular components of the LDL particle shown in Fig. 7.1 A is in agreement with the above listing of the lipid molecules in a LDL particle, and is as follows: 20 percent protein (gray), 20 percent phospholipids (dark blue, SM 16:0 and PC 16:0/18:2$^{\Delta 9;12}$), 40 percent CEs (yellow, 18:2$^{\Delta 9;12}$), 10 percent unesterified Chol (UC, red), and 5 percent TAG (green, 16:0/18:2$^{\Delta 9;12}$/14:0)) [97]. Domains that are rich in unesterified Chol, phospholipids, and APOB-100 apoprotein can be seen, as well as the penetration of the monolayer shell by core lipids. In summary, the composition of an LDL particle is quite complex. In addition, each category of lipids (CEs, TAG, SM, PC) has a broad variety of different chain lengths, the degrees of acyl chain unsaturation and of the isomerisation of the carbon chain (cis or trans). Fig. 7.1 B, C, and D show the chemical structures of three typical representatives of the lipid classes, such as a fatty acid methyl ester (FAME, methyl oleate 18:1) , a TAG (trioleate 3C18:1), and a CE (cholesteryl oleate C18:1), respectively. All molecules shown have the same chain length n_{C-C}=18 and degree of acyl chain unsaturation $n_{C=C}$=1. FAMEs do not occur in LDL particles. The molecular structure of all occuring lipids share the FAME lipid acyl chain,
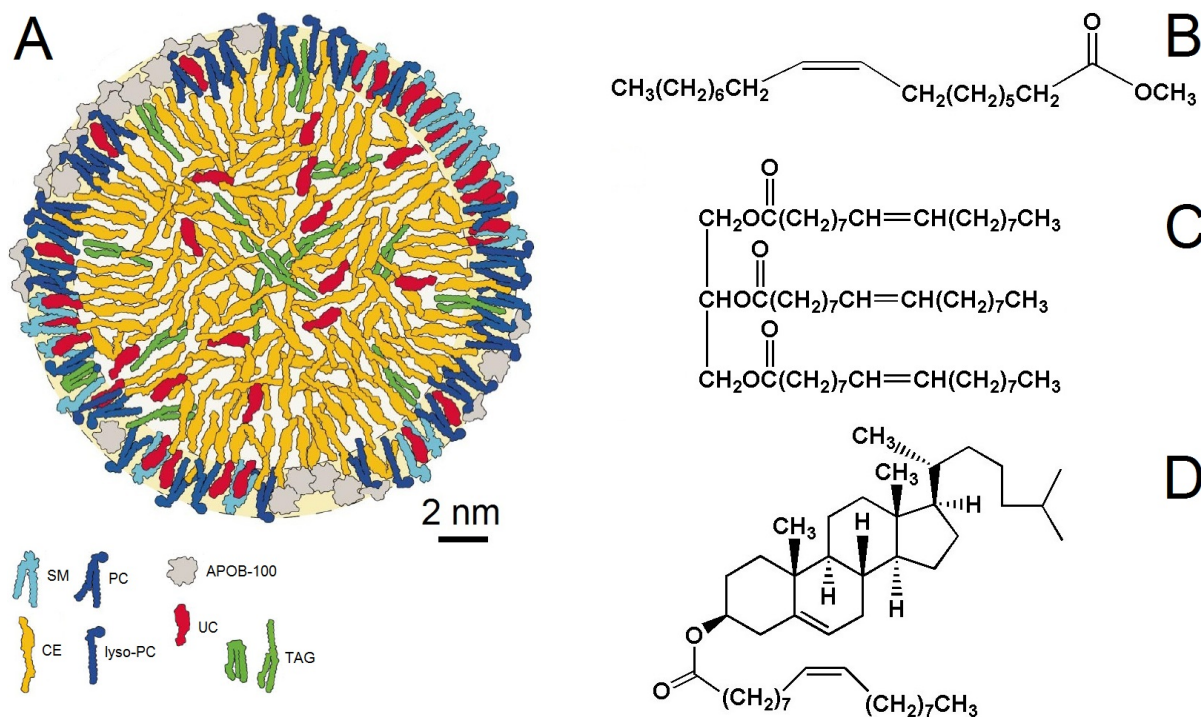
Figure 7.1: (A) Schematic structure and lipid composition of a low density lipoprotein (LDL) particle (modified from ref. [97]). (B) Chemical structures of FAME (methyl oleate 18:1), (C) TAG (trioleate 3C18:1), and (D) CE (cholesteryl oleate C18:1). See text for abbreviations.

only the residues differ. This makes FAMEs a good model to study the influence of acyl chain length and the degree of acyl unsaturation on the Raman spectrum. A FAME molecule consists of an acyl chain with an ester C=O bond. A certain number of double bonds separated by at least two single bonds can be present in the acyl chain. When three of these FAMEs are bound to glycerol, a TAG is obtained with the structure shown in fig. 7.1 C for trioleate 3C18:1. Within a TAG molecule, each of the three acyl chains can be different in length and saturation, meaning that using Raman spectroscopy only a representative average length and average degree of acyl chain unsaturation is measured. When the FAME acyl chain is connected with a Chol molecule (or in general an oxysterol), one obtains a CE as shown in fig. 7.1 D, where we can expect that as a first approximation the spectral properties of both Chol and FAME will be combined, which will be discussed in detail in section 7.3. In addition, in the case of unesterified Chol, oxidisation can lead to a variety of oxidisation products, such as oxysterols (see fig. 7.2).

The oxidisation of Cholesterol (cholest-5-en-3β-ol, see fig. 7.2 on the top) can be of enzymatic or non-enzymatic nature, resulting in oxysterols that contain additional groups attached to the Chol structure. These additional groups make oxysterols very biologically active, and this is where the interest in oxysterols stems from. Oxysterols like epoxy-, keto-, and hydroxy-cholesterol regulate cellular functions, de novo sterol and DNA synthesis [106], as well as the
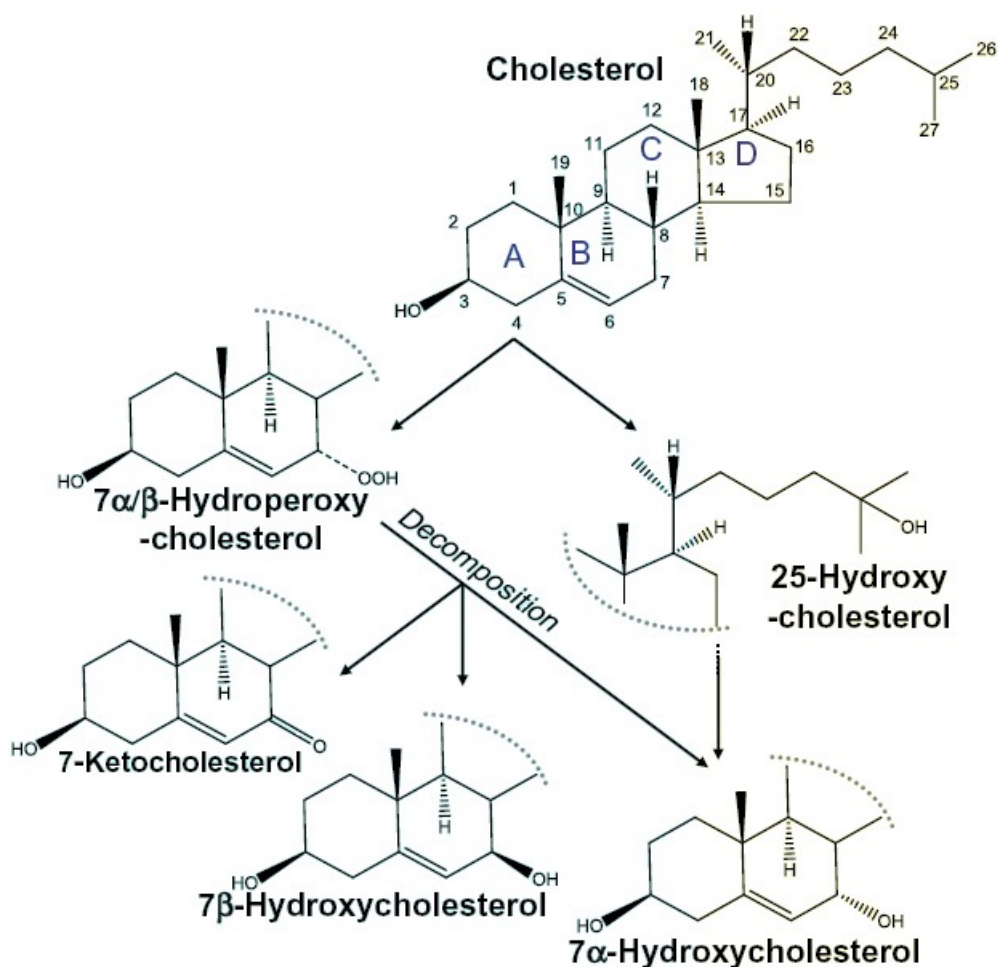
Figure 7.2: Molecular structures of Cholesterol and oxysterols in the non-enzymatic oxidisation pathway of cholesterol (adapted from ref. [105]).

plasma membrane structure in terms of permeability, hydrophobic thickness, and conformational order [107], only to name a few. They have as well been shown to be two orders of magnitude more reactive than unoxidized Chol [108]. Oxysterols can easily be produced by contact with air in presence of light and/or heat [109]. We will concentrate on the oxysterols that are involved in the non-enzymatic oxidisation of Chol. The corresponding pathway is given by Brown [105] in fig. 7.2. Starting with Chol at the top, reactive oxygen species (ROS) attack Chol, leading to a peroxyl radical (COO^-) by removing hydrogen from the carbon atom number 7 in the B-ring of Chol and to a subsequent reaction with molecular oxygen [110]. As an intermediate step, 7-α/β cholesterol hydroperoxides (7-α/β- OOHC) are formed. At early stages of non-enzymatic Chol oxidisation, this is the major oxysterol formed [110]. However, when transition metals are present, the (7-α/β- OOHC) are turned into alkoxy radicals (7-$\alpha/\beta - CO^-$), from which 7-α/β- hydroxycholesterol and 7-ketocholesterol are formed [105], [111], which are the major non-encymatically formed oxysterols in tissue. It has been shown that 7-β-hydroxycholesterol is connected with cardiovascular diseases [111], and is correlated

with atherosclerotic progression [112]. Chol, 7-α-hydroxycholesterol, and 7-ketocholesterol are used as models for CEs containing these structures. They lack the acyl chain, but the main focus is paid to distinguish Chol, 7-α-hydroxycholesterol, and 7-ketocholesterol from each other. The spectral properties of CEs containing both Chol (or oxysterols) and a fatty acid acyl chain, as a first approximation again will be treated as a linear combination. This will be discussed in detail in section 7.3. With the only difference between 7-α-hydroxycholesterol and 7-β-hydroxycholesterol being the direction, in which the OH group at position C-7 is pointing at, their spontaneous Raman spectra are expected to be indistinguishable. Therefore, 7-α-hydroxycholesterol is used to spectrally characterize both oxysterols.

With the sizes of LDL particles of approximately 20 *nm*, both spontaneous Raman and CARS spectroscopy will always measure average spectra of more than one LDL particle inside the focal detection volume. In order to be able to distinguish and quantify the LDL lipid constituents, we need to establish characteristic Raman spectral features for each lipid constituent, which serve as basis spectra for the decomposition of measured spectra. The strategy therefore is as follows: First, pure model standard lipids (FAMEs, a TAG, and CEs) will be analyzed. Once the spectral markers for the determination of the chain length, the degree of acyl chain unsaturation, and the type of isomerisation have been identified, these signatures will be used to calibrate the spontaneous Raman and reconstructed $Im[\chi_{Res}^{(3)}(\nu)]$ spectra of the LDL particles. This will then allow to quantify the LDL composition.

As already mentioned, we will concentrate on the oxysterols that are involved in the non-enzymatic oxidisation of Chol. It is known, that the uptake mechanism in human macrophages is different, when enzymatically modified lipoprotein particles (ELDL) and oxidised lipoprotein particles (OxLDL) are compared [113]. Before studying differences in living human macrophages using in vivo CARS spectroscopy (see chapter 8), here we first characterize the spectral signatures of oxysterols in ELDL, OxLDL, and native LDL particle solutions in vitro, using both spontaneous Raman and CARS spectroscopy.

7.2   Materials and methods

7.2.1   Preparation of LDL solutions

Isolation of human native LDL with densities ranging from 1.006 *mg/ml* to 1.063 *mg/ml* from plasma of healthy blood donors was carried out according to the method of Bligh and Dyer [114], and subsequent enzymatic degradation was performed by Margot Grandl in the laboratory of Prof. Dr. med. Gerd Schmitz at the University hospital in Regensburg [115]. LDL was diluted to 2 *mg/ml* protein in PBS (w/o Ca^{2+}, Mg^{2+}). Enzyme treatment was conducted with trypsin (6.6 $\mu g/ml$) (Sigma, Taufkirchen, Germany) and cholesterol esterase (40 $\mu g/ml$) (Roche

Biochemica, Mannheim, Germany) for 48 h at 37 °C. Oxidative modification of LDL was performed according to published protocols [116] by dialyzing LDL (1 mg of protein/ml) against 5 μM $CuSO_4$. Modified lipoproteins were stored at 4 °C. Prior to spectroscopic measurements, the stock solutions of LDL (concentrations: ELDL 2 mg/ml, LDL 4.5 mg/ml, OxLDL 0.94 mg/ml) were diluted by adding 1 ml of PBS buffer (Dulbecco's PBS, PAA Laboratories GmBH) to a final volume of 0.3 ml of each LDL solution. In order to increase the LDL concentration, these solutions were then ultra-centrifuged for 45 $min.$ in polycarbon tubes at 140 $krpm$ using a Discovery ME150 SE centrifuge (Thermo Fisher Scientific) at 4 °C, and then split into three parts with volumes 1050 μl, 150 μl and 100 μl ordered corresponding to the increasing LDL concentrations. The 100 μl fraction with the highest concentration was then used for spontaneous Raman measurements, as described in section 7.2.3.

7.2.2 Pure standard lipids investigated

The used FAME standards were methyl myristoleate, 14:1 (LGC, Wesel, Germany), methyl palmitoleate 16:1 (Sigma, Taufkirchen, Germany), methyl oleate 18:1 (LGC), methyl 11c-eicosenoate 20:1 (LGC), methyl erucate 22:1 (LGC), methyl stearate 18:0 (Sigma), methyl linoleate 18:2 (Sigma), methyl linolenate 18:3 (Sigma), methyl elaidate 18:1t (Sigma), and methyl linolelaidate 18:2t (Sigma). The used TAG standard was trioleate 3C18:1 (Sigma). The FAME and TAG standards have been stored at -20 °C prior to the spectroscopic measurements.

The CE standards were obtained from our collaboration partners at the University of Regensburg. The used CE standards were Cholesteryl palmitate C16:0, cholesteryl palmitoleate C16:1, cholesteryl stearate C18:0, cholesteryl oleate C18:1, cholesteryl linoleate C18:2, and cholesteryl arachidonate C20:4. The CE standards were dissolved as 1 mg/ml solution in a 1:1 n-Hexan-isopropanol solution. In order to measure the CE spectra without the solvent, the solvent was evaporated in the dark and at 4 °C prior to performing the spontaneous Raman measurements. Because the fully saturated CE (C18:0) is solid at room temperature, it was heated to a temperature above its phase transition temperature before recording the spectra.

The used cholesterol and oxysterols were Cholesterol (Sigma), 7-α-hydroxycholesterol (Avanti Polar Lipids, Alabaster, USA), and 7-ketocholesterol (Avanti Polar Lipids). Prior to sample preparation, the cholesterol and oxysterols were stored at -20 °C and under exclusion of light. Samples were dissolved in chloroform (Merck, Schwalbach, Germany) or in CCl_4 (Sigma).

7.2.3 Spontaneous Raman spectroscopy

Spontaneous Raman spectra of the pure FAME and TAG standards were recorded using the WITec CRM-200 system, described in section 4.1, at room temperature inside an aluminium reservoir that was covered during the measurements with a microscope cover slip of 150 μm

thickness (Roth Chemie, Karlsruhe, Germany, #H877). Measurement conditions: Excitation wavelength λ_{Ex} = 532 *nm*, laser power 21 *mW*, 40x 0.6 N.A. objective, 600 *g/mm* grating. Parallel- and perpendicular-polarized spectra were recorded using the 25 *μ*m (N.A. = 0.12) fibre with 10x2 *sec* integration time. Data analysis details: The CRR removal and the dark count subtraction was performed using the WITec software. No further background subtraction was performed in the CH-stretching region (2000 - 3445 cm^{-1}). In the fingerprint region (566 - 2040 cm^{-1}), the iterative polynomial approach (see description in section 4.3) was performed without subtraction of the glass reference spectrum. The order of the polynomial was $p = 5$.

The pure CEs were also transferred into an aluminium reservoir and covered during the measurements at room temperature with a microscope cover slip of 150 *μ*m thickness (Roth Chemie, Karlsruhe, Germany, #H877). SR spectra of the pure CEs were recorded using the WITec alpha 300 RA system, described in section 4.1. Measurement conditions: Excitation wavelength λ_{Ex} = 532 *nm*, laser power 32 *mW*, 100x objective, 600 *g/mm* grating. Unpolarized, parallel- and perpendicular-polarized time series spectra were recorded using the 50 *μ*m fibre with 1000x0.1 *sec* integration time at several positions. Time series spectra did not show any spectral signs of oxidisation except for C20:4. In the case of C20:4, 10 time series spectra were recorded using 100x0.1 *sec* integration time at 10 different positions. Data analysis details: The CRR removal, dark count subtraction and averaging of all time series spectra was performed using the WITec software. No further background subtraction was performed in the CH-stretching region (2000 - 3734 cm^{-1}). In the fingerprint region (335 - 2070 cm^{-1}), the iterative polynomial approach (see description in section 4.3) was performed without glass reference subtraction. The order of the polynomial was $p = 9$.

For cholesterol and all oxysterols investigated, solutions with 100 *mM* concentration were filled into a sample chamber made of a microscope slide (Roth Chemie, Karlsruhe, Germany, #H868) and a microscope cover slip of 150 *μ*m thickness (Roth Chemie, #H877), both being separated from each other by another microscope cover slip that acts as a spacer. These chambers then were sealed using sodium silicate to avoid evaporation of the chloroform and CCl_4 solvents. SR spectra were recorded using the WITec alpha 300 RA system, described in section 4.1. Measurement conditions: Excitation wavelength λ_{Ex} = 532 *nm*, laser power 32 *mW*, 100x objective, 600 *g/mm* grating. Unpolarized, parallel- and perpendicular-polarized time series spectra were recorded using the 100 *μ*m fibre with 1000x0.1 *sec* integration time for the chloroform dissolved sterols, and using the 50 *μ*m fibre with 5000x0.1 *sec* integration time for the CCl_4 dissolved sterols. Data analysis details: After CRR using the WITec software, dark count subtraction was performed using MATLAB. In the CH-stretching region, the chloroform solvent spectrum was subtracted. Supervised background correction was performed in the spectral regions 192-2302 cm^{-1} and 2303-3355 cm^{-1} using the iterative polynomial approach [50] followed by Akima spline background correction (see the description in section 3.3.2.1). The

orders of the polynomials were $p = 5$ and $p = 2$ in the fingerprint and CH-stretching regions, respectively.

Spontaneous Raman spectra of the LDL particle solutions extracted from patients were recorded using the WITec alpha 300 RA system, described in section 4.1. With the excitation wavelength at $\lambda_{Ex} = 532$ nm, fractions of β-carotene [117] are excited in (pre-)resonance to its excited electronic states. The Raman spectrum of the LDL particles therefore would be superimposed with a very strong Raman signal of β-carotene. To avoid this problem, bleaching of the β-carotene fraction prior to the measurements of the Raman spectra of the LDL particles was performed at a laser power of 32 mW for 30 min. Thereafter, the measurement conditions of the LDL solutions were: Excitation wavelength $\lambda_{Ex} = 532$ nm, laser power 32 mW, 100x objective, 600 g/mm grating. Unpolarized, parallel and perpendicular polarized time series spectra were recorded using the 100 μm fibre with integration times of 600x1 sec for LDL and 6000x0.1 sec for ELDL and OxLDL solutions. Data analysis details: The CRR removal and averaging of all time series spectra was performed using the WITec software. A first background subtraction was performed using the first-order polynomial background function of the WITec software, and a spectral mask consisting of off-resonant regions. Then, a second background correction was performed in the spectral regions 192-2302 cm^{-1} and 2303-3355 cm^{-1} using the iterative polynomial approach (see description in section 4.3). The orders of the polynomials were $p = 15$ and $p = 3$ in the fingerprint and CH-stretching regions, respectively. Subsequent Akima spline background correction was not necessary.

7.2.4 CARS spectroscopy

For the CARS measurements of the FAME standards and LDL solutions, the setup described in section 4.2 was used with supercontinuum generation and the spectrometer S1 (E in position E1 and mirror D in position D1). All CARS measurements have been performed at room temperature. The samples were transferred into a sample chamber consisting of two microscope cover slips of 150 μm thickness (Roth Chemie, Karlsruhe, Germany, #H877), separated by a spacer with an approximate thickness of 300 μm. The Pump wavelength was set to $\lambda_{Pump} = 808.1$ nm.

The following measurement conditions have been used for the FAME standards: Powers used were 20 mW and 10 mW for the Pump and Stokes beams, respectively. Time series containing 100 spectra with an integration time of 100 ms per spectrum have been measured for each FAME standard. Data analysis details: All 100 spectra per FAME standard have been reconstructed separately as described in section 5.3.3. The only supervised background subtraction was performed after the reconstruction using an Akima spline.

The following measurement conditions have been used for the LDL solutions: Powers used were 40 mW and 10 mW for the Pump and Stokes beams, respectively. Time series containing

300 spectra with an integration time of 100 *ms* per spectrum have been measured for each LDL solution. Data analysis details: All 300 spectra per LDL solution have been reconstructed separately as described in section 5.3.3. Because during the CARS measurement the signal intensity was fluctuating, only the spectra of the time series with the highest SNR have been used for the analysis. This leads to the following effective CARS spectrum integration times of 2.6 *sec* for OxLDL, 8 *sec* for ELDL and 1.8 *sec* for LDL. To minimize spurious remains of etaloning from the used CCD, a background spectrum was generated from the spectra with the smallest SNR. This background spectrum was smoothed and subtracted in the fingerprint region. The only supervised background subtraction was performed after the reconstruction using an Akima spline.

7.2.5 Mass spectroscopy

For comparison, mass spectroscopy has been carried out on the LDL, ELDL and OxLDL particles by our collaborators at the University hospital in Regensburg. After addition of chloroform and water, the samples were centrifuged (20 *min*/4 *krpm* at room temperature). The dried chloroform phase was dissolved for quantitative lipid analysis. Lipid extracts were analyzed by electrospray ionization tandem mass spectrometry (ESI-MS/MS) as described previously [118], [119], [120], [121], [122] and [123].

7.3 Spontaneous Raman spectra of pure lipid components

Fig. 7.3 presents the parallel-polarized spontaneous Raman (SR) spectra of CE C18:1, TAG 3C18:1, and FAME 18:1, whose molecular structures are shown in fig. 7.1 B-D. In all three cases, the number of double bonds in the acyl chain is $n_{C=C} = 1$, and the length of the carbon chain is $n_{C-C} = 18$. On the first glimpse, all three spectra are very much alike. The simplest lipid, both in terms of spectral features as well as the molecular structure, is the FAME (methyl oleate 18:1). In its spectrum, the most pronounced isolated bands in the fingerprint region are centered at 1267 cm^{-1} and 1655 cm^{-1} assigned to cis C=C double bonds at 1300 cm^{-1} and at 1440 cm^{-1} both assigned to the CH_2 bonds, and the C=O bond centered at 1740 cm^{-1} (see also the assignment table 7.1). In the CH-stretching region, overlapping contributions of symmetric and asymmetric CH_2 and CH_3 stretching modes are observed. Additionally, a band centered at around 3007 cm^{-1} assigned to cis C=C bonds is observed on top of the tail of the CH-stretching intensity. The most intense band in the CH-stretching region is the symmetric CH_2 stretching mode centered at 2848 cm^{-1}, typical for acyl-chains. When the spectrum of the TAG (trioleate 3C18:1) is compared with the FAME (methyl oleate 18:1), the only differences are the signal intensities of methyl oleate being more pronounced at 2947 cm^{-1} (assigned to
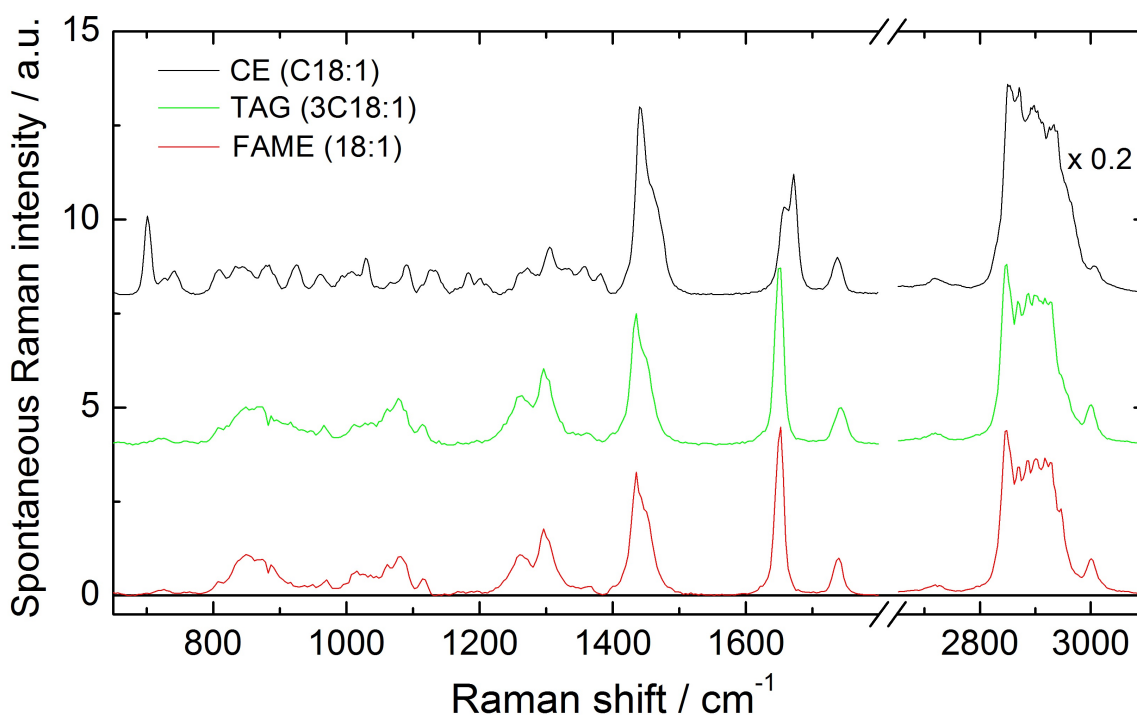
Figure 7.3: Parallel-polarized spontaneous Raman spectra of FAME (methyl oleate 18:1), TAG (trioleate 3C18:1), and CE (cholesteryl oleate C18:1). Spectra are normalized to the peak intensity at 1740 cm^{-1} and offset against each other for better visibility. Spectra in the CH-stretching region are scaled down by a factor of 0.2.

the asymmetric CH_3 stretch) and less pronounced in the region 2890-2910 cm^{-1} (assigned to the asymmetric CH_2 stretch) than those of trioleate. This can be directly understood from the molecular structures of methyl oleate and trioleate: To form a trioleate molecule, three terminal OCH_3 groups of the three methyl oleate molecules react to form the glycerol structure $CH_2OH - CHOH - CH_2OH$. Consequently, a TAG has three CH_3 groups less, but two CH_2 groups more than in three corresponding FAME molecules. When the spectrum of the CE (cholesteryl oleate C18:1) is compared with the FAME spectrum, more differences due to Chol show up. An isolated band at 700 cm^{-1} and a manifold of weak and overlapping bands covering the region from 710 cm^{-1} to 1400 cm^{-1} are assigned to the sterol rings and their C-C stretching modes.

In addition, a new band centered at 1674 cm^{-1} shows up, which is assigned to the cis C=C bond between carbon atoms five and six of the B ring of Chol. All bands observed in FAME can also be found in C18:1, but the intensity ratios have changed: The intensity of the broad band centered at 1440 cm^{-1} has increased, while the intensities of the bands at 1655 cm^{-1} and 2848 cm^{-1} have decreased. In first approximation, the CE spectrum can be understood as the linear

Table 7.1: Observed Raman peak frequencies ν_0 and their tentative assignment for FAMEs, CE standards, Cholesterol, 7-ketocholesterol, 7-α-hydroxycholesterol, LDL, OxLDL, and ELDL.

ν_0 / cm^{-1}	assignment	observed in species
546	-	Chol, 7-ketocholesterol and LDLs
600-610	-	Chol, 7-α-hydroxycholesterol, CEs and LDLs
700	-	Chol, CEs and LDLs
849	$C - H$ bending [124]	Chol, FAMEs, TAGs, CEs and LDLs
920	-	Chol and LDLs
1001	-	7-ketocholesterol and LDLs
1061	$C - C$ asym. skeletal vibrations [125]	FAMEs, TAGs, CEs and LDLs
1184	$C - C$ skeletal vibrations [125]	7-ketocholesterol and ELDL
1267	cis $= C - H$ in plane in alkyl chains [126]	FAMEs, TAGs, CEs and LDLs
1300	γ CH_2 twist, chain length [127]	FAMEs, TAGs, CEs and LDLs
1440	δ CH_2 bend, chain length [127], [125]	FAMEs, TAGs, CEs and LDLs
1460	δ CH_3 asym. bend [125]	FAMEs, TAGs, CEs and LDLs
~ 1630	$C = C$ stretch [128]	7-ketocholesterol and OxLDL
1655-1660	cis $C = C$ stretch in alkyl chains [126],[129]	FAMEs, TAGs, CEs and LDLs
1669	$C = O$ stretch [130], [124]	2-cyclohexen-1-one, 7-ketocholesterol, OxLDL and CEs
1669-1674	$C = C$ stretch [131], [132]	Chol, 7-ketocholesterol, 7-α-hydroxycholesterol and LDLs
1670	trans $C = C$ stretch in alkyl chains [129]	FAMEs
1720-1745	$C = O$ stretch [132]	FAMEs, TAGs, CEs, LDL and OxLDL
2740	$CH_2(\delta + \gamma)$ [133]	FAMEs, CEs, Chol and LDLs
2820-2855	CH_2 sym. [134]	FAMEs, CEs, Chol and LDLs
2855-2885	CH_3 sym. [134]	FAMEs, CEs, Chol and LDLs
2885-2940	CH_2 asym. [134]	FAMEs, CEs, Chol and LDLs
2940-2980	CH_3 asym. [134]	FAMEs, CEs, Chol and LDLs
3008	trans $= C - H$ in alkyl chains [129]	FAMEs, TAGs and CEs
3007, 3013-3019	cis $= C - H$ in alkyl chains [126], [129]	FAMEs, TAGs, CEs, LDL and ELDL
3032	$C = C - H$ stretch in six-membered rings [124]	Chol, 7-ketocholesterol, 7-α-hydroxycholesterol, CEs and OxLDL
3600	free hydroxyl stretching [128]	Chol, 7-ketocholesterol, 7-α-hydroxycholesterol and saturated CEs

combination of the FAME 18:1 and the Chol basis spectra.

7.3.1 Identification of spectral features for Cholesterol oxidisation

Fig. 7.4 shows the spectra of Chol and its oxysterols, 7-α-hydroxycholesterol and 7-ketocholesterol, dissolved in chloroform. For the assignment of the bands, see the table 7.1. The characteristic vibrational bands observed for cholesterol are at 700 cm^{-1}, 849 cm^{-1}, and
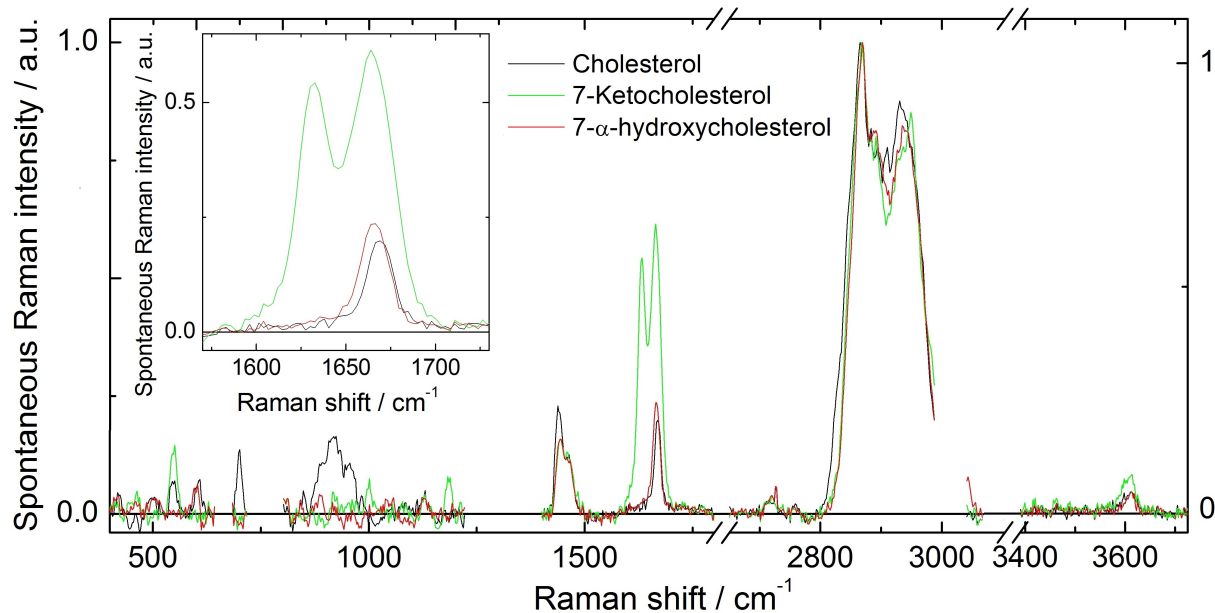
Figure 7.4: Parallel-polarized spontaneous Raman spectra of cholesterol and its oxysterols 7-α-hydroxycholesterol and 7-ketocholesterol, dissolved in chloroform. Spectra are normalized to the peak intensity at 2870 cm^{-1}. (In the spectral regions where the bands of the solvent chloroform reside, no data are shown).

a broad feature in the 920 cm^{-1} region. For 7-ketocholesterol, the bands at 1001 cm^{-1}, 1184 cm^{-1}, and a strong band at 1630 cm^{-1} are characteristic. Compared to Cholesterol, no band at 601 cm^{-1} is observed for 7-ketocholesterol. The spectrum of 7-α-hydroxycholesterol is almost identical with that of 7-ketocholesterol. The only characteristic spectral feature of 7-α-hydroxycholesterol is the missing band at 546 cm^{-1}.

In order to distinguish Chol from its oxysterols, we make use of the main spectral differences between the three compounds observed in the region between 1600 cm^{-1} and 1700 cm^{-1}, and shown in the inset of fig. 7.4. Chol has only one vibrational band at 1674 cm^{-1} that is assigned to the cis C=C double bond between carbons 5 and 6 of the B-ring (see the chemical structure given in fig. 7.2). In the B-ring of Chol, the vibrational energy of the cis C=C double bond is slightly increased when compared to the cis C=C double bond in acyl chains at 1655 cm^{-1}. Compared to Chol, the additional -OH group attached to position C-7 in 7-α-hydroxycholesterol results in a decrease of the vibrational energy of the cis C=C double bond in the B-ring. The spectrum

of 7-ketocholesterol however shows striking differences: Two strong bands appear, one band with a width of more than 20 cm^{-1} located at 1665 cm^{-1}, and a second band at 1632 cm^{-1} with a width of 15 cm^{-1}, which are assigned to the C=O double bond and the cis C=C double bond, respectively. These red-shifts of the Raman resonance frequencies of the C=O double bond and the cis C=C double bond have previously been observed for the structural changes in the B-ring subunit in cyclohexanone and 2-cyclohexen-1-one [130]: In cyclohexanone, which lacks the cis C=C double bond, the C=O double bond appears at 1709 cm^{-1}, while it shows up as two bands centered at 1669 cm^{-1} and 1682 cm^{-1} in the case of 2-cyclohexen-1-one, which contains a cis C=C double bond. This cis C=C double bond appears at $\approx$ 1616 cm^{-1} [135]. Although not spectrally resolved in 7-ketocholesterol, this double band character explains the increased width of the observed band at 1665 cm^{-1}, when compared with Chol or 7-α-hydroxycholesterol. These numbers can be compared with ketones of steroids, where the spectral position of the C=O band is characteristic to the structure. When attached to the six membered B-ring, the C=O band appears in the spectral region 1700 cm^{-1} – 1720 cm^{-1}. The conjugation of the cis C=C double bond and the C=O bond causes the resonance frequency of the latter to downshift by 30-40 cm^{-1} [124]. An infrared spectrum of 7-ketocholesterol is published by Chicoye et. al. [128], where two bands at approx. 1635 cm^{-1} and 1678 cm^{-1} have been observed, which provides further evidence that the band assignment for 2-cyclohexen-1-one can qualitatively be transferred to 7-ketocholesterol.

In all three spectra shown in fig. 7.4, the weak bands observed in the spectral region between 2720 cm^{-1} and 2760 cm^{-1} are assigned in the literature to either CH-stretching modes [136] or to combination modes of CH_2 ($\delta + \gamma$) [133]. However, the three molecules discussed here differ in the number of C-H bonds at position C-7: Chol has two C-H bonds, 7-α-hydroxycholesterol has one, and 7-ketocholesterol none at all. These differences suggest that their correct assignment is to combination modes of CH_2 ($\delta + \gamma$) [133]. Finally, we observe the band at 3600 cm^{-1}, which is assigned to free hydroxyl stretching modes [128].

In order to obtain spectra in the CH-stretching region without any overlap of the Raman bands of the solvent Chloroform, measurements of Chol, 7-α-hydroxycholesterol and 7-ketocholesterol were repeated in CCl_4, a solvent which is lacking per definition any CH-vibrations. The corresponding spontaneous Raman spectra are shown in fig. 7.5. All spectra have a similar form with two main maxima located at approximately 2870 cm^{-1} and 2940 cm^{-1}, assigned to symmetric CH_3 stretching and asymmetric CH_3 stretching modes, respectively. Although differences of the molecular structures between Chol, 7-α-hydroxycholesterol, and 7-ketocholesterol are small, they can be found in their spectra of the CH-stretching region. When compared with Chol, 7-ketocholesterol and 7-α-hydroxycholesterol have one CH_2 group less due to the C=O-bond and the hydroxy-group at C-7, respectively, which results in less intensities at 2850 cm^{-1}. In the case of 7-ketocholesterol, no hydrogen is connected to C-7. In
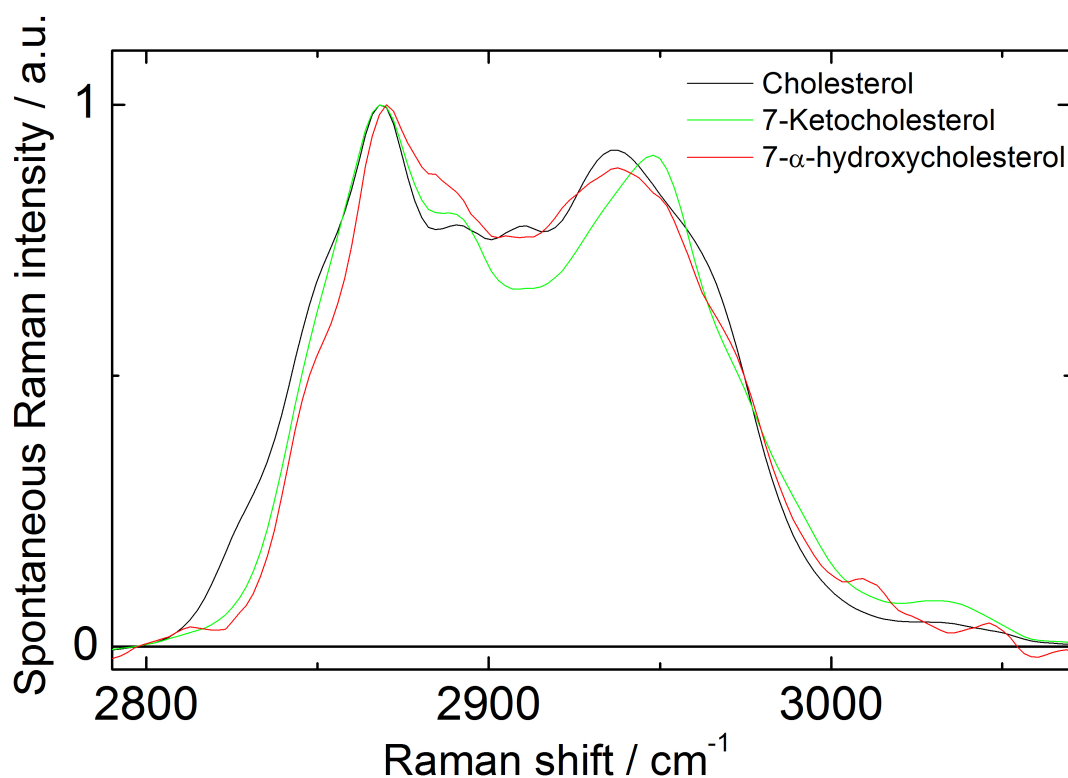
Figure 7.5: Unpolarized spontaneous Raman spectra of cholesterol and its oxysterols, 7-α-hydroxycholesterol and 7-ketocholesterol, dissolved in CCl_4. All spectra are normalized to the peak intensity at 2870 cm^{-1}.

the case of 7-α-hydroxycholesterol, there is one hydrogen left. However, the number of CH_3 groups is in both cases unchanged, and it is reasonable to normalize the spectra to the peak intensity of the symmetric CH_3 stretching mode. Around 2900 cm^{-1}, 7-ketocholesterol has the least intensity that might be related to the shift of the asymmetric CH_3 stretching mode at 2947 cm^{-1}, while for Chol and 7-α-hydroxycholesterol the spectral position is at 2938 cm^{-1}. A small red-shift of 2 cm^{-1} can be observed for the symmetric CH_3 stretching mode in the case of 7-α-hydroxycholesterol. The small features at 3010 cm^{-1} and 3040 cm^{-1} are assigned to noise. The cis C=C double bond from the B-ring shows up as a weak and broad band at around 3032 cm^{-1} in Chol, which is even weaker and difficult to see in 7-α-hydroxycholesterol. In the case of 7-α-hydroxycholesterol, the SNR is much lower than for the other two spectra, which is due to the poor solubility of 7-α-hydroxycholesterol in CCl_4.

In summary, because of the isolated resonances observed in the fingerprint region, it is clearly easier to distinguish cholesterol, 7-α-hydroxycholesterol, and 7-ketocholesterol in the fingerprint region rather than in the CH-stretching region. Thus, the key for being sensitive for the small changes induced in the molecular structure during oxysterol genesis is to have spectral information in the fingerprint region!

7.3.2 Identification of spectral signatures for the lipid chain length

Having introduced the classes of molecules that constitute LDL particles and intracellular lipids, in the next step, we will identify spectral Raman signatures that reflect their chemical structure differences in acyl chain length and the degree of acyl unsaturation, as represented by the number of carbon atoms n_{C-C} and the number of double bonds $n_{C=C}$, respectively. Fig. 7.6 shows the parallel-polarized SR spectra of a series of FAMEs with $n_{C=C} = 1$ fixed and n_{C-C} ranging from 14 to 22. With increasing chain length n_{C-C}, the relative intensities of the bands at 1300 cm^{-1}, 1440 cm^{-1}, and 2845 cm^{-1} increase, which reflect the increasing number of CH_2 groups in the lipid chain. The band at 1300 cm^{-1} representing n_{C-C} is overlapping with the band at 1267 cm^{-1}
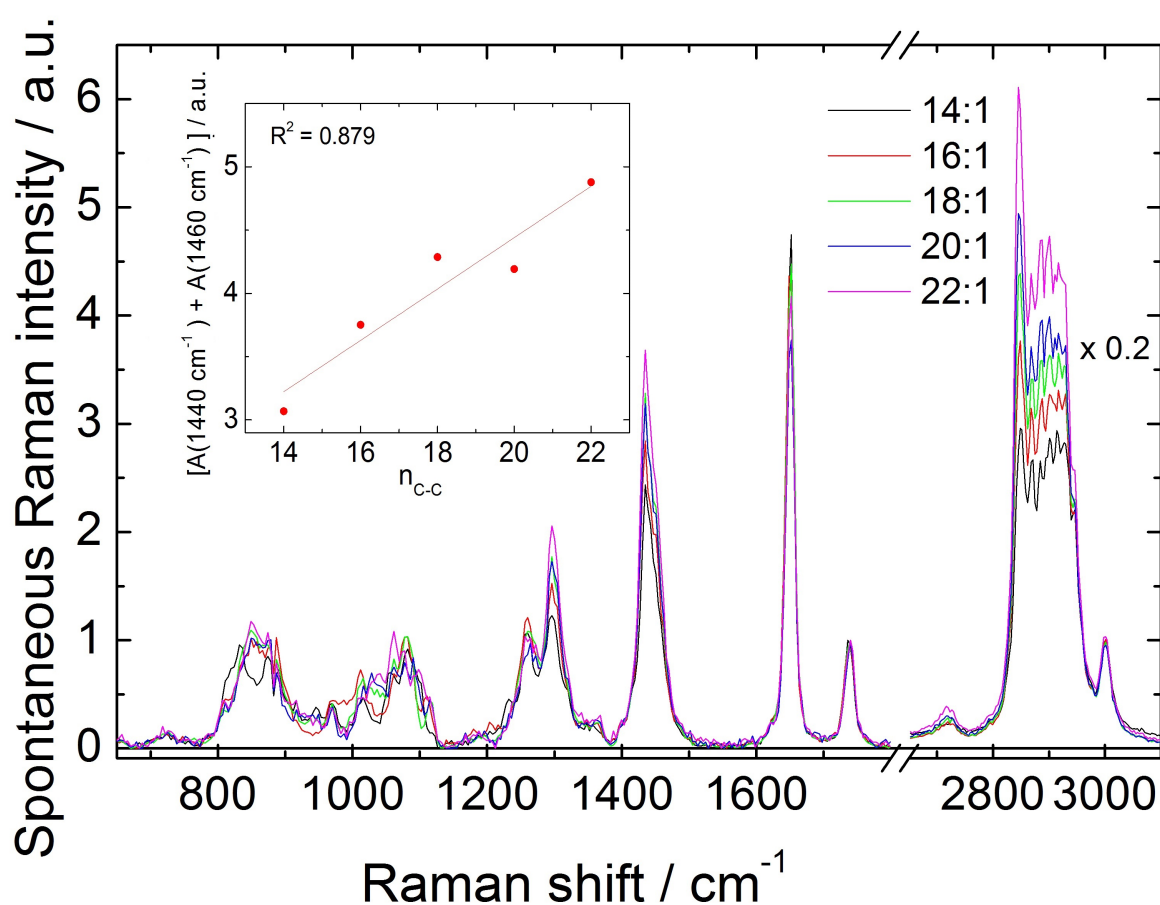
Figure 7.6: Parallel-polarized spontaneous Raman spectra of FAMEs with $n_{C=C} = 1$ fixed and varying n_{C-C}, showing the chain length dependence. Spectra are normalized to the peak intensity at 1740 cm^{-1}. Spectra in the CH-stretching region are scaled down by a factor of 0.2. The inset shows the linear dependence of the sum of the relative peak intensities of the resonances at 1440 cm^{-1} and 1460 cm^{-1} on the carbon chain length.

representing $n_{C=C}$, while the bands at 1440 cm^{-1} and 1460 cm^{-1} both representing n_{C-C} are well isolated from bands representing $n_{C=C}$. In the inset of fig. 7.6, the sum of the peak intensities

at 1440 cm^{-1} and 1460 cm^{-1} is normalized to the peak intensity at 1740 cm^{-1}, and plotted as a function of the chain length n_{C-C}. A linear dependence with a slope of 0.203 is observed. Besides the peak at 2845 cm^{-1}, the complete CH-stretching intensity is increasing with n_{C-C}. Therefore, the CH-stretching region is not very specific to determine lipid chain length. Finally, we observe again the weak bands at 2740 cm^{-1} and 2760 cm^{-1}, whose intensities are correlated with the intensities of the bands at 1300 cm^{-1} and 1440 cm^{-1}. This observation supports again the assignment of the bands at 2740 cm^{-1} and 2760 cm^{-1} to combination modes $CH_2(\delta + \gamma)$ [133].

Next, we will investigate the chain length dependence in the more complex CEs. Fig. 7.7 shows the parallel-polarized spontaneous Raman spectra of two saturated CEs ($n_{C=C} = 0$) with $n_{C-C} = 16$ and $n_{C-C} = 18$. When compared with the corresponding spectra for the chain length dependence of the FAMEs series (fig. 7.6), we obtain a quite similar picture. The entire spec-
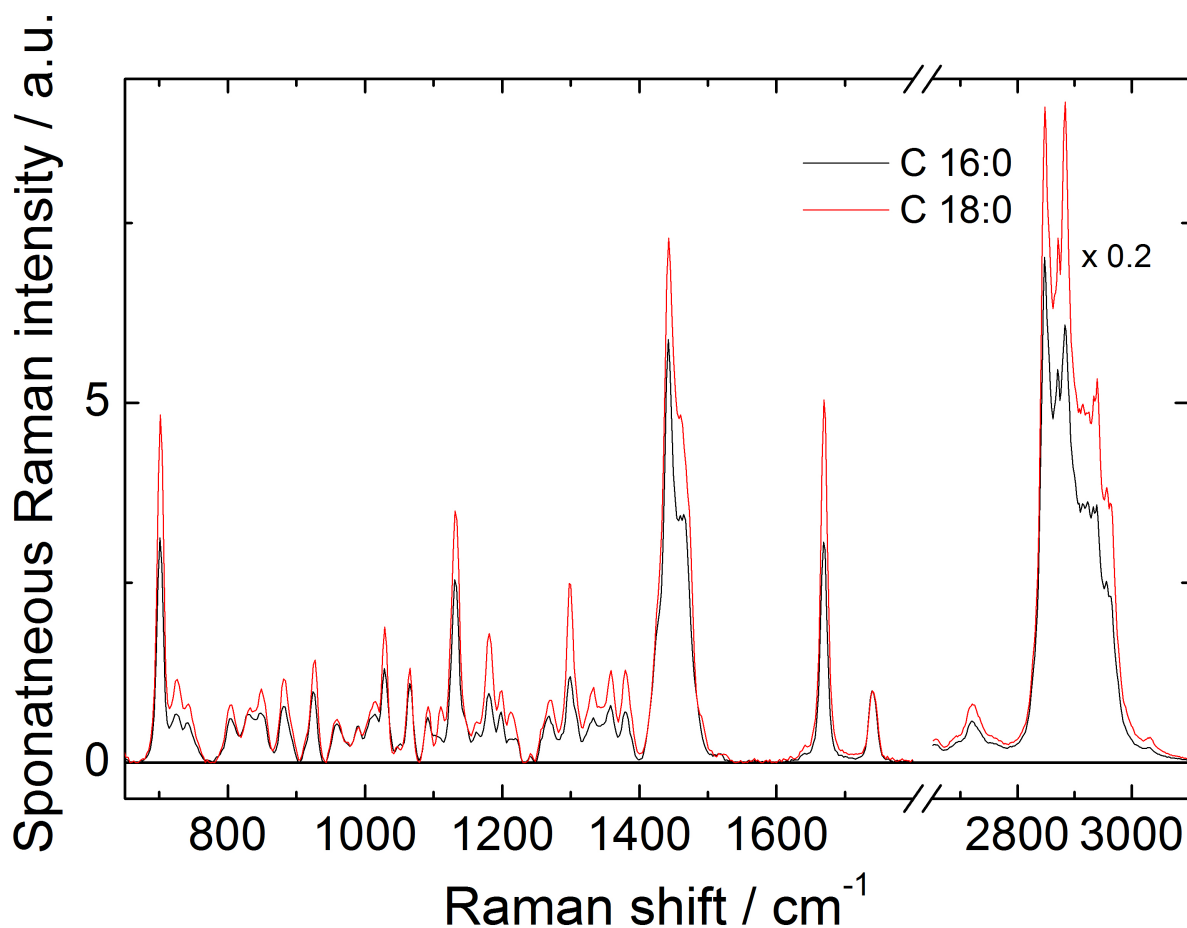
Figure 7.7: Parallel-polarized spontaneous Raman spectra of CEs with $n_{C=C} = 0$ fixed and $n_{C-C} = 16$ compared with $n_{C-C} = 18$. Spectra are normalized to the peak intensity at 1740 cm^{-1}. Spectra in the CH-stretching region are scaled down by a factor of 0.2.

trum intensity is increasing with increasing chain length n_{C-C}. The sum of the peak intensities at 1440 cm^{-1} and 1460 cm^{-1} normalized for the peak intensity at 1740 cm^{-1} increases by a factor

of 1.25, which is slightly higher than the factor of 1.14 obtained for the FAMEs. This difference can be explained by the spectral contribution of Chol to the intensity at 1440 cm^{-1}. Like in the FAME series, we see a similar picture for the weak bands at 2740 cm^{-1} and 2760 cm^{-1} in CEs, whose intensities are again increasing with the chain length. If no double bonds are present in the acyl chain of CEs, additional Raman bands residing in the range between 2400 cm^{-1}-2660 cm^{-1} are observed (not shown). Note that in both CE spectra shown in fig. 7.7 the band at 3032 cm^{-1} assigned to the cis double bond in the B ring of Chol is clearly visible.

7.3.3 Identification of spectral signatures for the degree of acyl chain unsaturation in lipids

In fig. 7.8, the parallel-polarized spontaneous Raman spectra of a series of FAMEs with $n_{C-C} = 18$ fixed and $n_{C=C}$ of cis type ranging from 0 to 3 are shown. The following dependencies are observed: With increasing degree of acyl chain cis-unsaturation, the relative intensities of the bands at 863 cm^{-1}, 1267 cm^{-1}, 1655 cm^{-1} and 3007 cm^{-1} increase. The band at
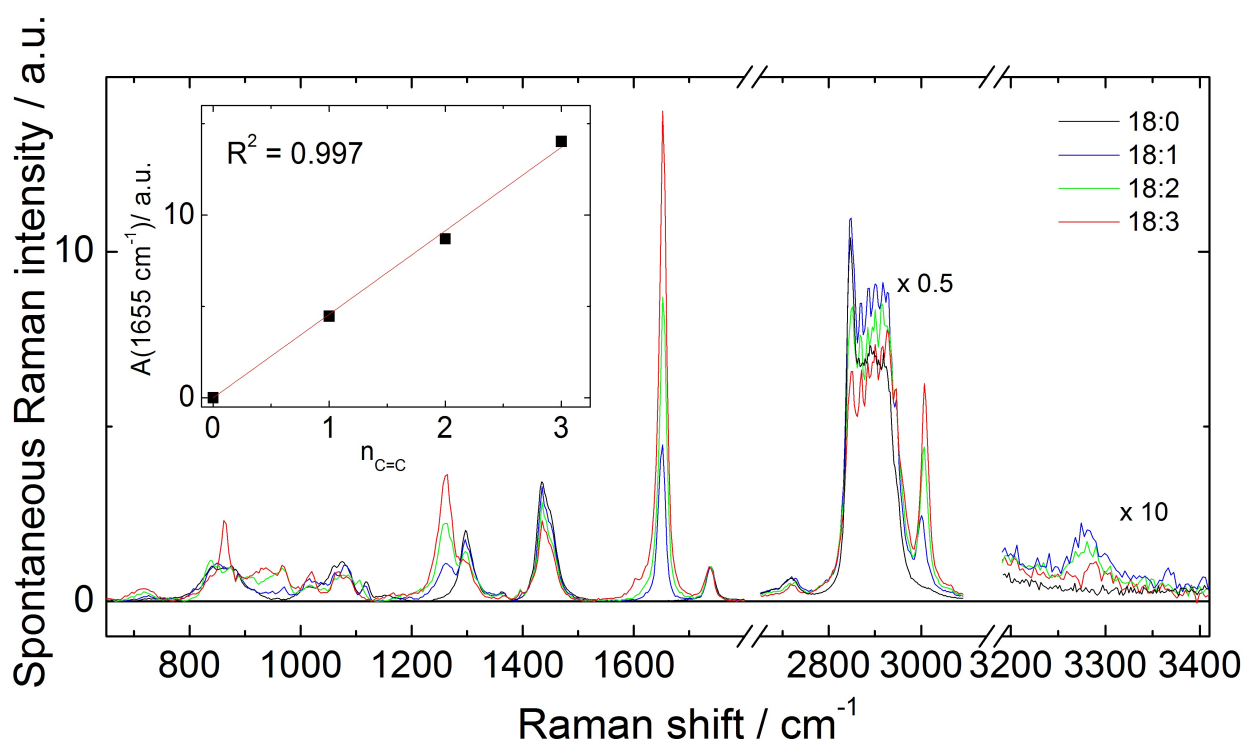
Figure 7.8: Parallel-polarized spontaneous Raman spectra of FAMEs with $n_{C-C} = 18$ fixed and varying $n_{C=C}$, showing the influence of the cis-double bonds. Spectra are normalized to the peak intensity at 1740 cm^{-1}. Spectra in the CH- and OH-stretching regions are scaled by a factor of 0.5 and 10, respectively. The inset shows the linear dependence of the relative Raman peak intensity at 1655 cm^{-1} on the degree of acyl chain cis-unsaturation.

1655 cm^{-1} assigned to the $C = C$ stretching mode is the most isolated one, and therefore is a good candidate for the characterization of the degree of acyl chain unsaturation. The relative peak Raman intensity at 1655 cm^{-1} is plotted as a function of $n_{C=C}$ in the inset of fig. 7.8. A linear dependence is observed with a slope of 4.57. On the other hand, the relative intensities of the bands at 1300 cm^{-1}, 1440 cm^{-1}, 2740 cm^{-1}, 2760 cm^{-1}, 2845 cm^{-1}, and of the whole CH-stretching region decrease. This observation is again in agreement with the assignment of the bands at 2740 cm^{-1} and 2760 cm^{-1} to combination modes of CH_2 $(\delta + \gamma)$ [133]. Each introduction of a double bond reduces the number of CH_2 groups per molecule by two. Surprisingly, a weak band at 3280 cm^{-1} catches the eye that has to the best of my knowledge not been reported in literature yet. It clearly shows a dependence on the number of cis double bonds, and is tentatively assigned to the second harmonic overtone of the 1655 cm^{-1} vibration.

In fig. 7.9, the parallel-polarized spontaneous Raman spectra of a series of FAMEs with $n_{C-C} = 18$ fixed and $n_{C=C}$ of trans type ranging from 0 to 2 are shown. The following depen-
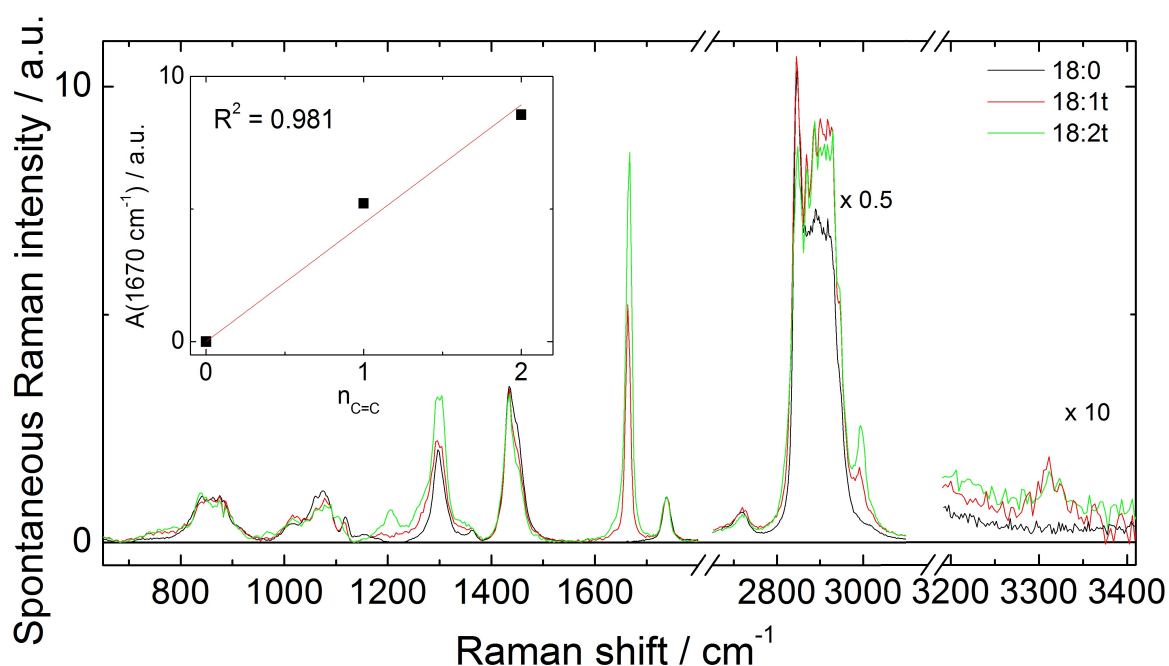
Figure 7.9: Parallel-polarized spontaneous Raman spectra of FAMEs with $n_{C-C} = 18$ fixed and varying $n_{C=C}$, showing the influence of the trans-double bonds. Spectra are normalized to the peak intensity at 1740 cm^{-1}. Spectra in the CH- and OH-stretching regions are scaled by a factor of 0.5 and 10, respectively. The inset shows the linear dependence of the relative Raman peak intensity at 1670 cm^{-1} on the degree of acyl chain trans-unsaturation.

dencies are observed: With increasing degree of acyl chain trans-unsaturation, the intensities of the bands at 1670 cm^{-1} and 3000 cm^{-1} increase. The same dependence holds for the intensities

of the band at 1300 cm^{-1} and of the CH-stretching bands. Again, the band at 1670 cm^{-1} is the most isolated, and is therefore a good candidate for the characterization of the degree of acyl chain trans unsaturation. The relative peak Raman intensity at 1670 cm^{-1} is plotted as a function of the number of $n_{C=C}$ in the inset of fig. 7.9. A linear dependence is observed with a slope of 4.5. The overtone band is now shifted to 3320 cm^{-1}, supporting its assignment to the second harmonic overtone of the 1670 cm^{-1} vibrational mode. On the other hand, the intensity of the band at 2845 cm^{-1} is the only one that is decreasing. When cis- and trans-acyl chain unsaturation are compared, the following spectral differences exist: In the trans-case, no bands occur at 863 cm^{-1} and 1267 cm^{-1}. Instead, a new band occurs at 1206 cm^{-1}. The bands at 1655 cm^{-1} and 3007 cm^{-1} in the cis-case are shifted to 1670 cm^{-1} and approximately 3000 cm^{-1} in the trans case, respectively.

Next, the degree of acyl chain unsaturation $n_{C=C}$ of cis-type is characterized for a series of CEs. Fig. 7.10 shows the parallel-polarized spontaneous Raman spectra of CEs with n_{C-C} = 18 fixed and $n_{C=C}$ of cis type ranging from 0 to 2. Most of the dependencies that have been observed in the case of FAMEs (fig. 7.8) are also found for the CEs. Although the fully saturated C18:0 may possibly contain crystalline residues, as indicated by the relatively sharp Raman bands at 2845 cm^{-1} and 2900 cm^{-1}, the main purpose of showing this spectrum is the lack of any Raman intensity at 1657 cm^{-1} and 3007 cm^{-1}, when double bonds in the acyl chain are absent, while a Raman band at 3032 cm^{-1} assigned to the cis double bond of the B-ring of Chol remains. However, the Raman band representing the degree of acyl chain cis unsaturation in FAMEs at 1657 cm^{-1} is now partially overlapping with the band at 1674 cm^{-1} originating from Chol. The relative peak Raman intensity at 1657 cm^{-1} is plotted as a function of $n_{C=C}$ in the inset of fig. 7.10. A good linear fit with a slope of 2.56 is obtained. Note that only for the spectrum of the fully saturated CE, the band at 3032 cm^{-1} assigned to the cis double bond in the B ring of Chol is clearly visible. For $n_{C=C} > 0$, this band is masked. If we look carefully, we observe again a similar intensity dependence for the weak bands at 2740 cm^{-1} and 2760 cm^{-1}. Like in FAMEs, their intensities are decreasing with of $n_{C=C}$.

7.3.4 Extracting chain length and degree of acyl chain unsaturation of unknown lipids

Obtaining the dependence of Raman spectral intensities on either the carbon chain length or the acyl chain unsaturation of lipids can indeed often be found in the literature, where only one of these two chemical structure parameters is varied, while the other is fixed [137], [138]. In most cases, the peak intensities at 1440 cm^{-1} and at 1655 cm^{-1} are independently used for calibrating the chain length [137] and the degree of acyl chain cis unsaturation [138], respectively. However, we found that both peak intensities rather depend on both structure parameters simul-
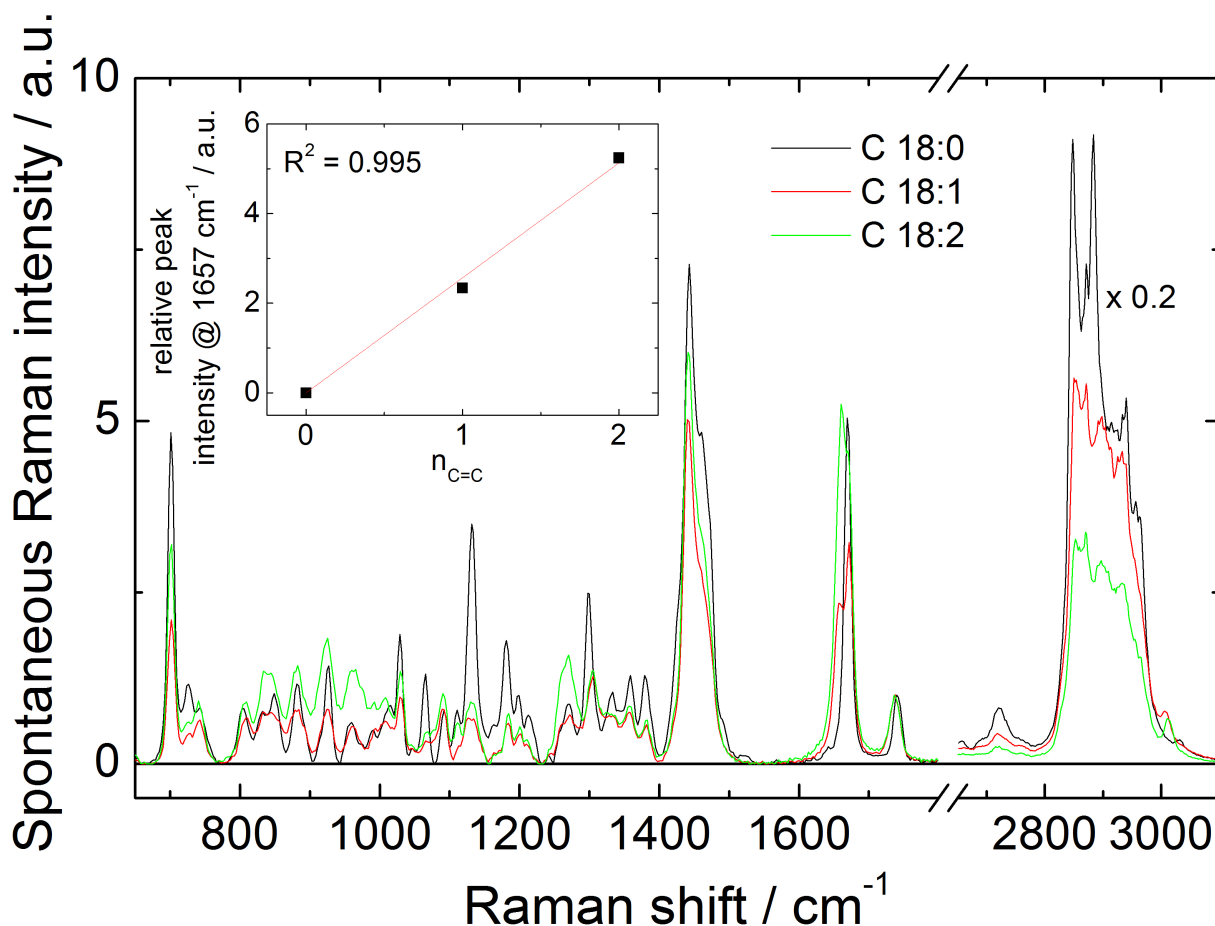
Figure 7.10: Parallel-polarized spontaneous Raman spectra of CEs with $n_{C-C} = 18$ fixed and $n_{C=C} = 0$ compared with $n_{C=C} = 1$ and $n_{C=C} = 2$ showing the influence of the cis-double-bonds. Spectra are normalized to the relative peak intensity at 1740 cm^{-1}. Spectra in the CH-stretching region are scaled down by a factor of 0.2. The inset shows the linear dependence of the peak intensity at 1657 cm^{-1} on the degree of acyl chain cis-unsaturation.

taneously. For example, the intensity at 1655 cm^{-1} is increasing with increasing number of cis double bonds, (fig. 7.8), but is decreasing with increasing chain length (fig. 7.6). Likewise, the relative peak intensity at 1440 cm^{-1} is decreasing with increasing number of cis double bonds (fig. 7.8), while it is increasing with increasing chain length (fig. 7.6). This dependence of Raman spectral signatures on both structure parameters leads to a false extraction of one or the other parameter, when only a single linear dependence of relative peak intensities is used. To give another example using the linear dependence shown in the inset in fig. 7.6, the chain length of the FAME 18:3 would incorrectly be determined to be $n_{C-C} = 12$ instead of $n_{C-C} = 18$! To circumvent such misinterpretation, it is first useful to identify Raman peak intensities, which only depend on a single chemical structure parameter. It turns out the sum of the relative peak intensity values at 1440 cm^{-1} and 1460 cm^{-1} exhibits the strongest dependence on the chain-

length n_{C-C}, while its sensitivity to $n_{C=C}$, the number of double bonds, is the weakest. In the FAMEs series, the linear fit results of the relative peak intensities dependencies of n_{C-C} and $n_{C=C}$, as extracted from the spectra shown in figs. 7.6 and 7.8, respectively, are summarized in tab. 7.2. Regarding the sensitivity to the degree of acyl chain unsaturation, the slopes of 4.014

Table 7.2: Results of the linear fit to $y = ax + b$ of the relative peak dependencies of n_{C-C} and $n_{C=C}$, as extracted for the FAME series, shown in fig. 7.6 and fig. 7.8, respectively.

	$y = \frac{A(1440\ cm^{-1})+A(1460\ cm^{-1})}{A(1740\ cm^{-1})}$	$y = \frac{A(1655\ cm^{-1})}{A(1740\ cm^{-1})}$	$y = \frac{A(3005\ cm^{-1})}{A(1740\ cm^{-1})}$
$x = n_{C-C}$			
slope a	0.203	-0.086	-0.035
offset b	0.382	5.856	4.635
$x = n_{C=C}$			
slope a	-0.570	4.570	4.014
offset b	4.575	0	0

and 4.570 for the $n_{C=C}$ dependencies of the intensities of the relative peak intensities at 3005 cm^{-1} and 1655 cm^{-1}, respectively, only differ by about 14 %. However, the comparison of the corresponding slopes for the n_{C-C} dependencies indicates that the relative peak intensities at 3005 cm^{-1} is about three times less sensitive on the chain length n_{C-C} when compared to the relative peak intensity at 1655 cm^{-1}. Therefore, we do not suffer any loss of sensitivity towards extracting $n_{C=C}$ in FAMEs when the peak intensity ratio $\frac{A(3005\ cm^{-1})}{A(1740\ cm^{-1})}$ is used. Another benefit for choosing this ratio for the extraction of the degree of the acyl chain unsaturation is that only cis double bonds contribute to the intensity at this particular frequency, while at 1655 cm^{-1} not only water but also the Amide I band of proteins can contribute to extracted intensities in biological samples. Consequently, in order to disentangle the chain length and the number of cis double bonds, it is necessary to obtain good spectra in both the fingerprint and the CH-stretching region! Using tab. 7.2, it is of course possible to determine $n_{C=C}$ and n_{C-C} from the measurement of two relative peak intensities. However, this approach brakes down, when lipids are analyzed, with $n_{C=C}$ and n_{C-C} not covered by the FAMEs standard series that are used for the calibration.

7.4 Spontaneous Raman spectra of LDL particles

We now turn to the Raman spectroscopic characterization of the LDL, ELDL, and OxLDL particles suspended in buffer and subsequent to bleaching of β-carotene. Their unpolarized spectra are shown in fig. 7.11. Characteristic for Chol and oxysterols are the band at 700 cm^{-1} (most pronounced in LDL), the bands at 725 cm^{-1} and 746 cm^{-1} (most pronounced in LDL
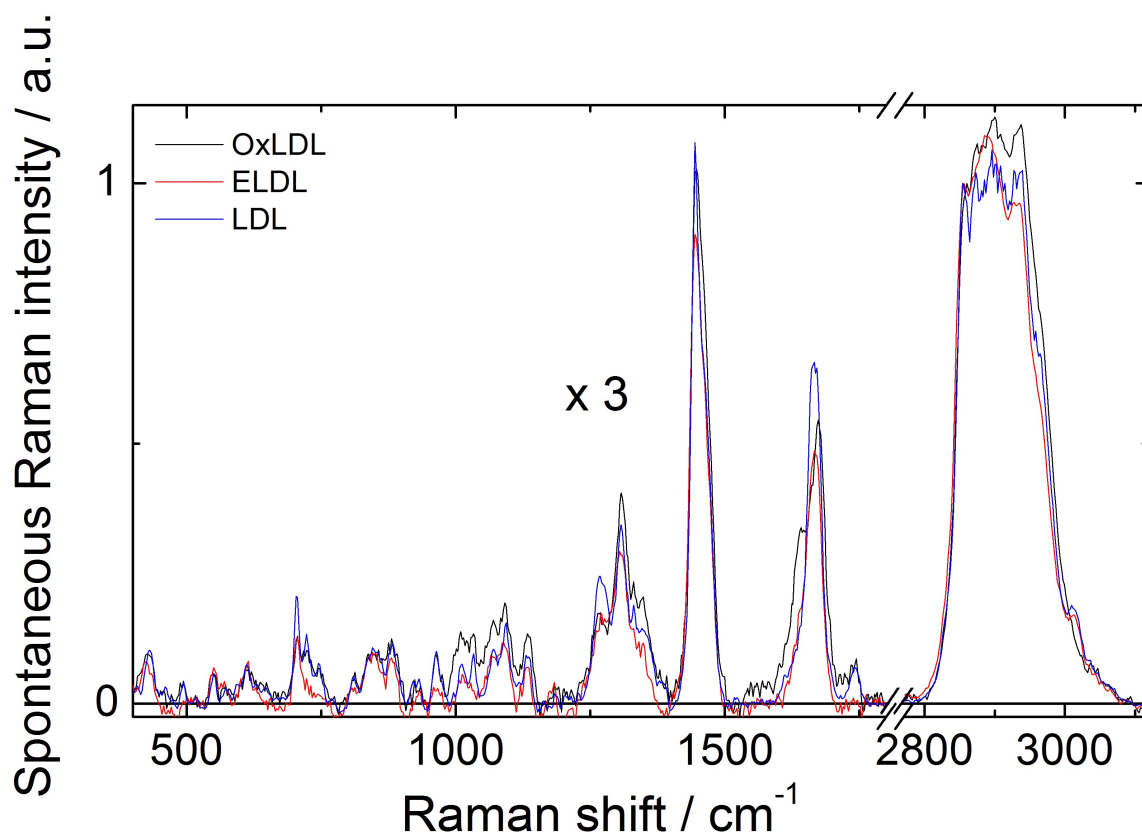
Figure 7.11: Unpolarized spontaneous Raman spectra of OxLDL, ELDL and LDL particles suspended in buffer solution. Spectra are normalized to the peak intensity at 2850 cm^{-1}. Spectra in the fingerprint region are magnified by a factor of 3.

and OxLDL), and the bands at 1674 cm^{-1} and at 3032 cm^{-1} (most pronounced in OxLDL). Characteristic for the unsaturated (cis type) acyl chains are the bands at 1267 cm^{-1}, 1655 cm^{-1} and 3007 cm^{-1}, which are most pronounced in LDL and ELDL. The prominent bands of LDL, ELDL and OxLDL are also listed and assigned in table tab. 7.1. Especially the band at 3007 cm^{-1} indicates the complete lack of cis double bonds in OxLDL, which cannot be directly seen from the bands at 1267 cm^{-1} and 1655 cm^{-1} due to the strong spectral overlap with the spectral features of Chol. This is a good example for the necessity of recording the full Raman spectrum containing information of both the fingerprint region and the CH-stretching region! The band at 1740 cm^{-1} assigned to the C=O bond in methyl esters is most intense for LDL and OxLDL. However, the main spectral difference is observed in the spectral region between 1600 cm^{-1} and 1700 cm^{-1}. With no trans double bonds expected, the broad bands appearing at 1667 cm^{-1} in ELDL and LDL can be explained by the overlap of the 1655 cm^{-1} band of the acyl chain and the band at 1674 cm^{-1} assigned to Chol, similar to the spectrum of the CE containing two double bonds (see fig. 7.10). OxLDL, however, shows an additional band appearing at 1636 cm^{-1}! The only candidate substance that has a band at 1636 cm^{-1} is 7-ketocholesterol. This interpretation is in agreement with the result of Brown and coworkers [106], who state that 7-ketocholesterol

represents the second prevalent sterol (after Chol) in copper-oxidized LDL with a total sterol content of 28-33 %.

To model the spectra of the LDL particles, we assume that they are described as linear combinations of pure CEs (C16:0, C16:1, C18:1, and C18:2), 7-ketocholesterol, 7-α-hydroxycholesterol, and free Chol spectra, which serve as basis spectra:

$$I(\nu)_{LDL} = c_{C16:0}I(\nu)_{C16:0} + c_{C16:1}I(\nu)_{C16:1} + c_{C18:1}I(\nu)_{C18:1} + c_{C18:2}I(\nu)_{C18:2}$$

$$+c_{7-ketocholesterol}I(\nu)_{7-ketocholesterol} + c_{7-\alpha-hydroxycholesterol}I(\nu)_{7-\alpha-hydroxycholesterol} + c_{Chol}I(\nu)_{Chol}$$

$$(7.1)$$

The approximate composition of an LDL particle is then obtained by a linear fit of its spectrum to eq. 7.1, using the retrieved spectrum and the normalized basis spectra shown in fig. 7.12. The CEs and Chol basis spectra are normalized to the sterol band at 700 cm^{-1}. The 7-ketocholesterol and the 7-α-hydroxycholesterol basis spectra were then scaled such to match with the normalized Chol basis spectrum in the CH-stretching region. The fractions c_x of the xth constituents represent the free fit parameters. Figs. 7.12 A, B, and C show the decomposition of the measured OxLDL, LDL, and ELDL spectra, respectively. The corresponding best fit results in relative fractions for each component are summarized in tab. 7.3. Fig. 7.13 compares the relative fractions of free Chol (FC), oxysterols (CEOx), and of CEs for the native LDL, ELDL, and OxLDL solutions. Here, the total fraction of CE is the sum of all relative fractions of the individual CEs, and the total fraction of CEOx is the sum of the relative fractions of 7-ketocholesterol and 7-α-hydroxycholesterol. Fig. 7.13 (A) reveals that for all LDL particles the relative fractions of CEs dominate. In the case of OxLDL, the best fit was obtained when the relative fraction of both 7-α-hydroxycholesterol and free Chol were set to zero. Free Chol was only found in ELDL particles, while CEOx is most pronounced in native LDL particles. For LDL and ELDL particles, the major CE fraction is C18:2, while in OxLDL particles C16:0 dominates, as can be seen from fig. 7.13 (B). Finally, we have to compare our results with the gold standard in lipidomic research, which is mass spectroscopy. The results of the mass spectra analysis that correspond to the same three particle samples are given in fig. 7.14. Fig. 7.14 (A) reveals that for all LDL particles the relative fractions of CEs dominate. Most of free Chol is found in ELDL particles, while CEOx is most pronounced in OxLDL particles. The major CE fraction is C18:2, while the C16:0 fraction is most pronounced for OxLDL particles, as can be seen from fig. 7.14 (B). From this comparison we see that within the error bars the same relative fractions of CEs concerning the chain length and the degree of acyl chain unsaturation are obtained from the spontaneous Raman spectra. This is a very useful result because it demonstrates the capability of spontaneous Raman spectroscopy to characterize LDL particles in their native state! However, concerning the determination of the relative contents of free Chol (FC), its oxysterols, and oxidised CEs using SR has limitations: For example, we cannot distinguish between 7-ketocholesterol and an oxidized CE in a mixture of both components, which is a
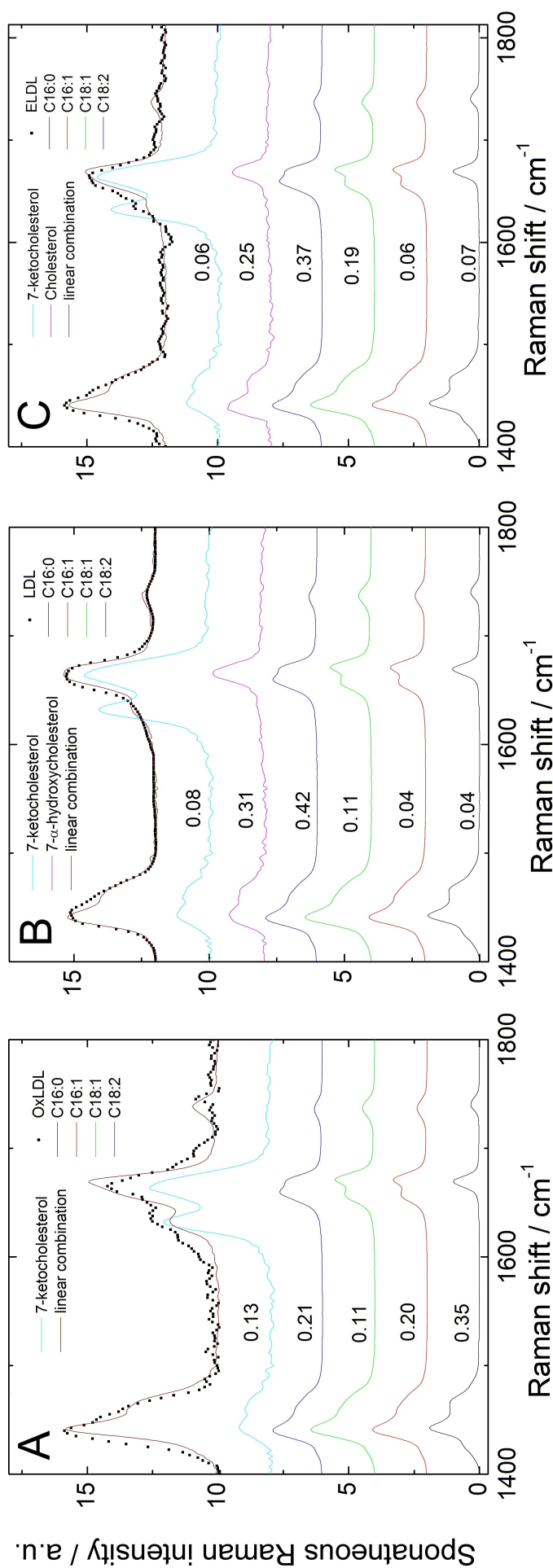
Figure 7.12: Linear decomposition of the measured (A) OxLDL, (B) LDL, and (C) ELDL spectra into the CE C16:0, CE C16:1, CE C18:1, CE C18:2, 7-ketocholesterol, 7-α-hydroxycholesterol, and Chol basis spectra. All spectra are parallel-polarized, and are plotted with an offset. The extracted relative fractions of the basis spectra are indicated by numbers. The relative fractions of Chol in (A) and (B), and 7-α-hydroxycholesterol in (C), were fixed to zero.
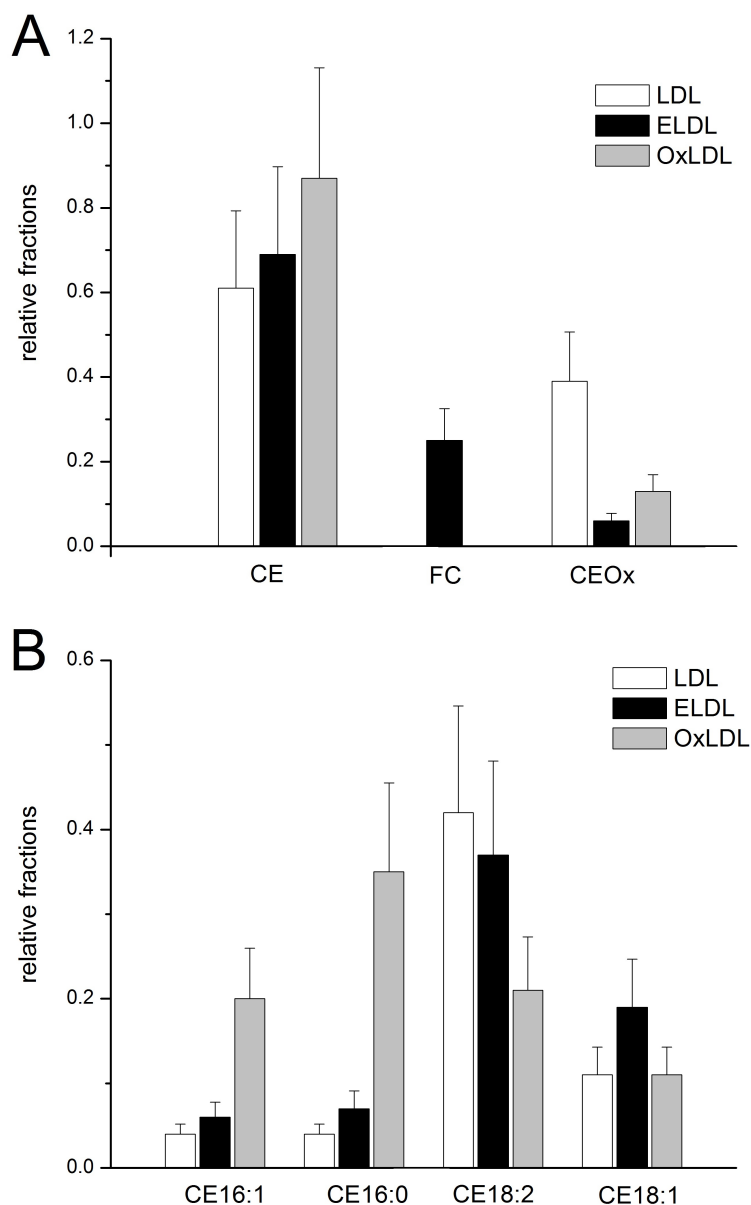
Figure 7.13: Relative fractions of (A) total CEs, free Chol (FC) and oxysterols (CEOx), and (B) of the different CE species, separated by their chain length and their degree of unsaturation for the native LDL, ELDL, and OxLDL particle solutions as obtained by the linear decomposition of their spontaneous Raman spectra (see fig. 7.12). Error bars represent a conservative estimate of the error of ±30%.

task that is easily fulfilled by mass spectroscopy. However, we see the highest relative contribution of 7-ketocholesterol in the OxLDL sample, and the highest relative contribution of Chol in the ELDL sample, both results being in agreement with the relative fractions obtained by the mass spectra as shown in fig. 7.14 A. Although both spectroscopy methods are very different approaches, the qualitative pictures obtained from each method are the same!
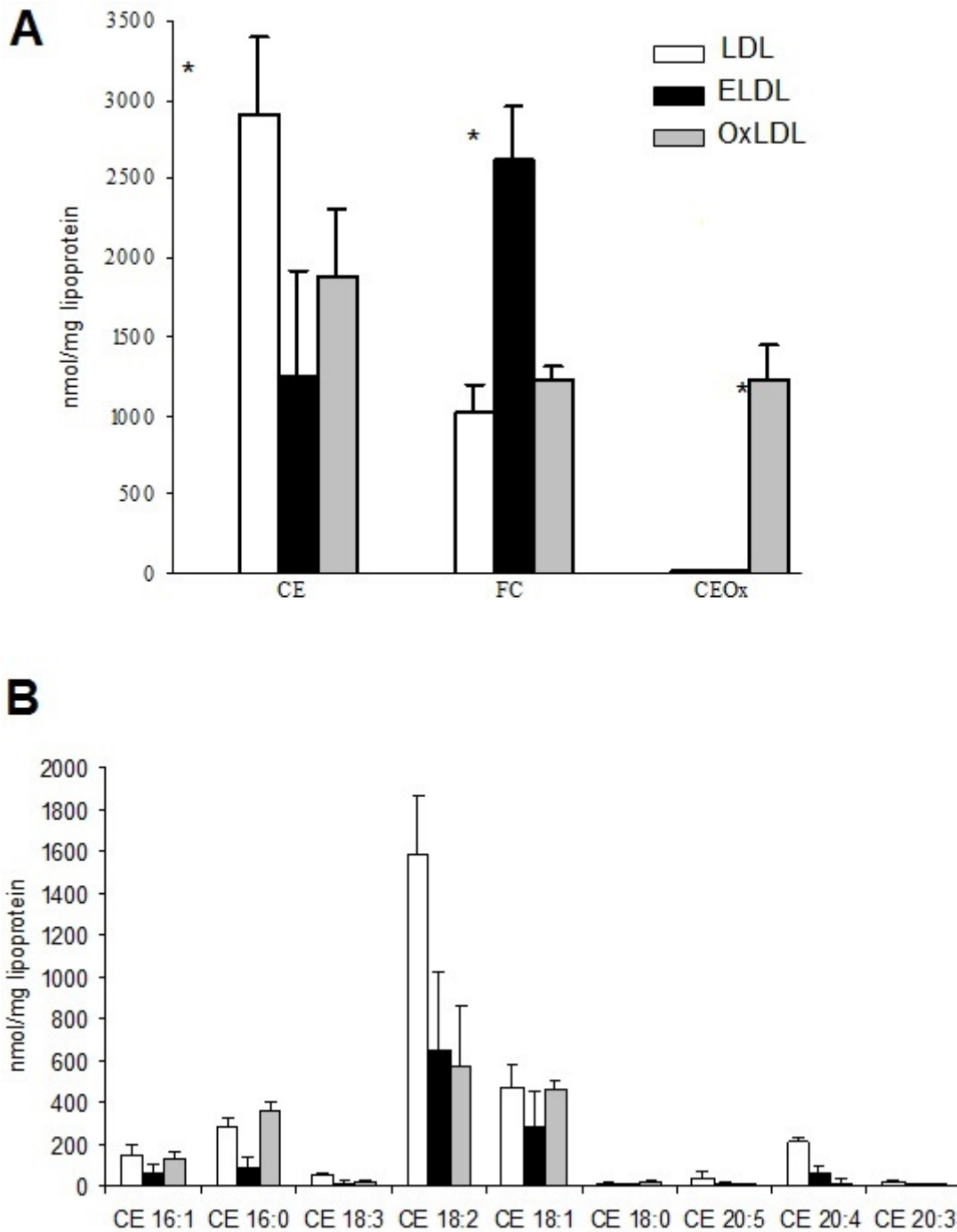
Figure 7.14: Mean concentrations of (A) total CEs, free Chol (FC), and oxysterols (CEOx) and (B) the different CE species separated by their chain length and their degree of acyl chain unsaturation for the LDL, ELDL, and OxLDL particle solutions, as obtained by mass spectroscopy by Margot Grandl and Gerd Schmitz, Institute of Clinical Chemistry and Laboratory Medicine from the University of Regensburg. Error bars represent ± the mean standard deviation from three independent experiments, each performed in triplicate.

Table 7.3: Comparison of fractions of CEs relative to total CEs obtained by Raman and mass spectroscopies.

	Raman spectroscopy			Mass spectroscopy		
	OxLDL	LDL	ELDL	OxLDL	LDL	ELDL
C16:0	$(40 \pm 12)\%$	$(7 \pm 2)\%$	$(10 \pm 3)\%$	$(24 \pm 3)\%$	$(12 \pm 2)\%$	$(9 \pm 4)\%$
C16:1	$(23 \pm 7)\%$	$(7 \pm 2)\%$	$(9 \pm 3)\%$	$(8 \pm 2)\%$	$(6 \pm 2)\%$	$(6 \pm 3)\%$
C18:1	$(13 \pm 4)\%$	$(18 \pm 5)\%$	$(28 \pm 8)\%$	$(30 \pm 3)\%$	$(19 \pm 5)\%$	$(26 \pm 14)\%$
C18:2	$(24 \pm 7)\%$	$(69 \pm 21)\%$	$(54 \pm 16)\%$	$(37 \pm 19)\%$	$(63 \pm 11)\%$	$(59 \pm 32)\%$

7.5 CARS spectra of pure lipid components

The purpose of the studies presented in this section is the demonstration of the spectral identification of characteristic spectral signatures for the chemical structure parameters in pure lipids and LDL particles (see section 7.3 and section 7.4), when $Im[\chi_{Res}^{(3)}(\nu)]$ spectra are reconstructed from measured CARS spectra in the correct and quantitative manner. Therefore, we first directly compare the measured spontaneous Raman spectrum and the reconstructed $Im[\chi_{Res}^{(3)}(\nu)]$ spectrum for one and the same lipid, i.e. methyl linolenate 18:3, in fig. 7.15. Except for the different scaling factors used to normalize the spectra in the fingerprint and the CH-stretching regions, which may be caused by the different excitation wavelength used in the spontaneous Raman and the CARS measurements, both spectra match outstandingly well. Even in the congested and strongly overlapping high wavenumber region, every spectral detail in the spontaneous Raman spectrum is correctly reproduced in the reconstructed $Im[\chi_{Res}^{(3)}(\nu)]$ spectrum. For example, the intensity ratio between the isolated bands corresponding to the C=C and C=O bonds centered at 1655 cm^{-1} and 1740 cm^{-1}, respectively, is correctly reproduced by the CARS measurement. Fig. 7.15 demonstrates that the same spectral information is obtained, regardless of whether spontaneous or coherent Raman scattering is performed. However, in the case of the CARS experiment, the spectral profile of the pump pulse is convoluted with the Raman line profile (see eq. 3.23), leading to a slightly reduced spectral resolution in the reconstructed $Im[\chi_{Res}^{(3)}(\nu)]$ spectrum when compared to the spectral resolution in the spontaneous Raman spectrum. The lower spectral resolution of the CARS experiment translates into an apparent smoothing of the sharp bands and smaller relative amplitudes when compared to those in the spontaneous Raman spectrum. In order to use the Raman spectral signatures for chain length and degree of acyl chain unsaturation previously identified in sections 7.3.2 and 7.3.3, respectively, we have obtained the reconstructed $Im[\chi_{Res}^{(3)}(\nu)]$ spectra for the same series of FAME lipids. Fig. 7.16 is the analogue to fig. 7.6, showing the dependence of the reconstructed $Im[\chi_{Res}^{(3)}(\nu)]$ spectra
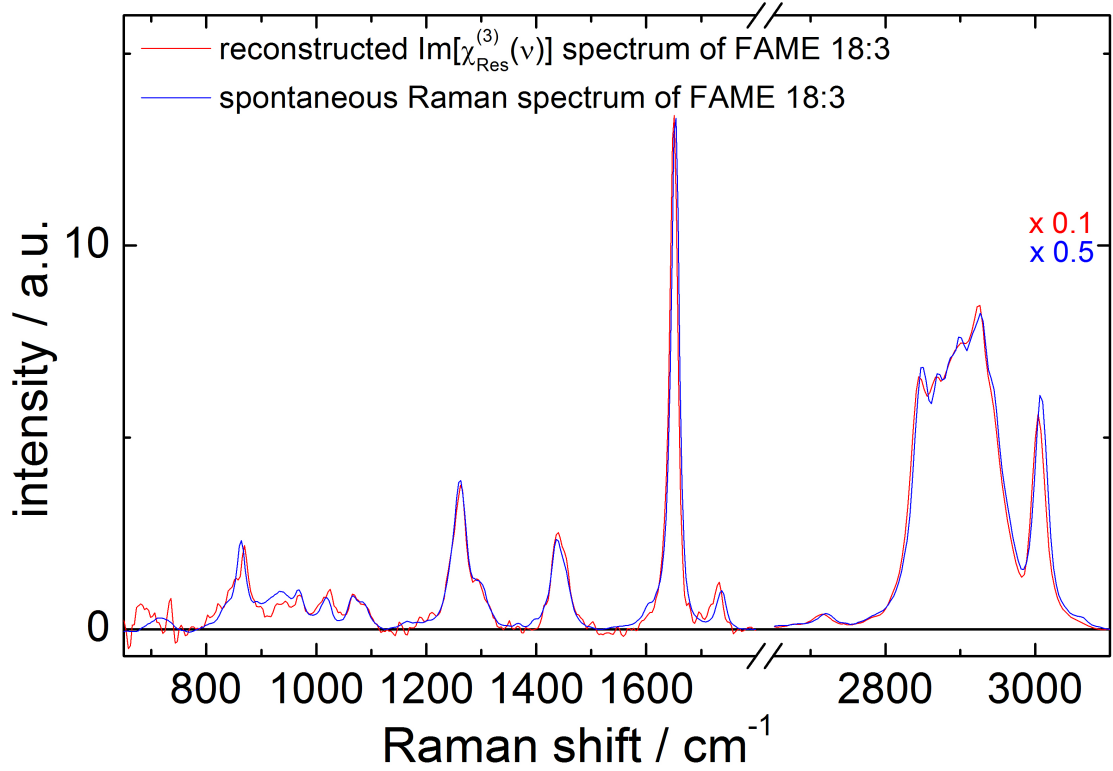
Figure 7.15: Reconstructed $Im[\chi_{Res}^{(3)}(\nu)]$ and the parallel-polarized spontaneous Raman spectrum of FAME 18:3, revealing that the same information is obtained from spontaneous or coherent Raman spectroscopy. The spectra are normalized to the peak intensity at 1740 cm^{-1}. The spectra in the CH-stretching region are scaled down by factors of 0.5 and 0.1 in the case of the spontaneous and the reconstructed $Im[\chi_{Res}^{(3)}(\nu)]$ spectrum, respectively. The spontaneous Raman spectrum is smoothed to match the lower spectral resolution of the reconstructed $Im[\chi_{Res}^{(3)}(\nu)]$ spectrum.

for a series of FAMEs with $n_{C=C} = 1$ on the chain length. We obtain a very similar picture to fig. 7.6. All trends are reproduced by the series of reconstructed $Im[\chi_{Res}^{(3)}(\nu)]$ spectra, even for the weak band at 2760 cm^{-1}. The sum of the relative peak intensities at 1440 cm^{-1} and 1460 cm^{-1} shows a linear dependence on the chain length with a slope of 0.149. Compared to the corresponding spontaneous Raman case (fig. 7.6) with a slope of 0.203, the reduced slope is predominantly attributed to the bilateral filtering applied to denoise the $Im[\chi_{Res}^{(3)}(\nu)]$ spectra (see appendix A.4.2).

In addition to the corresponding spontaneous Raman case, information regarding the pure electronic susceptibility is obtained by extracting the effective phase angles ϕ_{eff} using eq. 5.38 with $|\chi_{E\ eff}^{(3)}| = \sqrt{S_{NR}}$ extracted from the CARS spectra in the spectral range from 1818 cm^{-1} to 1855 cm^{-1} and fixed. As shown in fig. 7.17, the extracted ϕ_{eff} linearly increases with n_{C-C},
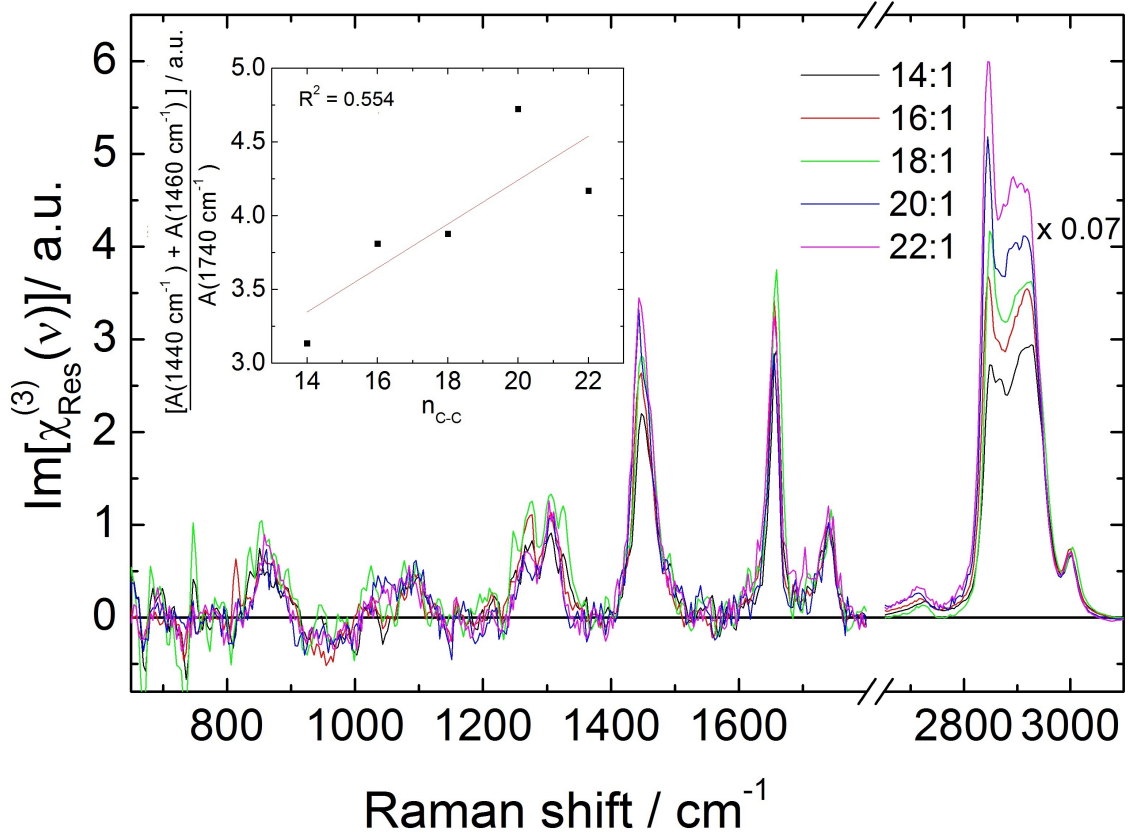
Figure 7.16: Reconstructed $Im[\chi_{Res}^{(3)}(\nu)]$ spectra of FAMEs with $n_{C=C} = 1$ fixed and varying n_{C-C} showing the chain length dependence. The spectra are normalized to the peak intensity at 1740 cm^{-1}. The spectra in the CH-stretching region are scaled down by a factor of 0.07. The inset shows the linear dependence of the sum of the relative peak intensities of the resonances at 1440 cm^{-1} and 1460 cm^{-1} on the carbon chain length.

while $|\chi_{E\,eff}^{(3)}| = \sqrt{S_{NR}}$ remains constant within $\pm 1\%$. The linear fit through the zero origin of ϕ_{eff} results in a slope of 0.04. This observed dependence correlates with the red-shift of the UV absorption peak with increasing acyl chain length within the FAME series, as reported for saturated hydrocarbons in ref. [139]. This red-shift results in an increasing contribution of the electronic susceptibility $\chi_{E\,eff}^{(3)}$ to the measured CARS spectrum.

Fig. 7.18 shows the influence of the number of cis-double bonds on the reconstructed $Im[\chi_{Res}^{(3)}(\nu)]$ spectra for a series of FAMEs with $n_{C-C} = 18$ fixed and varying $n_{C=C}$. Again, all trends observed in the spontaneous Raman case (fig. 7.8) are reproduced by the series of reconstructed $Im[\chi_{Res}^{(3)}(\nu)]$ spectra. From the relative peak intensity of the band at 1655 cm^{-1}, a linear dependence on the degree of acyl chain unsaturation with a slope of 3.3 is obtained. When compared to the value of 4.57 obtained in the spontaneous Raman case, the discrepancy is predominantly caused by the spectral convolution of the pump pulse that reduces the relative amplitude of the narrow band at 1655 cm^{-1}. Bilateral filtering reduces the slope by only 6 %.

Fig. 7.19 is the analogue of fig. 7.9, showing the dependence of the reconstructed
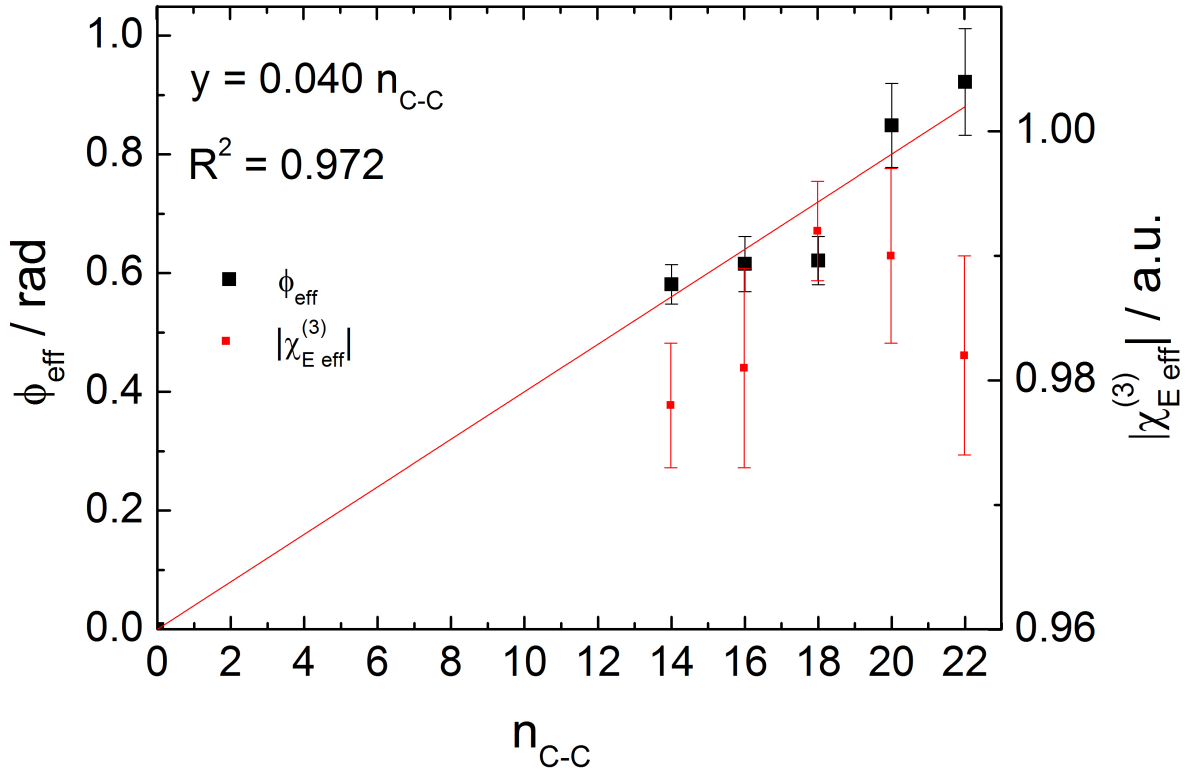
Figure 7.17: Effective phase angles ϕ_{eff} and $|\chi^{(3)}_{E\,eff}| = \sqrt{S_{NR}}$, as extracted by eq. 5.38, of FAMEs with $n_{C=C} = 1$ fixed and varying n_{C-C} representing the chain length dependence of the pure electronic susceptibility contribution $\chi^{(3)}_{E\,eff}$ to the measured CARS spectrum. Error bars represent $\pm$ the standard deviation.

$Im[\chi^{(3)}_{Res}(\nu)]$ spectra on the number of trans-double bonds for a series of FAMEs with $n_{C-C} = 18$ fixed. As in the case of FAME 18:3 (see fig. 7.15), the reconstructed $Im[\chi^{(3)}_{Res}(\nu)]$ spectra are nicely reproducing the spontaneous Raman spectra shown in fig. 7.9, taking the different spectral resolutions into account. The relative peak intensity at $1670\ cm^{-1}$ shows a linear dependence on the number of trans double bonds with a slope of 3.60, which compares to a slope of 4.5 obtained in the spontaneous Raman case (fig. 7.9). Just like in the spontaneous Raman case, the slopes obtained for the number of cis- and trans double bonds are identical within the errors.

To conclude this section, the same structure parameter information of lipids regarding the chain length and acyl chain unsaturation can be obtained, regardless whether spontaneous or coherent Raman scattering spectroscopy is performed. However, as a consequence of the convolution of the spectral profile of the pump pulse with the vibrational band-width in CARS spectroscopy, the slopes of the linear dependencies of the chain length and the degree of unsaturation are different. In order to quantify the chain length or the degree of acyl chain unsaturation based on reconstructed $Im[\chi^{(3)}_{Res}(\nu)]$ spectra, the linear dependencies plotted in fig. 7.16
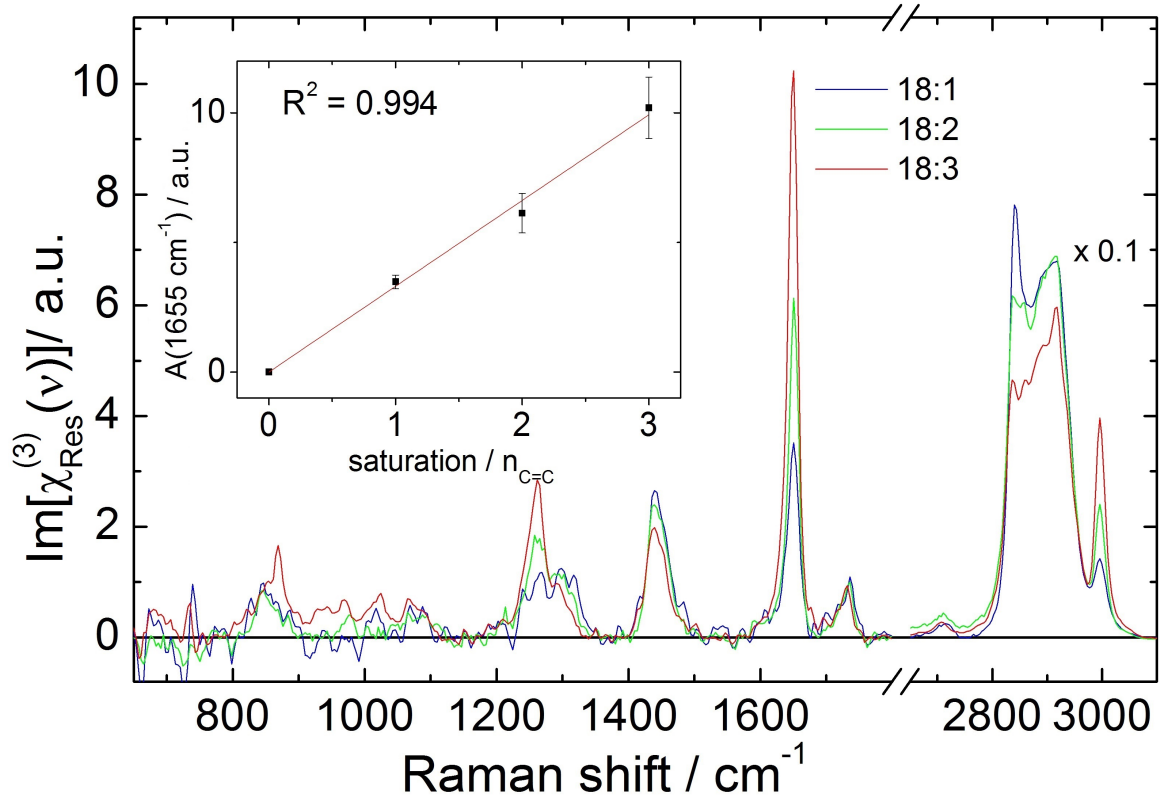
Figure 7.18: Reconstructed $Im[\chi_{Res}^{(3)}(\nu)]$ spectra of FAMEs with $n_{C-C} = 18$ fixed and varying $n_{C=C}$, showing the influence of acyl chain cis-unsaturation. The spectra are normalized to the peak intensity at 1740 cm^{-1}. The spectra in the CH-stretching region are scaled down by a factor of 0.1. The inset shows the linear dependence of the relative peak intensity at 1655 cm^{-1} on the acyl chain cis-unsaturation. Error bars represent $\pm$ the standard deviation.

- fig. 7.19 need to be used. The linear fit results are summarized in tab. 7.4. Comparing the different slopes clearly demonstrates that the band at 3005 cm^{-1} is 44.5 times more sensitive to $n_{C=C}$ when compared to n_{C-C}, and thus is the signature band of choice for the determination of $n_{C=C}$. Though less sensitive for the extraction of the chain length n_{C-C}, the sum of peak amplitudes at 1440 cm^{-1} and 1460 cm^{-1} will be used.

7.6 CARS spectra of LDL particles

Next, we want to answer the question if we can also distinguish between the different types of LDL particles using CARS spectroscopy. The reconstructed $Im[\chi_{Res}^{(3)}(\nu)]$ spectra of the LDL, ELDL, and OxLDL particle suspensions are shown in fig. 7.20. Again, their main spectral differences are reproduced. Especially, the band assigned to 7-ketocholesterol at 1636 cm^{-1} is clearly visible for the OxLDL particles. Also, the shift to higher wavenumbers of the band at 1660 cm^{-1} when going from ELDL to OxLDL is clearly visible. In the CH-stretching re-
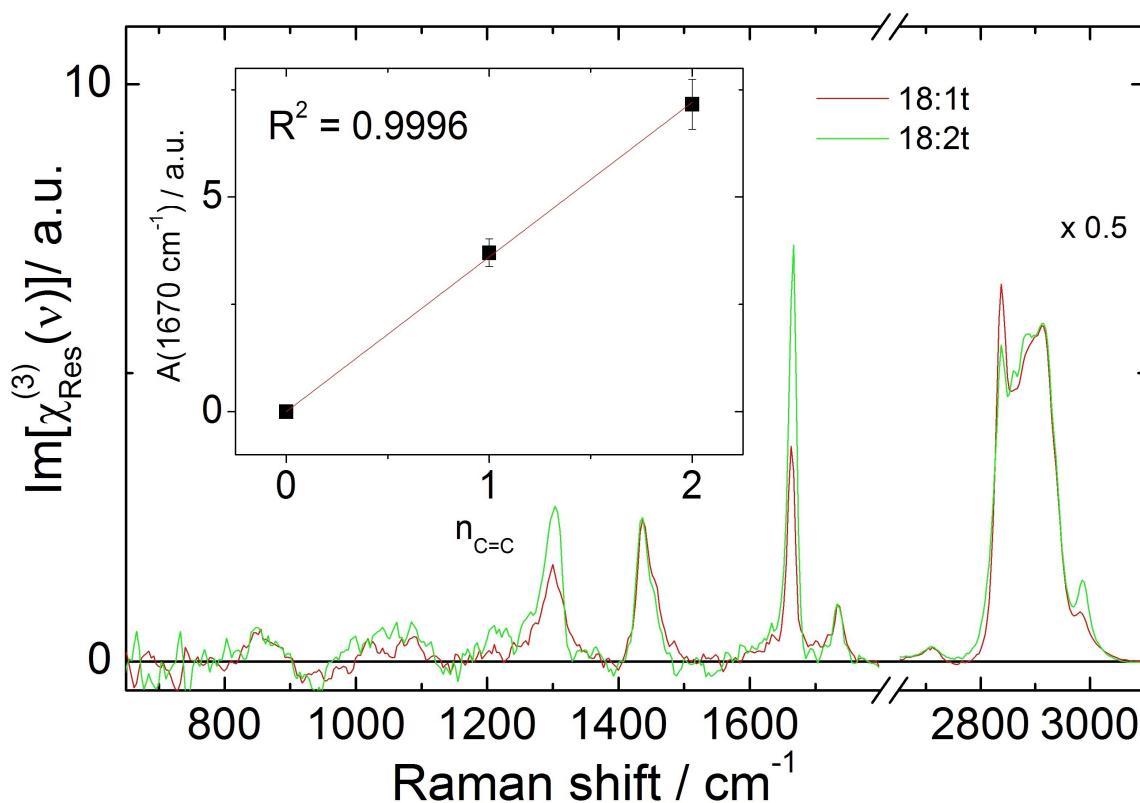
Figure 7.19: Reconstructed $Im[\chi_{Res}^{(3)}(\nu)]$ spectra of FAMEs with $n_{C-C} = 18$ fixed and varying number of trans double bonds $n_{C=C}$, showing the influence of acyl chain trans-unsaturation. The spectra are normalized to the relative peak intensity at 1740 cm^{-1}. The spectra in the CH-stretching region are scaled down by a factor of 0.5. The inset shows the linear dependence of the peak intensity at 1670 cm^{-1} on the acyl chain trans-unsaturation. Error bars represent ± the standard deviation.

Table 7.4: Results of the linear fit to $y = ax + b$ of the relative peak dependencies of n_{C-C} and $n_{C=C}$, as extracted for the FAME series, shown in fig. 7.16 and fig. 7.18, respectively.

	$y = \frac{A(1440\ cm^{-1})+A(1460\ cm^{-1})}{A(1740\ cm^{-1})}$	$y = \frac{A(3005\ cm^{-1})}{A(1740\ cm^{-1})}$
$x = n_{C-C}$		
slope a	0.149	-0.359
offset b	1.260	18.889
$x = n_{C=C}$		
slope a	-0.285	13.340
offset b	4.237	0
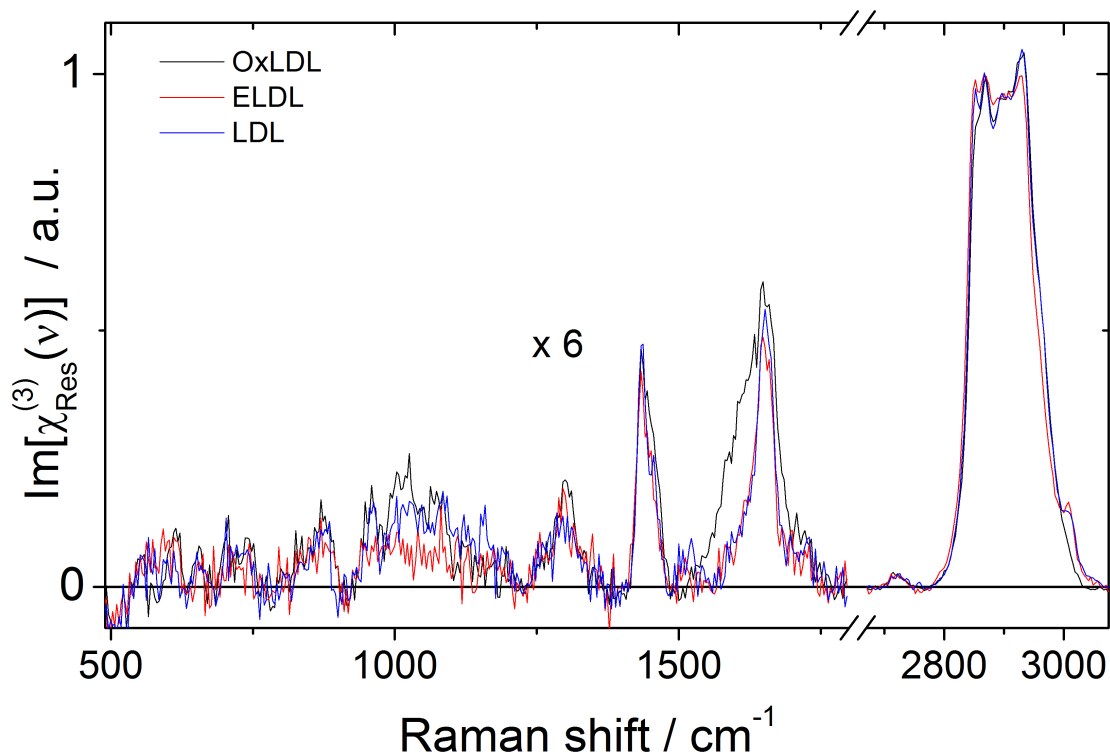
Figure 7.20: Reconstructed $Im[\chi_{Res}^{(3)}(\nu)]$ spectra of OxLDL, ELDL, and LDL particles in solution. The spectra are normalized to the peak intensity at 2850 cm^{-1}. The spectra in the fingerprint regions are magnified by a factor of 6.

gion, each LDL spectrum has its unique shape. In order to directly compare the reconstructed $Im[\chi_{Res}^{(3)}(\nu)]$ spectra with the corresponding spontaneous Raman scattering spectra in fig. 7.21, the spontaneous Raman spectra are plotted together with the reconstructed $Im[\chi_{Res}^{(3)}(\nu)]$ counterparts for OxLDL, ELDL, and LDL. For OxLDL particles (fig. 7.21 A), all major bands observed in the spontaneous Raman scattering spectrum are also found in the reconstructed $Im[\chi_{Res}^{(3)}(\nu)]$ spectrum as well. Clearly, the mentioned shoulder at 1636 cm^{-1} assigned to 7-ketocholesterol and the missing band around 3005 cm^{-1} assigned to the cis=C-H mode are evident in both spectra. The missing band at 3005 cm^{-1} indicates that the intensity at 1655 cm^{-1} must originate from Chol or its oxysterols! For ELDL particles (fig. 7.21 B) and LDL particles (fig. 7.21 C), all major bands in the spontaneous Raman scattering spectrum are also found in the reconstructed $Im[\chi_{Res}^{(3)}(\nu)]$ spectrum, and qualitatively match each other within their SNR.

   We have seen that CARS spectra of LDL particles reproduce all main spectral features of lipids, Chol, and oxysterol. Thus, we can describe them as mixtures of CEs, Chol, and its oxysterols, and a linear decomposition analysis of reconstructed $Im[\chi_{Res}^{(3)}(\nu)]$ spectra of the LDL particles, as performed in section 7.4 holds.
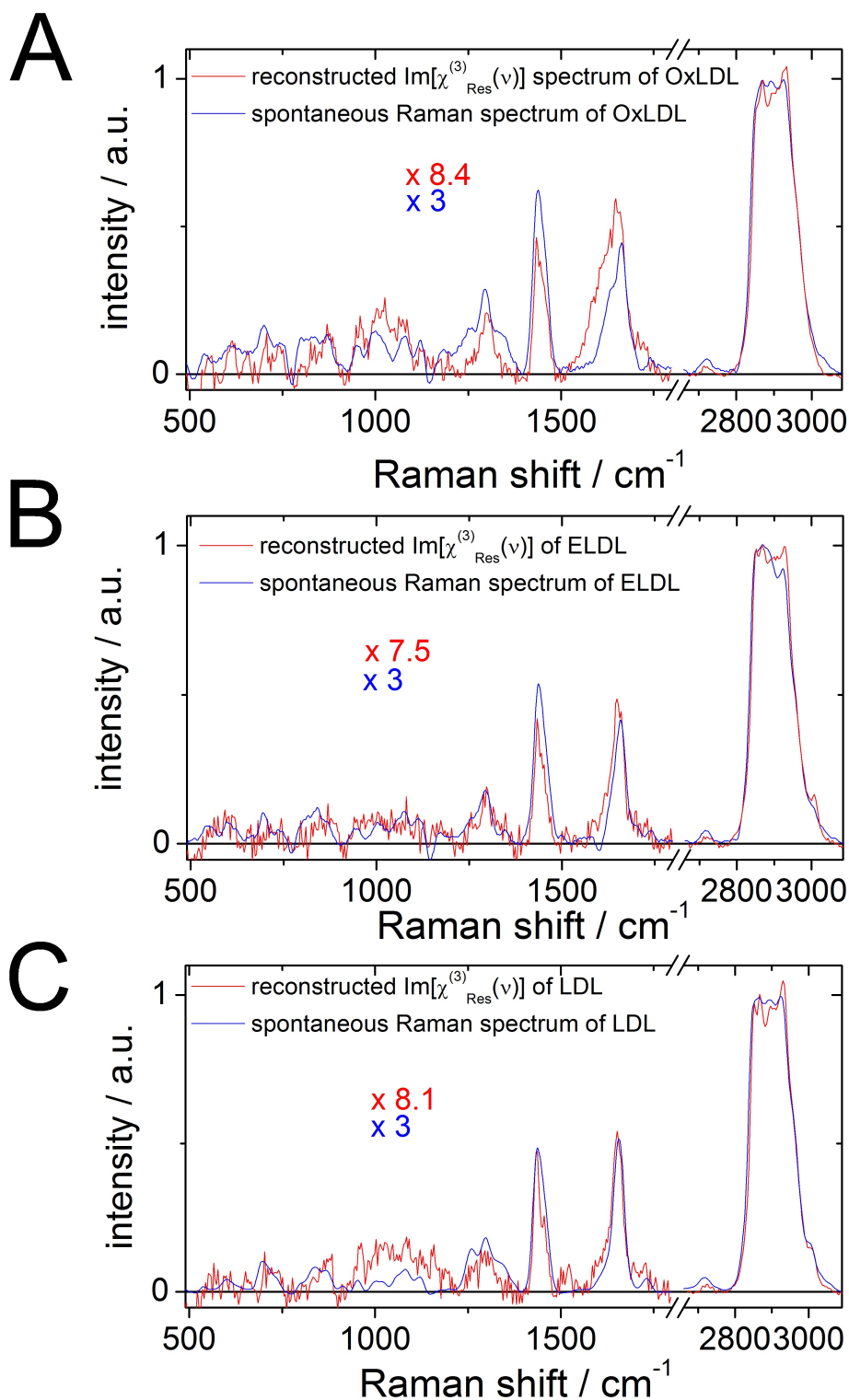
Figure 7.21: Reconstructed $Im[\chi_{Res}^{(3)}(\nu)]$ and parallel-polarized spontaneous Raman spectra of (A) OxLDL, (B) ELDL and (C) LDL particles in solution. The spectra are normalized to the peak intensity at 2850 cm^{-1}. The spectra in the fingerprint regions are magnified by a factor given in the figures. The spontaneous Raman spectra are smoothed in order to match the lower spectral resolution of CARS measurements.

7.7 Summary and conclusions

For a series of model compounds (FAMEs and CEs) for aliphatic lipid chains, it has been demonstrated that the chain length n_{C-C} is proportional to the sum of the relative peak amplitudes of the CH_2 and CH_3 bending modes at 1440 cm^{-1} and 1460 cm^{-1}, when normalized to the peak intensity of the $C = O$ stretching mode of the ester mode in the lipid molecule. The degree of cis and trans acyl unsaturation $n_{C=C}$ has been demonstrated to be linearly dependent to the relative peak amplitudes of the $C = C$ stretching modes at 1655 cm^{-1} and 1670 cm^{-1}, respectively, when normalized to the peak intensity of the $C = O$ stretching mode of the ester mode. Likewise, it has been shown that the relative amplitude of the $= C - H$ stretch at 3005 cm^{-1} is also proportional to $n_{C=C}$ in both the cis and trans unsaturation. When compared to the relative peak amplitudes at 1655 cm^{-1} and 1670 cm^{-1}, the 3005 cm^{-1} relative amplitude depends much less on the chain length parameter n_{C-C}. We can distinguish FAMEs from CEs, and quantify them in terms of two chemical structure parameters. We can furthermore interpret the spectra of CEs as a linear combination of Chol and FAMEs spectra.

For Cholesterol, another important lipid class, we have identified spectral Raman signatures not only allowing the distinction from other aliphatic molecules, but also from its oxysterols. It has been demonstrated, that the disappearance of the $C = C$ double bond and of the $= C - H$ stretching modes assigned to the B-ring of Cholesterol at 1669 cm^{-1} and 3032 cm^{-1}, respectively, can be exploited as markers for Cholesterol oxidation. Moreover, the appearance of a new band at 1655 cm^{-1} in the 7-ketocholesterol, which is assigned to the $C = O$ bond in the B-ring of Cholesterol, demonstrates the high sensitivity of spontaneous Raman spectroscopy to a minor change in the molecular structure of Cholesterol.

The direct comparison of the reconstructed $Im[\chi_{Res}^{(3)}(\nu)]$ spectra obtained from CARS measurements with their spontaneous Raman counterparts for one and the same lipid model compound has confirmed their spectral identity. This agreement allows us to use the same spectral signatures for the acyl chain structure determined in the spontaneous Raman spectra as well as in the reconstructed $Im[\chi_{Res}^{(3)}(\nu)]$ spectra. For the characterization of structure parameters based on the relative amplitudes, the spectral resolution of the CARS and the spontaneous Raman methods must be taken into account.

Based on the identification and quantification of lipid classes discussed above, I demonstrated that by using pure lipid class basis spectra, I can decompose the vibrational response of the different LDL particles that consist of a heterogeneous mixture of CEs, CEOx, and Chol. Using both spontaneous Raman scattering and CARS, the relative fractions of these lipid classes were determined for native LDL, enzymatically degraded LDL (ELDL), and oxydized LDL (OxLDL) nanoparticles. All three variants of LDL were found to be spectroscopically distinguishable because of differences in their relative compositions of CEs, Chol and oxysterols. In

the spectrum of OxLDL, we could directly identify the presence of 7-ketocholesterol, as one of the products of in atherosclerotic lipoproteins. The linear decomposition of the LDL particles spectra resulted in the relative fractions of CEOx, Chol, and the relative abundancies of chain length and degree of acyl chain unsaturation. A direct comparison with the corresponding abundancies obtained from mass spectroscopy measurements of the same LDL particle solutions gives a good qualitative agreement. In contrast to invasive mass spectroscopy, the relative abundancies obtained by using CARS and spontaneous Raman methods are noninvasive by nature!

In summary, we provide recipes for the identification of lipid structure and composition of a priori unknown lipid species. This is the prerequisite for live cell studies presented in the subsequent chapter.

8 Mapping chemical structure parameters of lipids in living cells

In ch. 7, the Raman spectral signatures of chemical structures of lipids in LDL particles and their ingredients, such as oxysterols, TAGs and CEs, and model compounds for TAGs have been characterized. A linear intensity dependence of Raman marker bands in the chain length and the degree of acyl chain unsaturation was established for the lipid model compounds. In this chapter, CARS spectral imaging will now be applied for rapid mapping of these chemical structure parameters of lipids in living macrophages loaded with the different lipoprotein particles. Section 8.3 will characterize the different types of cells on the single-cell and single-organelle levels, with respect to the spatial distribution of lipids, of their chain length n_{C-C}, and of their degrees of acyl chain unsaturation $n_{C=C}$.

8.1 The LDL uptake mechanism in human macrophages

As was described in section 7.1, LDL particles transport lipids and cholesterol to macrophages. The uptake, intracellular transportation, and storage of LDL particles in human macrophages involves several subcellular specialized compartments, called organelles, that have specific functions and distinctive chemical compositions. In eukaryotes, complex, dynamic and mobile organelles called lipid droplets serve as the main lipid store [140]. Endosomes are another type of organelles specialized for the membrane transport of substances (endocytosis). One differentiates between early endosomes (EE), located close to the cell membrane and late endosomes (LE), located closer to the cell nucleus. The LE organelles transport lipids that are by then already processed by the cell to the lipid droplets where they are stored.
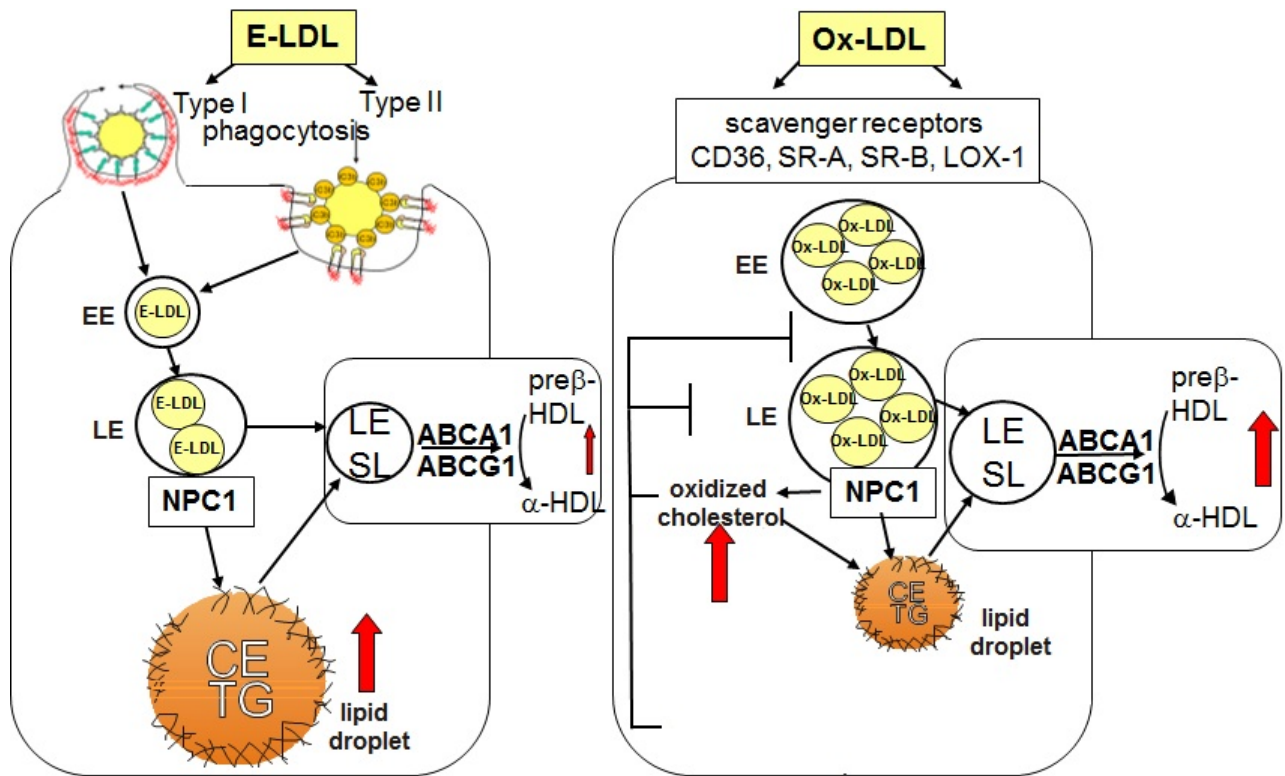
Figure 8.1: Schematic illustration of the different uptake and storage mechanisms of ELDL (left) and OxLDL (right) particles in human macrophages (modified, from Schmitz et. al. [113]).

Based on mass spectroscopy by Grandl et. al. [141], it was found that the uptake mechanisms of lipoprotein depends upon the type of loaded LDL particles. Fig. 8.1 illustrates the main differences between the uptake mechanisms of ELDL and OxLDL particles in human macrophages, as reported by Schmitz et. al. [113]. The EE is bigger in OxLDL-loaded cells, while bigger lipid droplets are observed in ELDL-loaded cells. An increased relative fraction of oxidised Chol in OxLDL-loaded cells is expected. Although mass spectroscopy was the basis for the model given in fig. 8.1, and is still the most used technique in lipidomic research today, it is an invasive technique by its nature and averages over many cells. Mass spectroscopy, therefore, cannot give any insight in the spatial arrangement and the temporal evolution of the lipid composition inside a living cell, hence still many questions remain unanswered.

The questions that we want to answer are manifold: Can CARS microscopy distinguish the lipid composition and their spatial distribution not only within the living cell, but also within a single living organelle? Can we spectrally differentiate the intracellular distribution of the lipid composition between unloaded, OxLDL-, and ELDL-loaded cells?

8.2 Materials and methods

8.2.1 Preparation of cell lines

Two human monocyte cell lines, HL-60 and THP-1, were investigated in this work, which were derived from a patient with acute promyelocytic and monocytic leukemia [142], [143], respectively.

HL-60 cells are white blood cells, isolated from healthy, normolipidemic volunteers by Margot Grandl and Gerd Schmitz from the Institute of Clinical Chemistry and Laboratory Medicine from the University of Regensburg. The isolation was carried out with the apolipoprotein E3/E3 genotype (this is the common type found in the majority of the population) by leukapheresis followed by counterflow elutriation. The isolated cells then were shipped on dry ice to Stuttgart, where they have been cultured by Dr. Andrea Zappe in IMDM(PAN-Biotech) + 20 % FBS. A cryo-cup of the cells was sowed in 40 ml medium in a medium sized cell culture flask and incubated for roughly 10 days at 37 °C, 5 % CO_2. When treated with phorbol 12-myristate 13-acetate (PMA), they differentiate to macrophages [144]. The concentration of the PMA stock solution was 2 mg/ml, and 1.48 μl PMA has been put on 30 ml Medium (IMDM(PAN-Biotech) + 20 % FBS) (conc. 0.1 $\mu g/ml$). In this medium the cells were sowed in 10 cm dishes (300 000 $cells/ml$ Medium). After three days the cells were differentiated and have attached themselves to the bottom of the dishes. The cells have been washed twice with PBS buffer and were trypsinated afterwards. Now the cells have been sowed into glass bottom culture dishes (MatTek), and they were given time until the next day to attach themselves. Next, the cells were loaded as follows: 200 μl of the OxLDL stock solution (concentration 2 mg/ml) was put on 10 ml of medium without PMA (concentration 60 $\mu g/ml$). 674 μl of the ELDL stock solution (concentration 0.89 mg/ml) was put on 10 ml of medium without PMA (concentration 40 $\mu g/ml$). Of this medium 3 ml was put on a culture dish with medium and incubated for 24 h.

THP-1 cells have been used for mass spectroscopy measurements by Margot Grandl from the Institute of Clinical Chemistry and Laboratory Medicine from the University of Regensburg. The cells were cultured in macrophage serum-free medium (Invitrogen, Karlsruhe, Germany) with recombinant human monocyte-colony stimulating factor (M-CSF) 50 ng/ml (R&D Systems, Minneapolis, Minnesota) at 37 °C/5 % CO_2 to induce phagocytic differentiation as previously described [145]. Cells were cultured at 106 $cells/ml$ either on plastic petri dishes, Ultra Low Attachment 6-well plates (Costar Corning, Bodenheim, Germany) or Lab-Tek II glass chamber slides (Nalge Nunc Intl., Naperville, IN). On the fourth day loading with ELDL (40 $\mu g/ml$) or OxLDL (80 $\mu g/ml$) was performed for 48 h. Cells were harvested on day(s) 1 (initial state), 4 (M-CSF differentiated) and 6 (loaded) respectively and experiments were performed. Cells were checked at all incubation states for apoptosis by flow cytometry using AnnexinV-FITC and Propidiumiodid (PI) staining as described previously [146].

The cells have been kept in the incubator at 37 °C and 5% CO_2 prior to the measurements.

8.2.2 Mass spectroscopy

Lipid extracts were analyzed by Margot Grandl from the Institute of Clinical Chemistry and Laboratory Medicine from the University of Regensburg using electrospray ionization tandem mass spectroscopy (ESI-MS/MS), as described in [118].

8.2.3 CARS spectral imaging of living HL-60 cells

The conditions for the CARS measurements were as follows: The Pump wavelength was centered at $\lambda_{Pump} = 801.6\ nm$. Actual power levels varied but did not exceed 30 mW and 15 mW for the Pump and Stokes beams, respectively, and are indicated in the figure captions. Actual pixel spectrum integration times varied for the different experiments ranging from 10 ms to 200 ms, and are also given in the figure captions. The de-etaloning of raw spectra was performed with a de-modulation spectrum recorded at an image region outside of any cells, this way assuring that the de-modulation spectrum is free of any vibrational resonance features of interest. If in a close-up image scan, no such pixel spectra were available, the de-modulation spectrum of the preceding large area image scan was used. Because of the limited signal-to-noise ratio of the CARS spectrum above 4000 cm^{-1}, where the wings of the very broad water bands reside, each CARS pixel spectrum has been substituted using a model for water prior performing the phase retrieval. Here, a spontaneous Raman spectrum of water was described as a linear combination of complex Lorentzian bands according to eq. 3.19. In this way, the CARS spectrum of water is simulated, and then fitted to every measured CARS pixel spectrum using the model $S(x, y, z, \nu)_{water} = |\mathbf{c}_{H_2O}(x, y, z)\chi^{(3)}_{Res\ H_2O}(\nu)e^{-i\phi_{H_2O}(x,y,z)} + \chi^{(3)}_{NR}(x, y, z)|^2$ with the weight $c_{H_2O}(x, y, z)$ and the phase $\phi_{H_2O}(x, y, z)$ as parameters. In doing so, the measured CARS spectra have been extrapolated up to approximately 6800 cm^{-1}, allowing for the robust phase retrieval of both lipids and water. Prior to the analysis of the chain length n_{C-C} and the degree of acyl chain unsaturation $n_{C=C}$, the mean of the reconstructed cytoplasm pixel spectra was scaled according to the intensity of water at 3400 cm^{-1}, and subsequently subtracted from every pixel spectrum, resulting in lipid vibrational features only, as was described in section 5.3.3. If in a close-up image scan of an individual organelle no cytoplasm pixel spectra were available, the mean cytoplasm spectra of the preceding large area image scan was used. Denoising of the reconstructed pixel spectra was performed using the bilateral filtering method described in appendix A.4.2. Only neighbouring pixels not resolved within the diffraction limit of our setup are considered in the bilateral filter kernel. Depending on the scan step size and the reconstructed $Im[\chi^{(3)}_{Res}(\nu)]$ amplitudes, the half widths of the Gaussian filter kernels, σ and σ_{range}, varied between 2 and 6 and between 6 and 34, respectively. An increase of the SNR of approximately three was

achieved. Univariate spectral data analysis was performed for every pixel spectrum in the fingerprint and the CH-stretching regions in order to extract chemical structure parameters. Here, the peak amplitudes of resonances of interest were obtained by using the Pseudo-Voigt model given by eq. 4.9. In order to not affect the statistics of the extracted chemical structure parameters, the univariate data analysis was performed using the not denoised spectra. In order to identify and select lipid-rich organelles inside the cytoplasm of the cells, a threshold of 3.2 times the integrated CH-stretching signals inside the cytoplasm was defined. If in a close-up image scan no such thresholds could be defined, the threshold of 3.2 times the integrated signal of the preceding large area image scan was used.

8.3 Comparison of intracellular lipids in unloaded, ELDL-, and OxLDL-loaded HL-60 cells

8.3.1 Extracting the vibrational response of lipid-rich organelles

As an example, fig. 8.2 A shows a typical map of an ELDL-loaded HL-60 cell, as obtained when the reconstructed $Im[\chi^{(3)}_{Res}(\nu)]$ is integrated in the CH-stretching region. While the pixel contrast is almost zero outside the cells, inside the cytoplasm, a rather homogeneous image contrast predominantly due to proteins and a strong contrast of lipid-rich organelles are observed. Fig. 8.2 B shows the image mask for those selected image pixels that are representative for lipid-rich organelles in the cell. In order to count the number of individual organelles and to obtain their pixel spectra of maximum intensity, only isolated maxima that are separated by the diffraction limit of our setup are considered. The 71 identified isolated organelles are marked as red points in fig. 8.2 B. Representative mean reconstructed $Im[\chi^{(3)}_{Res}(\nu)]$ spectra of water, the cytoplasmic proteins and of lipids shown in fig. 8.2 C, were obtained by spatially averaging image pixels outside the cell, inside the cytoplasm, and over the selected pixel of maximum CH-stretch intensity in the lipid organelles, respectively. While the mean reconstructed $Im[\chi^{(3)}_{Res}(\nu)]$ spectrum of water represents a pure species spectrum, the mean cytoplasm spectrum is a mixture of predominantly proteins and water. The mean $Im[\chi^{(3)}_{Res}(\nu)]$ spectrum of the identified lipid organelles shows strong spectral contributions that are typical for lipids, water, and weaker contributions of cytoplasmic proteins. For example, when compared with the peak intensity of water recorded outside the cell, approximately half of the water intensity is observed in pixel spectra of the lipid organelles. In other words, there are no pixels that contain only lipids! Assuming that every pixel spectrum can be described as a linear combination of basis spectra of pure water, cytoplasmic proteins, and lipids, the spectrum of the lipid organelles is obtained by subtracting the properly scaled mean reconstructed $Im[\chi^{(3)}_{Res}(\nu)]$ spectra of the cytoplasm and water for every pixel spectrum.
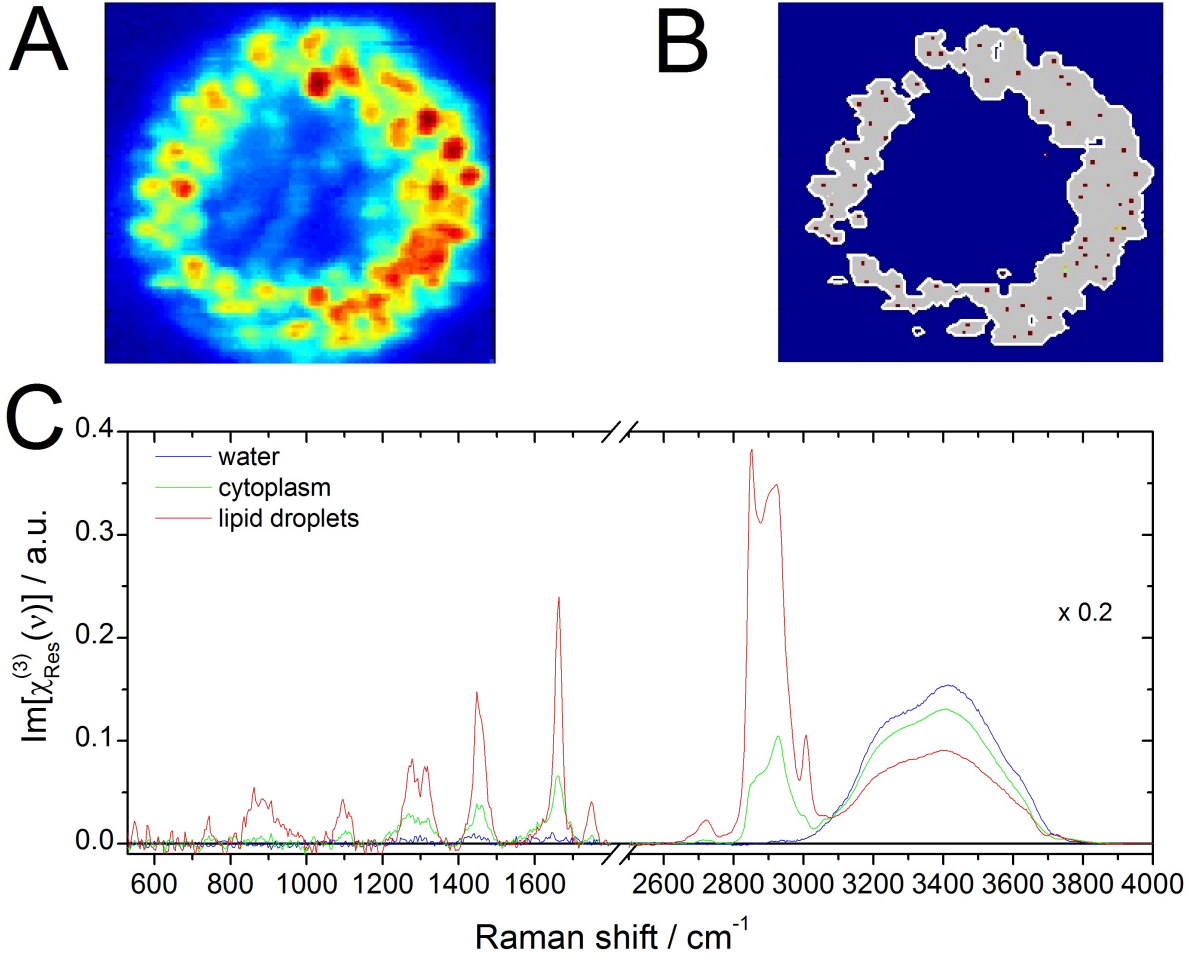
Figure 8.2: Live-cell CARS spectral imaging of an ELDL-loaded HL-60 cell. (A) image contrast generated by integrating the reconstructed $Im[\chi_{Res}^{(3)}(\nu)]$ spectra within the interval $[2750\ cm^{-1}, 3050\ cm^{-1}]$. (B) Threshold-based definition of an image mask for the selection of individual lipid-rich organelles, whose maximum spectral intensities are indicated by red points. (C) Typical mean reconstructed $Im[\chi_{Res}^{(3)}(\nu)]$ spectra of water, the cytoplasmic proteins, and of the selected lipid-rich organelles for this cell as obtained by spatial averaging over 20, 619, and 71 image pixels, respectively. Spectra in the CH-stretching region are scaled down by a factor of 0.2. The image dimensions are 14.08 $\mu m \times$ 12.95 μm (100 pixel $\times$ 91 pixel), the laser powers used were 30 mW and 15 mW for the pump and Stokes beams, respectively, and the spectrum integration time per pixel was 100 ms.

8.3.2 Spatial distributions of lipid structure parameters

Next, we will map and compare the density of cis $C = C$, the acyl chain length n_{C-C}, and the degree of acyl chain unsaturation $n_{C=C}$ of the intracellular lipids for the different types of cells using the amplitude of $Im[\chi_{Res\ lipid}^{(3)}(\nu)]$ at 1665 cm^{-1}, the ratios $\frac{A(1440\ cm^{-1})+A(1460\ cm^{-1})}{A(1740\ cm^{-1})}$ and $\frac{A(3005\ cm^{-1})}{A(1740\ cm^{-1})}$, respectively, as defined from the FAME model lipids in ch. 7. Corresponding maps that are representative for an unloaded, an OxLDL-loaded, and an ELDL-loaded cell are shown

in fig. 8.3. In the first column, the maps proportional to the density of cis $C = C$ bonds reveal the presence of lipid rich organelles in all three types of cells. However, they are increasing both in size and density when going from the unloaded to the OxLDL-loaded and the ELDL-loaded cell. These observed morphological changes of lipid organelles are in agreement with the biological uptake and storage model given in fig. 8.1. In the second column, the degree of acyl chain unsaturation is directly mapped for the three cells. A rather homogeneous map is obtained in the case of the unloaded cell, while the cells loaded with OxLDL and ELDL particles exhibit heterogeneous distributions with strong deviations of up to a factor of two around their averages. The mean of the unsaturation ratio is increasing from 3.6 for the unloaded, to 5 for the OxLDL-loaded and to 8.3 for the ELDL loaded cells. Among all cell types studied, not only the mean value of the cell is highest for ELDL-loaded cells, but also the highest image pixel values are found in this cell type. In the third column, the amplitude ratio representing the acyl chain length of lipids is mapped for the same three cells. All types of cells have approximately the same mean value of 4.5. However, the unloaded cell has a slightly higher mean value than the OxLDL- and ELDL-loaded cells. The chain length ratio map of the unloaded cell again appears more homogeneous, while the corresponding maps of the OxLDL- and ELDL-loaded cells show image pixel ratio values that vary by a factor of up to two around their mean values.

When the values for the acyl chain length n_{C-C} and for the degree of the acyl chain unsaturation $n_{C=C}$ would be extracted from tab. 7.4, rapidly growing errors have to be expected for values that are not contained in the series of the FAME model lipids used in the calibration. To avoid these errors, the observed differences in the spatial distribution maps representing the chain length n_{C-C} and of the degree of acyl chain unsaturation $n_{C=C}$ and their mutual correlation will next be statistically analyzed by means of two-dimensional histograms of the ratios $r_{C-C} = \frac{A(1440\ cm^{-1}) + A(1460\ cm^{-1})}{A(1740\ cm^{-1})}$ and $r_{C=C} = \frac{A(3005\ cm^{-1})}{A(1740\ cm^{-1})}$, representing the acyl chain length n_{C-C} and the degree of acyl chain unsaturation $n_{C=C}$, respectively. The upper row of fig. 8.4 plots the two-dimensional histograms using only the pixel spectra of maximum intensity inside the selected lipid organelles in those unloaded, OxLDL-loaded, and ELDL-loaded cells shown in fig. 8.3. For comparison, the lower row shows the corresponding two-dimensional histograms using all pixel spectra within the image mask of selected lipid-rich organelles. The lines represent the dependencies for the degree of acyl chain unsaturation where $n_{C-C} = 18$ is fixed (red line) and for the acyl chain length where $n_{C=C} = 1$ is fixed (green line), as observed for the FAME model compounds shown in figs. 7.18 and 7.16, respectively. The most narrow 2D-distribution is observed for the unloaded cell, as shown in the first column in fig. 8.4. Assuming 2D normal distributions, mean and standard deviation values of $(\langle r_{C=C} \rangle, \langle r_{C-C} \rangle) = (3.6, 4.7)$ and $(\delta_{r_{C=C}}, \delta_{r_{C-C}}) = (1.3, 0.7)$, respectively, are observed for all pixel spectra of organelles within the image mask, which agrees well with $(\langle r_{C=C} \rangle, \langle r_{C-C} \rangle) = (3.4, 4.7)$ and $(\delta_{r_{C=C}}, \delta_{r_{C-C}}) = (1.1, 0.7)$ observed when only the maximum pixel spectra of the selected lipid organelles are considered.
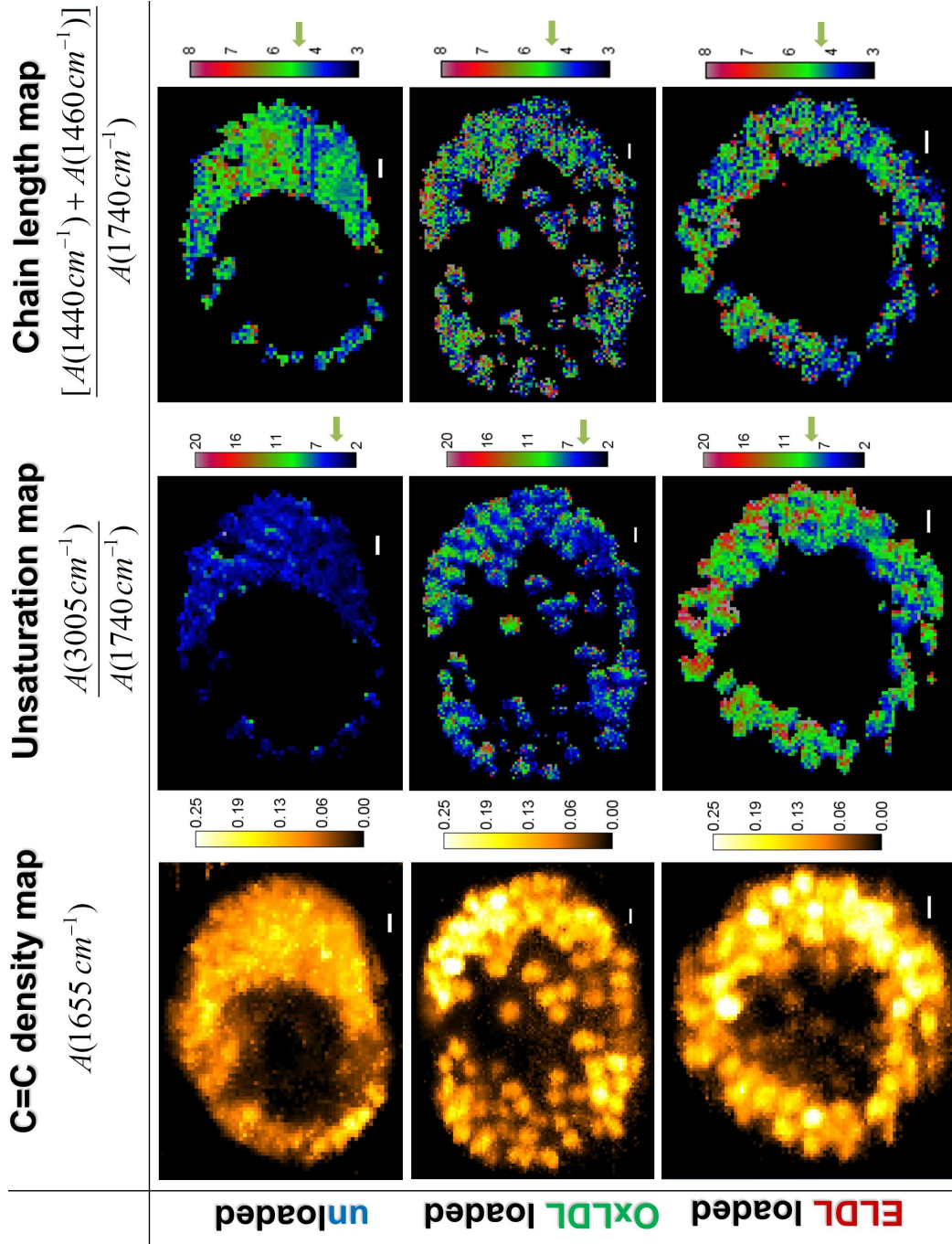
Figure 8.3: Comparison of the intracellular distribution maps of the density of cis $C = C$ stretching modes, the degree of $n_{C=C}$ acyl chain unsaturation and the degree of n_{C-C} chain length of lipids in representative unloaded, OxLDL-loaded, and ELDL-loaded HL-60 cells, using the peak amplitude at 1655 cm^{-1}, the peak amplitude ratios $\frac{A(3005\ cm^{-1})}{A(1740\ cm^{-1})}$, and $\frac{A(1440\ cm^{-1})+A(1460\ cm^{-1})}{A(1740\ cm^{-1})}$, respectively, of reconstructed $Im[\chi^{(3)}_{Res\ lipid}(\nu)]$ pixel spectra. The mean values of these ratios obtained by averaging all image pixels are indicated by arrows in the color lookup tables. All CARS measurements were recorded at the same powers of 30 mW pump and 15 mW Stokes and pixel integration times of 100 ms. The scan step sizes were 200 nm, 157 nm and 141 nm for the unloaded, the OxLDL-, and the ELDL-loaded HL-60 cells, respectively. Scale bars are 1 μm.

144
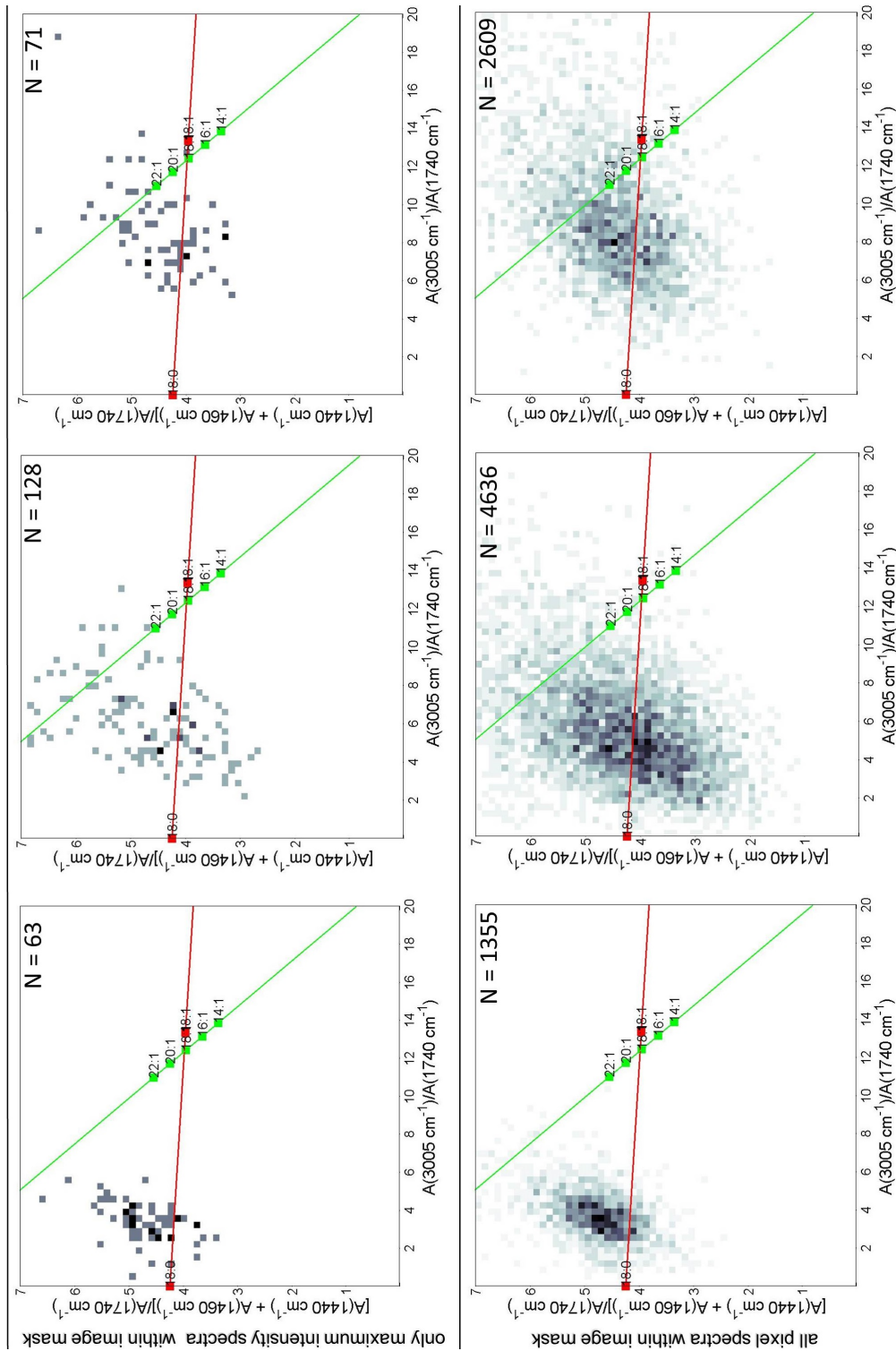
Figure 8.4: Two dimensional histograms of the amplitude ratios of $\langle r_{C-C} \rangle = \frac{A(1440\ cm^{-1}) + A(1460\ cm^{-1})}{A(1740\ cm^{-1})}$ and $\langle r_{C=C} \rangle = \frac{A(3005\ cm^{-1})}{A(1740\ cm^{-1})}$ that are representative for the chainlength and the degree of acyl chain unsaturation, respectively, of the unloaded, OxLDL-loaded, and ELDL-loaded HL-60 cells shown in fig. 8.3. Histograms are obtained by either considering only the pixels of maximum spectral intensities (upper row) or all pixel spectra within the image mask (lower row). Also shown are the calibration lines corresponding to the measurement of FAME lipid standards (tab. 7.4).

145

The comparison of $(\langle r_{C=C} \rangle, \langle r_{C-C} \rangle)$ with respect to the FAME calibration lines of $n_{C=C} = 1$ and $n_{C-C} = 18$ suggests a mean value (standard deviation) of 0.3(0.1) for the degree of unsaturation $\langle n_{C=C} \rangle$ and of 24(4) for the chainlength $\langle n_{C-C} \rangle$, respectively. However, concerning the distributions belonging to OxLDL-loaded cells, completely different pictures are obtained. The distributions are much broader when compared with the case of the unloaded cell.

For the OxLDL-loaded cell, the 2D-distribution over all pixel values within the lipid droplet organelle mask exhibits mean values of $(\langle r_{C=C} \rangle, \langle r_{C-C} \rangle) = (5.2, 4.3)$ with standard deviations of $(\delta_{r_{C=C}}, \delta_{r_{C-C}}) = (2.9, 1.4)$. These values correspond to a mean chain length value of $(\langle n_{C-C} \rangle = 22(7)$ and an average degree of acyl chain unsaturation of $\langle n_{C=C} \rangle = 0.4(0.2)$. However, within the broad distribution approximately half the pixel values are located below the line $n_{C-C} = 18$ with apparent low mean values of the number of $\langle n_{C=C} \rangle$ when compared with the case of the unloaded cell. Again, a very similar distribution is observed for the OxLDL-loaded cell, when only the maximum intensity spectra are used, where the mean values of $\langle r_{C=C} \rangle, \langle r_{C-C} \rangle) = (5.7, 4.5)$ and $(\delta_{r_{C=C}}, \delta_{r_{C-C}}) = (2.4, 1.4)$.

The broadest distribution is obtained for the ELDL loaded cell. Using a Gaussian fit, the distribution of all pixels within the lipid organelles mask yields $(\langle r_{C=C} \rangle, \langle r_{C-C} \rangle) = (8.6, 4.5)$ and $(\delta_{r_{C=C}}, \delta_{r_{C-C}}) = (3.2, 1.1)$. These values correspond to a mean (standard deviation) chain length value of $\langle n_{C-C} \rangle = 23(6)$ and for the degree of acyl chain unsaturation $\langle n_{C=C} \rangle = 0.6(0.2)$. The mean number of double bonds is approximately twice the value of that observed for the unloaded loaded cell. Note that some pixel spectra even indicate the existence of two double bonds! Again, a very similar distribution with $(\langle r_{C=C} \rangle, \langle r_{C-C} \rangle) = (8.0, 4.4)$ and $(\delta_{r_{C=C}}, \delta_{r_{C-C}}) = (2.4, 0.9)$ is obtained, when only the maximum pixel spectrum intensity of lipid organelles is considered. As for the other two cells samples, we conclude that the intracellular statistics is not influenced by choosing the spectra with maximum densities of lipids only.

8.3.3 Control experiments

In order to evaluate the origin of the observed lipid heterogeneity in the living HL-60 cells, we have performed two control experiments. First, we tested if the diffusion dynamics of the cell will cause the apparent heterogeneity. Second, by imaging individual polystyrene beads in aqueous environment, which act as model systems for individual intracellular organelles of similar sizes but having a well defined homogeneous distribution of Raman peak amplitudes throughout the bead, we tested the intrinsic limit for the distribution width and the accuracy of reconstructing $Im[\chi_{Res}^{(3)}(v)]$ amplitudes.

8.3.3.1 Time dynamics of lipid organelles inside the living cell

A representative organelle inside an OxLDL-loaded cell is shown in fig. 8.5, where the peak amplitudes $A(1655\ cm^{-1})$ of the reconstructed $Im[\chi^{(3)}_{Res\ lipid}(\nu)]$ are mapped in the x-y plane together with their corresponding z-y cross-section map of a single selected lipid organelle. With
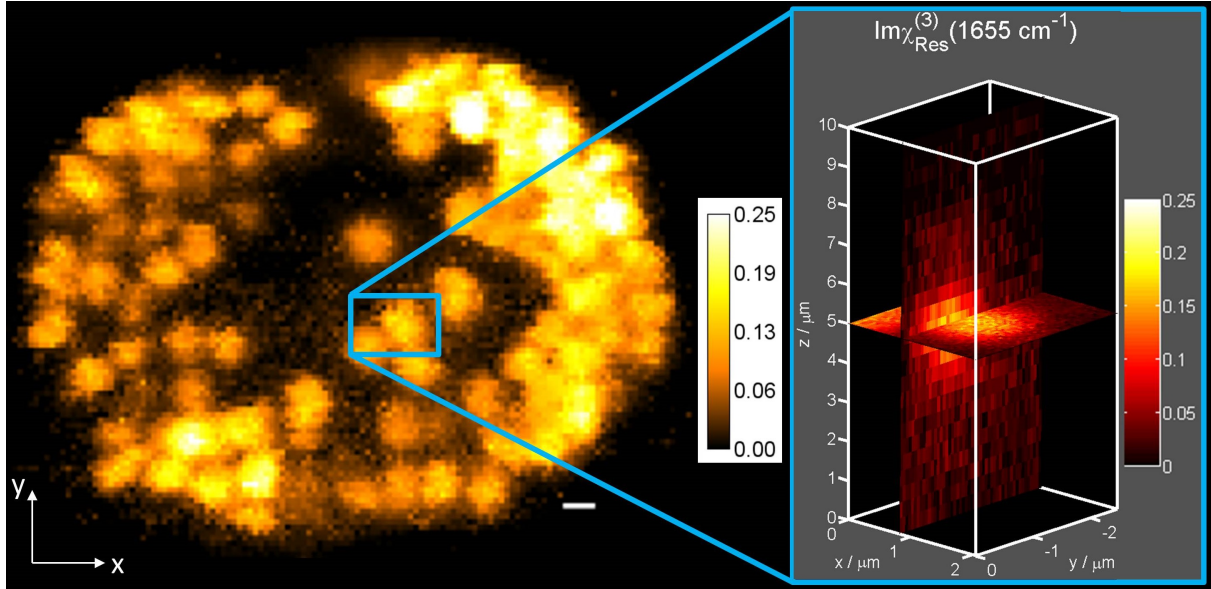
Figure 8.5: Density maps of $C = C$ stretching modes using the peak amplitude of $Im[\chi^{(3)}_{Res\ lipid}(\nu)]$ at 1655 cm^{-1} for a HL-60 cell loaded with OxLDL particles. Measurement conditions were 30 mW and 15 mW for the pump and Stokes beams, respectively. The pixel dwell time was 100 ms. The scan step sizes were 157 nm in the x-y map of the whole cell. The 3D zoom-in was scanned in steps of 49 nm and 400 nm for the x-y and z-y cross-section maps, respectively. The scale bar is 1 μm.

a pixel dwell time of 100 ms and 150×109 pixel spectra for the whole cell map, every 15 seconds, a new line was scanned. It is interesting to investigate the time scales of possible dynamics of lipid organelles in the cells. For the same lipid organelle shown in the close-up image in fig. 8.5, a time series was measured over almost 4 minutes, taking a spectrum every 100 ms without moving the scan table. The temporal profiles of the total $Im[\chi^{(3)}_{Res\ lipid}(\nu)]$ amplitudes integrated within the range from 2600 cm^{-1} to 3050 cm^{-1} (red curve) and the relative fraction of water (blue curve) are shown in fig. 8.6. One observes relative changes in the order of 12 % on the time scales of seconds. When the temporal profile of the relative fraction of water in the focal volume is compared with that of the integrated lipid amplitudes, they show an anticorrelation in time with relative changes of > 30% on the time scale of minutes (see times > 100 sec). This is not too surprising for a living and therefore dynamic system. The observed dynamics must be caused by tiny movements of either the lipid organelle inside the cell, or the whole cell on the sub-μm level. The time scale of the slow diffusion dynamics is much higher than the mentioned
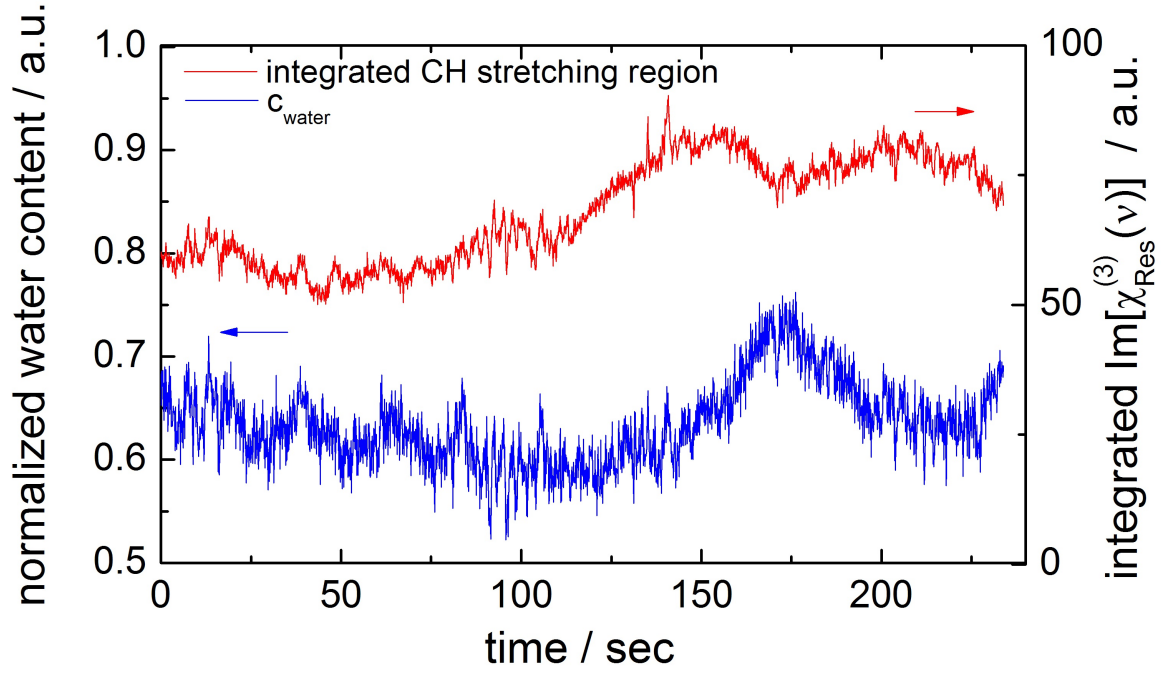
Figure 8.6: Temporal profiles of the integrated $Im[\chi^{(3)}_{Res\ lipid}(\nu)]$ spectrum (red curve) after subtraction of the scaled mean cytosplasm spectrum and of the relative water content (blue curve), when focussed on the single lipid organelle inside the OxLDL-loaded cell shown in the 3D zoom-in in fig. 8.5. The spectrum integration time is 100 *ms* for the object and reference spectrum, the total length of the time series is 234 seconds. Powers are 30 *mW* and 15 *mW* for the pump and Stokes beams, respectively.

15 seconds, a line scan takes. Therefore, the effect of cell dynamics or intracellular organelle dynamics on neighboring pixel spectra is assumed to be negligible.

8.3.3.2 Mapping the homogeneous chemical distribution inside a single 750 nm-polystyrene bead

Next, the pixel-to-pixel accuracy of the reconstructed $Im[\chi^{(3)}_{Res}(\nu)]$ for a well defined microscopic model system with homogeneous chemical composition will be investigated. Fig. 8.7 A shows a representative $Im[\chi^{(3)}_{Res}(\nu)]$ spectrum when focussed on a single polystyrene (PS) bead (see the diploma thesis by Stefan Gomes da Costa [147]). Subsequent to its CARS spectral imaging, each reconstructed pixel spectrum has been fitted to a sum of Lorentzian bands, resulting in a map of $Im[\chi^{(3)}_{Res}(\nu)]$ amplitudes at 3030 cm^{-1}, shown in the insert. The corresponding statistical distribution of normalized peak amplitude values at 3030 cm^{-1}, where normalization is performed with the total spectrum integrated from 2700 cm^{-1} to 3400 cm^{-1}, is shown in fig. 8.7 B. The width of the normalized amplitude distribution is a measure for the relative error of the reconstruction within the microscopic beads of homogeneous chemical composition. The standard deviation is ± 6.2%. Consequently, only relative amplitude changes exceeding this value
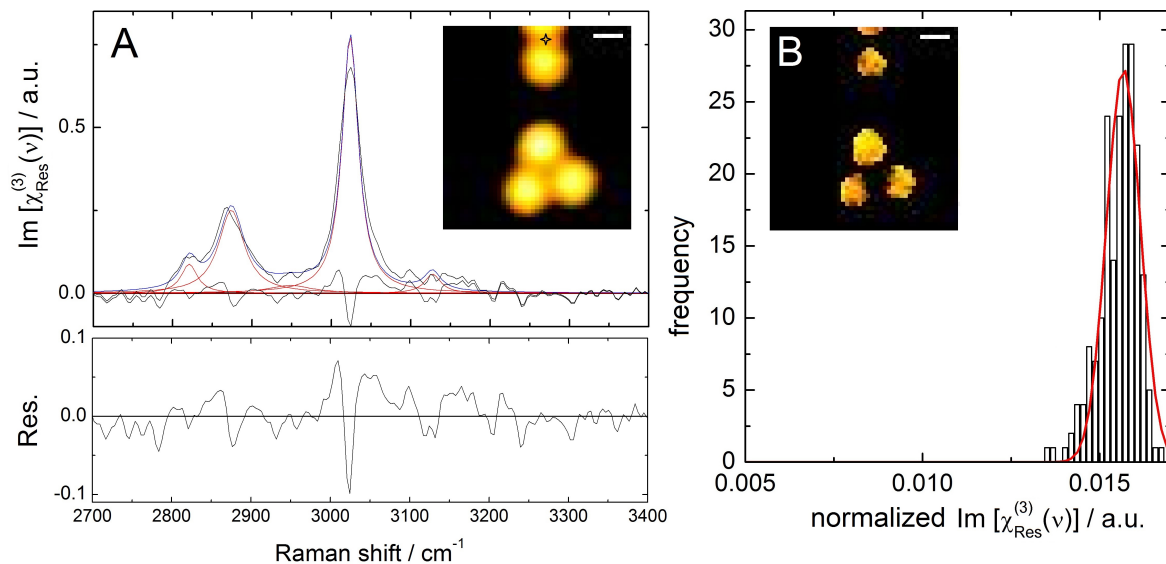
Figure 8.7: Control experiment that maps the homogeneous chemical distribution inside 750 nm-beads in water. (A) Reconstructed $Im[\chi_{Res}^{(3)}(\nu)]$ pixel spectrum recorded at the position indicated in the insert map together with a fit to Lorentzian bands. The insert shows the map of peak amplitudes of the Lorentzian band centered at 3030 cm^{-1}. (B) The corresponding histogram of peak amplitudes exhibits a narrow distribution with a relative FWHM of 12.4%. The insert shows the map of peak amplitudes when normalized by the sum of the areas of all Lorentzian bands of the fits. The scale bars are 500 nm. The measurement step size is 68.3 nm. Powers are 20 mW and 5 mW for the pump and Stokes beams, respectively. The spectrum integration time is 100 ms for the object and reference spectrum (see the diploma thesis by Stefan Gomes da Costa [147]).

will be considered to be significant for the identification of lipid composition heterogeneities inside living cells.

8.3.4 Determination of the composition of lipids

We next will compare the mean reconstructed $Im[\chi_{Res}^{(3)}(\nu)]$ spectra of the lipid organelles and cytoplasms of the different types of cells. In fig. 8.8, the cytoplasm spectra used in the reconstruction to obtain the pure lipid spectra are compared for all three cell types. Vibrational bands can be observed at 580 cm^{-1} and 747 cm^{-1} (assigned to tryptophane), at 1021 cm^{-1} (assigned to phenylalanine) and at 1114 cm^{-1} (assigned to C-C, respectively C-N stretching vibrations in proteins). In the spectral range from 1200 cm^{-1} to 1700 cm^{-1}, first the amide III appears around 1250 cm^{-1}, followed by the CH_2 bending mode at 1450 cm^{-1}. The amide II appears as a shoulder at approximately 1550 cm^{-1} of the amide I at 1664 cm^{-1} with both being on top of the bending mode of water at 1629 cm^{-1}. In the CH-stretching region, all cytoplasm spectra show signatures typical for proteins with the maximum intensity at about 2930 cm^{-1}. The spectra

149
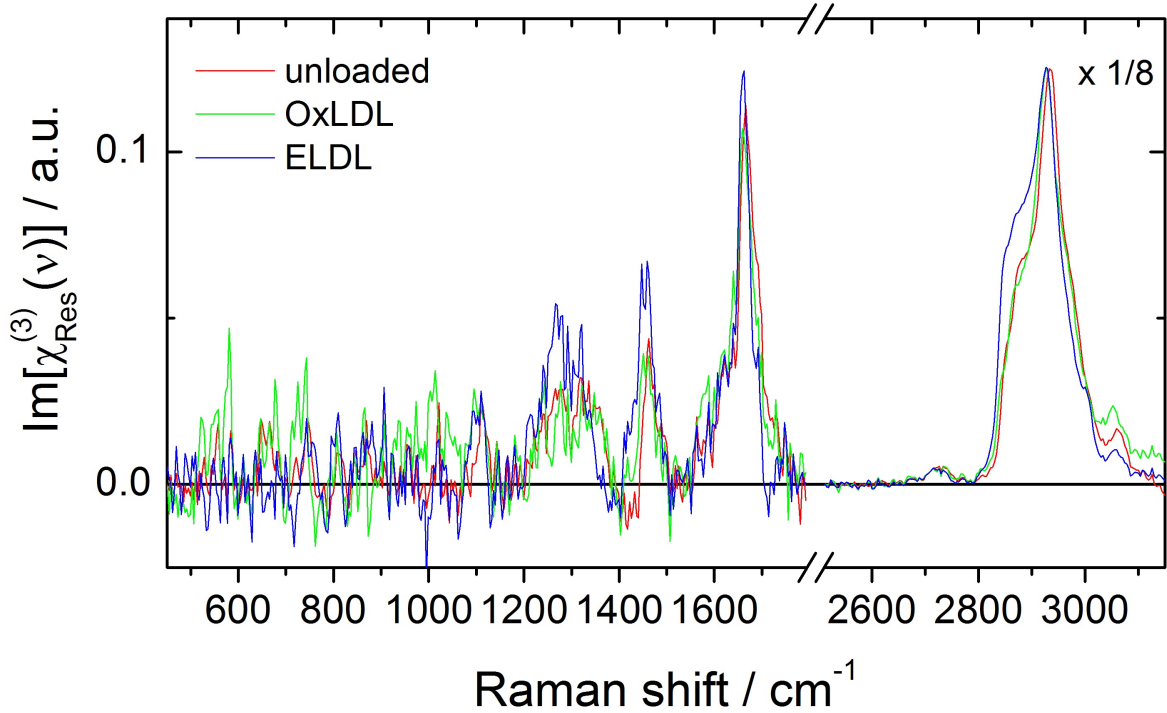
Figure 8.8: Mean cytoplasm spectra of the unloaded, the OxLDL-loaded, and the ELDL-loaded HL-60 cells shown in fig. 8.3, as obtained by spatial averaging over 617, 1064, and 619 spectra, respectively. All three CARS measurements were recorded at 30 mW and 15 mW for the pump and Stokes beams, respectively. The pixel spectrum integration time was 100 ms. All spectra are normalized to the peak intensity at 2930 cm^{-1} assigned to the CH_2 asymmetric stretch vibrations of proteins. Spectra in the CH-stretching region are scaled down by $\frac{1}{8}$.

represent a mixture of cytoplasmic proteins, but do not show any spectral features of lipids. No significant differences between the three types of cells are observed.

In fig. 8.9, the mean spectra of the selected pure lipid droplet organelles belonging to these three cells are compared. Note the striking similarity when compared with the spontaneous Raman spectra of the FAME model lipids presented in figs. 7.6 and 7.8, or with the reconstructed $Im[\chi_{Res}^{(3)}(\nu)]$ spectra of the FAME model lipids shown in figs. 7.16 and 7.18. All major bands found in the FAME model lipids can also be found in the mean lipid organelle spectra. When the normalized mean lipid organelle spectra are compared regarding the different LDL particle loading, the following four observations are noticeable. First, the normalized spectra show almost the same peak intensities at 1080 cm^{-1}, 1300 cm^{-1}, and 1440 cm^{-1}, which indicates that the mean lipid chain lengths are comparable. This is in agreement with the maps of the chain length given in fig. 8.3, which have similar contrast. Second, we observe a trend of increasing peak amplitudes of $Im[\chi_{Res}^{(3)}(\nu)]$ at 870 cm^{-1}, 1267 cm^{-1}, 1655 cm^{-1}, and at 3005 cm^{-1}, when going from the unloaded, OxLDL-loaded, to the ELDL-loaded cell. Consequently, the mean
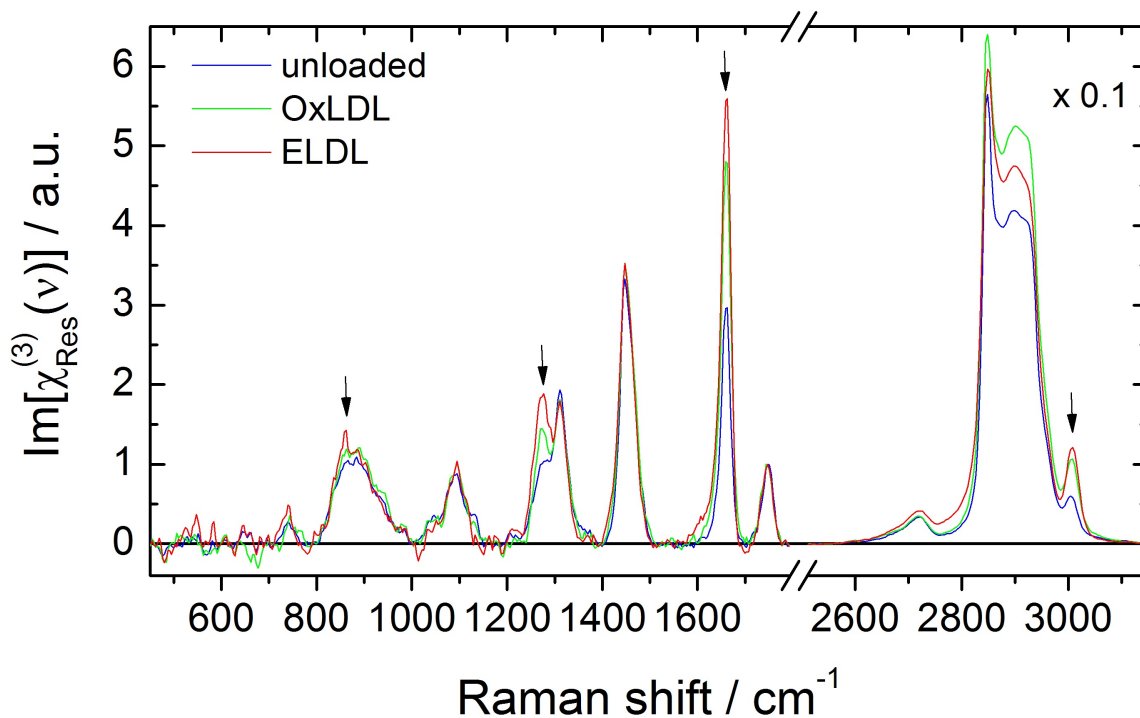
Figure 8.9: Mean spectra of selected lipid droplets organelles of the unloaded, the OxLDL-loaded, and the ELDL-loaded HL-60 cells shown in fig. 8.3, as obtained by averaging over 63, 128, and 71 lipid organelles, respectively. All three CARS measurements were recorded at 30 mW and 15 mW for the pump and Stokes beams, respectively. The pixel spectrum integration time was 100 ms. All spectra are normalized to the peak intensity at 1740 cm^{-1} assigned to the C=O-bond. Spectra are scaled down in the CH-stretching region by a factor of 0.1

degree of unsaturation follows a trend as $\langle n_{C=C\ unloaded} \rangle < \langle n_{C=C\ OxLDL\ loaded} \rangle < \langle n_{C=C\ ELDL\ loaded} \rangle$, which is again in agreement with the increase of contrast in the map of the degree of the acyl chain unsaturation shown in fig. 8.3. To conclude, while the mean cytoplasm spectra do not, the mean lipid organelle spectra clearly allow to differentiate between the cells. However, the mean lipid organelle spectra are not identical with the mean reconstructed $Im[\chi^{(3)}_{Res}(\nu)]$ spectra of the pure LDL particle solutions (see fig. 7.20 presented in ch. 7). This indicates that between uptake and storage the living cell has influenced the lipid composition of the LDL particles.

As shown in fig. 8.9, the mean reconstructed $Im[\chi^{(3)}_{Res}(\nu)]$ spectra of the selected lipid organelles do not reveal spectral features typical for CEs, Chol, or oxysterols. Consequently, the lipid organelle spectra are well described by using a linear combination of the simple FAME standard spectra. Though FAMEs are not present in cells, here we exploit the fact that they are spectrally almost identical to TAGs (see the molecular structure in fig. 7.1 and the spontaneous Raman spectrum in fig. 7.3), that make up the organelles. Therefore, the results for FAMEs listed in tab. 7.4 will be used in order to estimate the chain length and their degree

of acyl chain unsaturation in the organelle. In fig. 8.10, the mean reconstructed reconstructed
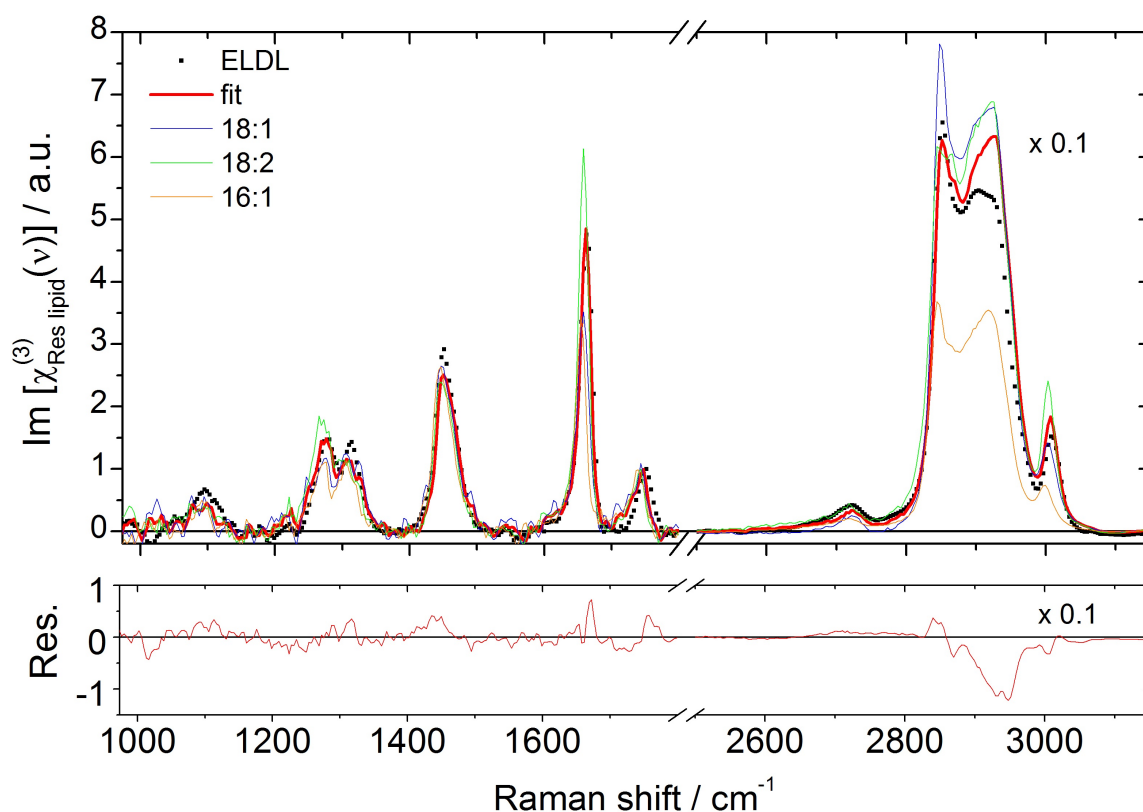
Figure 8.10: Linear decomposition of the mean spectrum of identified lipid organelles in the ELDL-loaded cell shown in fig. 8.3 into the 16:1, 18:1, and 18:2 FAME lipid basis spectra. Spectra (see fig. 7.16 and fig. 7.18) in the CH-stretching region are scaled down by a factor of 0.1.

$Im[\chi_{Res}^{(3)}(\nu)]$ spectra of all 71 selected lipid organelles in the ELDL-loaded cell, shown in fig. 8.3, is plotted together with the mean reconstructed $Im[\chi_{Res}^{(3)}(\nu)]$ spectra of the 16:1, 18:1, and 18:2 FAMEs. Also shown is the best fit result of a linear combination of these three FAMEs, resulting in relative weights of 30.8% 18:1, 53.8% 18:2, and 15.4% 16:1 FAMEs, respectively. Less good agreement is observed in the spectral region from 2880 cm^{-1} to 2960 cm^{-1}, which can be explained by a possible presence of 16:0 FAME in the lipid organelles. The latter is not accounted for in the decomposition model, because no reconstructed $Im[\chi_{Res}^{(3)}(\nu)]$ spectrum is available. However, when we consult the spontaneous Raman spectrum of the 18:0 FAME, a linear combination including 16:0 would improve the result not only in the spectral region from 2880 cm^{-1} to 2960 cm^{-1}, but also at 1300 cm^{-1}, 1440 cm^{-1} and 2850 cm^{-1} where saturated FAMEs have slightly higher relative intensities when compared with unsaturated FAMEs of the same chain length (see fig. 7.8).

Having estimated the mean acyl chain length and the mean degree of acyl chain unsaturation in the lipid organelles, we now have to compare our findings with the established gold standard

in lipid research: Fig. 8.11 summarizes the result of a typical mass spectroscopy measurement of THP-1 cells, which are another type of human monocytes, loaded with OxLDL and ELDL particles, as obtained by our collaboration partners at the Institute for Clinical Chemistry and Laboratory Medicine, University of Regensburg. In good agreement with the relative weights
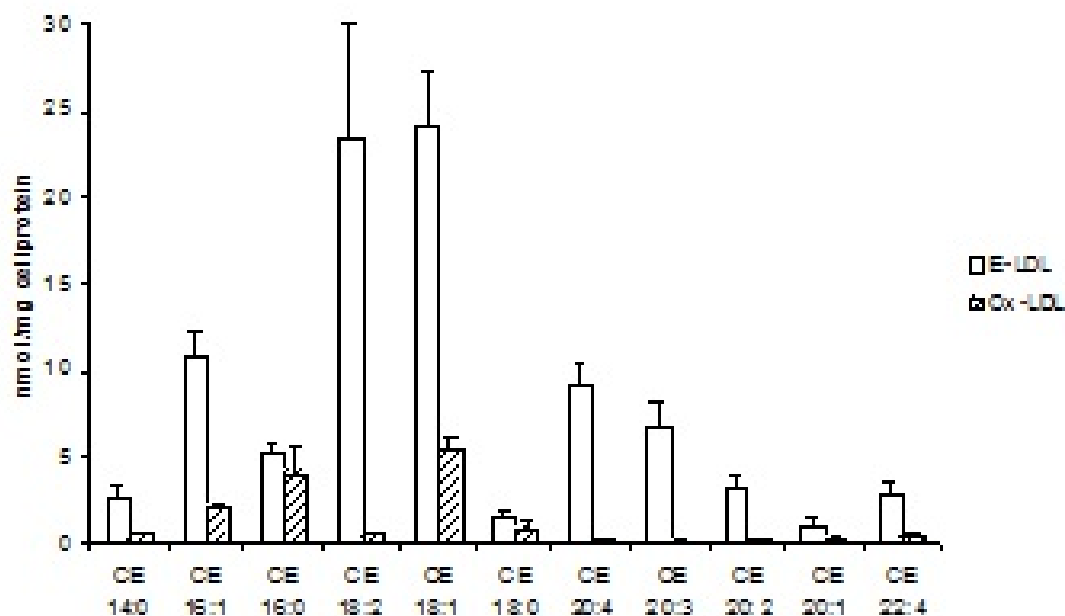
Figure 8.11: Mean concentrations of CEs species standards separated by their chain length and degree of acyl chain unsaturation for typical ELDL- and OxLDL-loaded THP1-cells, as obtained from mass spectroscopy experiments by Margot Grandl and Gerd Schmitz, Institute for Clinical Chemistry and Laboratory Medicine, University of Regensburg. Error bars represent ± the mean standard deviation.

obtained from the linear analysis of the mean spectrum of individual organelles in the ELDL-loaded cells, as shown in fig. 8.10, the mass spectroscopy results in a lipid composition of ELDL-loaded cells consisting primarily of equal parts of C18:1 and C18:2 fractions (see fig. 8.11). The relative fractions of those CE species sharing the same chain length n_{C-C} relative to the total of CE species in ELDL- and OxLDL-loaded THP-1 cells arranged according to their chain length n_{C-C} as obtained from mass spectroscopy are summarized in tab. 8.1. The relative fractions of those CE species sharing the same degree of acyl chain unsaturation $n_{C=C}$ relative to the total of CE species in ELDL- and OxLDL-loaded THP-1 cells arranged according to their degree of acyl chain unsaturation $n_{C=C}$ as obtained from mass spectroscopy are summarized in tab. 8.2. A mean (FWHM) of the chain length distribution of $\langle n_{C-C} \rangle = 18.1(2.7)$ and a mean (FWHM) degree of acyl chain unsaturation of $\langle n_{C=C} \rangle = 1.4(1.1)$ for ELDL-loaded THP-1 cells is obtained, when normal distributions are assumed. Compared with the values obtained

Table 8.1: Fractions of CE species sharing the same chain length n_{C-C} relative to the total of CE species in ELDL- and OxLDL-loaded THP-1 cells arranged according to their chain length n_{C-C} as obtained from mass spectroscopy (see fig. 8.11).

n_{C-C}	ELDL-loaded THP-1 cells	OxLDL-loaded THP-1 cells
14	0.023	0.05
16	0.16	0.37
18	0.50	0.44
20	0.20	0.05
22	0.03	0.05

Table 8.2: Fractions of CE species sharing the same degree of acyl chain unsaturation $n_{C=C}$ relative to the total of CE species in ELDL- and OxLDL-loaded THP-1 cells arranged according to their degree of acyl chain unsaturation $n_{C=C}$ as obtained from mass spectroscopy (see fig. 8.11).

$n_{C=C}$	ELDL-loaded THP-1 cells	OxLDL-loaded THP-1 cells
0	0.10	0.34
1	0.36	0.39
2	0.27	0.07
3	0.07	0.02
4	0.08	0.05

from the two-dimensional histogram shown in fig. 8.4, within the errors, these values are in agreement with the values obtained by the mass spectroscopy.

Using tabs. 8.1 and 8.2, an average chain length of $\langle n_{C-C} \rangle = 17.0(1.2)$ and an average degree of acyl chain unsaturation of $\langle n_{C=C} \rangle = 0.6(1.3)$ for OxLDL-loaded THP-1 cells is obtained, when normal distributions are assumed. When compared with the values obtained from the two-dimensional histograms, the values again match within the errors. Furthermore, most of the pixel spectra with a chain length below $\langle n_{C-C} \rangle = 14$ are observed in the two-dimensional histograms belonging to the cell loaded with OxLDL particles. The results obtained by mass and CARS spectroscopies are compared in tab. 8.3.

The comparison presented in tab. 8.3 demonstrates that the results obtained using mass and CARS spectroscopies agree within the error bars. Both techniques reveal the same trends. Twice the value of the mean degree of acyl chain unsaturation $\langle n_{C=C} \rangle$ and a small increase of

Table 8.3: Comparison of the means (standard deviations) of the distributions of the degree of unsaturation of $\langle n_{C=C} \rangle$ and the mean chain length $\langle n_{C-C} \rangle$ of the CE species in ELDL- and OxLDL-loaded THP-1 cells as obtained by using mass and CARS spectroscopies.

	ELDL-loaded cells	OxLDL-loaded cells
$\langle n_{C-C} \rangle$ obtained by mass spectroscopy	18.1(2.7)	17.0(1.2)
$\langle n_{C-C} \rangle$ obtained by CARS spectroscopy	23(6)	22(7)
$\langle n_{C=C} \rangle$ obtained by mass spectroscopy	1.4(1.1)	0.6(1.3)
$\langle n_{C=C} \rangle$ obtained by CARS spectroscopy	0.6(0.2)	0.4(0.2)

the mean acyl chain length $\langle n_{C-C} \rangle$ is observed for the ELDL-loaded cells when compared with the OxLDL-loaded cells.

8.4 Summary and conclusions

This chapter has demonstrated the characterization and mapping of chemical structure parameters of lipids, such as the mean degree of acyl chain unsaturation $\langle n_{C=C} \rangle$ and the mean acyl chain length $\langle n_{C-C} \rangle$ using CARS spectroscopy, based on the quantitative reconstruction of solely the pure vibrational response of the lipid component $Im[\chi^{(3)}_{Res\ lipid}(\nu)]$. Such a quantitative reconstruction of the lipid response only is possible based on the novel approach of reconstructing $Im[\chi^{(3)}_{Res}(\nu)]$ that was developed in chapter 5.

A comparison of the reconstructed vibrational response $Im[\chi^{(3)}_{Res\ lipid}(\nu)]$ of the LDL particle solutions with the mean response $Im[\chi^{(3)}_{Res\ lipid}(\nu)]$ of the lipid organelles of living cells after loading with these LDL particles revealed significant differences: Despite feeding LDL, known to contain Chol derivatives, to the cells, no clear spectral evidence of Chol derivatives was observed in the cells. All lipid droplet spectra are well described using the reconstructed $Im[\chi^{(3)}_{Res}(\nu)]$ spectra of the simple FAME model standards. This suggest that the cells did digest the LDL particles, and predominately TAG molecules are stored in the lipid organelles.

Concerning the comparison of unloaded, ELDL- and OxLDL-loaded cells, CARS spectroscopy revealed the presence of lipid organelles in all three types of cells. An increasing trend regarding both the size and the density of lipid organelles is observed when going from the unloaded to the OxLDL- and the ELDL-loaded cells. This result is in agreement with a previous fluorescence-based high-content study performed by Grandl and Schmitz [141], but using CARS spectroscopy this confirmation is obtained in a label-free manner! When going from the unloaded to the OxLDL- and the ELDL-loaded cells, the mean chemical structure

parameters $\langle n_{C=C} \rangle$ and $\langle n_{C-C} \rangle$ where found to increase and remain constant, respectively. Heterogeneous maps and rather broad distributions of the lipid structure parameters are obtained for the OxLDL- and ELDL-loaded cells, when compared with the unloaded cells. These results have not been observed inside a living cell to date. Control experiments demonstrated that neither fluctuations nor experimental shortcomings cause the observed broad distributions. All observed distributions of lipid structure parameters exceeding the relative standard deviation of $\pm$ 6.2% as obtained for PS beads of homogeneous chemical composition are considered to be genuine.

The comparison of the mean values of $\langle n_{C=C} \rangle$ and $\langle n_{C-C} \rangle$ obtained by using mass and CARS spectroscopies (see tab. 8.3) reveals a good agreement with each other. However, using CARS spectroscopy allows the investigation of individual lipid organelles in a living cell in space and time with sub-micron spatial resolution in a non-invasive manner. In contrast, mass spectroscopy, by its nature is invasive and relies on the measurement of an ensemble of many cells. On the other hand, it has a much higher resolution in differentiating lipid structure parameters allowing the identification of different chain lengths, where CARS only gives an average. CARS microspectroscopy thus was demonstrated to be a promising tool for spatial and/or time resolved live cell studies to answer open questions in lipidomics.

9 Conclusions and Outlook

A big part of this thesis deals with the mathematical and computational methodology needed for the quantitative analysis in CARS micro-spectroscopy that then was successfully applied to study systems ranging from the material sciences (see ch. 6) over biochemistry (see ch. 7) to medicine (see ch. 8). Therefore, a whole software bundle involving many subroutines needed to be developed (see ch. 4). Windowing at the spectral ends was removed by using a real-valued discrete cosine transform (DCT) instead of the FFT. This approach turned out to remove the same problem occuring when the Hilbert transform is used as well. Replacing the Levinson Durbin solver with a more advanced CPCG solver turned out to remove the windowing problem as well, but in addition drastically reduces the computational cost for the MEM based phase retrieval. The new and faster solver offers $O\left(N_0 log N_0\right)$ complexity and thus allows the real-time analysis of tenthousands of spectra per second. This fast solver is therefore well suited for time-critical applications and/or applications, where very long vectors need to be processed using MEM. This involves the application of MEM in fluorescence correlation spectroscopy (FCS, see [148]), real-time flood forecasting [149], image deconvolution [150] or the calculation of the Lyapunov exponent of chaotic systems [151]. The CPCG solver approach only needs several iteration steps and thus has reached its limits regarding the computation speed. However, the hierarchical $\mathfrak{H}$-Matrices introduced by Hackbusch in 1999 [87] are possibly a powerful alternative as they offer $O\left(N_0\right)$ complexity.

The really challenging problem solved was the development of a more general reconstruction scheme capable of giving exact results in all possible experimental cases involving cases, where all prior concepts fail. This concept is based on a more general model of coherent Raman spectra and it is this concept, that allows to deliver the correct $\chi^{(3)}_{Res}(\nu)$ for all potential experimental cases in a straightforward manner. Additional information regarding the electronic susceptibilities $\chi^{(3)}_E$ can now be extracted using the same setups previously used or even by re-analyzing old data. For the first time, the true vibrational susceptibility $\chi^{(3)}_{Res}(\nu)$ can be retrieved even in cases where $\chi^{(3)}_{Res}(\nu)$ exhibits strong spectral overlap with $\chi^{(3)}_E$. Now quantitative CARS micro-spectroscopy can be performed in unknown, complex and heterogeneous samples like biopolymers, tissues or living cells. Several possible applications of the newly developed methods in other fields come into mind, first other phase-sensitive spectroscopies such as e.g. sum

frequency generation [152], optical reflectance spectroscopy [153] or for cases in spontaneous Raman spectroscopy, where the line-shapes are of Breit-Wigner-Fano-type like the G-band in graphene [154]. In principle, the newly developed methods are interesting for all cases, where resonances (discrete states) are coherently coupled to an e.g. electronic continuum and the power spectrum of the corresponding complex function is measured. This involves cases like Fano coupling [155],[156], resonant ultrasound spectroscopy [157],[158],[159], and measurements of complex quantities such as the complex admittance of resonators in engineering [160].

The bilateral filter was demonstrated in this thesis to be a powerful tool regarding the denoising of reconstructed or spontaneous Raman spectra. The trilateral filter [161], an enhanced bilateral filter, seems to be even more powerful regarding the denoising. First tests regarding certain combinations of bilateral or trilateral filtering with SVD or its dimensionality matched extensions to tensors like PARAFAC (see [162]) or Tucker-n (see [163] for the three-dimensional case) have been promising not only regarding the improved reduction of noise, but as well regarding the possibility of a drastic reduction of storage needed for large reconstructed hyperspectra, when such tensor factorization techniques are used. The ultimate goal regarding both, denoising and data reduction, is an independent component analysis, where using the alternating least squares approach very promising first results have been obtained during the work involved in this thesis. The reconstruction approach developed in this thesis allows in principle to determine for a single CARS spectrum, how many individual species with different electronic susceptibilities $\chi_E^{(3)}$ are present. When performed in a frequency resolved manner, unsupervized background estimation is within reach. Furthermore two datasets are available: The measured spectra on the one hand and the integrated reconstructed spectra as a function of the effective phase ϕ_{eff} on the other. The determination of the effective phase ϕ_{eff} based on the ratio of maximum to minimum excursions in the retrieved estimated phase could help to reduce the number of fit parameters, when isolated resonances are present in the hyperspectral dataset.

Quantitative CARS micro-spectroscopy was applied in order to answer questions arising in material sciences. The conventional MEM-based reconstruction of $Im[\chi_{Res}^{(3)}(\nu)]$ was applied for the non-invasive 2D and 3D visualization of the micro-domain structure in polymers in ch. 6. The demonstration of very fast mapping of the crystallinity in PP and PE polymer thin films by CARS micro-spectroscopy raises expectations regarding the investigation of more complex polymer systems such as copolymers (mixtures of two or more polymers) or polymer blends. The identification of 7-keto-Chol in the OxLDL particle suspensions using CARS micro-spectroscopy offers the possibility to determine its concentration in human patients in a non-invasive and fast manner. However, in the same manner as 7-keto-Chol was identified, other lipids or proteins could be detected. Concerning the calibration using lipid models, the complex landscape spanned by the parameters chain length and number of double bonds would need to be sampled using more calibration points. This would allow to formulate a better model and would

then allow to transform the intensity ratios into absolute values of chain length and number of double bonds for a bigger range of possible combinations of chain length and number of double bonds. The demonstrated capabilities of CARS micro-spectroscopy characterizing the average lipid composition in single lipid organelles in living cells can be transferred to other systems such as investigating lipid bilayers, lipid domains or the secondary structure of proteins such as collagen. Fast characterization of lipids and proteins in living cells or tissue is essential in lipid research, where both, high speed data acquisition and non-invasiveness is highly desirable. This is why lipid research is a growing application of CARS micro-spectroscopy. In summary, the results achieved in this thesis are of high interest for the field of CARS micro-spectroscopy and beyond. The main results are currently prepared for publication.

10 Acknowledgments

11 Bibliography

[1] H. A. Rinia, K.N.J. Burger, M. Bonn, and M. Müller. Quantitative Label-Free Imaging of Lipid Composition and Packing of Individual Cellular Lipid Droplets Using Multiplex CARS Microscopy. *Biophysical Journal*, **95**(10):4908–4914, 2008.

[2] C.H.Jr. Camp, Y.L. Lee, J.M. Heddleston, C.M. Hartshorn, A.R.H. Walker, J.N. Rich, J.D. Lathia, and M.T. Cicerone. High-speed coherent Raman fingerprint imaging of biological tissues. *Nature photonics*, **8**:627–634, 2014.

[3] K.H. Hellwege. *Einführung in die Physik der Molekülen.* Heidelberger Taschenbücher. Springer, Heidelberg, 1974.

[4] A.D. Long. *The Raman Effect: A Unified Treatment of the Theory of Raman Scattering by Molecules.* John Wiley and Sons, West Sussex, 2002.

[5] F. Siebert and P. Hildebrandt. *Vibrational spectroscopy in life science.* Wiley-VCH, Weinheim, 2008.

[6] S. Mukamel. *Principles of Nonlinear Optical Spectroscopy.* Oxford University Press, New York, 1995.

[7] A. Smekal. Zur Quantentheorie der Dispersion. *Die Naturwissenschaften*, **11**(43):873–875, 1923.

[8] C.V. Raman and K.S. Krishnan. A New Type of Secondary Radiation. *Nature*, **121**(3048):501–502, 1928.

[9] G.S. Landsberg and L.I. Mandelstam. Eine neue Erscheinung bei der Lichtzerstreuung in Krystallen. *Naturwissenschaften*, **16**(28):557–558, 1928.

[10] C.V. Raman. A change of wavelength in light scattering. *Nature*, **121**:619, 1928.

[11] H.W. Schrotter and H.W. Klockner. *Raman scattering cross sections in gases and liquids.*, volume 11 of *Topics in Current Physics*. Springer, Berlin, 1979.

[12] G. Placzek. *Handbuch der Radiologie.*, volume 6. Akademische Verlagsgesellschaft, Leipzig, 1934.

[13] D. Heiman, R.W. Hellwarth, M.D. Levenson, and G. Martin. Raman-Induced Kerr Effect. *Phys. Rev. Lett.*, **36**(4):189–192, 1976.

[14] P.D. Maker and R.W. Terhune. Study of Optical Effects Due to an Induced Polarization Third Order in the Electric Field Strength. *Physical Review*, **137**(3A):A801–A817, 1965.

[15] A. Volkmer. Vibrational imaging and microspectroscopies based on coherent anti-Stokes Raman scattering microscopy. *Journal of Physics D: Applied Physics*, **38**(5):R59–R81, 2005.

[16] R.W. Boyd. *Nonlinear Optics.* Academic Press, Burlington, 3 edition, 2008.

[17] M.A. Yuratich and D.C. Hanna. Coherent anti-Stokes Raman spectroscopy (CARS). *Molecular Physics*, **33**(3):671–682, 1977.

[18] D.A. Kleinmann. Nonlinear Dielectric Polarization in Optical Media. *Phys. Rev. Lett.*, **126**(6):1977–1979, 1962.

[19] J.X. Cheng, A. Volkmer, L.D. Book, and X.S. Xie. An Epi-Detected Coherent Anti-Stokes Raman Scattering (E-CARS) Microscope with High Spectral Resolution and High Sensitivity. *J. Phys. Chem. B*, **105**(7):1277–1280, 2001.

[20] S.A.J. Druet, B. Attal, T.K. Gustafson, and J.-P. E. Taran. Electronic resonance enhancement of coherent anti-Stokes Raman scattering. *Phys. Rev. A*, **18**(4):1529–1557, 1978.

[21] A. Voroshilov, C. Otto, and J. Greve. On the coherent vibrational phase in polarization sensitive resonance CARS spectroscopy of copper tetraphenylporphyrin. *J.Chem.Phys.*, **106**(7):2589–2598, 1997.

[22] G.W.H. Wurpel, J.M. Schins, and M. Müller. Direct Measurement of Chain Order in Single Phospholipid Mono- and Bilayers with Multiplex CARS. *J. Phys. Chem. B*, **108**(11):3400–3403, 2004.

[23] A. Burian, P. Kuosmanen, and C. Rusu. 1-D direct phase retrieval. *Signal Processing*, **82**(8):1059–1066, 2002.

[24] J.W. Fleming and C.S. Johnson Jr. A Practical Analysis for Coherent Anti-Stokes Raman Scattering (CARS) Spectra. *Journal of Raman Spectroscopy*, **8**(5):284–290, 1979.

[25] R. de L. Kronig. On the Theory of Dispersion of X- Rays. *Journal of the Optical Society of America.*, **12**(6):547–557, 1926.

[26] H.A. Kramers. La diffusion de la lumière par les atomes. *in Atti del Congresso Internazionale dei Fisici*, **2**:545–557, 1928.

[27] E. Vartiainen. Phase retrieval approach for coherent anti-Stokes Raman scattering spectrum analysis. *Journal of the Optical Society of America.*, **9**(8):1209–1214, 1992.

[28] J.M. Bostick and L.A. Carreira. Fourier-Domain Analysis of Complex Line Shapes. *Applied Spectroscopy*, **43**(1):38–44, 1989.

[29] P.P. Kircheva and G.B. Hadjichristov. Kramers-Kronig relations in FWM spectroscopy. *J. Phys. B: At. Mol. Opt. Phys.*, **27**:3781–3793, 1994.

[30] N. Kirov and G.B. Hadjichristov. Nonlinear optics in materials: integral transformation of optical four-wave mixing spectra. *Journal of materials science: Materials in electronics*, **14**:725–728, 2003.

[31] M.T. Cicerone, K.A. Aamer, Y.J. Lee, and E. Vartiainen. Maximum entropy and time-domain Kramers-Kronig phase retrieval approaches are functionally equivalent for CARS microspectroscopy. *J. Raman Spectrosc.*, **43**:637–643, 2012.

[32] E. Vartiainen and K.-E. Peiponen. Meromorphic degenerate nonlinear susceptibility: Phase retrieval from the amplitude spectrum. *Physical Review B*, **50**(3):1941–1944, 1994.

[33] S.M. Kay and S.L. Marple. Spectrum Analysis - A Modern Perspective. *Proceedings of the IEEE*, **69**(11):1380–1419, 1981.

[34] E.T. Jaynes. *Where do we stand on maximum entropy?* in The Maximum Entropy Formalism. M. I. T. Press, Cambridge, 1979.

[35] E.T. Jaynes. On The Rationale of Maximum-Entropy Methods. *Proceedings of the IEEE*, **70**(9):939–942, 1982.

[36] E.T. Jaynes. *Where do we go from Here?* in Maximum-Entropy and Bayesian Methods in Inverse Problems. D. Reidel, Dordrecht, 1985.

[37] S. Haykin. *Nonlinear Methods of Spectral Analysis.* Springer Verlag, Berlin, 2nd. edition, 1983.

[38] K.-E. Peiponen. *Dispersion, Complex Analysis and Optical Spectroscopy.* Springer Tracts in Modern Physics. Springer, Berlin Heidelberg, 1999.

[39] J.P. Burg. *Maximum entropy spectral analysis.* PhD thesis, Stanford University, 1975.

[40] J.A. Edward and M.M. Fitelson. Notes on Maximum-Entropy Processing. *IEEE transactions on Information theory*, **19**(2):232–234, 1973.

[41] C.E. Shannon. A Mathematical Theory of Communication. *Bell System Technical Journal*, **27**(3):379–423, 1948.

[42] A. Van den Bos. Alternative interpretation of maximum entropy spectral analysis. *IEEE transactions on Information theory*, **17**(4):493 – 494, 1971.

[43] J. Makhoul. Linear Prediction: A Tutorial Review. *Proceedings of the IEEE.*, **63**(4):561–580, 1975.

[44] A. Bultheel and M. Van Barel. Linear prediction: mathematics and engineering. *Bull. Belg. Math. Soc.*, **1**(1), 1994.

[45] L. Marple. A New Autoregressive Spectrum Analysis Algorithm. *IEEE Trans. on Acoustics, Speech and Signal Processing*, **28**(4):441–454, 1980.

[46] F. Remacle and R.D. Levine. Time domain information from resonant Raman excitation profiles: A direct inversion by maximum entropy. *The Journal of Chemical Physics*, **99**(7):4908–4925, 1993.

[47] E. Vartiainen, H.A. Rinia, M. Müller, and M. Bonn. Direct extraction of Raman lineshapes from congested CARS spectra. *Optics Express*, **14**(8):3622–3630, 2006.

[48] E. Vartiainen, K.-E. Peiponen, and T. Asakura. Phase Retrieval in Optical Spectroscopy: Resolving Optical Constants from Power Spectra. *Applied spectroscopy*, **50**(10):1283–1289, 1996.

[49] W.H. Press. *Numerical Recipies in Fortran.*, volume 2nd. Cambridge University Press, New York, 1992.

[50] B.D. Beier and A.J. Berger. Method for automated background subtraction from Raman spectra containing known contaminants. *Analyst*, **134**(6):1198–1202, 2009.

[51] K. Böhmer. *Spline-Funktionen.* B.G.Teubner, Stuttgart, 1974.

[52] H. Akima. A New Method of Interpolation and Smooth Curve Fitting Based on Local Procedures. *Journal of the Association for Computing Machinery.*, **17**(4):589–602, 1970.

[53] J. Fried and S. Zietz. Curve Fitting by Spline and Akima Methods: Possibility of Interpolation Error and its Suppression. *Phys.Med. Biol.*, **18**(4):550–558, 1973.

[54] E.O. Potma, D.J. Jones, J.-X. Cheng, X.S. Xie, and J. Ye. High-sensitivity coherent anti-Stokes Raman scattering microscopy with two tightly synchronized picosecond lasers. *Optics Letters*, **27**(13):1168–1170, 2002.

[55] C. Camerlingo, F. Zenone, G.M. Gaeta, R. Riccio, and M. Lepore. Wavelet data processing of micro-Raman spectra of biological samples. *Measurement Science and Technology*, **17**(2):298–303, 2006.

[56] R.J. Meier. On art and science in curve-fitting vibrational spectra. *Vibrational Spectroscopy*, **39**(2):266–269, 2005.

[57] P.R. St-Pierre and N.O. Peterson. Relative ligand binding to small or large aggregates measured by scanning correlation spectrocopy. *Biophysical Journal*, **58**(2):503–511, 1990.

[58] N.O. Petersen, P.L. Höddelius, P.W. Wiseman, O. Seger, and K.-E. Magnusson. Quantitation of membrane receptor distributions by image correlation spectroscopy: concept and application. *Biophysical Journal*, **65**(3):1135–1146, 1993.

[59] A.K. Jain. *Fundamentals of digital image processing.* Information and systems sciences series. Prentice-Hall, Englewood Cliffs, 1989.

[60] J.W. Cooley and J.W Tukey. An Algorithm for the Machine Computation of the Complex Fourier Series. *Mathematics of Computation*, **19**(90):297–301, 1965.

[61] M.J. Narasimha and A.M. Peterson. On the Computation of the Discrete Cosine Transform. *IEEE trans. on Communications*, **26**(6):934–936, 1978.

[62] C. Benoit. Note sur une méthode de résolution des équations normales provenant de l'application de la méthode des moindres carrés à un système d'équations linéaires en nombre inférieur à celui des inconnues. *Bulletin Géodésique*, **2**:67–77, 1924.

[63] N. Levinson. The Wiener RMS (root-mean-square) error criterion in filter design and prediction. *J. Math. Phys.*, **25**:261–278, 1947.

[64] R.R. Bitmead and B.D.O. Anderson. Asymptotically fast solution of toeplitz and related systems of linear equations. *Linear Algebra and its Applications*, **34**:103–115, 1980.

[65] R.P. Brent, F.G. Gustavson, and D.Y.Y. Yun. Fast Solution of Toeplitz Systems of Equations and Computation of Padé Approximants. *Journal of Algorithms*, **1**(3):259–295, 1980.

[66] M. R. Hestenes and E. Stiefel. Methods of Conjugate Gradients for Solving Linear Systems. *Journal of Research of the National Bureau of Standards*, **49**(6):409–436, 1952.

[67] A. Meister. *Numerik linearer Gleichungssysteme.* Numerische Mathematik. Vieweg, Wiesbaden, 3.rd edition, 2008.

[68] J. Durbin. The Fitting of Time-Series models. *Review of the International Statistical Institute*, **28**(3):233–244, 1960.

[69] M.K. Ng. *Iterative Methods For Toeplitz Systems.* Numerical Mathematics and Scientific Computation. Oxford University Press, New York, 2004.

[70] W.F. Trench. An Algorithm for the Inversion of Finite Toeplitz Matrices. *Journal of the Society for Industrial and Applied Mathematics*, **12**(3):515–522, 1964.

[71] S. Zohar. Toeplitz Matrix Inversion: The Algorithm of W. F. Trench. *Journal of the Association for Computing Machinery*, **16**(4):592–601, 1969.

[72] G. Strang. A proposal for Toeplitz Matrix Calculations. *Stud.Appl.Math.*, **74**(2):171–176, 1986.

[73] J.R. Bunch. Stability of methods for solving Toeplitz systems of equations. *SIAM J. Sci. Stat. Comput.*, **6**(2):349–364, 1985.

[74] G.S. Ammar and W.B. Gragg. Superfast Solution of Real Positive Definite Toeplitz Systems. *SIAM Journal on Matrix Analysis and Applications*, **9**(1):61–76, 1988.

[75] P.J. Davis. *Circulant Matrices.* Wiley, New York, 1979.

[76] R.H. Chan and M.K. Ng. Conjugate Gradient Methods for Toeplitz Systems. *SIAM Review*, **38**(3):427–482, 1996.

[77] U. Grenander. *Toeplitz forms and their application.* Chelsea, New York, 1984.

[78] M.E. Domínguez-Jiménez and P.J.S.G. Feirreira. A New Preconditioner for Toeplitz Matrices. *IEEE Signal Processing Letters*, **16**(9):758–761, 2009.

[79] P.C. Hansen. Deconvolution and regularization with Toeplitz matrices. *Numerical Algorithms*, **29**(4):323–378, 2002.

[80] J.R. Shewchuk. An Introduction to the Conjugate Gradient Method Without the Agonizing Pain. Technical report, School of Computer Science, Carnegie Mellon University, 1994.

[81] G.H. Golub. *Matrix computations.* Johns Hopkins University Press, Baltimore, 3rd ed. edition, 1996.

[82] J.K. Reid. On the method of conjugate gradients for the solution of large sparse systems of linear equations. In *Large sparse sets of linear equations*. Academic Press, London, New York, 1971.

[83] J.P. Gram. Über die Entwicklung reeller Funtionen in Reihen mittels der Methode der kleinsten Quadrate. *Journal für die reine und angewandte Mathematik*, **94**:41–73, 1883.

[84] E. Schmidt. Zur Theorie der linearen und nichtlinearen Integralgleichungen. I. Teil: Entwicklung willkürlicher Funktionen nach Systemen vorgeschriebener. *Mathematische Annalen*, **63**:433–476, 1907.

[85] W.W. Hager and H. Zhang. A survey of nonlinear conjugate gradient methods. *Pacific journal of Optimization*, **2**(1):35–58, 2006.

[86] E. Polak and G. Ribiere. Note sur la convergence de méthodes de directions conjugées. *Rev. Fr. Inform. Rech. Oper.*, **3**(1):35–43, 1969.

[87] W. Hackbusch. A Sparse Matrix Arithmetic Based on H-Matrices. Part I: Introduction to H-matrices. *Computing*, **62**(2):89–108, 1999.

[88] R.R. Ernst. Numerical Hilbert Transform and Automatic Phase Correction in Magnetic Resonance Spectroscopy. *Journal of Magnetic Resonance*, **1**(1):7–26, 1969.

[89] G. Kanig. Kristallisier- und Schmelzvorgänge bei Polymeren. *Colloid & Polymer Science*, **260**(4):356–377, 1982.

[90] J.R. Isasi, L. Mandelkern, M.J. Galante, and R.G. Alamo. The Degree of Crystallinity of Monoclinic Isotactic Poly(propylene). *Journal of Polymer Science: Part B*, **37**(4):323–334, 1999.

[91] S. Saito, Y. Moteki, and M. Nakagawa. High-Resolution Solid-state 13C NMR Study of Isotactic Polypropylenes Isothermally Crystallized from the Melt. *Macromolecules*, **23**(13):3256–3260, 1990.

[92] M.A. Martynov and Vylegzhanina K.A. X-ray diffraction of polymers. *Khimiya*, 1972.

[93] A.S. Nielsen, D.N. Batchelder, and R. Pyrz. Estimation of crystallinity of isotactic polypropylene using Raman spectroscopy. *Polymer*, **43**(9):2671–2676, 2002.

[94] T. Hahn, W. Suen, S. Kang, S.L. Hsu, H.D. Stidham, and A.R. Siedle. An analysis of the Raman spectrum of syndiotactic polypropylene. 1. Conformational defects. *Polymer*, **42**(13):5813–5822, 2001.

[95] M. Arruebarrena de Báez, P.J. Hendra, and M. Judkins. The Raman spectra of oriented isotactic polypropylene. *Spectrochimica Acta Part A*, **51**(12):2117–2124, 1995.

[96] S.A. Gordeev, G.Y. Nikolaeva, and K.A. Prokhorov. Raman Spectroscopic Investigation of the Oriented Process of Linear Polyethylene. *Polymer Science Ser. A*, **38**(5):517–524, 1996.

[97] T. Hevonoja, M.O. Pentikäinen, M.T. Hyvönen, P.T. Kovanen, and M. Ale-Korpela. Structure of low density lipoprotein (LDL) particles: Basis for understanding molecular changes in modified LDL. *Biochimica et Biophysica Acta*, **1488**(3):189–210, 2000.

[98] E. Ikonen. Cellular cholesterol trafficking and compartmentalization. *Nat. Rev. Mol. Cell. Biol.*, **9**(2):125–138, 2008.

[99] H. Esterbauer, J. Gebicki, H. Puhl, and G. Jürgens. The role of lipid peroxidation and antioxidants in oxidative modification of LDL. *Free Radical Biology and Medicine*, **13**(4):341 – 390, 1992.

[100] S. Lund-Katz and C. Phillips. Packing of cholesterol molecules in human low-density lipoprotein. *Biochemistry*, **25**(7):1562–1568, 1986.

[101] A. Sommer, E. Prenner, R. Gorges, H. Stütz, H. Grillhofer, G.M. Kostner, F. Paltauf, and A. Hermetter. Organization of phosphatidylcholine and sphingomyelin in the surface monolayer of low density lipoprotein and lipoprotein(a) as determined by time-resolved fluorometry. *J. Biol. Chem.*, **267**(34):24217–24222, 1992.

[102] F. Lalanne, V. Pruneta, S. Bernard, and G. Ponsin. Distribution of diacylglycerols among plasma lipoproteins in control subjects and in patients with non-insulin-dependent diabetes. *European Journal of Clinical Investigation*, **29**(2):139–144, 1999.

[103] S.L. Schissel, J. Tweedie-Hardman, J.H. Rapp, G. Graham, K.J. Wiliams, and I. Tabas. Rabbit aorta and human atherosclerotic lesions hydrolyze the sphingomyelin of retained low-density lipoprotein. Proposed role for arterial-wall sphingomyelinase in subendothelial retention and aggregation of atherogenic lipoproteins. *J. Clin. Invest.*, **98**(6):1455–1464, 1996.

[104] A. Ravendi, A. Kuksis, and N.A. Shaikh. Glycated phosphatidylethanolamine promotes macrophage uptake of low density lipoprotein and accumulation of cholesteryl esters and triacylglycerols. *J. Biol. Chem.*, **274**(23):16494–6500, 1999.

[105] A.J. Brown and W. Jessup. Oxysterols: Sources, cellular storage and metabolism, and new insights into their roles in cholesterol homeostasis. *Molecular Aspects of Medicine*, **30**(3):111–122, 2009.

[106] A.J. Brown, R.T. Dean, and W. Jessup. Free and esterified oxysterol: formation during copper-oxidation of low density lipoprotein and uptake by macrophages. *Journal of Lipid Research*, **37**(2):320–335, 1996.

[107] M.A. Kamal and V.A. Raghunathan. Effect of ring-substituted oxysterols on the phase behaviour of dipalmitoylphosphatidylcholine membranes. *Eur. Biophys. J.*, **41**(10):891–900, 2012.

[108] G. Poli, B. Sottero, S. Gargiulo, and G. Leonarduzzi. Cholesterol oxidation products in the vascular remodeling due to atherosclerosis. *Molecular Aspects of Medicine*, **30**(9):180–189, 2009.

[109] B. Janoszka. 7-Ketocholesterol and 7-hydroxycholesterol in pork meat and its gravy thermally treated without additives and in the presence of onion and garlic. *Meat Science*, **86**(4):976–984, 2010.

[110] A.J. Brown, S.-L. Leong, R.T. Dean, and W. Jessup. 7-Hydroperoxycholesterol and its products in oxidized low density lipoprotein and human atherosclerotic plaque. *Journal of Lipid Research*, **38**(9):1730–1745, 1997.

[111] A.J. Brown and W. Jessup. Oxysterols and atherosclerosis. *Atherosclerosis*, **142**(1):1–28, 1999.

[112] H. Larsson, Y. Böttiger, L. Iuliano, and U. Diczfalusy. In vivo interconversion of 7β-hydroxycholesterol and 7-ketocholesterol, potential surrogate markers for oxidative stress. *Free Radical Biology Medicine*, **43**(5):695–701, 2007.

[113] G. Schmitz and M. Grandl. Endolysosomal phospholipidosis and cytosolic lipid droplet storage and release in macrophages. *Biochimica et Biophysica Acta - Molecular and Cell Biology of Lipids*, **1791**(6):524–539, 2009.

[114] E.G. Bligh and W.J. Dyer. A rapid method of total lipid extraction and purification. *Can. J. Biochem. Physiol.*, **37**(8):911–917, 1959.

[115] S. Bhakdi, M. Torzewski, M. Klouche, and M. Hemmes. Complement and atherogenesis: Binding of CRP to degraded, nonoxidized LDL enhances complement activation. *Arterioscler. Thromb. Vasc. Biol.*, **19**(10):2348–2354, 1999.

[116] E. Wieland, S. Parthasarathy, and D. Steinberg. Peroxidase-dependent metal-independent oxidation of low density lipoprotein in vitro: A model for in vivo oxidation? *Proc. Natl. Acad. Sci.*, **90**(13):5929–5933, 1993.

[117] S.P. Verma, J.R. Philippot, B. Bonnet, J. Sainte-Marie, Y. Moschetto, and D.F. Wallach. Resonance Raman spectra of beta-carotene in native and modified low-density lipoprotein. *Biochemical and biophysical research communications*, **122**(2):867–875, 1984.

[118] G. Liebisch, W. Drobnik, M. Reil, B. Trümbach, R. Arnecke, B. Olgemöller, A. Roscher, and G. Schmitz. Quantitative measurement of different ceramide species from crude cellular extracts by electrospray ionization tandem mass spectrometry (ESI-MS/MS). *Journal of Lipid Research*, **40**(8):1539–1546, 1999.

[119] B. Brügger, G. Erben, R. Sandhoff, F.T. Wieland, and W.D. Lehmann. Quantitative analysis of biological membrane lipids at the low picomole level by nano-electrospray ionization tandem mass spectrometry. *Proc. Natl. Acad. Sci.*, **94**(6):2339–2344, 1997.

[120] G. Liebisch, W. Drobnik, B. Lieser, and G. Schmitz. High-throughput quantification of lysophosphatidylcholine by electrospray ionization tandem mass spectrometry. *Clin. Chem.*, **48**(12):2217–2224, 2002.

[121] G. Liebisch, B. Lieser, J. Rathenberg, W. Drobnik, and G. Schmitz. High-throughput quantification of phosphatidylcholine and sphingomyelin by electrospray ionization tandem mass spectrometry coupled with isotope correction algorithm. *Biochimica et Biophysica Acta*, **1686**(1-2):108–117, 2004.

[122] G. Liebisch, M. Binder, R. Schifferer, T. Langmann, B. Schulz, and G. Schmitz. High throughput quantification of cholesterol and cholesteryl ester by electrospray ionization tandem mass spectrometry (ESI-MS/MS). *Biochimica et Biophysica Acta*, **1761**(1):121–128, 2006.

[123] B. Lieser, G. Liebisch, W. Drobnik, and G. Schmitz. Quantification of sphingosine and sphinganine from crude lipid extracts by HPLC electrospray ionization tandem mass spectrometry. *Journal of Lipid Research*, **44**(11):2209–2216, 2003.

[124] H.L.J. Makin and D.B. Gower. *Steroid analysis.* Analytical and Bioanalytical Chemistry. Springer, Dordrecht, London, 2nd edition, 2011.

[125] S. Bresson, M. El Marssi, and B. Khelifa. Raman spectroscopy investigation of various saturated monoacid triglycerides. *Chemistry and Physics of Lipids*, **134**(2):119–129, 2005.

[126] B. Muik, B. Lendl, A. Molina-Diaz, and M.J. Ayora-Canada. Direct monitoring of lipid oxidation in edible oils by Fourier transform Raman spectroscopy. *Chemistry and Physics of Lipids*, **134**(2):173–182, 2005.

[127] R.E. Oakes, J.R. Beattie, B.W. Moss, and S.E.J. Bell. DFT studies of long-chain FAMEs: Theoretical justification for determining chain length and unsaturation from experimental Raman spectra. *Journal of Molecular Structure (Theochem)*, **626**(1):27–45, 2003.

[128] E. Chicoye, W.D. Powrie, and O. Fennema. Synthesis, Purification and Characterization of 7-Ketocholesterol and Epimeric 7-Hydroxycholesterols. *Lipids*, **3**(6):551–556, 1968.

[129] V. Baeten, P. Hourant, M.T. Morales, and R. Aparicio. Oil and Fat Classification by FT-Raman Spectroscopy. *J. Agric. Food Chem.*, **46**(7):2638–2646, 1998.

[130] I.N. Sang, E.S. Min, Y.M. Jung, and M.S. Lee. Fermi Resonance and Solvent Dependence of the C=O Frequency Shifts of Raman Spectra: Cyclohexanone and 2-Cyclohexen-1-one. *Bull. Korean Chem. Soc.*, **22**(9):989–993, 2001.

[131] C. Krafft, L. Neudert, T. Simat, and R. Salzer. Near infrared Raman spectra of human brain lipids. *Spectrochimica Acta Part A*, **61**(7):1529–1535, 2005.

[132] S. Bresson, D. Bormann, and B. Khelifa. Raman studies of the C=C and C=O stretching modes in various cholesteryl alkanoates. *Physical Review E*, **55**(6):7429–7433, 1997.

[133] F. Capelle, F. Lhert, D. Blaudez, H. Kellay, and J.M. Turlet. Thickness and organization of black films using confocal micro-Raman spectroscopy. *Colloids and Surfaces A: Physicochemical and Engineering Aspects*, **171**(1-3):199–205, 2000.

[134] S. Bresson, D. Bormann, and B. Khelifa. Raman studies of the C-H stretching modes in various cholesteryl alkanoates. *Vibrational Spectroscopy*, **16**(2):163–171, 1998.

[135] M. Z. M. Rishard and J. Laane. Vibrational spectra of 2-cyclohexen-1-one and its 2,6,6-d3 isotopomer. *Journal of Molecular Structure (Theochem)*, **976**(1-3):56–60, 2010.

[136] C. E. Da Silva, P. Vandenabeele, H.G.M. Edwards, and L.F. Cappa de Oliveira. NIR-FT-Raman spectroscopic analytical characterization of the fruits, seeds, and phytotherapeutic oils from rosehips. *Analytical and Bioanalytical Chemistry*, **392**(7-8):1489–1496, 2008.

[137] J.R. Beattie, S.E.J. Bell, and B.W. Moss. A Critical Evaluation of Raman Spectroscopy for the Analysis of Lipids: Fatty Acid Methyl Esters. *Lipids*, **39**(5):407–419, 2004.

[138] Y. Takai, T. Masuko, and H. Takeuchi. Lipid structure of cytotoxic granules in living human killer T lymphocytes studied by Raman microspectroscopy. *Biochimica et Biophysica Acta*, **1335**(1-2):199–208, 1997.

[139] W. Rothman, F. Hirayama, and S. Lipsky. Fluorescence of saturated hydrocarbons. III. Effect of molecular structure. *The Journal of Chemical Physics*, **58**(4):1300–1317, 1973.

[140] S. Martin and R.G. Parton. Lipid droplets: A unified view of a dynamic organelle. *Nature Reviews Molecular Cell Biology*, **7**(5):373–378, 2006.

[141] M. Grandl and G. Schmitz. Fluorescent high-content imaging allows the discrimination and quantitation of E-LDL-induced lipid droplets and Ox-LDL-generated phospholipidosis in human macrophages. *Cytometry*, **77A**(3):231–242, 2010.

[142] R. Gallagher, S. Collins, J. Trujillo, K. McCredie, M. Ahearn, S. Tsai, R. Metzgar, G. Aulakh, R. Ting, F. Ruscetti, and R. Gallo. Characterization of the continuous, differentiating myeloid cell line (HL-60) from a patient with acute promyelocytic leukemia. *Blood*, **54**(3):713–733, 1979.

[143] S. Tsuchiya, M. Yamabe, Y. Yamaguchi, Y. Kobayashi, T. Konno, and K. Tada. Establishment and characterization of a human acute monocytic leukemia cell line (THP-1). *International Journal of Cancer*, **26**(2):171–176, 1980.

[144] C.W. Lee, J.A. Sokoloski, A.C. Sartorelli, and R.E. Handschumacher. Induction of the differentiation of HL-60 cells by phorbol 12-myristate 13-acetate activates a Na+-dependent uridine-transport system: Involvement of protein kinase C. *Biochemical Journal*, **274**(Pt 1):85–90, 1991.

[145] J. Stöhr, G. Schindler, G. Rothe, and G. Schmitz. Enhanced upregulation of the Fc gamma receptor IIIa (CD16a) during in vitro differentiation of ApoE4/4 monocytes. *Arterioscler. Thromb. Vasc. Biol.*, **18**(9):1424–1432, 1998.

[146] G.M. Dry, Y.I. Yasinskaya, J.K. Williams, G.D. Ehrlich, R.A. Preston, F.Z. Hu, J.S. Gruss, R.G. Ellenbogen, and M.L. Cunningham. Inhibition of Apoptosis: A Potential Mechanism for Syndromic Craniosynostosis. *Plastic and Reconstructive Surgery*, **107**(2):425–432, 2001.

[147] S. Gomes da Costa. Aufbau und Anwendung eines CARS-Mikrospektrometers. Diplomarbeit 3. Physikalisches Institut Universität Stuttgart, 2010.

[148] P. Sengupta, K. Garai, J. Balaji, N. Periasamy, and S. Maiti. Measuring Size Distribution in Highly Heterogeneous Systems with Fluorescence Correlation Spectroscopy. *Biophysical Journal*, 84(3):1977–1984, 2003.

[149] P.F. Krstanovic and V.P. Singh. A Real-Time Flood Forecasting Model Based on Maximum-Entropy Spectral Analysis: I. Development. *Water Resources Management*, **7**(2):109–129, 1993.

[150] S.-G. Xing, Y. Su, J.-Q. Feng, and C.-L. Li. The Deconvolution of Lunar Brightness Temperature based on Maximum Entropy Method using Chang€™E-2 Microwave Data. *Research in Astron. Astrophys.*, **15**(2):293–304, 2015.

[151] P. Biswas, H. Shimoyama, and L.R. Mead. Lyapunov exponents and the natural invariant density determination of chaotic maps: an iterative maximum entropy ansatz. *J. Phys. A: Math. Theor.*, **43**(125103):1–12, 2010.

[152] A.G.F. de Beer, J.-S. Samson, W. Hua, Z. Huang, and X. Chen. Direct comparison of phase-sensitive vibrational sum frequency generation with maximum entropy method: Case study of water. *J. Chem. Phys.*, **135**(22):224701–1–9, 2011.

[153] E. Vartiainen and K.-E. Peiponen. Optical and terahertz spectra analysis by the maximum entropy method. *Rep. Prog. Phys.*, **76**(6):1–20, 2013.

[154] N. Jung, B. Kim, A.C. Crowther, N. Kim, C. Nuckolls, and L. Brus. Optical Reflectivity and Raman Scattering in Few-Layer-Thick Graphene Highly Doped by K and Rb. *ACS Nano*, **5**(7):5708–5716, 2011.

[155] M. Tomita, K. Totsuka, R. Hanamura, and T. Matsumoto. Tunable Fano interference effect in coupled microsphere resonator-induced transparency. *J. Opt. Soc. Am. B*, **26**(4):813–818, 2009.

[156] S. Satpathy, A. Roy, and A. Mohapatra. Fano interference in classical oscillators. *Eur. J. Phys.*, **33**(4):863–871, 2012.

[157] R.B. Schwarz and J.F. Vuorinen. Resonant ultrasound spectroscopy: Applications, current status and limitations. *Journal of Alloys and Compounds*, **310**(1):243–250, 2000.

[158] E.K.H. Salje and M.A. Carpenter. Thermally activated proton hopping in lawsonite, the ferroelectric transition at 125 K, and the co-elastic phase transition at 270 K. *J. Phys.: Condens. Matter*, **23**(11):1–6, 2011.

[159] R.G. Leisure, K. Foster, J.E. Hightower, and D.S. Agosta. Internal friction studies by resonant ultrasound spectroscopy. *Materials Science and Engineering A*, **370**:34–40, 2004.

[160] A.O. Niedermayer, T. Voglhuber-Brunnmaier, J. Sell, and B. Jakoby. Methods for the robust measurement of the resonant frequency and quality factor of significantly damped resonating devices. *Meas. Sci. Technol.*, **23**(085107):1–11, 2012.

[161] P. Choudhury and J. Tumblin. The Trilateral Filter for High Contrast Images and Meshes. In Per Christensen and Daniel Cohen-Or, editors, *Eurographics Symposium on Rendering*, 2003.

[162] R. Bro. PARAFAC. Tutorial and applications. *Chemometrics and Intelligent Laboratory Systems*, **38**(2):149–171, 1997.

[163] L.R. Tucker. Some mathematical notes on three-mode factor analysis. *Psychometrika*, **31**(3):279–311, 1966.

[164] A. Papoulis. *The Fourier integral and its applications.* Mc. Graw-Hill Co., New York, 1962.

[165] A. Cusmariu. Fractional analytic signals. *Signal Processing*, **82**(2):267–272, 2002.

[166] D. Gabor. Theory of communication. Part 1: The analysis of information. *Journal of the Institution of Electrical Engineers. Part III: Radio and Communication Engineering*, **93**(26):429–441, 1946.

[167] G. Todoran, R. Holonec, and C. Iakab. Discrete Hilbert Transform. Numeric Algorithms. *Acta Electrotehnica*, **49**(4):485–490, 2008.

[168] B. Gold, A.V. Oppenheim, and C.M. Rader. Theory and Implementation of the Discrete Hilbert Transform. *Proc. Symp. Comput. Proces. Commun.*, pages 235–250, 1970.

[169] L. Vanbeylen and J. Schoukens. Comparison of Filter Design Methods to generate Analytic Signals. *Instrumentation and Measurement Technology Conference, 2006. IMTC 2006. Proceedings of the IEEE.*, pages 883–887, 2006.

[170] S.C. Pei and S.-B. Jaw. Computation of Discrete Hilbert Transform through Fast Hartley Transform. *IEEE Transactions on Circuits and Systems*, **36**(9):1251–1252, 1989.

[171] L.S. Marple. Computing the Discrete-Time Analytic Signal via FFT. *IEEE Transactions on Signal Processing*, **47**(9), 1999.

[172] H. Olkkonen, P. Pesola, and J.T. Olkkonen. Computation of Hilbert Transform via Discrete Cosine Transform. *Journal of Signal and Information Processing*, **1**(1):18–23, 2010.

[173] J.A. Aseltine. *Transform Method in Linear System Analysis.* Mc Graw-Hill, New York, 1958.

[174] S. Mallat. *A Wavelet Tour of Signal Processing.* Academic press, San Diego, London, 2nd edition, 1999.

[175] K.R. Rao and P.C. Yip. *The Transform and Data Compression Handbook.* Electrical Engineering and Applied Signal Processing Series. CRC Press, Boca Raton, London, New York, Washington D.C., 1st edition, 2000.

[176] Y. Liu and S.D. Brown. Wavelet multiscale regression from the perspective of data fusion: New conceptual approaches. *Anal. Bioanal. Chem.*, **380**(3):445–452, 2004.

[177] H. Tan and S.D. Brown. Wavelet analysis applied to removing non-constant, varying spectroscopic background in multivariate calibration. *Journal of chemometrics*, **16**(5):228–240, 2002.

[178] S.G. Mallat. A Theory for Multiresolution Signal Decomposition: The Wavelet Representation. *IEEE trans. on Pattern analysis and machine intelligence*, **11**(7):674–693, 1989.

[179] E.R. Malinowski. *Factor Analysis in Chemistry.* Wiley-Interscience, New York, 3rd edition, 2002.

[180] G.W. Stewart. On the early history of the singular value decomposition. *IMA Preprint Series*, 952:1–24, 1992.

[181] N. Uzunbajakava, A. Lenferink, Y. Kraan, E. Volokhina, G. Vrensen, J. Greve, and C. Otto. Nonresonant Confocal Raman Imaging of DNA and Protein Distribution in Apoptotic Cells. *Biophysical Journal*, **84**(6):3968–3981, 2003.

[182] H.-J. Van Manen, Y. M. Kraan, D. Roos, and C. Otto. Intracellular Chemical Imaging of Heme-Containing Enzymes Involved in Innate Immunity Using Resonance Raman Microscopy. *J. Phys. Chem. B*, **108**(48):18762–18771, 2004.

[183] G.H. Golub and C. Reinsch. Singular Value Decomposition and Least Squares Solutions. *Numer. Math.*, **14**:403–420, 1970.

[184] L. Zhang and M.J. Henson. A Practical Algorithm to Remove Cosmic Spikes in Raman Imaging Data for Pharmaceutical Applications. *Applied spectroscopy*, **61**(9):1015–1020, 2007.

[185] J.R. Beattie, J.V. Glenn, M.E. Boulton, A. W. Stitt, and J.J. McGarvey. Effect of signal intensity normalization on the multivariate analysis of spectral data in complex 'real-world' datasets. *J. Raman Spectrosc.*, **40**(4):429–435, 2008.

[186] A. Cichocki, R. Zdunek, A.H. Phan, and S.-I. Amari. *Nonnegative Matrix and Tensor Factorizations.* Wiley, Chichester, 1 edition, 2009.

[187] G.H. Golub and W. Kahan. Calculating the Singular Values and Pseudo-Inverse of a Matrix. *SIAM J. Numer. Anal.*, **2**(2):205–224, 1965.

[188] S. Danaher, D.J. Fegan, and J. Hagan. Application of singular value decomposition (SVD) in high energy γ-ray astronomy (E > 0.1 TeV). *Astroparticle Physics 1*, **1**(4):357–368, 1993.

[189] C. Tomasi and R. Manduchi. Bilateral filtering for gray and color images. In *Proc. IEEE Int. Conf. on Computer Vision*, pages 836–846, Bombay, 1998.

[190] V. Aurich and J. Weule. Non-Linear Gaussian Filters Performing Edge Preserving Diffusion. In *Proceedings of the DAGM Symposium*, pages 538–545, Bielefeld, 1995.

[191] S.M. Smith and J.M. Brady. SUSAN-A New Approach to Low Level Image Processing. *International Journal of Computer Vision*, **23**(1):45–78, 1997.

[192] W. Jiang, M.L. Baker, Q. Wu, C. Bajaj, and W. Chiu. Applications of a bilateral denoising filter in biological electron microscopy. *Journal of Structural Biology*, **144**(1-2):114–122, 2003.

[193] R.S. Pantelic, R. Rothnagel, C.-Y. Huang, D. Muller, D. Woolford, M.J. Landsberg, A. McDowall, B. Pailthorpe, P.R. Young, J. Banks, B. Hankamer, and G. Ericksson. The discriminative bilateral filter: An enhanced denoising filter for electron microscopy data. *Journal of Structural Biology*, **155**(3):395–408, 2006.

[194] H. Bao, C. Rao, Y. Zhang, Y. Dai, X. Rao, and Y. Fan. Hybrid filtering and enhancement of high-resolution adaptive-optics retinal images. *Optics Letters*, **34**(22):3484–3486, 2009.

[195] S. Paris and F. Durand. A fast approximation of the bilateral filter using a signal processing approach. *International Journal of Computer Vision*, **81**(1):24 – 52, 2009.

12 Statement of Authorship

This PhD thesis is the result of my own work. Published or unpublished work of others is credited to the author in the text. Except where references are made, the thesis contains no material published elsewhere or extracted in whole or in part from a thesis presented by me for another degree or diploma.

....

(Stuttgart, date) (Signature, Gregor Hehl)

13 List of figures

181

14 List of tables

15 List of symbols

$\aleph_{CPCG}$ .... Operator that solves eq. 5.19 using CPCG

α .... Electrical polarizability $[\frac{Cm^2}{V}]$

α_0 .... Time independent electrical polarizability $[\frac{Cm^2}{V}]$

$\alpha_{min\ i}$ .... ith minimum of the quadratic form $\mathbf{f}(\mathbf{\bar{a}})$

β .... MEM coefficient

$\chi^{(1)}$ .... Linear electrical susceptibility

$\chi^{(3)}_{1111}$ .... Independent tensor element of $\chi^{(3)}$ $[\frac{m^2}{V^2}]$

$\chi^{(3)}_{1221}$ .... Independent tensor element of $\chi^{(3)}$ $[\frac{m^2}{V^2}]$

$\chi^{(3)}_{E}$ .... Electronic third-order susceptibility $[\frac{m^2}{V^2}]$

$\chi^{(3)}_{E\ eff}$ ...... Effective nonresonant electronic susceptibility $[\frac{m^2}{V^2}]$

$\chi^{(3)}_{E\ eff\ j}$ ...... Effective nonresonant electronic susceptibility of the jth chemical component $[\frac{m^2}{V^2}]$

$\chi^{(3)}_{NR}$ .... Nonresonant part of $\chi^{(3)}$ $[\frac{m^2}{V^2}]$

$\chi^{(3)}_{NR\ ref}$ ...... Nonresonant part of the reference spectrum $[\frac{m^2}{V^2}]$

$\chi^{(3)}_{NR\ ref}$ ...... Nonresonant susceptibility of the reference $[\frac{m^2}{V^2}]$

$\chi^{(3)}_{NR\ sample}$ .... Nonresonant part of the sample spectrum $[\frac{m^2}{V^2}]$

$\chi^{(3)}_{NR\ sample}$ .... Nonresonant susceptibility of the sample $[\frac{m^2}{V^2}]$

$\chi^{(3)}_{Res}(\nu)$ ...... Resonant part of $\chi^{(3)}(\nu)$ $[\frac{m^2}{V^2}]$

$\chi^{(3)}_{Res}(\nu, x, y, z, t)$ Resonant susceptibility $[\frac{m^2}{V^2}]$

$\chi^{(3)}_{Res\ j}(\nu)$ ..... Resonant susceptibility of the jth chemical component $[\frac{m^2}{V^2}]$

$\chi^{(3)\ mix}_{E\ eff}$ .... Effective complex susceptibility of a n-component mixture $[\frac{m^2}{V^2}]$

$\chi^{(3)\ mix}_{tot}(\nu)$ .... Total susceptibility of a n-component mixture $[\frac{m^2}{V^2}]$

$\chi^{(3)\ mix\ est}_{Res}(\nu, \phi^{est}_{eff})$ Estimated vibrational resonant susceptibility of an n-component mixture $[\frac{m^2}{V^2}]$

$\chi^{(n)}$ .... Nonlinear electrical susceptibility of order n $[(\frac{m}{V})^{n-1}]$

χ_{el} .... Electric susceptibility

χ_{mag} .... Magnetic susceptibility

$\chi^{(3)}_{tot}(\nu)$ .... Third order susceptibility in the presence of an electronic resonance $[\frac{m^2}{V^2}]$

$\delta S(\nu)$ .... Simulated noise amplitude in the normalized CARS spectrum $[cm^{-2}]$

$\Delta\chi_{Res\,1}^{(3)}(\nu)$ ... Error made when the first component is rotated by an effective phase shift ϕ_{eff}^{est}

$\delta\phi_{MEM}(\nu)$ .... Simulated noise amplitude in the MEM phase [rad]

$\delta I_{CARS\,ref}(\nu)$. Simulated shot noise amplitude in the reference CARS spectrum, $\delta I_{CARS\,ref}(\nu) = \Delta_G \sqrt{I_{CARS\,ref}(\nu)}$ [cm^{-2}]

$\delta I_{CARS\,sample}(\nu)$ Simulated shot noise amplitude in the sample CARS spectrum, $\delta I_{CARS\,sample}(\nu) = \Delta_G \sqrt{I_{CARS\,sample}(\nu)}$ [cm^{-2}]

$\delta Im[\chi_{Res}^{(3)}(\nu)]$. Simulated noise amplitude in the reconstructed $Im[\chi_{Res}^{(3)}(\nu)]$ amplitude [cm^{-1}]

$\Delta\nu(x,y,z,t)$. Spectral shift correction map [cm^{-1}]

δ_{Dirac} .... Delta function [$\frac{1}{s}$]

$\delta_{Dirac\,+}(t - nT)$ Dirac comb [$\frac{1}{s}$]

Δ_G .... Width of Gaussian noise [cm^{-2}]

δ_m .... Diagonal elements of $\mathbf{D}$

δ_R .... sign correction parameter for eq. A.50

δ .... Detuning parameter, $\delta = \nu_0 - (\nu_{Pump} - \nu_{Stokes})$ [cm^{-1}]

ϵ_0 .... Vacuum permittivity [$\frac{F}{m}$]

ϵ_r .... Relative permittivity [$\frac{F}{m}$]

η .... Spatial lag coordinate [m]

γ_{as} .... Antisymmetric anisotropy, $\gamma_{as} = \frac{3}{4} \sum_{\rho\sigma} (\alpha_{\rho\sigma} - \alpha_{\sigma\rho})^2$ [$\frac{C^2 m^4}{V^2}$]

Γ_G .... Width of a Gaussian band $G(\nu)$ [cm^{-1}]

Γ_L .... Width of a Lorentzian band $L(\nu)$ [cm^{-1}]

γ_m .... mth Schur parameter

γ_s .... Symmetric anisotropy, $\gamma_s = \frac{1}{2} \sum_{\rho\sigma} (\alpha_{\rho\rho} - \alpha_{\sigma\sigma})^2 + \frac{3}{4} \sum_{\rho\sigma} (\alpha_{\rho\sigma} + \alpha_{\sigma\rho})^2$ [$\frac{C^2 m^4}{V^2}$]

Γ_{virt} .... half width of the virtual state

$\hat{p}_\rho$ .... electric dipole operator for the Cartesian coordinates ρ [Cm]

$\hat{p}_\sigma$ .... electric dipole operator for the Cartesian coordinates σ [Cm]

λ_{Ex} .... Excitation wavelength [nm]

λ_k .... Eigenvalues of $\mathbf{C_{Circulant}}$

$\mathbf{\Lambda}$ .... Diagonal matrix holding eigenvalues λ_k of $\mathbf{C_{Circulant}}$, $\mathbf{\Lambda} = diag(\lambda_1, \ldots, \lambda k)$

$\rho_{\mathbf{D}}$ .... Density matrix

$\mathbf{B}_{Poly}$ .... Matrix holding polynomial interpolation coefficients

$\mathbf{Cov}$ .... Covariance matrix, covariance of a vector $\mathbf{g}$: $\mathbf{Cov} = \begin{bmatrix} cov(g_1, g_1) & \ldots & cov(g_1, g_n) \\ & \ddots & \\ cov(g_n, g_1) & \ldots & cov(g_n, g_n) \end{bmatrix}$

$\mathbf{c}$ .... First column of $\mathbf{C}_{Circulant}$

$\mathbf{C}(m, n)$ ...... Autocorrelation matrix, relation with $\mathbf{Cov}$: $C_{i,j} = \frac{\mathbf{Cov}_{i,j}}{\sqrt{\mathbf{Cov}_{i,i}\mathbf{Cov}_{j,j}}}$

$\mathbf{C}_{Circulant}$ ..... Circulant matrix of size $N_0 \times N_0$, $C_{Circulant\,ij} = C_{Circulant\,kl}$, when $j - i \equiv l -$

μ	....	Weight of the Lorentzian contributions in a Voigt band $V(\nu)$
μ_0	....	Vacuum permeability $[\frac{H}{m}]$
μ_r	....	Relative permeability $[\frac{H}{m}]$
ν	....	Normalized frequency $[\frac{1}{cm}]$
ν_0	....	Raman resonance frequency $[cm^{-1}]$
ν_{max}	....	Upper limit of the normalized frequency $[\frac{1}{cm}]$
ν_{min}	....	Lower limit of the normalized frequency $[\frac{1}{cm}]$
$\nu_{Nyq} = N/2$	..	Nyquist frequency $[\frac{1}{cm}]$
ν_n	....	Discrete set of normalized frequencies $\nu_n = \frac{n}{N} = \frac{n}{(N=(2K+1)(N_0-1)+1)}$ ($n = 0, 1, \ldots, N$) $[\frac{1}{s}]$
ω	....	Frequency $[\frac{1}{s}]$
ω_0	....	Frequency of the sample's vibration $[\frac{1}{s}]$
$\omega_{anti-Stokes}$	...	anti-Stokes frequency $\omega_{anti-Stokes} = \omega_L + \omega_0$ $[\frac{1}{s}]$
ω_{CARS}	....	CARS field frequency $[\frac{1}{s}]$
ω_L	....	Frequency of the incident light field $[\frac{1}{s}]$
ω_{Probe}	....	Probe field frequency $[\frac{1}{s}]$
ω_{Pump}	....	Pump field frequency $[\frac{1}{s}]$
ω_{Stokes}	....	Stokes field frequency $[\frac{1}{s}]$
ω_{Stokes}	....	Stokes frequency $\omega_{Stokes} = \omega_L - \omega_0$ $[\frac{1}{s}]$
ω_S	....	Frequency of the scattered Raman light field $[\frac{1}{s}]$
$\overline{\alpha}$	....	Mean polarizability, $\overline{\alpha} = \frac{1}{3} \sum_{\rho\rho} \alpha_{\rho\rho}$ $[\frac{Cm^2}{V}]$
ϕ	....	Phase $[rad]$
ϕ_{eff}^{est}	....	Estimated effective phase shift $[rad]$
$\phi_{eff\ j}^{mix}$	....	Effective phase shift of $\chi_{Res\ j}^{(3)}(\nu)$ of the jth chemical component $[rad]$
$\phi_{E\ eff}^{mix}$	....	Phase angle of the effective complex susceptibility of a n-component mixture $[rad]$
$\phi_{MEM}^{mix}(\nu)$	.....	MEM-phase of a n-component mixture $[rad]$
ϕ_{CARS}	....	Phase of the sample CARS field $[rad]$
ϕ_{eff}	....	Effective phase shift $[rad]$
$\phi_{eff\ j}$	....	Effective phase shift of the jth chemical component $[rad]$
$\phi_{error}(\nu, x, y, z, t)$		Slowly varying error-phase $[rad]$
$\phi_{estimated}(\nu, x, y, z, t)$		Estimated phase (KK or MEM based) $[rad]$
ϕ_E	....	Phase of $\chi_E^{(3)}$ $[rad]$
$\phi_{E\ eff}$	....	Offset phase $[rad]$
$\phi_{E\ eff\ j}$	......	Phase angle of the effective nonresonant electronic susceptibility of the jth chemical component $[rad]$
$\phi_{MEM}(\nu, x, y, z, t)$		Phase obtained using the MEM procedure $[rad]$

$\phi_{MEM\ NR}(\nu, x, y, z, t)$ Nonresonant points / regions of $\phi_{MEM}(\nu, x, y, z, t)$ [*rad*]

ϕ_{NTO} ....   Phase of the intra-Stokes CARS field [*rad*]

$\phi_{retrieved}(\nu, x, y, z, t)$ Retrieved phase phase (KK or MEM based) [*rad*]

ϕ_R ....   Phase acting on $\chi_{Res}^{(3)}(\nu)$ [*rad*]

$\phi_{R\ j}$ ....   Phase acting on $\chi_{Res\ j}^{(3)}(\nu)$ of the *j*th chemical component [*rad*]

$\phi_{tot}(\delta)$ ....   Phase $\phi_{tot}(\delta) = tan^{-1}\frac{Im[\chi_{tot}^{(3)}(\delta)]}{Re[\chi_{tot}^{(3)}(\delta)]}$ [*rad*]

$\Psi(t)$ ....   Mother wavelet

$\Psi_{\mathfrak{s},\mathfrak{t}}(t)$ ....   Wavelet basis function

$\psi_{e=1}$ ....   Wave function of an electronic resonance

ρ ....   Molecule coordinate [*m*]

ρ_{depol} ....   Depolarization ratio

$\rho_{depol\ NR}$ ....   Depolarization ratio for the nonresonant part $\chi_{NR}^{(3)}$

$\rho_{depol\ Res}$ ....   Depolarization ratio for the resonant part $\chi_{Res}^{(3)}$

σ ....   Molecule coordinate [*m*]

σ_i ....   *i*th singular value

σ_{Raman} ....   Spontaneous Raman scattering cross section [$\frac{cm^2}{sr}$]

a ....   Vector holding the MEM or prediction coefficients a_k

B ....   Magnetic field [*T*]

b ....   Vector holding the MEM coefficients

c$_x$ ....   Fraction of the *x*th basis spectrum in a linear combination

d$_i$ ....   Search vector of the *i*th iteration step

E ....   Electric field [$\frac{V}{m}$]

E$_{Probe}$ ....   Electric probe field [$\frac{V}{m}$]

E$_{Pump}$ ....   Electric pump field [$\frac{V}{m}$]

E$_{Stokes}$ ....   Electric Stokes field [$\frac{V}{m}$]

f$(\tilde{\mathbf{a}})$ ....   Quadratic form of $\tilde{\mathbf{C}}_{Circulant}\ \tilde{\mathbf{a}} = \tilde{\mathbf{b}}$, $\mathbf{f}(\tilde{\mathbf{a}}) = \frac{1}{2}\tilde{\mathbf{a}}^T\tilde{\mathbf{C}}_{Circulant}\tilde{\mathbf{a}} - \mathbf{b}^T\tilde{\mathbf{a}} + const.$

H ....   Hierarchical matrix

H ....   Magnetic field strength [$\frac{A}{m}$]

j ....   Current [*A*]

k$_{CARS}$ ....   Wave vector of the anti-Stokes field [$\frac{1}{m}$]

k$_{Pump}$ ....   Wave vector of the Pump field [$\frac{1}{m}$]

k$_{Stokes}$ ....   Wave vector of the Stokes field [$\frac{1}{m}$]

M ....   Preconditioner matrix

P ....   Polarization [$\frac{C}{m^2}$]

P$^{(3)}$ ....   Induced third-order nonlinear polarization, $\mathbf{P}_{CARS}^{(3)} = \chi^{(3)}\mathbf{E}_{Pump}\mathbf{E}_{Probe}\mathbf{E}_{Stokes}^*$ [$\frac{C}{m^2}$]

r$_i = -\nabla\mathbf{f}(\tilde{\mathbf{a}}_i)$ ..   Residual at the *i*th iteration step

W ....   Matrix embedding $\mathbf{C}_{Toeplitz}$ into $\mathbf{C}_{Circulant}$, where $\mathbf{W}_{ij} = w_{i-j}, w_i = C_{Toeplitz\ i-N_0}$

for $i > 0$ and $w_i = C_{Toeplitz\ i+N_0}$ for $i < 0$, element w_0 is arbitrary

$\tilde{\mathbf{a}}$ .... Vector holding the MEM or prediction coefficients a_k in eq. 5.19

$\tilde{\mathbf{b}}$ .... Vector holding the MEM coefficients in eq. 5.19

$\tilde{\mathbf{c}}$ .... First row of $\tilde{\mathbf{C}}_{Circulant}$ with size $2N_0$

$\tilde{\mathbf{C}}_{Circulant}$ ..... Circulant of size $2N_0$ x $2N_0$ with $\mathbf{C}_{Toeplitz}$ embedded

ξ .... Spatial lag coordinate [m]

ζ_i .... Gram-Schmidt coefficients

A .... Area of an image [μm^2]

A_{ijkl} .... Amplitude of a Raman resonance [cm^{-1}]

a_k .... MEM or prediction coefficient

A_M .... Fourier components, a CARS spectrum $S(v, x, y, z, t, K)$ is decomposed in

$C(m)$ .... Autocorrelation coefficients

c_0 .... Vacuum speed of light [$\frac{m}{s}$]

C_a .... Scaling factor in the case a

C_b .... Scaling factor in the case b

C_c .... Scaling factor in the case c

c_{PE} .... Normalized amplitude of the 1420 cm^{-1} band in Polyethylene (PE)

c_{PP} .... Normalized amplitude of the 810 cm^{-1} band in Polypropylene (PP)

$c_{PP}^{2\ bands}$ ...... Crystallinity in Polypropylene (PP) using two bands and eq. 6.5

$c_{PP}^{3\ bands}$ ...... Normalized amplitude of the 810 cm^{-1} band in Polypropylene (PP) using four bands and eq. 6.4

$c_{PP}^{3\ bands}$ ...... Normalized amplitude of the 810 cm^{-1} band in Polypropylene (PP) using three bands and eq. 6.3

$e_m(t)$ .... Prediction error sequence [s]

$f^*(t)$ .... Sampled data [s]

$F_1(\phi_{eff}, \chi^{(3)}_{E\ eff})$ Single component functional

$F_2(\phi_{eff}, \chi^{(3)}_{E\ eff})$ $n = 2$-component functional

$F_{mix}(\phi_{eff}, \sqrt{S_{NR}})$ Functional minimizing only the negative part $f^- = max(-f, 0) = min(f, 0)$ of $Im[\chi^{(3)}_{tot}(v)]$

$F_n(\phi_{eff}, \chi^{(3)}_{E\ eff})$ n-component functional

$G(\eta, \xi)$ ...... 2D autocorrelation function with spatial lag coordinates η and ξ

$g(\eta, \xi)$ .... Normalized 2D autocorrelation function with spatial lag coordinates η and ξ

$G(v)$ .... Gaussian band

$g(t)$ .... Time response function [s]

$g_{Noise}(0, 0)$ ... Noise peak at $(\eta, \xi) = (0, 0)$ with width w_{Noise}

h .... Entropy [$\frac{J}{K}$]

$i(x, y)$ .... Image with spatial coordinates x and y

$I_\perp$ .... Perpendicular to the xz-plane polarized component of the CARS intensity $[\frac{W}{m^2}]$

$I_\parallel$ .... Parallel to the xz-plane polarized component of the CARS intensity $[\frac{W}{m^2}]$

$I_{CARS}(v)$ ..... CARS spectral profile $[\frac{W}{m^2}]$

$I_{CARS}(v)$ ..... CARS intensity $[\frac{W}{m^2}]$

$I_{CARS\ ref}(v)$ .. CARS intensity generated in the reference $[\frac{W}{m^2}]$

$I_{CARS\ ref}(\omega_{CARS})$ CARS intensity of the reference $[\frac{W}{m^2}]$

$I_{CARS\ sample}(v)$ CARS intensity generated in the sample $[\frac{W}{m^2}]$

$I_{CARS\ sample}(\omega_{CARS})$ CARS intensity of the sample $[\frac{W}{m^2}]$

$I_{NTO}(v)$ ..... Intra-Stokes CARS intensity $[\frac{W}{m^2}]$

$I_{NTO\ ref}(v)$ ... Intra-Stokes CARS intensity of the reference $[\frac{W}{m^2}]$

$I_{NTO\ sample}(v)$ Intra-Stokes CARS intensity of the sample $[\frac{W}{m^2}]$

$I_{total}(v)$ ...... Total CARS intensity (sample and intra-Stokes CARS) $[\frac{W}{m^2}]$

$I_{total\ ref}(v)$ .... Total CARS intensity (sample and intra-Stokes CARS) of the reference $[\frac{W}{m^2}]$

$I_{total\ sample}(v)$. Total CARS intensity (sample and intra-Stokes CARS) of the sample $[\frac{W}{m^2}]$

$Im[\chi^{(3)}_{Res\ solvent}(v)]$ Resonant susceptibility of the solvent $[\frac{m^2}{V^2}]$

$L(v)$ .... Lorentzian band

M .... Number of autocorrelation values

m .... Lag number or order of AR process

m_{deg} .... Degeneracy, number of equal input frequencies

N .... Length of a discrete signal

N .... Number of samples in a squeezed CARS spectrum $S(v, x, y, z, t, K)$ of length N_0, $N = (2K + 1)(N_0 - 1) + 1$

N_0 .... Number of samples in a CARS spectrum $S(v, x, y, z, t, K)$

N_{Obj} .... Number of correlated objects in an image $i(x, y)$ $[\frac{objects}{\mu m^2}]$

N_{Scat} .... Number density of molecules

r_{C-C} .... Ratio representing the chain length n_{C-C}: $r_{C-C} = \frac{A(1440\ cm^{-1}) + A(1460\ cm^{-1})}{A(1740\ cm^{-1})}$

$r_{C=C}$ .... Ratio representing the degree of acyl chain unsaturation $n_{C=C}$: $r_{C=C} = \frac{A(3005\ cm^{-1})}{A(1740\ cm^{-1})}$

$r_{Im[\chi^{(3)}_{tot}(v)]}$ ..... Normalized ratio of maximum to minimum excursion of reconstructed $Im[\chi^{(3)}_{tot}(v)]$, $r_{Im[\chi^{(3)}_{tot}(v)]} = \frac{max(Im[\chi^{(3)}_{tot}(v)]) - min(Im[\chi^{(3)}_{tot}(v)])}{max(Im[\chi^{(3)}_{tot}(v)])}$

r_{phase} .... Normalized ratio of maximum to minimum estimated phase excursion, $r_{phase}(\phi_{estimated}(v)) = \frac{max(\phi_{estimated}(v)) - min(\phi_{estimated}(v))}{max(\phi_{estimated}(v))}$

s .... Complex frequency variable $[\frac{1}{s}]$

$S(v_n, x, y, z, t)'$ CARS spectrum $S(v_n, x, y, z, t)$ with a reversed copy appended as used in the DCT

$s(t)$ .... Signal [s]

$S^{mix}(v)$ ...... CARS spectrum of a n-component mixture $[cm^{-2}]$

$s_{\mathfrak{s}}(\nu_n)$ . . . . Approximation component $[cm^{-1}]$

$s_{analytic}(t)$ . . . . Analytic signal [s]

$s_{background}(\nu)$ . . Background component $[cm^{-1}]$

$s_i(\nu_n)$ . . . . Detail component, $(i = 1, \ldots, \mathfrak{s})$ $[cm^{-1}]$

S_{max} . . . . Relative maximum in a CARS spectrum $S(\nu)$

S_{min} . . . . Relative minimum in a CARS spectrum $S(\nu)$

$s_{noise}(\nu)$ . . . . . . Noise component $[cm^{-1}]$

$S_{NR}(\nu, x, y, z, t)$ Nonresonant region of a normalized CARS spectrum

$s_{scaling}$ . . . . Scaling factor in general

$s_{signal}(\nu)$ . . . . . Signal component $[cm^{-1}]$

T . . . . Sampling interval [s]

t_{int} . . . . Integration time for recording a spectrum [s]

$V(\nu)$ . . . . Voigt band

$V_{j,j}$ . . . . variances

w_η . . . . Half-width of $g(\eta, \xi)$ along the η-direction [m]

w_ξ . . . . Half-width of $g(\eta, \xi)$ along the ξ-direction [m]

w_{Noise} . . . . Half-width of the noise peak $g_{Noise}(0, 0)$ [m]

z . . . . interaction path length in the Raman active medium [m]

ρ_{free} . . . . Charge [C]

$\mathbf{c}(\xi, \sigma)$ . . . . . . fixed $\mathbf{d}$ dimensional Gaussian filter kernel

$\mathbf{k}$ . . . . Wave vector $[\frac{1}{m}]$

$\mathbf{r}$ . . . . Position vector [m]

$\mathbf{s}(\xi, \sigma_{range})$ . . . $\mathbf{d}$-dimensional Gaussian filter kernel

K . . . . Squeezing parameter

n . . . . Index of refraction

Q(t) . . . . Nuclei coordinate [m]

Appendices

A.1 Used transforms

A.1.1 Fourier transform (FT), discrete FT (DFT), and fast Fourier transform (FFT)

For an arbitrary given signal function $x(t)$, the Fourier transform (FT) $X(\omega)$ allows to rewrite $x(t)$ as [164]

$$x(t) = \frac{1}{2\pi} \int_{\infty}^{-\infty} X(\omega) e^{i\omega t} d\omega \ , \tag{A.1}$$

with $X(\omega)$ being

$$X(\omega) = \int_{\infty}^{-\infty} x(t) e^{-i\omega t} dt \ . \tag{A.2}$$

We can consider eq. A.2 and eq. A.1 as the forward and inverse Fourier transform, respectively. In practice, the continuous signal $x(t)$ will be sampled with a certain sampling interval T, and will become a discrete signal. In the discrete FT (DFT), the integral becomes a sum, ranging from the first to the Nth sample. The following equations A.3 and A.4 are the MATLAB notation of the fast Fourier transform (FFT) and of the inverse FFT (IFFT), respectively , using the Cooley Tukey FFT algorithm [60]:

$$\mathcal{F}(x(t)) = X(k) = \sum_{j=1}^{N} x(j) w_N^{(j-1)(k-1)} \ , \tag{A.3}$$

$$\mathcal{F}^{-1}(x(t)) = x(j) = \frac{1}{N} \sum_{k=1}^{N} X(k) w_N^{-(j-1)(k-1)} \ , \tag{A.4}$$

$$w_N = e^{\frac{-2\pi \ i}{N}} \ , \tag{A.5}$$

with eq. A.5 being the Nth root of unity. For a real input signal $x(t)$, the FFT will be a hermitian symmetric function, which will be symmetric around the Nyquist frequency $v_{Nyq} = \frac{N}{2}$. All information is contained in the positive frequencies, and $\mathcal{F} = \mathcal{F}^{-1}$. In other words, for $x(t)$ being real, it makes no sense to use complex basis functions $e^{\frac{2\pi i}{N}}$, as in the FFT. More appropriate is to define a real transform using the cosine basis functions, as will be introduced in section 5.1.

A.1.2   The Hilbert transform (HT) and the discrete Hilbert transform (DHT)

The Hilbert transform (HT) (David Hilbert, 1862-1943) $\mathscr{H}$ of a signal $s(t)$ is obtained via the following singular integral operator [165]:

$$\mathscr{H}(s(t)) = \frac{\mathscr{P}}{\pi} \int_{-\infty}^{\infty} \frac{s(x)}{t-x} dx \ , \tag{A.6}$$

where $\mathscr{P}$ denotes the Cauchy principal value. It is important that eq. A.6 is understood in the Cauchy principal value sense, meaning that zero is approximated in the exact same manner from $\pm\infty$ omitting the singularities in the direct neighborhood: $\mathscr{H}(s(t)) = \frac{\mathscr{P}}{\pi} lim_{\epsilon \to 0} \int_{|t-x|>\epsilon} \frac{s(t)}{t-x} dx$. Eq. A.6 corresponds to a convolution of $s(t)$ with a singular kernel

$$\mathscr{H}(s(t)) = s(t) * \frac{1}{\pi t} \ , \tag{A.7}$$

which corresponds to a phase shift of the whole signal $s(t)$ by $-\frac{\pi}{2}$. This phase shift corresponds to a time delay of the signal, but because this time delay may be different for every t, the determination of the phase shift is not trivial! In the frequency domain, $\mathscr{F}\mathscr{H}(s(t))(\omega) = -i \, sign(\omega)\mathscr{F}s(t)$, the phase shifting can be understood as follows: When $s(t)$ is represented as a linear combination of pure frequencies $cos(\omega t + \phi)$, the phase shifted version of this reads $sign(x)sin(\omega t + \phi)$. To complexify a real signal or to obtain a complex analytic function $s_{analytic}(t)$, the use of the HT was introduced by Gabor in 1946 [166]. The analytic signal obtained then reads:

$$s_{analytic}(t) = s(t) + i\mathscr{H}(s(t)) = s(t) * \left[\delta_{Dirac}(t) + \frac{i}{\pi t}\right] \ , \tag{A.8}$$

which is sometimes called Gabors complex signal. In eq. A.8, $s(t)$ and $\mathscr{H}(s(t))$ form a Hilbert pair with $s(t)$ being the in-phase component and $\mathscr{H}(s(t))$ being the quadrature component of the analytic signal $s_{analytic}(t)$. In practice, the HT is approximated with a discrete HT (DHT). Several techniques and algorithms for calculating the DHT have been presented, most of them being FFT based [167], [168],[169], [170], and [171]. The analytic signal is calculated by performing a FFT on $s(t)$, replacing all negative frequencies with zero, and transforming back via IFFT [171]. However, the FFT kernel as used in the MATLAB implementation of the algorithm [171] is giving rise to the windowing phenomenon at the spectral ends. This can be avoided when the FFT kernel is replaced by a discrete cosine transform (DCT) kernel [172]. Olkkonen et. al. [172] are going one step further by replacing the cosine kernel in the modified DHT's DCT kernel by a sine kernel, claiming this algorithm being faster and more robust against noise than the FFT kernel. The modified DCT kernel based DHT will be used in this thesis. The relevant properties of the HT are:

1. computational cost of the HT is of $\mathcal{O}2Nlog(N)$, with N being the length of the discretised signal $s(t)$,

2. $\mathscr{H}c = 0$ (c = const.),

3. $\mathscr{H}\mathscr{H}[s(t) + c] = -s(t)$ (c = const.).

The HT is used in signal processing (eg. calculating envelopes of signals), engineering (e.g. Bose transforms), network theory (where the so called allpass filter, a filter that only shifts the phase ϕ of a signal, comes very close to a Hilbert transformer) and in optics with the Kramers Kronig relations. The latter application is discussed in section 3.3.1, where the different phase retrieval methods are laid out.

A.1.3   The z transform

The z-transform $\mathscr{Z}$ is the discrete analogon of the Laplace transform $\mathscr{L}$. It is a complex function. The theory of sampled data approximates the data as trains of impulse functions $f^*(t) = \sum_{n=0}^{\infty} f(nT)\delta_{Dirac\,+}(t - nT)$. Here, the Dirac comb $\delta_{Dirac\,+}(t - nT)$ represents the nth sampling of the data at time nT, with T being the sampling interval. The Laplace transform $\mathscr{L}$ of such a discrete sampled function is $\mathscr{L}(f^*(t)) = \sum_{n=0}^{\infty} f(nT)e^{-snT}$, with s being the complex frequency variable of the kernel e^{-st} of the Laplace transform $\mathscr{L}(f^*(t)) = \int_0^{\infty} f(t)e^{-st}dt$. The notation $\delta_{Dirac\,+}$ represents the condition $\lim_{\eta \to 0} \delta(t - \eta) = \delta_+(t)$, meaning that this pulse is covered by the integration range of the $\mathscr{L}$ integral. Substituting the variable $z = e^{sT}$ leads for $T = 1$ to the z-transform $\mathscr{Z}$:

$$\mathscr{Z}(f(n)) = \sum_{n=0}^{\infty} f(T)z^{-n} \ , \tag{A.9}$$

with the inverse z-transform $\mathscr{Z}^{-1}$ being $\mathscr{Z}^{-1}[\mathscr{Z}(f(n))] = f(n)$ [173]. The z-transform will be used in section 3.3.1.2 to deduce the maximum entropy model.

A.1.4   The wavelet transform (WT) and the discrete wavelet transform (DWT)

The continuous Wavelet transform (WT) $\mathscr{W}$ of a signal $s(t)$ is given as [174],[175],[176]:

$$\mathscr{W}(s(t)) = \int s(t)\Psi_{\mathfrak{s},\mathfrak{t}}^*(t)dt \ , \tag{A.10}$$

with $\Psi_{\mathfrak{s},\mathfrak{t}}(t)$ being the wavelet basis functions that are generated from a so-called mother wavelet $\Psi(t)$ by scaling with scale $\mathfrak{s}$ and translation with $\mathfrak{t}$:

$$\Psi_{\mathfrak{s},\mathfrak{t}}^*(t) = \frac{1}{\sqrt{\mathfrak{s}}}\Psi\left(\frac{t - \mathfrak{t}}{\mathfrak{s}}\right) \ . \tag{A.11}$$

Similar to the calculation of the Fourier transformation $\mathscr{F}$ via the FFT, the WT is calculated via a fast discrete Wavelet transform (DWT). Note that equation A.10 is projecting the one-dimensional signal $s(t)$ to a two dimensional scale-time $(\mathfrak{s}, \mathfrak{t})$ representation. This gives rise

to the main difference between FFT and DWT. In the FFT case, a signal is decomposed into plane waves, while the DWT decomposes the signal into wave packages with a finite frequency bandwidth. In the FFT case the sine basis functions are completely delocalized in the frequency domain and localized in the time domain, while Wavelets are fairly localized in both domains. As a consequence, the DWT has the ability to decompose a signal spectrum into different frequency components, while retaining the original spectral resolution of the signal $s(t)$.

A.2 Polynomial error-phase estimation

To efficiently solve the polynomial interpolation of the error-phase spectrum $\phi_{error}(v)$ using eq. 3.56 in chapter 3, the coefficients $\mathbf{B}_{Poly}$ need to satisfy the following system

$$\mathbf{V_{Van}} \begin{bmatrix} B_{Poly}(0) \\ B_{Poly}(1) \\ \vdots \\ B_{Poly}(p) \end{bmatrix} = \begin{bmatrix} 1 & v(0) & \cdots & v(0)^p \\ 1 & v(1) & \cdots & v(1)^p \\ \vdots & \vdots & & \vdots \\ 1 & v(p) & \cdots & v(p)^p \end{bmatrix} \begin{bmatrix} B_{Poly}(0) \\ B_{Poly}(1) \\ \vdots \\ B_{Poly}(p) \end{bmatrix} = \begin{bmatrix} \phi_{error}(v(0)) \\ \phi_{error}(v(1)) \\ \vdots \\ \phi_{error}(v(p)) \end{bmatrix}, \qquad \text{(A.12)}$$

where $\mathbf{V_{Van}}$ is the Vandermonde matrix. Especially for calculating all $\phi_{error}(v, x, y, z, t)$ vectors of a hyperspectrum, the following approach is very computationally cost effective. The computing routine to determine the polynomial interpolations of order p for all error-phase spectra $\phi_{error}(v, x, y, z, t)$ for a hyperspectrum is as follows

$\mathbf{V_{Van}}(:, \mathbf{1} : (\mathbf{p} + \mathbf{1})) = \mathbf{1}$	Prepare Vandermonde matrix
for i=n:1	For order p=n to p=1:
$\quad \mathbf{V_{Van}}(:, \mathbf{i}) = v_{NR} \circ \mathbf{V}(:, \mathbf{i} + \mathbf{1})_{\mathbf{Van}}$	write polynomial
end	coefficients in rows of $\mathbf{V_{Van}}$
$[\mathbf{Q}, \mathbf{R}] = qr(\mathbf{V_{Van}}, 0)$	Perform QR decomposition
$\mathbf{B}_{Poly} = \mathbf{R} \backslash (\mathbf{Q}^T \phi_{MEM}(v, x, y, z, t)^T)$	Calculate polynomial coefficients
	using MATLAB's backslash operator
$\phi_{estimated}(v, x, y, z, t) = \phi_{MEM}(v, x, y, z, t)$	Prepare $\phi_{estimated}(v, x, y, z, t)$ matrix
for i=0:n	For order p=0 to p=n:
$\quad \phi_{estimated}(v, x, y, z, t) = \phi_{estimated}(v, x, y, z, t)$	
$\quad - \mathbf{B}_{Poly}(i + 1, :) \circ (v^T)^{(n-1)}$	Subtract polynomial matrix of order $n - 1$
end .	

Here, we have introduced the Hadamard product, which is denoted by $\circ$. $\mathbf{B}_{Poly}$ denotes a matrix holding the polynomial coefficients, $\mathbf{Q}$ and $\mathbf{R}$ are the matrices obtained by performing the QR

decomposition $\mathbf{V_{Van}} = \mathbf{QR}$ [81], using e.g. the Gram-Schmidt process mentioned in section 5.2.1.

A.3 Error-phase estimation using the wavelet prism (WP) decomposition

The wavelet transform is used in the wavelet prism (WP) decomposition [177] of an unknown discretized spontaneous Raman spectrum $s(\nu_n)$ of length N ($n = 1, 2, \ldots, N$) [55]. Using the Mallat pyramid algorithm [178], a discretized function $s(\nu_n)$ is decomposed into a sum of $\mathfrak{s}$ so called detail components $s_i(\nu_n)$, ($i = 1, \ldots, \mathfrak{s}$) and one approximation component $b_{\mathfrak{s}}(\nu_n)$:

$$s(\nu_n) = s_1(\nu_n) + s_2(\nu_n) + \ldots + s_{\mathfrak{s}}(\nu_n) + b_{\mathfrak{s}}(\nu_n) \ . \tag{A.13}$$

All these spectral components are mutually orthogonal. If no spectral overlap between the noise component $s_{noise}(\nu)$, the signal component $s_{signal}(\nu)$ of interest, and the background $s_{background}(\nu)$ is present, the summands given in eq. A.13 can be combined to

$$s(\nu) = s_{noise}(\nu) + s_{signal}(\nu) + s_{background}(\nu) \ . \tag{A.14}$$

The functionality of the WP decomposition and its differentiation from the FFT is demonstrated in Fig. A.1, where a simulated isolated Lorentzian band of $A = 1 \ cm^{-1}$ and $\Gamma = 20 \ cm^{-1}$ serving as the signal component $s_{signal\ simulated}(\nu)$ is added to a simulated slowly varying background component $s_{background\ simulated}(\nu) = -10^{-5}\nu + 2 * 10^{-12}\nu^3 + 0.05 \ sin(5 * 10^{-4}\nu)$ and a simulated Gaussian noise component $s_{noise\ simulated}(\nu)$ with a noise amplitude of 0.2. The WP settings are as follows: Decomposition level $\mathfrak{s} = 22$, used wavelet type *symlet* (sym8), $s_{noise}(\nu) = \sum_{i=1}^{6} s_i(\nu_n)$, $s_{signal}(\nu) = \sum_{i=7}^{12} s_i(\nu_n)$, and $s_{background}(\nu) = \sum_{i=13}^{\mathfrak{s}=22} s_i(\nu_n) + b_{\mathfrak{s}}(\nu_n)$. Fig. A.1 A clearly demonstrates the ability of the WP decomposition to recover the correct spectral components, such that $s_{noise}(\nu) \approx s_{noise\ simulated}(\nu)$, $s_{signal}(\nu) \approx s_{signal\ simulated}(\nu)$, and $s_{background}(\nu) \approx s_{background\ simulated}(\nu)$. Fig. A.1 B shows the dependence of the probability amplitude of each WP component on its scale $\mathfrak{s}$. The first 6 components are dominated by $s_{noise\ simulated}(\nu)$. For components 7 to 12, the signal $s_{signal\ simulated}(\nu)$ dominates. And for all higher components, the background $s_{background\ simulated}(\nu)$ is dominant. The different components can easily be distinguished by the relative minima representing the spectral overlap between the particular components. Next we will compare the ability of the FFT to separate these three spectral components with the WP approach. In fig. A.1 C the moduli of the FFT's $\mathscr{F}(s(\nu_n))$, $\mathscr{F}(s_{noise\ simulated}(\nu_n))$, $\mathscr{F}(s_{signal\ simulated}(\nu_n))$ and $\mathscr{F}(s_{background\ simulated}(\nu_n))$ are plotted for the first 150 Fourier frequencies. When compared with the WP approach, the FFT spectra do not offer the possibility to define relative minima as accurate differentiators between the components $s_{noise\ simulated}(\nu_n)$, $s_{signal\ simulated}(\nu_n)$ and $s_{background\ simulated}(\nu_n)$.
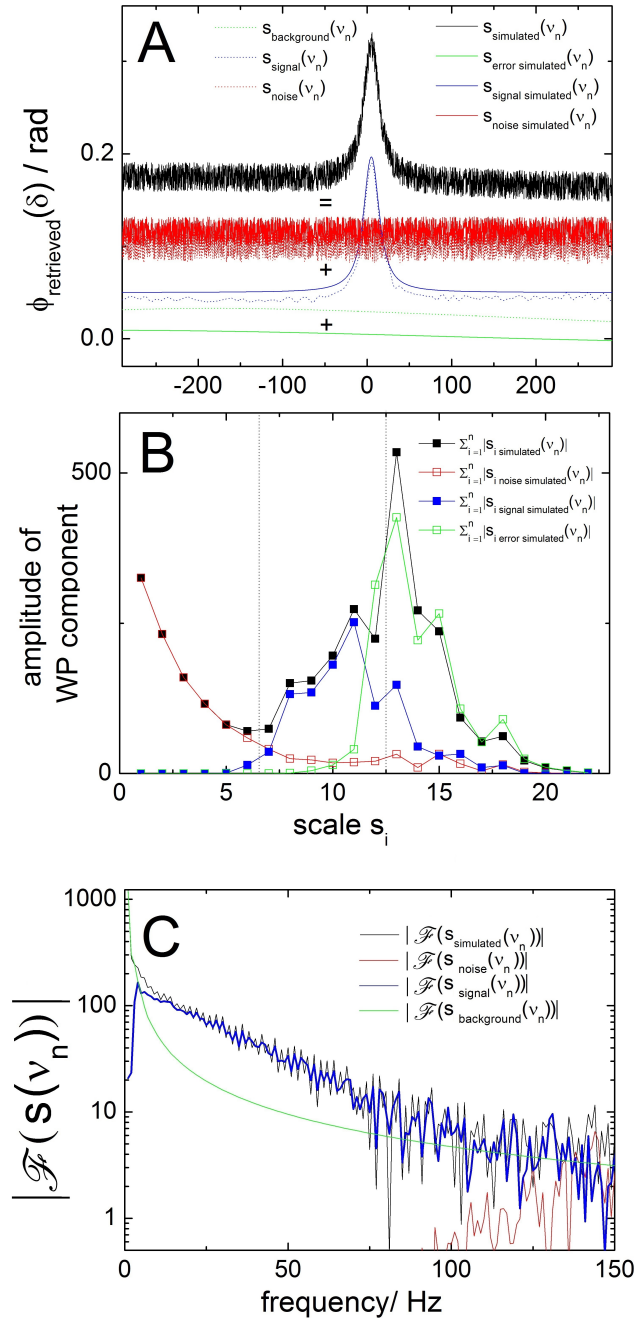
Figure A.1: (A) Simulation of a retrieved phase spectrum ($\phi_{retrieved}(\delta)$) consisting of a sum of an isolated Lorentzian band of $A = 1\ cm^{-1}$ and $\Gamma = 20\ cm^{-1}$ serving as a signal $s_{signal\ simulated}(v_n)$, a slowly varying background component $s_{background\ simulated}(v_n)$, and a Gaussian noise component $s_{noise\ simulated}(v_n)$ (solid curves). The corresponding recovered spectral components $s_{noise}(v_n)$, $s_{signal}(v_n)$, and $s_{background}(v_n)$ as obtained by the WP decomposition are also shown as dotted lines. (B) Probability amplitudes of the recovered spectral components $s_{noise}(v_n)$, $s_{signal}(v_n)$, and $s_{background}(v_n)$ as obtained by the WP decomposition. (C) Moduli of the FFT's $\mathscr{F}(s_{simulated}(v_n))$, $\mathscr{F}(s_{noise\ simulated}(v_n))$, $\mathscr{F}(s_{signal\ simulated}(v_n))$, and $\mathscr{F}(s_{background\ simulated}(v_n))$ for the first 150 Fourier frequencies.

In order to test the applicability of the WP error-phase estimation also for the reconstruction of broadband CARS spectra covering the entire Raman shift range of $> 3500\ cm^{-1}$, we compare the WP approach with the conventional polynomial error-phase estimation scheme for the MEM-phase spectrum of toluene in fig. A.2. The polynomial error-phase estimation was

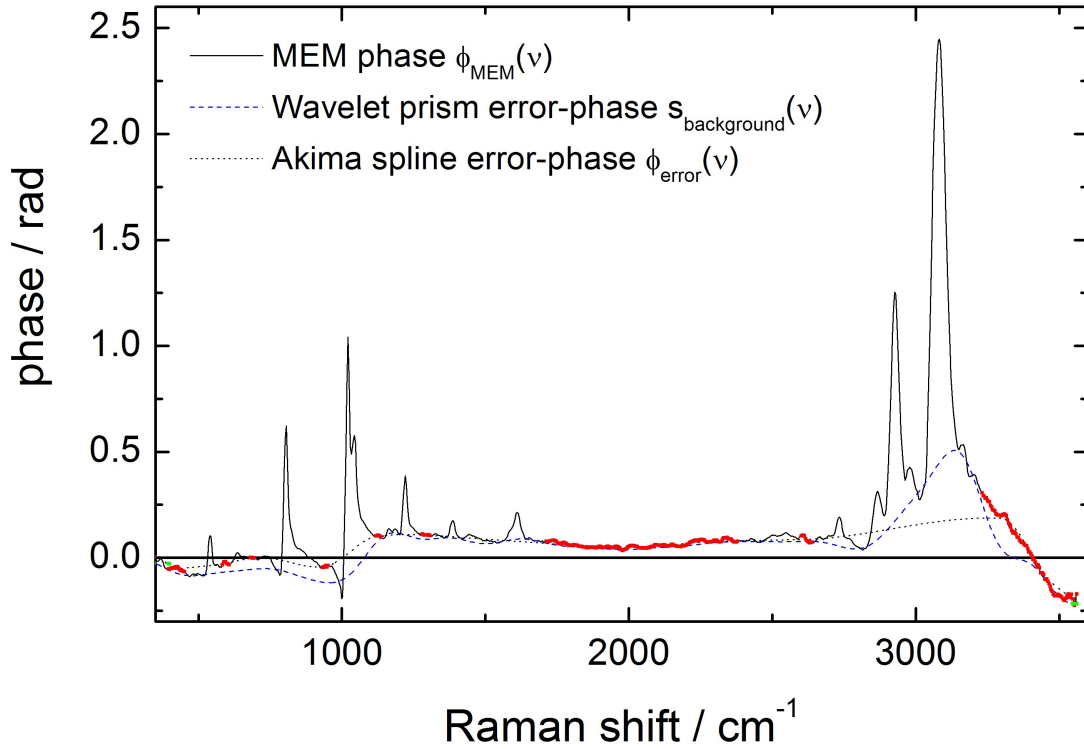Figure A.2: Comparison of the error-phase estimation $\phi_{error}(\nu)$ obtained using the Akima spline approach with the spectral component error-phase $s_{background}(\nu)$ as obtained by the Wavelet prism approach for a retrieved MEM-phase spectrum $\phi_{MEM}(\nu)$ of toluene.

performed using an Akima spline that fits the nonresonant spectral regions of the MEM-phase spectrum marked in red. The WP error-phase estimation was performed iteratively, using a decomposition level $\mathfrak{s} = 12$, a wavelet type symlet (sym12), and an error-phase spectrum defined as $s_{background}(\nu) = \sum_{i=7}^{\mathfrak{s}=12} s_i(\nu_n) + b_{\mathfrak{s}}(\nu_n)$. Each iteration step consists of (i) the WP decomposition of the MEM phase spectrum, (ii) the calculation of its WP background component $s_{background}(\nu)$, (iii) the fit of $s_{background}(\nu)$ to the nonresonant spectral end points of the MEM-phase spectrum (green points in fig. A.2), and (iv) the re-definition of the MEM phase spectrum by clipping and replacing its spectral amplitudes by the approximated $s_{background}(\nu)$ in those spectral regions where the MEM-phase spectrum amplitude exceeds $s_{background}(\nu)$ [50]. The iterative algorithm is terminated once the root-mean-square of the difference between $s_{background}(\nu)$ and its values of the preceding iteration is less than an empirically determined threshold, or until a predefined maximum number of iterations are performed. At this point, $s_{background}(\nu)$ is considered as an optimized estimate of the error-phase spectrum. When the error-phase spectrum estimated

using the Akima spline approach is compared with the WP background component spectrum, one observes good agreement in the spectral range from 1120 cm^{-1} to 2670 cm^{-1}. However, at around 1000 cm^{-1} and 3140 cm^{-1}, the WP decomposition result clearly identifies resonant features in the MEM phase spectrum as background, whereas the Akima spline error phase estimation fails.

In summary, the WP decomposition results in an acceptable error-phase spectrum estimation with the advantage of being unsupervized, that is no previous knowledge about nonresonant spectral regions is necessary. However, it is still a supervized approach with respect to choose $s_{noise}(v)$, $s_{signal}(v)$, and $s_{background}(v)$. If however knowledge about nonresonant spectral regions is available, using the Akima spline approach even results in a better estimation of the background spectrum. This is why in this thesis the polynomial error-phase estimation approaches described in section 3.3.2.1 are used.

A.4 Data denoising schemes

A.4.1 Denoising by singular value decomposition (SVD)

SVD is a matrix factorization or factor analysis method that can be used to construct a set of basis vectors for a given hyperspectral data set $Im[\chi^{(3)}(v, x, y, z, t)]$ using principal components analysis (PCA). The aim is to rewrite the data-matrix $Im[\chi^{(3)}(v, x, y, z, t)]$ as a linear sum of product terms [179]. This is performed by finding the eigenvalues and associated basis vectors or eigenvectors (EV's), which are ordered by sample variance subject to the constraint of orthogonality. By only taking a subset of basis vectors into account, a low-dimensional representation of the high-dimensional hyperspectral data set $Im[\chi^{(3)}(v, x, y, z, t)]$ is created. SVD is very popular for a wide range of applications. It can distinguish between EV's that differ only slightly and can become imperative to use for larger matrices containing more than several 1000 values. SVD makes use of the theorem, that any matrix $Im[\chi^{(3)}(v, x, y, z, t)]$ can be decomposed into a product of three matrices as follows

$$Im[\chi^{(3)}(v, x, y, z, t)] = \mathbf{U}\mathbf{S}\mathbf{V}^T \ .$$

(A.15)

Interestingly, the first occurrence of this idea can be dated back to the works of Eugenio Beltrami in 1873 [180]. Here, $\mathbf{U}$ and $\mathbf{V}$ are orthonormal matrices and fulfill $\mathbf{U}\mathbf{U}^T = \mathbf{V}\mathbf{V}^T = \mathbf{I}$, where $\mathbf{I}$ is the unity matrix. The columns of $\mathbf{U}$ hold orthonormalized EV's of the covariance matrix $Im[\chi^{(3)}(v, x, y, z, t)]Im[\chi^{(3)}(v, x, y, z, t)]^T$. Thus, $\mathbf{U}$ spans the row space of $Im[\chi^{(3)}(v, x, y, z, t)]$. The columns of $\mathbf{V}$ hold orthonormalized EV's of the covariance matrix $Im[\chi^{(3)}(v, x, y, z, t)]^T Im[\chi^{(3)}(v, x, y, z, t)]$. Consequently, $\mathbf{V}$ spans the column space of $Im[\chi^{(3)}(v, x, y, z, t)]$. The diagonal matrix $\mathbf{S} = diag(\sigma_1, \ldots, \sigma_n)$

holds n singular values σ_i, being the square roots of the respective eigenvalues of $Im[\chi^{(3)}(v, x, y, z, t)]^T Im[\chi^{(3)}(v, x, y, z, t)]$: $\mathbf{S}^2 = \mathbf{V}^T Im[\chi^{(3)}(v, x, y, z, t)]Im[\chi^{(3)}(v, x, y, z, t)]^T \mathbf{V} = \mathbf{U}^T Im[\chi^{(3)}(v, x, y, z, t)]Im[\chi^{(3)}(v, x, y, z, t)]^T \mathbf{U}$.

We are interested in using SVD for increasing the signal to noise ratio in the data sets $Im[\chi^{(3)}(v, x, y, z, t)]$ as shown by Otto and coworkers [181], [182]. The data set will be arranged as follows: $\mathbf{U}$ is a position-independent orthonormal basis set, while $\mathbf{V}$ takes into account the position dependent variation of the vectors in $\mathbf{U}$. The singular values in $\mathbf{S}$ simply represent the degree of how much their respective vectors in $\mathbf{U}$ and $\mathbf{V}$ contribute to $Im[\chi^{(3)}(v, x, y, z, t)]$. The singular values σ_i are now ordered as $\sigma_1 >= \sigma_2 >= \ldots >= \sigma_n >= 0$. When $Im[\chi^{(3)}(v, x, y, z, t)]$ has rank $r < n$, it follows that $\sigma_{r+1} = \sigma_{r+2} = \ldots = \sigma_n = 0$ [183]. In practice, this is the case when the EV's are neither completely independent nor $Im[\chi^{(3)}(v, x, y, z, t)]$ is completely dominated by noise. Then, instead of using all n EV's, a good approximation of $Im[\chi^{(3)}(v, x, y, z, t)]$ is obtained using only k EV's with $r \leq k \leq n$. Reconstructing $Im[\chi^{(3)}(v, x, y, z, t)]$ using only the first k singular values in $\mathbf{S}$ is simply performed with the matrix multiplication eq. A.15. This directly leads to the following advantageous properties of the SVD: discarding higher dimensions will significantly reduce the noise level in the data, provided the noise is assumed to be white (or in other words, the noise content along all dimensions is the same). This reduction of the dimensionality further comes along with a significant data reduction.

In order to choose the number k of the first singular values in $\mathbf{S}$, it is helpful to plot the ordered singular values as a function of dimensionality, as is shown in fig. A.3. For the singular values of the example data set shown, only the first $k = 7$ are of importance, because all singular values of higher dimensionality than $k = 7$ are of minor significance.

It is important to mention the following disadvantages and pitfalls when using SVD as a data denoising tool. First, we have to keep in mind that the EV's do not have any physical representation until they are projected onto the real basis vector corresponding to the independent components making up the data set $Im[\chi^{(3)}(v, x, y, z, t)]$. If this is not performed, the EV's can have negative values and mixes spectral features of several independent components. For example, in the case of single-events like cosmic rays, this results in the cosmic ray being mixed into several EV's, which introduces an artefact in all spectra. Therefore, it is mandatory to remove single-events prior performing SVD [184]. Normalization of $Im[\chi^{(3)}(v, x, y, z, t)]$ is another issue. Being based on detecting spectral variations, the ordering of the singular values depends on the variation of the amplitudes of the rows and columns in $Im[\chi^{(3)}(v, x, y, z, t)]$, and absolute intensity variation can mask the variation of signals of interest [185]. In addition, the noise in the data set is not white but of Poissonian distribution linked to the absolute peak intensities (for a detailed discussion visit appendix A.6). Therefore, SVD should be performed only with data sets having comparable absolute peak intensities. Finally, SVD and PCA treat the hyperspectrum $Im[\chi^{(3)}(v, x, y, z, t)]$ as a matrix. So even when the rank of
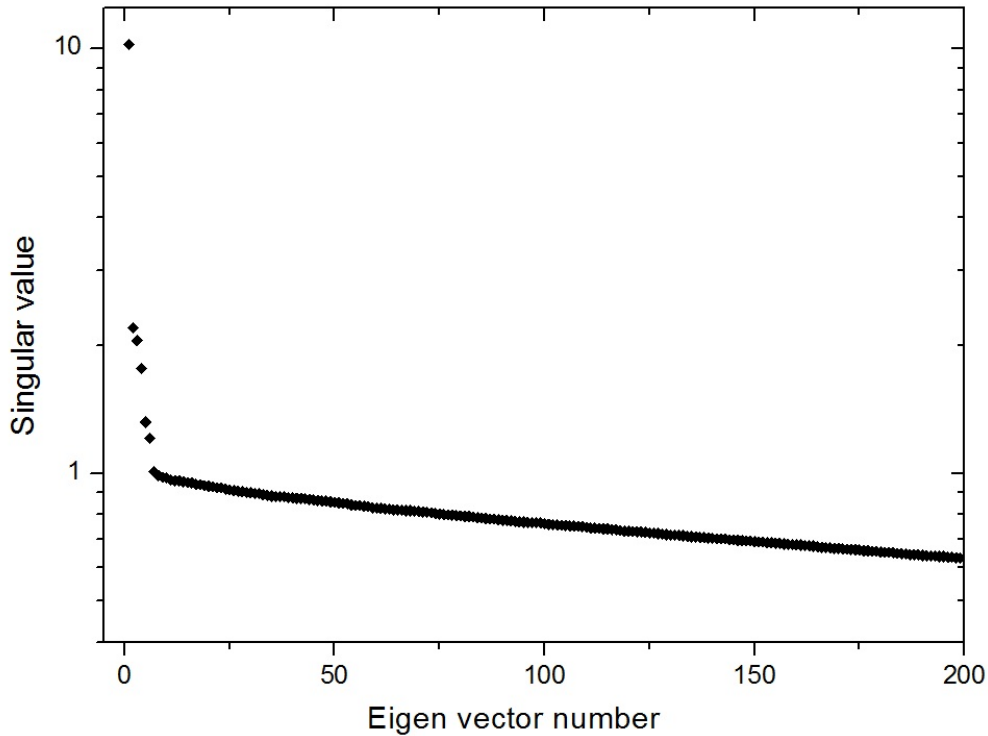
Figure A.3: Semilogarithmic plot of the first 200 singular values for a typical experimental data set of 3800 reconstructed Raman scattering spectra of an unloaded HL-60 cell.

$Im[\chi^{(3)}(v, x, y, z, t)]$ is higher than two, it is treated in a vectorized 2D form of the data-matrix, as $Im[\chi^{(3)}(v, x, y, z, t)] = vec\ Im[\chi^{(3)}(v, x, y, z, t)]$ [186]. This means that the information about the arrangement of the data is not taken into account!

In this thesis the SVD was computed in MATLAB, using the two-phase algorithm introduced by Golub [187],[183]. First, the data set $Im[\chi^{(3)}(v, x, y, z, t)]$ is transformed into an upper bidiagonal form. Next, this matrix is factorized using a QR decomposition. The computational cost of the QR decomposition is of order $O\ n^3$. Therefore, for large data sets $Im[\chi^{(3)}(v, x, y, z, t)]$ with dimensions $m \times n$ ($m, n > 1000$; $m > n$), it is appropriate to calculate the economy sized SVD. Instead of calculating $\mathbf{U}$, $\mathbf{S}$, and $\mathbf{V}$ with dimensions $m \times m, m \times n, n \times n$, respectively, the smaller matrices $\mathbf{U}$ and $\mathbf{S}$ of sizes $m \times n$ and $n \times n$, respectively, are calculated [188].

A.4.2 Denoising by bilateral filtering

For cases where the requirements are to increase the SNR of a hyperspectral data set $Im[\chi^{(3)}(v, x, y, z, t)]$ without loosing both weak spectral intensity features and the information about neighboring spectra, the bilateral filtering method was developed. The basic idea is to use the intensity correlation between neighboring values along all dimensions (see tab. A.1), and to decide whether the intensity value of interest, e.g. $Im[\chi^{(3)}(v, x, y, z, t)]$, is correlated with its

neighboring values in at least one of its five dimensions. If they are completely uncorrelated, they represent noise. In this way, the information, which pixel spectra are adjacent is not only maintained but exploited! If we look at the number of direct neighboring pixels as a function of the dimensionality **d** of the data, we can consider the following cases listed in tab. A.1 A

Table A.1: Table showing the rapidly increasing number of direct neighboring pixels in hyperspectra of dimensionality **d**.

dimensionality d	example	number of neighboring pixels $3^{\mathbf{d}} - 1$
0	point measurement, for example $Im[\chi^{(3)}(2850\ cm^{-1})]$	0
1	single spectrum, for example $Im[\chi^{(3)}(\nu)]$	2
2	time series, for example $Im[\chi^{(3)}(\nu, t)]$	8
3	3D hyper spectrum, for example $Im[\chi^{(3)}(\nu, x, y)]$	26
4	4D hyper spectrum, for example $Im[\chi^{(3)}(\nu, x, y, z)]$	80

hyperspectral data-set with a high dimensionality **d** and a high number of direct neighboring pixels allows a robust and efficient filtering of uncorrelated noise. All we need is to define a Gaussian filter kernel $\mathbf{c}(\boldsymbol{\xi}, \boldsymbol{\sigma})$ of the same dimensionality **d** as the hyperspectral data set

$$\mathbf{c}(\boldsymbol{\xi}, \boldsymbol{\sigma}) = e^{\left(\frac{-\xi}{\sigma}\right)^2} \ , \tag{A.16}$$

where for the case of **d**=4 in table A.1 $\boldsymbol{\xi} = (\nu, x, y, z)$ is the four-dimensional coordinate vector, and $\boldsymbol{\sigma} = \left(\sigma_\nu, \sigma_x, \sigma_y, \sigma_z\right)$ is the four-dimensional half widths vector. Then the actual filter process is the convolution of the **d**-dimensional input data $Im[\chi^{(3)}(\boldsymbol{\xi})]_{in}$ with the **d**-dimensional Gaussian filter kernel $\mathbf{c}(\boldsymbol{\xi}, \boldsymbol{\sigma})$ [189]:

$$Im[\chi^{(3)}(\boldsymbol{\xi})]_{out} = \left(\mathbf{c} * Im[\chi^{(3)}]_{in}\right)(\boldsymbol{\xi}) = \int e^{-\left(\frac{\|\boldsymbol{\xi}-\mathbf{r}\|}{\sigma}\right)^2} \times Im[\chi^{(3)}(\mathbf{r})]_{in} d\mathbf{r} \ . \tag{A.17}$$

The expression $\|\boldsymbol{\xi} - \mathbf{r}\|$ in eq. A.17 denotes the Euclidian norm, which is the distance between the coordinates $\boldsymbol{\xi}$ and $\mathbf{r}$. However, the disadvantage of this naïve filtering approach by convolution is a reduction of the resolution along all dimensions. This is demonstrated in fig. A.4, where a 3D hyperspectrum with $\boldsymbol{\xi} = (\nu, x, y)$ of a size of 130 pixel $\times$ 128 pixel $\times$ 128 pixel is simulated. The 3D hyperspectrum $Im[\chi^{(3)}(\boldsymbol{\xi})]_{in}$ consists of the species A (FAME 18:1, see ch. 7 for details) spectra in one half of the x-y-subspace, and of the species B (FAME 18:3) spectra in the other half. Gaussian noise was added to each spectrum artificially reducing the SNR to ≈ 10. The spectra of species A and B have different intensities at 2860 cm^{-1}, which results in the spatial
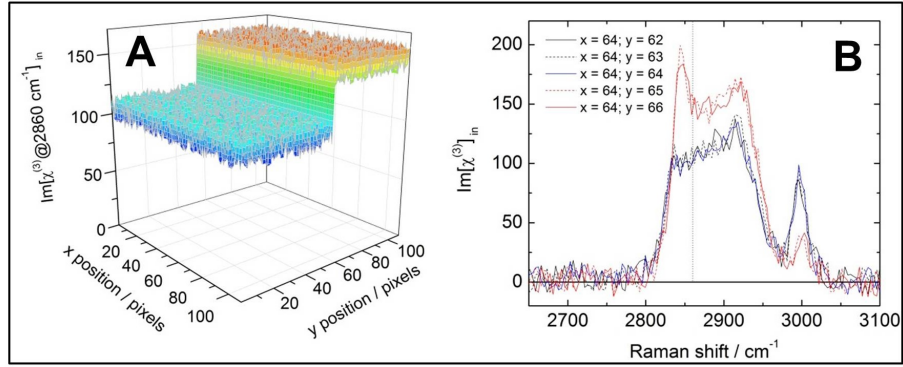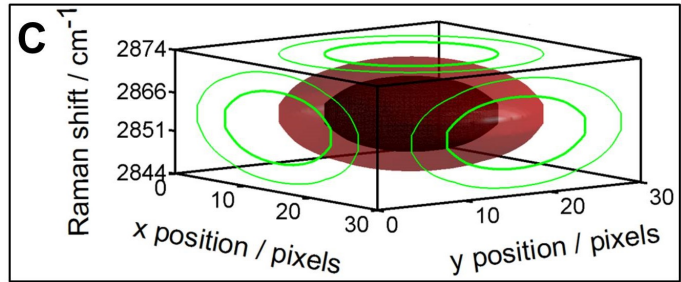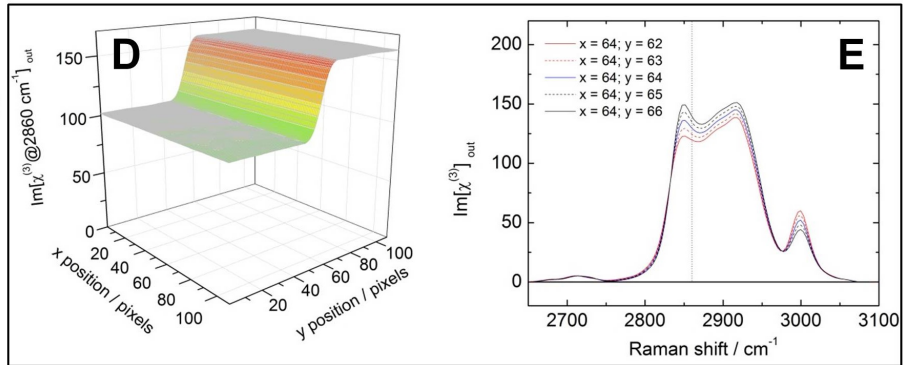
Figure A.4: Illustration of the result of filtering a 3D hyperspectrum $Im[\chi^{(3)}(\xi)]_{in}$ (A,B) using a fixed 3D Gaussian kernel $\mathbf{c}(\xi,\sigma)$ (C) with chosen half-widths of $\sigma_x = \sigma_y = 10$ spatial pixels and $\sigma_v = 4$ spectral pixels, corresponding to 14.8 cm^{-1}. The resulting output hyperspectrum $Im[\chi^{(3)}(\xi)]_{out}$ (D,E).

step that can be seen in fig. A.4 A. Fig. A.4 C shows the normalized and fixed Gaussian kernel as given by eq. A.16, with the isosurfaces for 0.2 and 0.5 (FWHM) indicated in red. The 2D projections are plotted in green. By applying eq. A.17, we have reduced effectively the spatial and the spectral noise levels. However, at the same time, both the spatial and the spectral resolutions have been reduced. After filtering, the sharp spatial step appears smeared out (see fig. A.4 D) and so do the spectral features, as can be seen in spectra belonging to neighboring pixels across the step (see fig. A.4 E).

So far, the intensity itself has not yet been exploited as an information independent of the spatial and spectral dimensions. Using this extra dimension for denoising images is known as

bilateral or Tomasi-Manduchi filtering [190], [191], [189]. Jiang et. al. [192] describe the math for **d**=2, which will here be generalized for data of higher dimensionality. In addition to the filtering using the Gaussian $\mathbf{c}(\xi, \sigma)$ defined in eq. A.16 (in this context called closeness function), a second Gaussian $\mathbf{s}(\xi, \sigma_{range})$ (in this context called similarity function) is defined for the range filtering

$$\mathbf{s}(\xi, \sigma_{range}) = e^{-\left(\frac{Im[\chi^{(3)}(\xi)]_{in}}{\sigma_{range}}\right)^2} \quad , \tag{A.18}$$

where for the case of **d** = 3 in tab. A.1 $\xi = (\nu, x, y)$ and $\sigma_{range} = (\sigma_{range\ \nu}, \sigma_{range\ x}, \sigma_{range\ y})$. The convolution integral with the combined filtering kernel then reads as follows

$$Im[\chi^{(3)}(\xi)]_{out} = \left((\mathbf{c} \times \mathbf{s}) * Im[\chi^{(3)}]_{in}\right)(\xi) = \int e^{-\left(\frac{\|\xi - \mathbf{r}\|}{\sigma}\right)^2} \times e^{-\left(\frac{\|Im[\chi^{(3)}(\xi)]_{in} - Im[\chi^{(3)}(\mathbf{r})]_{in}\|}{\sigma_{range}}\right)^2} \times Im[\chi^{(3)}(\mathbf{r})]_{in} d\mathbf{r} \quad . \tag{A.19}$$

When compared with eq. A.17, the new vector σ_{range} denotes the half widths used for the intensity similarity along each dimension. With other words, for every pixel-value the fixed Gaussian kernel $\mathbf{c}(\xi, \sigma)$ is weighted with another Gaussian $\mathbf{s}(\xi, \sigma_{range})$ representing the intensity difference between a pixel value and its neighboring pixel values. For the case of 2D data sets (**d**=2), bilateral filtering was successfully used in cryo-electron microscopy [192], [193], and imaging [194], [195]. However, to the best of my knowledge, bilateral filtering has not been applied to high dimensional spectroscopic data sets yet.

It is straight forward to generalize the bilateral filtering principle to more dimensions, as is illustrated in fig. A.5 for the same 3D-hyperspectrum, previously shown in fig. A.4. Here, the 3D Gaussian kernel $\mathbf{c}(\xi, \sigma)$ is weighted with a 3D similarity function $\mathbf{s}(\xi, \sigma_{range})$ that represents the intensity difference along the two spatial dimensions and along the spectral dimension. The combined 3D-bilateral filter kernel $\mathbf{c}(\xi, \sigma) \times \mathbf{s}(\xi, \sigma_{range})$ is shown in fig. A.5 (C) for a representative pixel spectrum located at the boundary separating species A from species B (see the blue spectrum in fig. A.5 B and E, $x = y = 64$), and a Raman shift of 2860 cm^{-1}. The normalized combined 3D-bilateral filter kernel is again plotted together with the isosurfaces for 0.2 and 0.5 (FWHM) indicated in red. The 2D projections are plotted in green. The noise is reduced while preserving the spatial and spectral resolution (compare fig. A.5 A and B with fig. A.5 D and E). The spatial step and all spectral features are preserved, and no 'mixing' of the spectra belonging to the two spectrally distinct species nearby the boundary is observed. The implementation of the bilateral filter in MATLAB is done by **d**-dimensional Gaussian filtering. In order to not reduce the resolution in any dimension, the FWHM must be set corresponding to the data's resolution along each corresponding dimension. Because of the weighting of the fixed Gaussian kernel $\mathbf{c}(\xi, \sigma)$, the bilateral filter is data adaptive which results in a slower computational processing of the convolution given in eq. A.19. By using the algorithm given by Paris [195] based on a signal processing approach, shorter calculation times can be achieved.

Input
$Im\ [\chi^{(3)}\ (\xi)]_{in}$
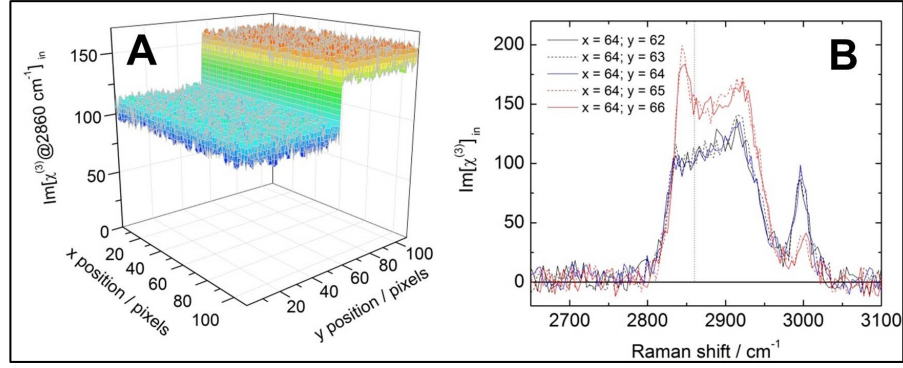
3D-bilateral filter kernel
$\mathbf{c}(\xi,\sigma)\ \mathbf{s}(\xi,\sigma_{range})$

shown for $\xi = \begin{pmatrix} x = 64 \\ y = 64 \\ \nu = 2860\ cm^{-1} \end{pmatrix}$
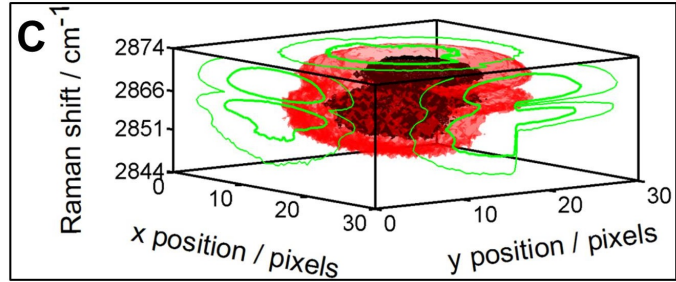
Output
$Im\ [\chi^{(3)}\ (\xi)]_{out}$
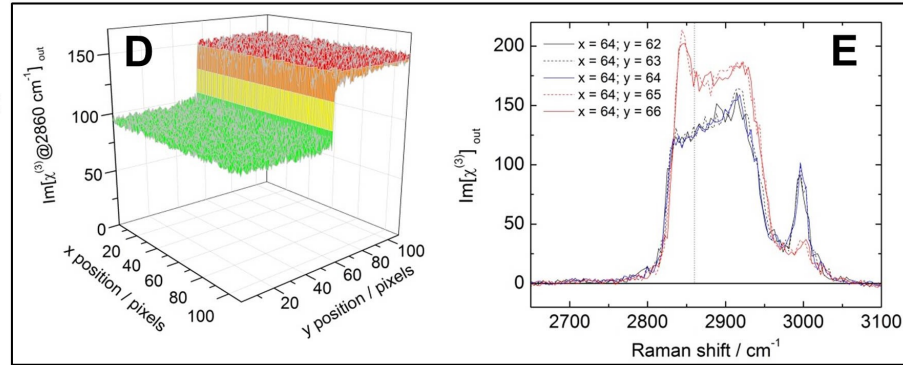
Figure A.5: Illustration of the result of filtering a 3D hyperspectrum $Im[\chi^{(3)}\ (\xi)]_{in}$ (A,B) using a fixed 3D Gaussian kernel $\mathbf{c}(\xi,\sigma)$ weighted with another 3D Gaussian similarity function $\mathbf{s}(\xi,\sigma_{range})$ with chosen half-widths of $\sigma_x = \sigma_y = 10$ spatial pixels, $\sigma_\nu = 4$ spectral pixels, corresponding to 14.8 cm^{-1}, and $\sigma_{range\ \nu} = \sigma_{range\ x} = \sigma_{range\ y} = 0.02$. The resulting output hyperspectrum $Im[\chi^{(3)}\ (\xi)]_{out}$ (D,E).

A.5   Influence of an offset to the CARS spectrum

Here, the influence of an offset to the measured CARS spectrum $S(\nu)$ is considered. Such an offset can be caused by an erroneous dark count correction of raw spectra, by two photon fluorescence background originating from the sample, or by a wrong normalization with an incorrectly determined reference spectrum $I_{CARS\ reference}(\nu)$ (see eq. 3.26). Using the same model for $\chi^{(3)}_{tot}(\delta)$ as used in the simulations shown in fig. 3.6, offsets of $+0.2$ and -0.2 are added to the normalized CARS spectrum $|\chi^{(3)}_{tot}(\delta)|^2$ (see fig. A.6 A). Here, we are first interested

in the spectral shapes of the retrieved phase $\phi_{tot}^{(3)}(\delta)$. We notice that asymmetric line shapes for the single Lorentzian line are obtained when the CARS spectra are offset. The plot of the corresponding reconstructed $\chi_{tot}^{(3)}(\delta)$ in the complex plane (fig. A.6 B) reveals that the resonances are no more exactly circular but have a curd or kidney-like shape, depending on the sign of the offset. The points of zero detuning ($\delta = 0$) and maximum detuning ($\delta = \pm\infty$) are no longer superimposed upon each other. Note that all $\chi_{tot}^{(3)}(\delta)$ curves remain almost completely in the first and fourth quadrant of the complex plane, and thus the susceptibility remains causal (see the 100 x close up in fig. A.6 C). However, the asymmetric line shape does not affect the determination of the frequency independent phase ϕ_{eff} needed for the reconstruction of the complex $\chi_{Res}^{(3)}(\delta)$. The maximum error caused by the simulated offsets of $S(\nu) = \pm0.2$ is found to be 11.2 % of $Im[\chi_{Res}^{(3)}(\delta)]$. Thus, the functional in eq. 5.38 in section 5.3.3 is very robust against an erroneous dark count correction of the raw spectra. Nevertheless, the asymmetry introduced by such an erroneous dark count correction can not be removed, and therefore must be avoided in the first place.

A.6 Influence of noise and relative amount of $\chi_{\mathbf{NR}}^{(3)}$ amplitudes on reconstructing $Im[\chi_{\mathbf{Res}}^{(3)}]$ amplitudes

A.6.1 Introduction

When normalizing measured CARS spectra of a sample by a purely nonresonant reference CARS spectrum (see eq. 3.26), we have assumed that the latter is measured under exactly the same experimental conditions. Because within a heterogeneous sample $\chi_{NR\,Ref}^{(3)} \neq \chi_{NR\,sample}^{(3)}(\nu, x, y, z, t)$, a single reference spectrum cannot normalize the nonresonant background in every spectrum of a hyperspectrum as $\chi_{NR\,sample}^{(3)} = f(\nu, x, y, z, t)$ to unity. Furthermore, when we want to compare the different samples, we also have to deal with different reference CARS spectra $|\chi_{NR\,Ref}^{(3)}|^2$. We have seen in the simulation presented in section 3.2.2 (fig. 3.8) that a variation of $\chi_{NR\,sample}^{(3)}$ affects both the CARS spectra and the corresponding phase spectra. Here, we will simulate the influence of noise and relative $\chi_{NR}^{(3)}$ amplitudes on the reconstructed $Im[\chi_{Res}^{(3)}(\nu)]$ amplitudes for the following three cases of normalizing the CARS spectrum:

The first case (*a*) deals with a heterogeneous sample, where $\chi_{NR\,sample}^{(3)}$ is fixed, and scales by a factor $C_a(x, y, z, t)$ in space and time, i.e. $\chi_{sample}^{(3)}(\nu, x, y, z, t) = C_a(x, y, z, t)\chi_{NR\,sample}^{(3)} + \chi_{Res\,sample}^{(3)}(\nu, x, y, z, t)$. This scenario was simulated in section 3.2.2 (fig. 3.8), and corresponds, for example, to bleaching of electronic contributions of carotenoids over time. The corresponding equation for the normalized CARS spectrum $S(\nu)$ thus reads:

$$S(\nu, x, y, z, t) = \frac{|C_a(x, y, z, t)\chi_{NR\,sample}^{(3)} + \chi_{Res\,sample}^{(3)}(\nu, x, y, z, t)|^2}{|\chi_{NR\,Ref}^{(3)}|^2} \quad . \tag{A.20}$$
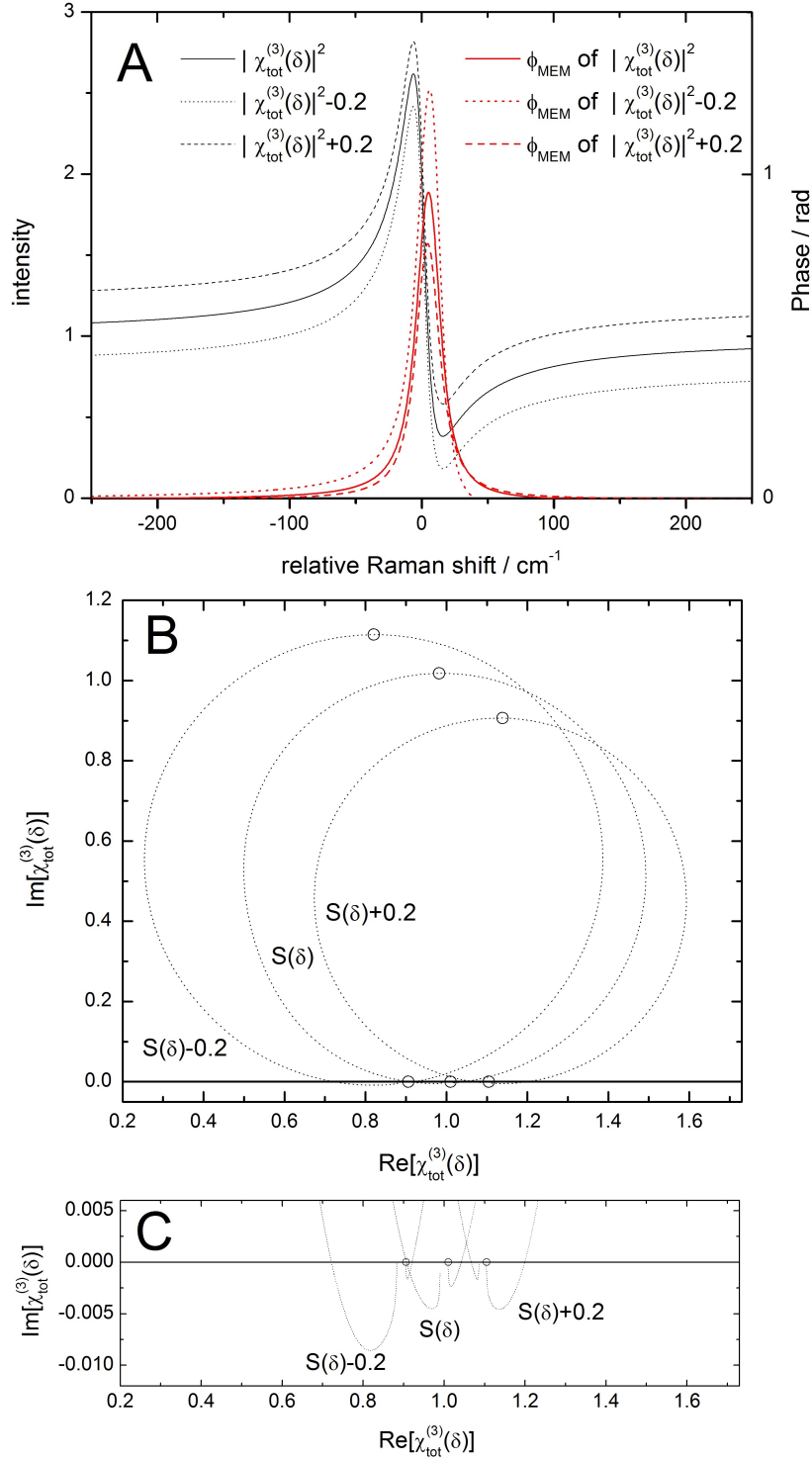
Figure A.6: Simulation of constant offsets of ± 0.2 added to the normalized CARS spectrum $S(\delta) = |\chi_{tot}^{(3)}(\delta)|^2$ of an complex isolated Lorentzian $\chi_{Res}^{(3)}(\delta)$ in the presence of a nonresonant background $\chi_{NR}^{(3)}$. (A) CARS spectra $S(\delta) - 0.2$, $S(\delta)$, $S(\delta) + 0.2$ and the corresponding MEM phase spectra $\phi_{MEM}(\delta)$, calculated using eq. 3.28 and eq. 3.53, respectively. Plots of the corresponding reconstructed $\chi_{tot}^{(3)}(\delta)$ in the complex plane (B, C). The simulation parameters are $A = 1 \ cm^{-1}$, $\chi_{NR}^{(3)} = 1$, and $\Gamma = 20 \ cm^{-1}$.

Case (*b*) deals with a heterogeneous sample, where both $\chi^{(3)}_{NR\ sample}(\nu, x, y, z, t)$ and $\chi^{(3)}_{Res\ sample}(\nu, x, y, z, t)$ scale likewise by a factor $C_b(x, y, z, t)$, i.e. $\chi^{(3)}_{sample}(\nu, x, y, z, t) = C_b(x, y, z, t)(\chi^{(3)}_{NR\ sample} + \chi^{(3)}_{Res\ sample}(\nu))$. This case corresponds to one species present in different concentrations. The corresponding equation for the normalized CARS spectrum $S(\nu)$ thus reads:

$$S(\nu, x, y, z, t) = C_b(x, y, z, t)^2 \frac{|\chi^{(3)}_{NR\ sample} + \chi^{(3)}_{Res\ sample}(\nu)|^2}{|\chi^{(3)}_{NR\ Ref}|^2} \quad . \tag{A.21}$$

Case (*c*) deals with different reference spectra, which corresponds to comparing independent CARS measurements. The corresponding equation for the normalized CARS spectrum $S(\nu)$ thus reads:

$$S(\nu, x, y, z, t) = \frac{|\chi^{(3)}_{sample}(\nu, x, y, z, t)|^2}{|C_c \chi^{(3)}_{NR\ Ref}|^2} \quad . \tag{A.22}$$

All simulations have been performed in MATLAB. The noise of the simulated sample and reference CARS spectra is assumed to be shot noise. This is taken into account by adding Gaussian noise of width Δ_G, which is weighted by the square root of the simulated CARS amplitudes, resulting in noise amplitudes of $\delta I_{CARS\ sample}(\nu) = \Delta_G \sqrt{I_{CARS\ sample}(\nu)}$ and $\delta I_{CARS\ ref}(\nu) = \Delta_G \sqrt{I_{CARS\ ref}(\nu)}$. The normalized CARS spectra $S(\nu)$ are then simulated for the different Gaussian width Δ_G and different ratios C_a, C_b, and C_c, according to eq. 3.26. The corresponding $Im[\chi^{(3)}_{Res}(\nu)]$ spectra are reconstructed using the DCT-MEM (see ch. 5). The simulation parameters for a single Lorentzian resonance centered at $\nu_0 = 0\ cm^{-1}$ are $A = 1\ cm^{-1}$ and $\Gamma = 20\ cm^{-1}$ (see eq. 3.28). Noise amplitudes for the CARS spectra $\delta S(\nu)$, the MEM phase $\delta \phi_{MEM}(\nu)$, and the reconstructed $Im[\chi^{(3)}_{Res}(\nu)]$ amplitude $\delta Im[\chi^{(3)}_{Res}(\nu)]$ were calculated as standard deviations for the first 100 points within the nonresonant region from $-5000\ cm^{-1}$ to $-4900\ cm^{-1}$ and within the frequency interval $\pm 2\ cm^{-1}$ around the center frequency $\nu_0 = 0\ cm^{-1}$. The nonresonant contributions $\chi^{(3)}_{NR\ Ref}$ and $\chi^{(3)}_{NR\ sample}$ are set to unity. The simulated Gaussian noise widths are Δ_G $0\ cm^{-2}$, $0.001\ cm^{-2}$, $0.01\ cm^{-2}$, $0.1\ cm^{-2}$ and $1\ cm^{-2}$.

A.6.2 Simulation results

We are first interested in the noise amplitudes $\delta S(\nu)$, $\delta \phi_{MEM}(\nu)$, and $\delta Im[\chi^{(3)}_{Res}(\nu)]$ in the nonresonant regions as a function of C_a, C_b, and C_c. The results for the *case a* (eq. A.20) are shown as the first row in fig. A.7. Fig. A.7 A shows the quadratic dependence of the noise amplitude in the nonresonant region of the simulated CARS spectra on C_a. The noise amplitude in the nonresonant region of the corresponding MEM phase spectra is shown in Fig. A.7 B. Without added noise, the phase noise in the nonresonant region is decreasing with increasing C_a. With
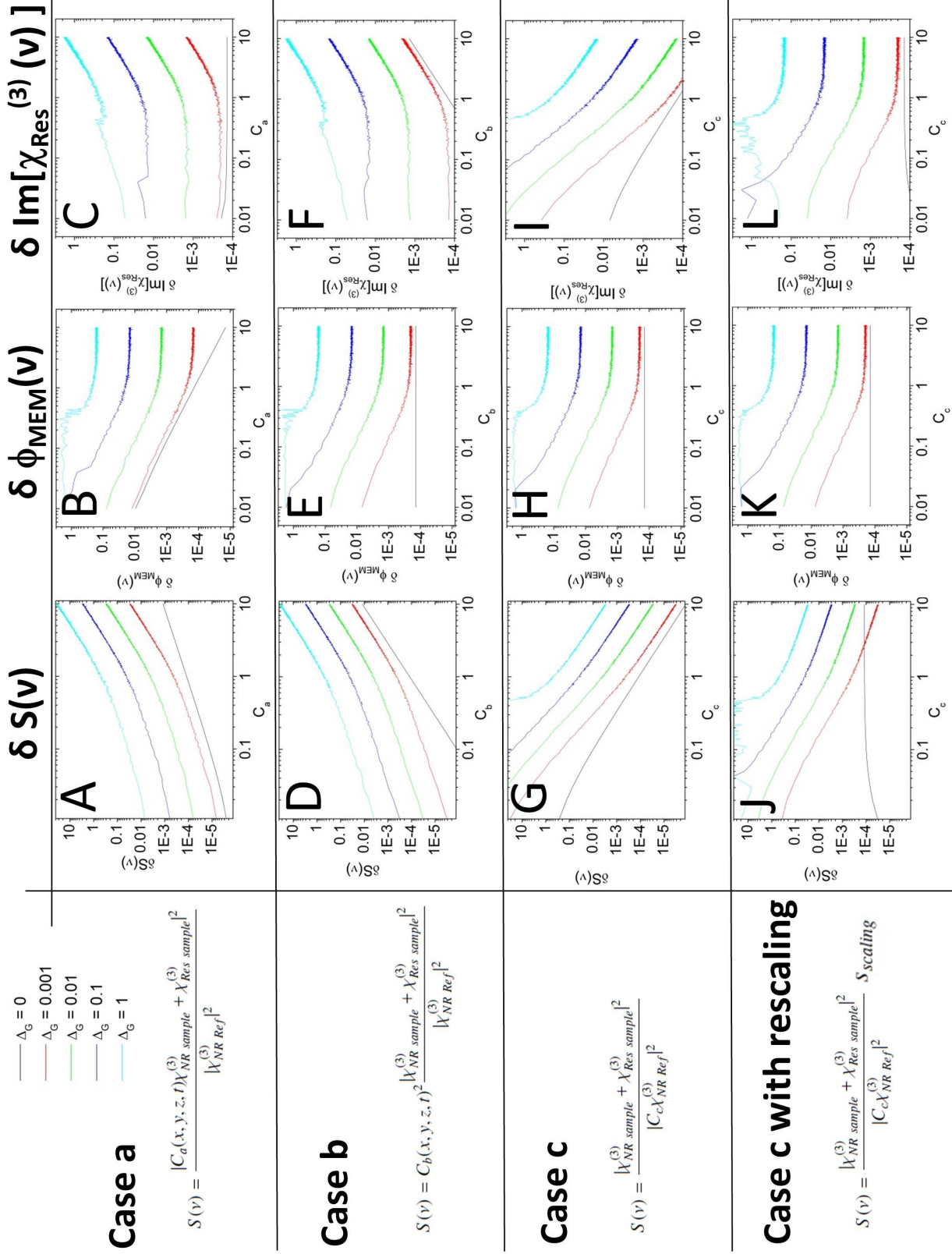
Figure A.7: Influence of simulated Gaussian noise of width Δ_G on the noise amplitudes $\delta S(\nu)$, $\delta\phi_{MEM}(\nu)$, and $\delta Im[\chi_{Res}^{(3)}(\nu)]$ in the nonresonant region of simulated CARS spectra (first column), retrieved MEM phase $\phi_{MEM}(\nu)$ spectra (second column), and reconstructed $Im[\chi_{Res}^{(3)}(\nu)]$ spectra (third column), respectively, as a function of the scaling parameters C_a, C_b, and C_c, according to the cases a, b, and c, respectively. (See text for the simulation parameters used).

217

noise, $\delta\phi_{MEM}(\nu)$ becomes constant for values of $C_a \geq 1$. For $C_a < 1$ and high levels of simulated Δ_G, a kink in the phase noise is observed. In these cases, $\delta S(\nu)$ approaches zero values, which leads to maximum phase noise, i.e. the MEM-phase then arbitrary varies from $-\pi$ to π. In fig. A.7 C, the noise amplitude in the nonresonant region of the corresponding reconstructed $Im[\chi_{Res}^{(3)}(\nu)]$ is shown. Not surprisingly, one observes the impact of the above discussed trends. For $C_a < 1$, the dependencies of $\delta S(\nu)$ and $\delta\phi_{MEM}(\nu)$ cancel each other, leading to a constant $\delta Im[\chi_{Res}^{(3)}(\nu)]$. For $C_a \geq 1$, the quadratic dependence of $\delta S(\nu)$ leads to a linearly increasing $\delta Im[\chi_{Res}^{(3)}(\nu)]$ on C_a.

The next case simulated is *case b* (eq. A.21), the simulation results are shown in the second row in fig. A.7. The influence of δS (fig. A.7 D), $\delta\phi_{MEM}(\nu)$ (fig. A.7 E), and $\delta Im[\chi_{Res}^{(3)}(\nu)]$ (fig. A.7 F) on C_b is reproducing the respective dependencies observed for *case a*. However, without simulated noise, the MEM phase noise amplitude remains constant in the nonresonant region, as is expected when the phase does not change.

The results for *case c* (eq. A.22) are shown as the third row in fig. A.7. Here, the $\delta Im[\chi_{Res}^{(3)}(\nu)]$ is depending on C_c, and without the amount of C_c taken into account, wrong $Im[\chi_{Res}^{(3)}(\nu)]$ amplitudes are reconstructed! Also, $\delta S(\nu)$ shows different behaviour than in *cases a* and *b*: The opposite trend is observed for increasing C_c. The noise amplitude $\delta\phi_{MEM}(\nu)$ (fig. A.7 H) shows the same behaviour as in *case b*. A reference spectrum that has a nonresonant susceptibility different than the sample spectrum will act like scaling the CARS spectrum by a factor $\frac{1}{C_c^2}$ but will not affect the MEM phase spectrum. As a result, the reconstructed $Im[\chi_{Res}^{(3)}(\nu)]$ spectrum will be scaled by $\frac{1}{C_c}$. Consequently, $\delta Im[\chi_{Res}^{(3)}(\nu)]$ in the nonresonant region shows the opposite trends than in *case a* and *case b*, fig. A.7 C and F, respectively. To circumvent the dependence on C_c, we have to rescale the reconstructed $Im[\chi_{Res}^{(3)}(\nu)]$ spectrum with $\frac{1}{C_c}$. As a result of the rescaling, the dependencies of the $\delta S(\nu)$ and $\delta Im[\chi_{Res}^{(3)}(\nu)]$ on C_c resemble those of *cases a* and *b*, while the dependence of $\delta\phi_{MEM}(\nu)$ on C_c of course remains unchanged. The corresponding results of the rescaling are shown in the fourth row in fig. A.7.

Next, we are interested in the dependence of $\delta Im[\chi_{Res}^{(3)}(\nu)]$ in both the resonant and the nonresonant regions on C_i (i=a,b,c). The results for *cases a* and *b* are shown in fig. A.8 A and B, respectively. All curves show linear dependencies on C_a for values $C_a \geq 1$. Note, that the noise amplitudes are higher in the nonresonant region of $Im[\chi_{Res}^{(3)}(\nu)]$ than in the resonant region! The same observation holds for *case b* (fig. A.8 B). The results for *case c* with rescaling (not shown) again look like the mirrored version of *case b*.

However, we have not considered so far, whether or not there is an optimum ratio $\frac{\chi_{NR\ Sample}^{(3)}}{\chi_{NR\ Ref}^{(3)}}$, where the signal to noise ratio (SNR) of the reconstructed $Im[\chi_{Res}^{(3)}(\nu)]$ spectrum is maximized. Therefore, the ratio of the peak amplitude of the reconstructed $Im[\chi_{Res}^{(3)}(\nu)]$ spectrum at $\nu_0 = 0\ cm^{-1}$ to the standard deviation $\delta Im[\chi_{Res}^{(3)}]$ of the first 100 values in the nonresonant region of the reconstructed $Im[\chi_{Res}^{(3)}(\nu)]$ spectrum is determined and plotted as function of C_a, C_b, and
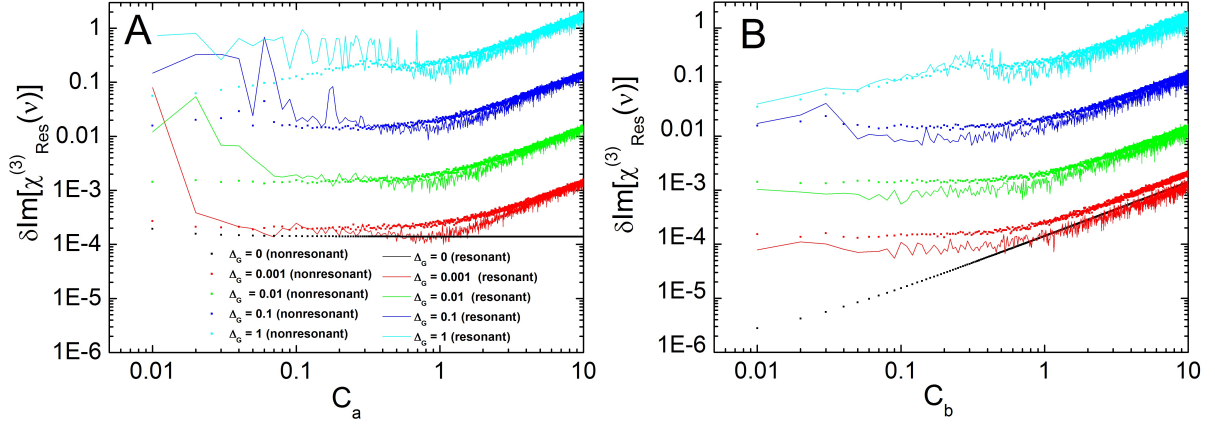
Figure A.8: Simulated $\delta Im[\chi_{Res}^{(3)}(\nu)]$ in the resonant (solid curves) and nonresonant region (dotted curves) for *case a* (A) and *case b* (B).

C_c for *cases a*, *b*, and *c* with rescaling, respectively. The results are plotted in fig. A.9. The
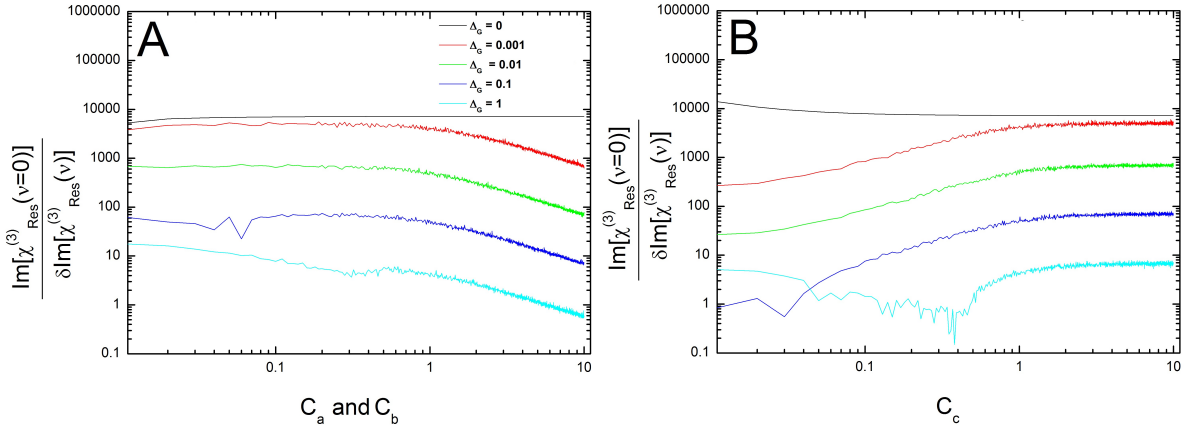

Figure A.9: Comparison of simulated SNR in reconstructed $Im[\chi_{Res}^{(3)}(\nu)]$ spectra corresponding to *cases a* and *b* (A), and *case c* with rescaling (B).

simulated SNR curves exhibit opposite dependencies, when *cases a* and *b* are compared to *c* with rescaling. We obtain the same SNR dependence, regardless of whether C_a (*case a*) or C_b (*case b*) is changed. In *cases a* and *b* shown in fig. A.9 A, the SNR is almost constant up to values of $C_a = 0.7$ and then drops. For *case c* with rescaling, shown in fig. A.9 B, the SNR is constant for $C_c \geq 1.3$, but drops for values below 1.3. Not surprisingly, for the SNR it makes no difference, if the reconstructed spectra are scaled by $\chi_{NR\ Ref}^{(3)}$ or not.

The CARS signal depends quadratically on the sample concentration, and under the assumption of Poissonian noise, the CARS noise amplitude δS is quadratic with the sample concentration. The CARS spectrum $S(\nu)$ contributes to the reconstructed $Im[\chi_{Res}^{(3)}(\nu)]$ spectrum as $\sqrt{S(\nu)}$, and so its noise amplitude $\delta Im[\chi_{Res}^{(3)}(\nu)]$ is linear with the sample concentration (*case b*). This is definitely not the case in spontaneous Raman scattering spectra, where the noise scales directly with $\sqrt{Im[\chi_{Res}^{(3)}(\nu)]}$, and therefore is independent of the sample concentration in

nonresonant regions. Fig. A.10 illustrates this situation for a spontaneous Raman spectrum simulated with a Poissonian noise amplitude of $\pm\ 0.1\ cm^{-1}\ \sqrt{Im[\chi_{Res}^{(3)}(\nu)]}$. There is almost no

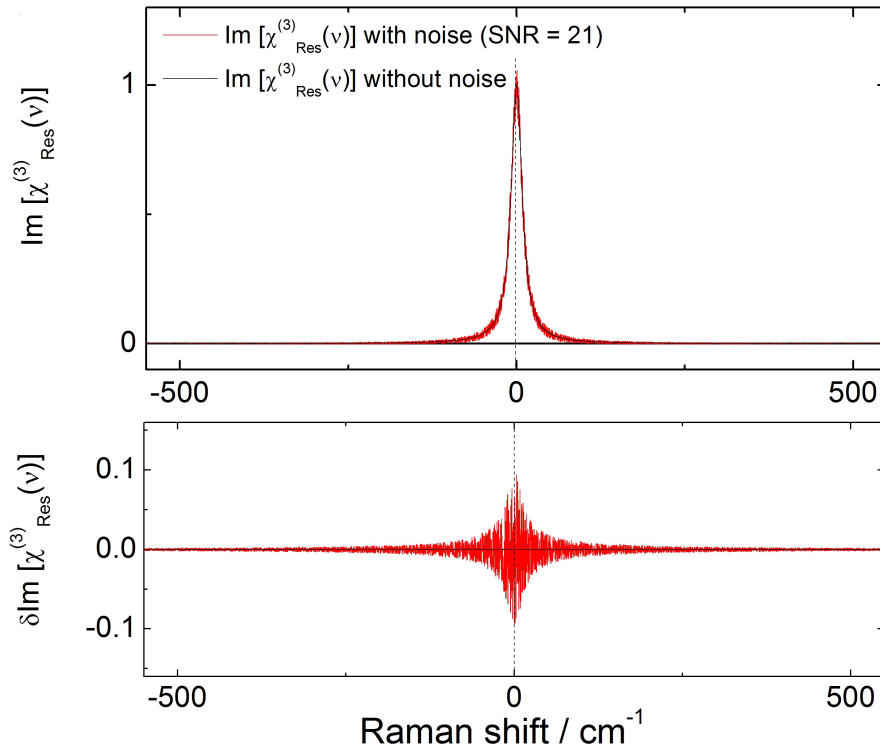Figure A.10: Simulated $Im[\chi_{Res}^{(3)}(\nu)]$ and $\delta Im[\chi_{Res}^{(3)}(\nu)]$ spectra corresponding to spontaneous Raman scattering with and without a simulated noise amplitude of $\pm\ 0.1$ $cm^{-1}\ \sqrt{Im[\chi_{Res}^{(3)}(\nu)]}$. (See text for the remaining simulation parameters used).

signal far away from the resonance center frequency, and therefore almost no noise. The noise amplitude $\delta Im[\chi_{Res}^{(3)}(\nu)]$ is highest at the center frequency, and the SNR at the resonance is determined to be approximately 21. (Here the noise amplitude $\delta Im[\chi_{Res}^{(3)}(\nu)]$ within the frequency interval $\pm 2\ cm^{-1}$ around the center frquency $\nu_0 = 0\ cm^{-1}$ was used). A completely different picture is obtained for the corresponding CARS simulations as shown in fig. A.11 for the *case b*. Similar results are obtained in *case a*. In contrast to the spontaneous Raman spectrum shown in fig. A.10, the noise amplitudes $\delta S(\nu)$ and $\delta Im[\chi_{Res}^{(3)}(\nu)]$ are not zero in the nonresonant region. Fig. A.11 A shows a maximum and a minimum of $\delta S(\nu)$, representing the regions of maximum constructive and destructive interferences, respectively. In $\delta Im[\chi_{Res}^{(3)}(\nu)]$ however (fig. A.11 B), only a minimum appears that is slightly shifted from the center frequency $\nu_0 = 0\ cm^{-1}$. This means, that in the case of CARS the noise amplitude of the $Im[\chi_{Res}^{(3)}(\nu)]$ spectrum is less close to the resonance compared with the noise in the nonresonant region! In both, *case a* and *case b*, the SNR has a higher value of ≈ 85 when compared to that obtained in the spontaneous Raman case. (Here, again the noise amplitude $\delta Im[\chi_{Res}^{(3)}(\nu)]$ within the frequency interval $\pm 2\ cm^{-1}$ around the center frquency $\nu_0 = 0\ cm^{-1}$ was used).
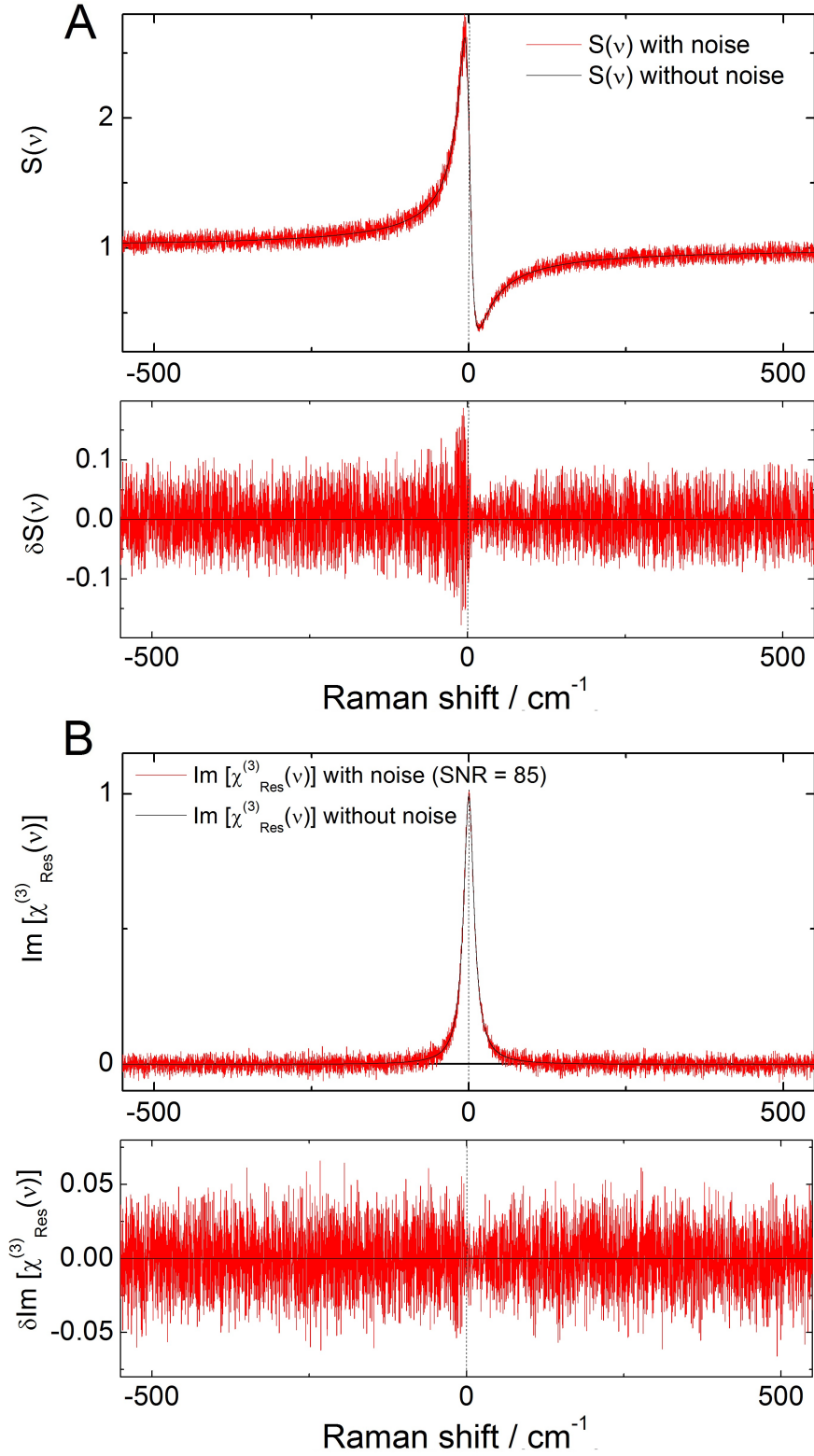
Figure A.11: Simulated $S(\nu)$ and $\delta S(\nu)$ (A) and $Im[\chi^{(3)}_{Res}(\nu)]$ and $\delta Im[\chi^{(3)}_{Res}(\nu)]$ (B) spectra corresponding to the CARS simulations for *case b*. The simulation parameters are $\Delta_G = \pm 0.1\ cm^{-2}$, and $\frac{\chi^{(3)}_{NR\ Sample}}{\chi^{(3)}_{NR\ Ref}} = 1$. (See text for the remaining simulation parameters used).

Generally, when we want to compare hyperspectra measured under different conditions, such as integration times, pump and Stokes powers, and different reference spectra, we have to rescale the reconstruction result. Different measurement conditions will be considered by introducing the scaling factor $s_{scaling}$:

$$s_{scaling} = \frac{\frac{\chi^{(3)}_{NR\ Sample1}(x,y,z,t)}{\chi^{(3)}_{NR\ Ref1}}}{\frac{\chi^{(3)}_{NR\ Sample2}(x,y,z,t)}{\chi^{(3)}_{NR\ Ref2}}} = \frac{C_{i\ 1}C_{c\ 2}}{C_{i\ 2}C_{c\ 1}}; \text{ with i = a or b } . \tag{A.23}$$

If the hyperspectra share the same reference spectrum, eq. A.23 simplifies to

$$s_{scaling} = \frac{\chi^{(3)}_{NR\ Sample1}(x,y,z,t)}{\chi^{(3)}_{NR\ Sample2}(x,y,z,t)} = \frac{C_{i\ 1}}{C_{i\ 2}}; \text{ with i = a or b } , \tag{A.24}$$

and if the hyperspectra share the same sample spectrum, eq. A.23 simplifies to

$$s_{scaling} = \frac{\chi^{(3)}_{NR\ Ref2}}{\chi^{(3)}_{NR\ Ref1}} = \frac{C_{c\ 2}}{C_{c\ 1}} . \tag{A.25}$$

So far, only simulation results have been presented. Next, eqs. A.23 - A.25 will be applied to experimental CARS spectra of a water sample with known concentration of 55.55 M. Water was measured under different measurement conditions and reconstructed using different reference spectra (for details, see ch. 7). The measurement conditions for the water (sample) spectrum are 200 ms spectrum dwell time, 15 mW pump power and 7.5 mW Stokes power. The measurement conditions for the reference spectrum A are the same as for the water spectrum. Measurement conditions for the reference spectrum B are 50 ms spectrum dwell time, 30 mW pump power and 15 mW Stokes power. For the reference spectra C and D, the measurement conditions were identical to that of spectrum B, except for the spectrum dwell times of 100 ms and 200 ms, respectively. The values of $\chi^{(3)}_{NR\ Ref}$ are 12.3, 16.84, 22.90, and 31.88 for spectrum A, B, C, and D, respectively. Using spectrum A as reference, the scaling factor $s_{scaling}$ becomes 1, 1.37, 1.86, and 2.59 for the spectra A, B, C, and D, respectively. Fig. A.12 shows the reconstructed $Im[\chi^{(3)}_{Res}(\nu)]$ spectrum of water obtained from CARS spectra using the different reference spectra measured under different conditions. Clearly, the unscaled reconstruction shown in fig. A.12 A results in different spectral amplitudes of one and the same sample, and thus we would not deduce the correct water concentrations. However, using the above determined scaling factors, the reconstructed spectra match almost perfectly, as shown in fig. A.12 B. The inset compares the determined concentration of water based on the reconstructed $Im[\chi^{(3)}_{Res}(\nu)]$ amplitude with and without scaling as a function of the ratio $\frac{\chi^{(3)}_{NR\ Sample}(\nu)}{\chi^{(3)}_{NR\ Ref}}$. For example for the ratio of $\frac{\chi^{(3)}_{NR\ Sample}(\nu)}{\chi^{(3)}_{NR\ Ref}} = 1.37$, the error of 24 % would already be significant!

Next, we consider the general case, where all four spectra ($\chi^{(3)}_{NR\ Sample1}(\nu)$, $\chi^{(3)}_{NR\ Ref1}$, $\chi^{(3)}_{NR\ Sample2}(\nu)$, $\chi^{(3)}_{NR\ Ref2}$) in eq. A.23 are needed. We will use the same spectrum A as in the

Figure A.12: Comparison of reconstructed $Im[\chi_{Res}^{(3)}(v)]$ spectra obtained from CARS measurements of neat water without (A) and with (B) taking into account the different measurement conditions for the reference spectra A, B, C, and D using the rescaling given by eq. A.25.

previous case, and compare it with a spectrum E recorded at 30 mW pump power, 5 mW Stokes power, and 100 ms spectrum dwell time. Both spectra are shown in fig. A.13 A. Using eq. A.23, the corresponding scaling factor $s_{scaling}$ reads $s_{scaling} = 1.1221$. As shown in fig. A.13 B,
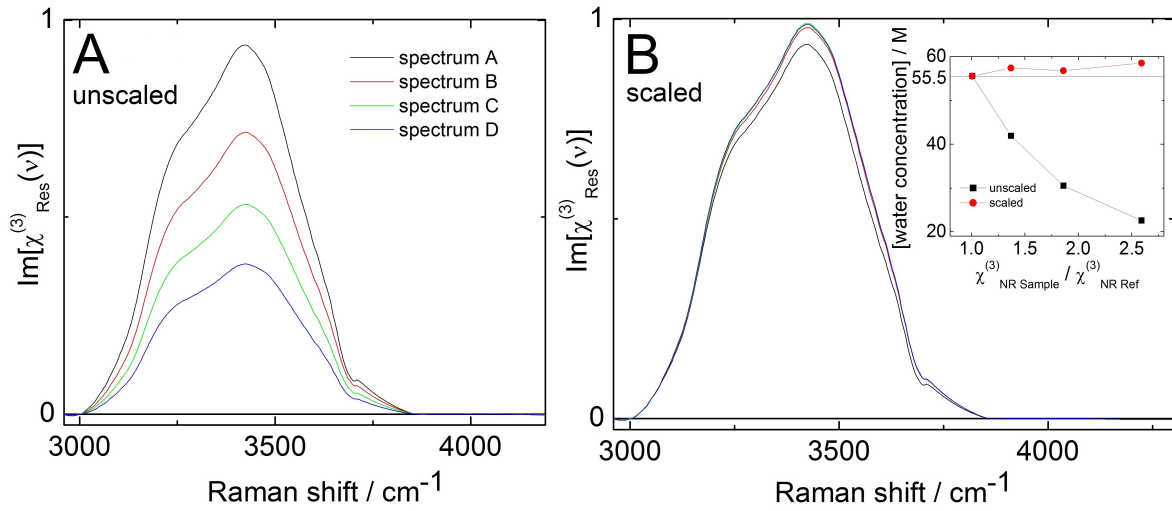
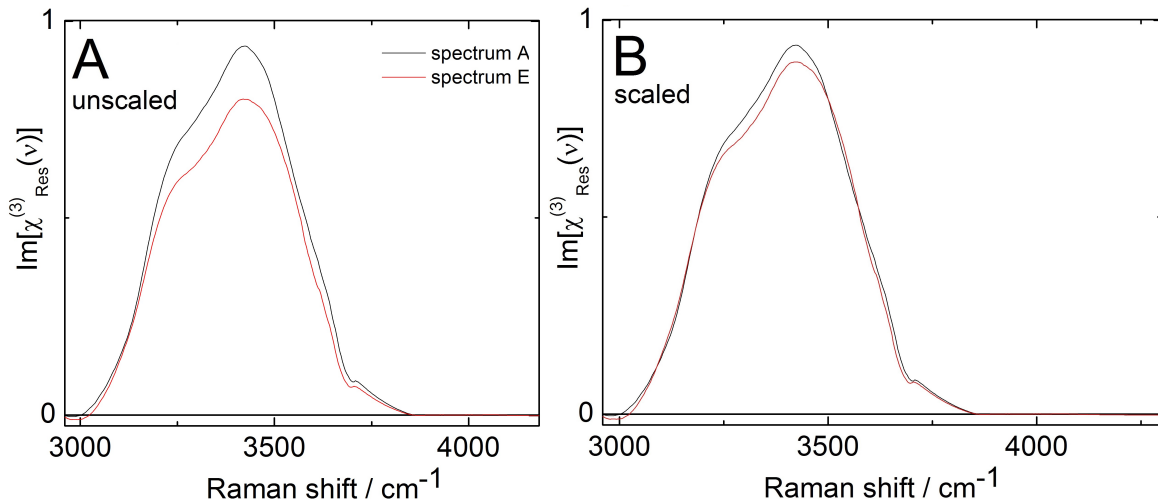

Figure A.13: Comparison of the reconstruction $Im[\chi_{Res}^{(3)}(v)]$ spectra obtained from CARS measurements of neat water without (A) and with (B) taking the different measurement conditions for spectra A and E into account, using the rescaling given by eq. A.23.

using the scaling factor results in almost perfectly matching peak intensities and thus a correct concentration is determined.

A.6.3 Conclusions

Reconstructed $Im[\chi^{(3)}_{Res}(\nu)]$ amplitudes from pixel spectra within one and the same hyperspectrum using the same reference CARS spectrum for the Stokes profile elimination can be directly compared with each other. However, the spectra that are reconstructed using different reference CARS spectra ($\chi^{(3)}_{NR\ Ref}$) for the Stokes profile elimination cannot directly be compared. By taking the scaling factor $s_{scaling}$ for the different reference spectra into account, the rescaled amplitudes of the reconstructed $Im[\chi^{(3)}_{Res}(\nu)]$ spectra can quantitatively be compared independent of which reference spectrum is used. The noise behaviour in reconstructed $Im[\chi^{(3)}_{Res}(\nu)]$ in nonresonant regions is in *cases a* and *b* the same. Fig. A.9 suggests, that it is favorable to use a reference CARS spectrum which results in $\frac{\chi^{(3)}_{NR\ Sample}}{\chi^{(3)}_{NR\ Ref}} = 1$. In practice, it is not possible to determine $\chi^{(3)}_{NR\ Ref}$ in an absolute manner, only the ratio $\frac{\chi^{(3)}_{NR\ Sample}(x,y,z,t)}{\chi^{(3)}_{NR\ Ref}}$ can be determined. Since it is a priori unknown, whether in the experiment *case a* or *case b* applies, this uncertainty can only be cicumvented by ensuring conditions where C_a and C_b are close to unity. In order to compare spectra that where processed using two different reference spectra $\chi^{(3)}_{NR\ Ref1} \neq \chi^{(3)}_{NR\ Ref2}$, the reconstructed amplitudes of $Im[\chi^{(3)}_{Res1}(\nu)]$ need to be rescaled by $\frac{\chi^{(3)}_{NR\ Ref2}}{\chi^{(3)}_{NR\ Ref1}}$ to allow for a quantitative comparison with the amplitudes $Im[\chi^{(3)}_{Res2}(\nu)]$.

The different cases laid out in this chapter do not need to be considered in spontaneous Raman scattering, where $Im[\chi^{(3)}_{Res}(\nu)]$ is measured directly. Another difference between spontaneous Raman spectroscopy and CARS is their noise characteristics. While there is no noise in a spontaneous Raman spectrum within the nonresonant region and the noise is highest at the resonance frequency, a different picture holds in the $Im[\chi^{(3)}_{Res}(\nu)]$ spectra reconstructed from CARS spectra. Due to the contribution of $\chi^{(3)}_{NR\ Sample}$ to the CARS spectra, noise is also present in the nonresonant region of the corresponding reconstructed $Im[\chi^{(3)}_{Res}(\nu)]$ spectrum. In *case b*, this noise is correlated with the sample concentration. Additionally, in CARS, the SNR is found to be smallest close but not on the resonance frequency. While the noise in a spontaneous Raman spectrum will be of Poissonain nature, it is not in the $Im[\chi^{(3)}_{Res}(\nu)]$ spectrum reconstructed from a measured CARS spectrum!

A.7 The Levinson Durbin recursion algorithm

Following Ng [69], the Levinson Durbin recursion algorithm for solving the Toeplitz equation in MEM (see section 3.3.1.2) will briefly be discussed here. We can solve the inverse Cholesky decomposition $\mathbf{U}^T\mathbf{C}\mathbf{U} = \mathbf{D}$ (with $\mathbf{D}$ being a diagonal matrix) by performing an **UDL** decomposition of $\mathbf{C}_m^{-1}$ at each iteration step m:

$$\mathbf{C}_{m+1}^{-1} = \begin{bmatrix} \mathbf{I_m} & \mathbf{r_m} \\ \mathbf{0} & \mathbf{1} \end{bmatrix} \begin{bmatrix} \mathbf{C}_m^{-1} & \mathbf{0} \\ \mathbf{0} & \delta_m^{-1} \end{bmatrix} \begin{bmatrix} \mathbf{I_m} & \mathbf{0} \\ \mathbf{r_m^T} & \mathbf{1} \end{bmatrix} \quad , m = 1, \ldots, (n-1) \quad , \tag{A.26}$$

while $\mathbf{C}_{m+1}$ can be written as an **LDU** decomposition:

$$\mathbf{C}_{m+1} = \begin{bmatrix} \mathbf{I_m} & \mathbf{0} \\ -\mathbf{r_m}^T & \mathbf{1} \end{bmatrix} \begin{bmatrix} \mathbf{C}_m & \mathbf{0} \\ \mathbf{0} & \delta_m \end{bmatrix} \begin{bmatrix} \mathbf{I_m} & -\mathbf{r_m} \\ \mathbf{0} & \mathbf{1} \end{bmatrix} \quad , m = 1, \ldots, (n-1) \ . \tag{A.27}$$

Here, the matrix $\mathbf{I_m}$ denotes the identity matrix. The matrices $\mathbf{C}_{m+1}^{-1}$ and $\mathbf{C}_{m+1}$ are connected via the anti-unity or exchange matrix $\mathbf{J_m}$, which is a matrix having all elements zero except the elements on the counterdiagonal being unity: $\mathbf{J}_m \mathbf{C}_m^T \mathbf{J}_m = \mathbf{C}_m$. In this way, we can calculate the scalar values δ_m, the diagonal elements of $\mathbf{D}$:

$$\delta_m = C_0 + \mathbf{C_m}^T \mathbf{J}_m \mathbf{r_m} \quad , m = 1, \ldots, (n-1) \ , \tag{A.28}$$

the Szegöe vectors $\mathbf{r_{m+1}}$ (the columns of $\mathbf{U}$):

$$\mathbf{r_{m+1}} = \begin{bmatrix} 0 \\ \mathbf{r_m} \end{bmatrix} + \gamma_m \begin{bmatrix} 1 \\ \mathbf{J}_m \mathbf{r_m} \end{bmatrix} \quad , m = 1, \ldots, (n-2) \ , \tag{A.29}$$

and the so called Schur parameters γ_m

$$\gamma_m = -\frac{C_{m+1} + \mathbf{C}_m^T \mathbf{r_m}}{\delta_m} \quad , m = 1, \ldots, (n-2) \ . \tag{A.30}$$

With $\mathbf{U}$ and $\mathbf{D}$ known, the solution is given by $a = \mathbf{U}\mathbf{D}^{-1}\mathbf{U}^T b$ and can be calculated via the Szegöe recurrence relation. It follows the Levinson Durbin algorithm as:

$$a_1 = \frac{b_1}{C_0} \qquad\qquad\qquad\qquad\qquad \text{solve 1x1 problem}$$

$$\delta_0 = C_0 \qquad\qquad\qquad\qquad\qquad \text{calculate first diagonal element of } \mathbf{D}$$

$$\textbf{for m=1:n-1} \qquad\qquad\qquad\qquad \text{Loop body, do up to the autocorrelation index } m$$

$$\gamma_{(m-1)} = -\frac{C_m + \mathbf{C}_{(1:m-1)}^T \mathbf{r}_{(1:\mathbf{m}-1)})}{\delta_{(m-1)}} \qquad\qquad \text{calculate new Schur parameter}$$

$$\mathbf{r}_{(2:m)} = \mathbf{r}_{(1:m-1)} + \gamma_{(m-1)}\mathbf{r}_{(m-1:-1:1)} \qquad\qquad \text{calculate new Szegöe vector}$$

$$r_1 = \gamma_{(m-1)}$$

$$\delta_m = C_0 + \mathbf{C}_{(1:m)}^T \mathbf{r}_{(m:-1:1)} \qquad\qquad \text{calculate diagonal elements of } \mathbf{D}$$

$$a_{(m+1)} = \frac{b_{(m+1)} + \mathbf{b}_{(1:m)}^T \mathbf{r}_{(1:m)}}{\delta_m} \qquad\qquad \text{induction step for entry } m+1 \text{ of solution vector}$$

$$\mathbf{a}_{(1:m)} = \mathbf{a}_{(1:m)} + a_{(m+1)}\mathbf{r}_{(1:m)} \qquad\qquad \text{update solution vector } \mathbf{a}$$

$$\tag{A.31}$$

A.8 Derivation of the dependence of the effective phase ϕ_{eff} from the ratio of maximum to minimum MEM phase excursions

The objective of this appendix is to find a relation between the maximum and minimum of the estimated phase spectrum $\phi_{estimated}(v)$ (see eq. 3.54) and the effective phase ϕ_{eff} (defined in eq. 3.42). The desired relation should be independent of the unknown $\chi^{(3)}_{Res}(v)$ and $\chi^{(3)}_{E\,eff}$. In order to deduce ϕ_{eff} from a normalized ratio of maximum to minimum estimated phase excursions

$$r_{phase}(\phi_{estimated}(v)) = \frac{max(\phi_{estimated}(v)) - min(\phi_{estimated}(v))}{max(\phi_{estimated}(v))} \quad , \tag{A.32}$$

we need to express the angles that characterize tangents of form $y = mx$ from the origin of the complex plane to the circle described by the vibrational resonance as a function of ϕ_{eff} (see fig. A.14). This is a circle of radius $\frac{max(Im[\chi^{(3)}_{Res}(v)])}{2}$ that is rotated around $[\chi^{(3)}_{E\,eff}, 0]$ by the angle ϕ_{eff}, and is given in cartesian coordinates as follows:

$$\left[x - \chi^{(3)}_{E\,eff} - \frac{max(Im[\chi^{(3)}_{Res}(v)])}{2} sin(\phi_{eff}) \right]^2 + \left[y - \frac{max(Im[\chi^{(3)}_{Res}(v)])}{2} cos(\phi_{eff}) \right]^2 = \left[\frac{max(Im[\chi^{(3)}_{Res}(v)])}{2} \right]^2 . \tag{A.33}$$

After substitution of $y = mx$ in eq. A.33 and rearranging, we first obtain a quadratic equation in x of the form $x^2 A_1 - xB_1 + C_1 = 0$ with

$$A_1 = (1 + m^2) \tag{A.34}$$

$$B_1 = 2\chi^{(3)}_{E\,eff} + max(Im[\chi^{(3)}_{Res}(v)])sin(\phi_{eff}) + m\,max(Im[\chi^{(3)}_{Res}(v)])cos(\phi_{eff}) \tag{A.35}$$

$$C_1 = \chi^{(3)}_{E\,eff} \left[max(Im[\chi^{(3)}_{Res}(v)])sin(\phi_{eff}) + \chi^{(3)}_{E\,eff} \right] . \tag{A.36}$$

We need the discriminant to be zero, so we need to solve $B_1^2 - 4A_1C_1 = 0$ for $m(\phi_{eff})$. This leads to a quadratic equation in m of the form $m^2 A_2 + mB_2 + C_2 = 0$ with

$$A_2 = (max(Im[\chi^{(3)}_{Res}(v)])cos(\phi_{eff}))^2 - 4\chi^{(3)}_{E\,eff} - 4max(Im[\chi^{(3)}_{Res}(v)])\chi^{(3)}_{E\,eff}sin(\phi_{eff}) \tag{A.37}$$

$$B_2 = 2(max(Im[\chi^{(3)}_{Res}(v)]))^2 sin(\phi_{eff})cos(\phi_{eff}) + 4max(Im[\chi^{(3)}_{Res}(v)])\chi^{(3)}_{E\,eff}cos(\phi_{eff}) \tag{A.38}$$

$$C_2 = (max(Im[\chi^{(3)}_{Res}(v)])sin(\phi_{eff}))^2 \quad , \tag{A.39}$$

with the solution

$$m_{1,2}(\phi_{eff}) = \frac{-cos(\phi_{eff})\left[sin(\phi_{eff})\left[\frac{max(Im[\chi^{(3)}_{Res}(v)])}{2} \right]^2 + \frac{max(Im[\chi^{(3)}_{Res}(v)])}{2}\chi^{(3)}_{E\,eff} \right] \pm \frac{max(Im[\chi^{(3)}_{Res}(v)])}{2}\sqrt{E(\phi_{eff})}}{\left[\frac{max(Im[\chi^{(3)}_{Res}(v)])cos(\phi_{eff})}{2} \right]^2 - sin(\phi_{eff})\chi^{(3)}_{E\,eff}max(Im[\chi^{(3)}_{Res}(v)]) - (\chi^{(3)}_{E\,eff})^2} \tag{A.40}$$

where $E(\phi_{eff}) = (\chi^{(3)}_{E\,eff})^2 + max(Im[\chi^{(3)}_{Res}(v)])\chi^{(3)}_{E\,eff}sin(\phi_{eff})$. $\tag{A.41}$

Now the slopes $m_1(\phi_{eff})$ and $m_2(\phi_{eff})$ correspond to the maximum and minimum phase angles as

$$max(\phi_{estimated}(\nu)) = tan^{-1}[m_1(\phi_{eff})]$$

$$min(\phi_{estimated}(\nu)) = tan^{-1}[m_2(\phi_{eff})] \ . \tag{A.42}$$

Substituting eq. A.40 and eq. A.42 into eq. A.32 results in a complex expression for r_{phase}, which is neither beautiful nor simple. Furthermore, $r_{phase}(\phi_{eff})$ will also be a function of the unknown $\chi^{(3)}_{Res}(\nu)$ and $\chi^{(3)}_{E\ eff}$.

To obtain a simplified expression for $r_{phase}(\phi_{eff})$, we use here a trigonometric approach, as illustrated in fig. A.14. With $b = cos(\phi_{eff})\frac{max(Im[\chi^{(3)}_{Res}(\nu)])}{2}$ and $c =$
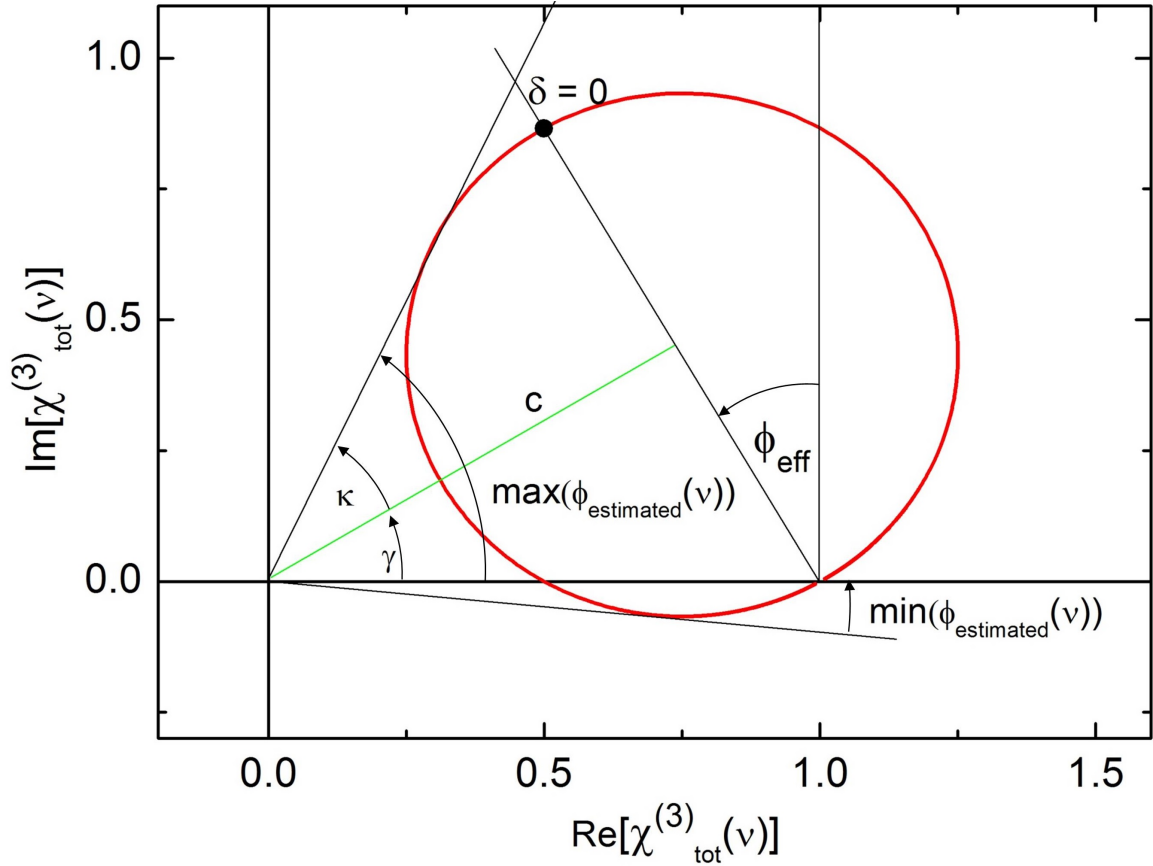

Figure A.14: Representation of a simulated total susceptibility $\chi^{(3)}_{tot}(\nu)$ in the complex plane for the geometrical derivation of the effective phase ϕ_{eff} from the ratio of maximum to minimum phase excursions. Simulation parameters are $A = 1 \ cm^{-1}$, $\chi^{(3)}_{E\ eff} = 1$, $\phi_{E\ eff} = 0$, and $\phi_{eff} = \phi_R = \frac{\pi}{6}$ using the full model given by eq. 3.40.

$\sqrt{(\chi^{(3)}_{E\ eff})^2 + sin(\phi_{eff})\chi^{(3)}_{E\ eff} max(Im[\chi^{(3)}_{Res}(\nu)]) + \left[\frac{max(Im[\chi^{(3)}_{Res}(\nu)])}{2}\right]^2}$, one obtains the angles $\kappa = sin^{-1}\left(\frac{b}{cos(\phi_{eff})c}\right)$ and $\gamma = sin^{-1}\left(\frac{b}{c}\right)$. In analogy to eq. A.42, we obtain the phase angle extrema as

$$max(\phi_{estimated}(\nu)) = \kappa + \gamma$$

$$min(\phi_{estimated}(\nu)) = \kappa - \gamma \ . \tag{A.43}$$

Substitution into eq. A.32 yields

$$\frac{1}{r_{phase}(\phi_{eff})} = \frac{1}{2}(1 + \frac{\gamma}{\kappa}) \ . \tag{A.44}$$

The $\chi_{tot}^{(3)}(\nu)$ values corresponding to the phase extrema, $\chi_{tot}^{(3)}(max(\phi_{estimated}(\nu, \phi_{eff})))$ and $\chi_{tot}^{(3)}(min(\phi_{estimated}(\nu, \phi_{eff})))$, are plotted in the complex plane as a function of the angle ϕ_{eff} and for different ratios of $1 \leq \frac{\chi_{Res}^{(3)}}{\chi_{E\,eff}^{(3)}} \leq 10$ in fig. A.15. It can be observed, how the
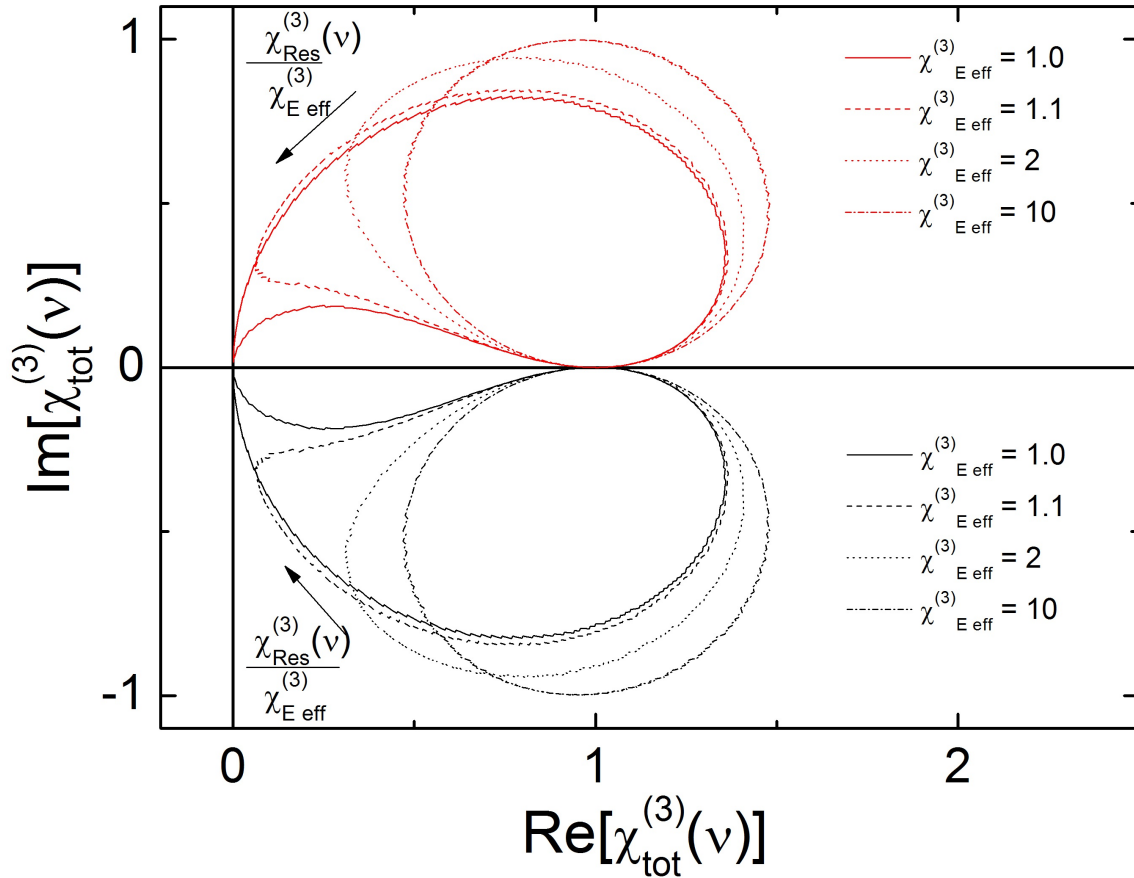

Figure A.15: Loci of $\chi_{tot}^{(3)}(max(\phi_{estimated}(\nu, \phi_{eff})))$ (red) and $\chi_{tot}^{(3)}(min(\phi_{estimated}(\nu, \phi_{eff})))$ (black) phase as a function of ϕ_{eff} and for different ratios of $\frac{\chi_{Res}^{(3)}}{\chi_{E\,eff}^{(3)}}$. Simulation parameters are $\chi_{Res}^{(3)}(\nu) = 1$, $\phi_{E\,eff} = 0$, $\chi_{E\,eff}^{(3)} = 1, 1.1, 2$, and 10 (eq. 3.40). The maximum and minimum of $\chi_{tot}^{(3)}(\phi_{estimated}(\nu, \phi_{eff}))$ follow more and more kidney-shaped curves with increasing ratio $\frac{\chi_{Res}^{(3)}}{\chi_{E\,eff}^{(3)}}$ in a counterclockwise or clockwise manner, respectively. (The loci corresponding to $\chi_{E\,eff}^{(3)} = 1.1, 2$, and 10 have been shifted to $\chi_{E\,eff}^{(3)} = 1$ for better visibility by 0.1, 1, and 9, respectively).

curve changes its form from being circular for $\frac{\chi_{Res}^{(3)}(\nu)}{\chi_{E\,eff}^{(3)}} \ll 1$ to becoming more and more kidney-shaped when $\frac{\chi_{Res}^{(3)}(\nu)}{\chi_{E\,eff}^{(3)}}$ approaches unity. However, the expression given in eq. A.44 still needs to be uncoupled from the unknowns $\chi_{Res}^{(3)}(\nu)$ and $\chi_{E\,eff}^{(3)}$. When we use the abbreviation

$$D = \frac{max(Im[\chi^{(3)}_{Res}(\nu)])}{2\sqrt{(\chi^{(3)}_{E\,eff})^2 + sin(\phi_{eff})\chi^{(3)}_{E\,eff}max(Im[\chi^{(3)}_{Res}(\nu)]) + \left[\frac{max(Im[\chi^{(3)}_{Res}(\nu)])}{2}\right]^2}}$$ and perform a Tailor expansion of the ratio

$\frac{\gamma}{\kappa} = \frac{sin^{-1}(cos(\phi_{eff})D)}{sin^{-1}(D)}$ around $D = 0$, one obtains

$$\frac{\gamma}{\kappa} = cos(\phi_{eff}) - \frac{1}{6}D^2cos(\phi_{eff})sin^2(\phi_{eff}) - O(D^4). \tag{A.45}$$

The Tailor expansion corresponds to the assumption that $\frac{Im[\chi^{(3)}_{Res}(\nu)]}{2} << c$, which rearranged gives the following condition

$$sin(\phi_{eff})Im[\chi^{(3)}_{Res}(\nu)] << \chi^{(3)}_{E\,eff} \tag{A.46}$$

Whenever $Im[\chi^{(3)}_{Res}(\nu)] \geq \chi^{(3)}_{E\,eff}$ and $\phi_{eff} \in [0, \pi]$, the rotated resonance can include the complex plane's origin, and the representation of phase angle extrema as being the tangents to the locus of the resonance becomes impossible. The limiting case where $Im[\chi^{(3)}_{Res}(\nu)] = \chi^{(3)}_{E\,eff}$ is also illustrated in fig. A.15. Here, the most left locus passes through the origin of the complex plane. When only the first term of eq. A.45, $\frac{\gamma}{\kappa} \cong cos(\phi_{eff})$, is substituted into A.44, one obtains

$$\frac{1}{r_{phase}(\phi_{eff})} = \frac{1}{2}(1 + cos(\phi_{eff})) = cos(\frac{\phi_{eff}}{2})^2. \tag{A.47}$$

Using $x = cos^{-1}(2y-1) = 2cos^{-1}(\sqrt{y})$ as the inverse of $y = cos(\frac{x}{2})^2$ gives the desired expression for ϕ_{eff} as a function of r_{phase}

$$\phi_{eff}(r_{phase}) = cos^{-1}\left(\frac{2}{r_{phase}} - 1\right). \tag{A.48}$$

In general, $\phi_{eff} \in \mathbb{R}$ can have any value $0 \leq \phi_{eff} \leq 2\pi$. By the order of the appearance of $min(\phi_{estimated}(\nu))$ and $max(\phi_{estimated}(\nu))$, (what "comes first"), one can determine $\phi_{eff} \in [0, \pi)$ or $\phi_{eff} \in (\pi, 2\pi]$. The factor δ_R then represents the sign correction parameter for eq. A.48

$$\delta_R = \begin{cases} 1 & \nu\Big|_{max(\phi_{estimated}(\nu))} < \nu\Big|_{min(\phi_{estimated}(\nu))} \\ -1 & \nu\Big|_{min(\phi_{estimated}(\nu))} < \nu\Big|_{max(\phi_{estimated}(\nu))} \end{cases} \tag{A.49}$$

Taking into account the above case analysis of eq. A.49, the final expression for the determination of the effective phase ϕ_{eff} is

$$\phi_{eff} = \delta_R\, cos^{-1}\left(\frac{2}{r_{phase}} - 1\right). \tag{A.50}$$

curriculum vitae

Personal information

- Full Name: Gregor Fabian Magnus Hehl

- Date of Birth: 16/02/1980 in Tübingen

- Nationality: German

Education

- PhD student at University Stuttgart, 3rd Institute of Physics (since 06/2008)

- Diploma in Physics at the University of Stuttgart (05/2008)

- Studies in Physics at the University of Stuttgart (10/2002 - 07/2008)

- Diploma in Engineering at the University of Cooperative Education Stuttgart (09/2002)

- Qualification as a state-certified engineer assistant (11/2001)

- Studies in Engineering at the University of Cooperative Education Stuttgart (10/1999 - 09/2002)

- Qualification as a state-certified physical-technical assistant (6/1999)

- A-levels at Kerschensteinerschule Stuttgart Feuerbach (6/1999)

Prices

- PCCP hot topic poster price, awarded at the Bunsentagung 2009 (21/05/2009-23/05/2009)

- Best poster price, awarded at the conference on Coherent Raman Scattering Microscopy (microCARS2012) (14/10/2012-16/10/2012)

Short term scientific missions

- Visiting researcher at the physics and astronomy department, University of Exeter, UK (18/01/2009-31/01/2009)

- Visiting researcher at the physics and astronomy department, University of Exeter, UK (31/01/2010-07/02/2010)